

Document Version

Final published version

Citation (APA)

Giri Ajay, A. (2026). *VAWTs Next? A Numerical Exploration into the Rotor and Wake Dynamics of Vertical-Axis Wind Turbines*. [Dissertation (TU Delft), Delft University of Technology]. <https://doi.org/10.4233/uuid:97663e4e-7db5-493e-9015-de1589129335>

Important note

To cite this publication, please use the final published version (if applicable).
Please check the document version above.

Copyright

In case the licence states "Dutch Copyright Act (Article 25fa)", this publication was made available Green Open Access via the TU Delft Institutional Repository pursuant to Dutch Copyright Act (Article 25fa, the Taverne amendment). This provision does not affect copyright ownership.
Unless copyright is transferred by contract or statute, it remains with the copyright holder.

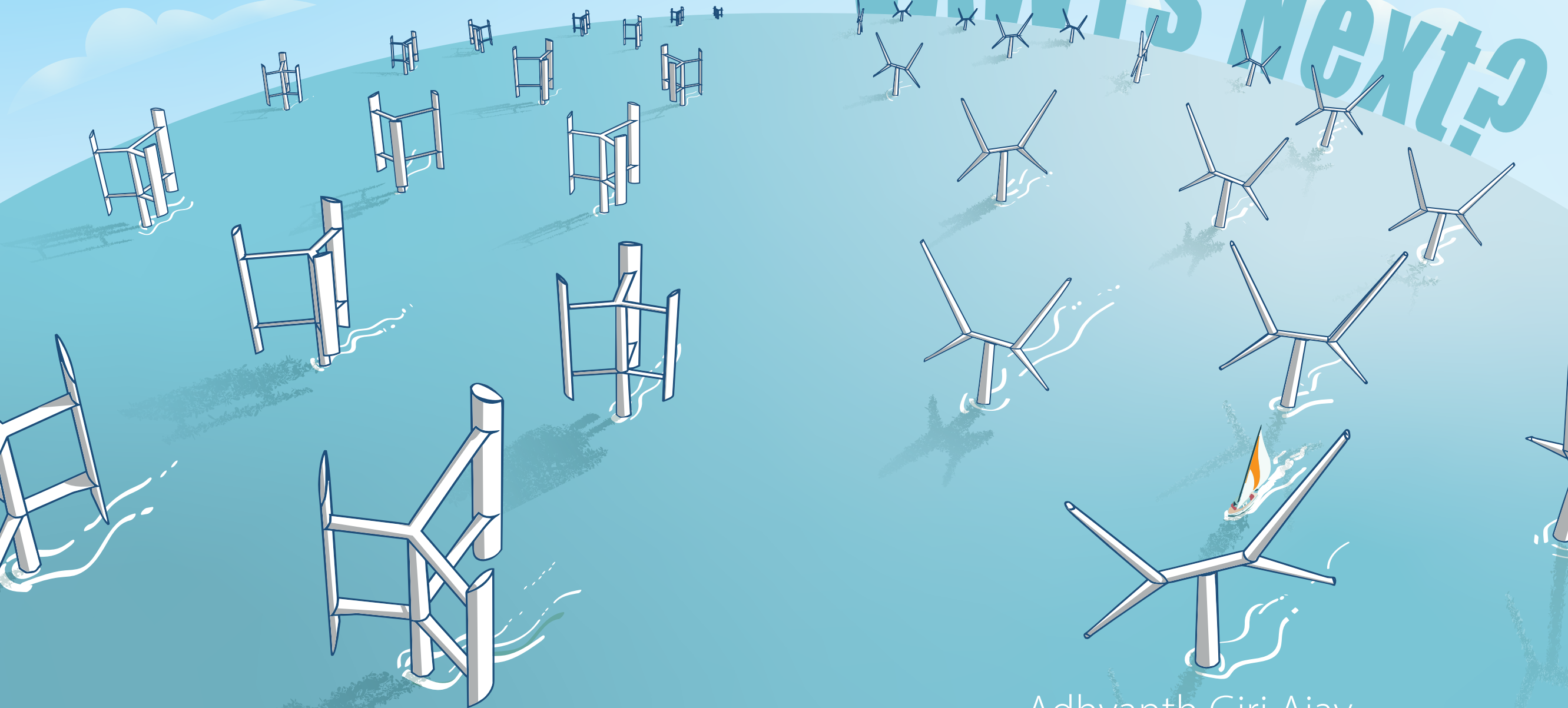
Sharing and reuse

Other than for strictly personal use, it is not permitted to download, forward or distribute the text or part of it, without the consent of the author(s) and/or copyright holder(s), unless the work is under an open content license such as Creative Commons.

Takedown policy

Please contact us and provide details if you believe this document breaches copyrights.
We will remove access to the work immediately and investigate your claim.

VAWTS Next?



Adhyanth Giri Ajay

VAWTs NEXT?

**A NUMERICAL EXPLORATION INTO THE ROTOR AND WAKE
DYNAMICS OF VERTICAL-AXIS WIND TURBINES**

Propositions

accompanying the dissertation

VAWTs NEXT?

by

Adhyanth GIRI AJAY

1. To catch up to horizontal-axis wind turbine technological maturity, researchers must shift to higher numerical fidelity to capture the inherent 3D aerodynamics of vertical-axis wind turbines. [Chapter 3]
2. Numerical validation of vertical-axis wind turbine wakes at low Reynolds numbers is fundamentally compromised by uncertainty in numerical inputs. [Chapter 6]
3. Blade pitch control establishes vertical-axis wind turbines as a viable technology for achieving higher power density in large-scale wind farms [Chapter 7]
4. Modern academic peer-reviews should undergo Turing tests before being accepted as a platform that advocates scientific rigour.
5. Procrastination is the PhD candidate's secret weapon to finish the thesis - pausing one task by making progress on another.
6. Tourist visas are illusions. It is bureaucracy's way of enforcing a system where the randomness of birth determines your right to roam.
7. If professional software companies truly believe in 'global markets,' then regional pricing should be mandatory. Anything else is exploitative.
8. Non-fiction books often inflate a core principle into hundreds of pages - prioritising commercial packaging over intellectual density.
9. Memes are the most effective way to keep up to date with geopolitics.
10. Video games have replaced novels as the most engaging form of storytelling today.

These propositions are regarded as opposable and defensible, and have been approved as such by the promotor Prof. dr. ir. R. De Breuker and copromotor Dr. ir. D.A.M. De Tavernier.

VAWTs NEXT?

**A NUMERICAL EXPLORATION INTO THE ROTOR AND WAKE
DYNAMICS OF VERTICAL-AXIS WIND TURBINES**

Dissertation

for the purpose of obtaining the degree of doctor
at Delft University of Technology
by the authority of the Rector Magnificus,
Prof. dr. ir. H. Bijl,
chair of the Board for Doctorates
to be defended publicly on
Wednesday 6 May 2026 at 17:30

by

Adhyanth GIRI AJAY

This dissertation has been approved by the (co)promotors

Composition of the doctoral committee:

Rector Magnificus,	chairperson
Prof. dr. ir. R. De Breuker,	Delft University of Technology, promotor
Prof. dr. ir. C.J. Simao Ferreira,	Delft University of Technology, promotor
Dr. ir. D.A.M. De Tavernier,	Delft University of Technology, copromotor

Independent Members:

Prof. dr. S.J. Watson,	Delft University of Technology
Prof. dr. ir. J.W. van Wingerden,	Delft University of Technology
Prof. dr. D.T. Griffith,	The University of Texas at Dallas
Dr. A. Goude,	Uppsala University
Dr. A. Sciacchitano,	Delft University of Technology, <i>reserve member</i>

This research was partially funded by the European Union's Horizon 2020 research and innovation program under grant agreement No. 101007135.



Keywords: Vertical-axis wind turbines, X-Rotor, Wakes, CFD, Numerical simulation, Wake control.

Printed by: Proefschriftspecialist

Cover: Designed by Adhyanth Giri Ajay and Prem Agaran

Style: TU Delft House Style, with modifications by Dr. Moritz Beller and Adhyanth Giri Ajay (<https://github.com/Inventitech/phd-thesis-template>)

Flipbook: Designed by Dr. Erik Fritz with modifications from Adhyanth Giri Ajay (<https://github.com/erikfritz/FlipbookPageFooter>)

ISBN 978-94-6518-296-4

An electronic version of this dissertation is available at
<http://repository.tudelft.nl>.

This dissertation contains no errors, only happy accidents.

CONTENTS

Summary	xi
Samenvatting	xiii
1 Introduction and motivation	1
1.1 Background and Context	2
1.2 Thesis aim and the research questions	4
1.3 Thesis structure	5
2 The state-of-the-art	9
2.1 History of VAWTs and VAWT designs	10
2.2 The X-Rotor turbine	11
2.3 VAWT aerodynamics	12
2.3.1 Rotor aerodynamics	12
2.3.2 Wake aerodynamics	15
2.4 VAWT modelling	19
2.4.1 Low fidelity models	19
2.4.2 Medium fidelity models	22
2.4.3 High fidelity models	24
2.4.4 Secondary effects	25
3 Numerical fidelity requirements to capture X-Rotor physics	27
3.1 Introduction	28
3.2 Methodology	28
3.2.1 Aerodynamic models	28
3.2.2 Test setup	29
3.3 Results and discussions	30
3.3.1 Study of rotor power and thrust	30
3.3.2 Study of blade forces	32
3.3.3 Vertical induction and inflow	36
3.4 Conclusions	38
4 Near-wake characterisation and validation of a scaled X-Rotor	41
4.1 Introduction	42
4.2 Experimental approach	42
4.2.1 Scaled X-Rotor model	42
4.2.2 Experimental set-up	43
4.2.3 Uncertainty of the flowfield measurements	43

4.3	Numerical setup	44
4.3.1	Free-wake vortex model	45
4.3.2	NACA0021 airfoil dataset and its uncertainty.	45
4.3.3	Dynamic stall and flow curvature models	45
4.3.4	Case matrix and simulation procedure	46
4.4	Results	47
4.4.1	Validation study - non-pitched case	47
4.4.2	Validation study - pitched case	51
4.4.3	Influence of cone angle on the velocity field	56
4.5	Conclusions	59
5	The effect of rotor geometry on wake recovery	61
5.1	Introduction	62
5.2	Methodology.	62
5.2.1	Simulation setup	62
5.2.2	Scaling the H-Rotor	63
5.2.3	Characteristic length scale for the wake similarity	63
5.2.4	Test geometry and setup	64
5.3	Results and discussion	65
5.3.1	Rotor performance and loads assessment.	65
5.3.2	Vortex system and corresponding velocity fields	67
5.3.3	Wake displacement.	72
5.3.4	Available Power (AP).	74
5.3.5	Streamwise momentum recovery rates	77
5.3.6	Mean kinetic energy flux.	80
5.4	Conclusions	83
6	Wake sensitivity to airfoil data, dynamic stall, and regularisation kernel	87
6.1	Introduction	88
6.2	Methodology.	88
6.2.1	Scaled X-Rotor model	88
6.2.2	Experimental setup of the X-Rotor	88
6.2.3	Numerical setup and computational domain	90
6.3	Results	92
6.3.1	Sensitivity to airfoil polar data	92
6.3.2	Sensitivity to dynamic stall and flow curvature effects	94
6.3.3	Sensitivity to regularisation kernel ϵ	96
6.3.4	Fixed blade pitch offsets	97
6.4	Conclusions	98
7	Wake recovery physics in wind farms with wake control	101
7.1	Introduction	102
7.2	Methodology.	102
7.2.1	Test cases and wind farm layout	102
7.2.2	Model setup	103

7.3	Results	104
7.3.1	Wake topology and vorticity system	105
7.3.2	Wake center deflection	107
7.3.3	Available Power	109
7.3.4	Mean kinetic energy flux	112
7.3.5	Rotor and farm performance	115
7.4	Conclusions and future expansion	117
8	Conclusions and future recommendations	119
8.1	Key findings	120
8.2	Future recommendations	122
A	Parametric definition of the blade geometry	125
B	Free-wake vortex azimuthal discretisation sensitivity	129
C	URANS CFD Setup	131
D	PowerFLOW Setup	133
E	Modifications to <i>turbinesFoam</i>	135
E.1	Tuning ϵ/Δ_{grid} for optimum blade load representation	135
E.2	Inclusion of cone angle	137
F	Wake center deflection	139
G	Turbulence intensity of the H- and X-Rotor	141
H	Sensitivity study: influence of vortex core size, dynamic stall, and the choice of Reynolds numbers	143
I	Turbulence intensity of the H-Rotor wind farm	147
	Bibliography	149
	Acknowledgments	167
	List of Publications	171
	Curriculum Vitæ	173

SUMMARY

The accelerating demand for renewable energy has intensified the search for efficient and innovative solutions, particularly within the offshore wind-energy sector. While horizontal-axis wind turbines currently dominate the market, vertical-axis wind turbines (VAWTs) have emerged as a promising alternative – especially for offshore and urban environments where compactness, reduced noise, and improved windfarm power density are crucial. Nevertheless, despite their potential, the large-scale deployment of VAWTs remains constrained by an incomplete understanding of their aerodynamic performance, wake dynamics, and the downstream effects of these wakes within wind farms.

Beyond conventional VAWT designs, novel turbine concepts are being developed to address the limitations of the traditional Darrieus rotor. One such concept, the X-Rotor, seeks to reduce the Levelised Cost of Energy (LCoE) and enhance the competitiveness of VAWTs in the offshore market. However, its geometry inherently induces strong three-dimensional flow features that cannot be adequately captured using the commonly employed, computationally economical, two-dimensional numerical tools.

This dissertation advances the understanding of VAWT aerodynamics in three key areas: (a) it identifies the discrepancies in blade loading predictions among numerical models that emerge when the inherently three-dimensional aerodynamic effects are neglected under operational conditions; (b) it establishes the relationships between rotor geometry and wake dynamics—both with and without wake control strategies—by quantifying wake recovery and energy replenishment resulting from changes in the vortex system; and (c) it assesses the effectiveness of blade pitch-based wake control strategies in large-scale offshore VAWT wind farms subjected to simulated offshore inflow conditions.

Firstly, this dissertation systematically compares the blade and rotor performance of the full-scale X-Rotor geometry across a range of numerical models, from two-dimensional (2D) Blade Element Momentum (BEM) methods to fully blade-resolved three-dimensional (3D) Computational Fluid Dynamics (CFD). Rotor performance metrics—including power, thrust, and blade normal and tangential forces—were evaluated across different tip-speed ratios and blade pitch angles. The study demonstrated that Free-wake Vortex Models (FVM), which account for the full three-dimensional flowfield, provide a practical balance between computational cost and accuracy for simulating VAWTs. Furthermore, the analysis quantified changes in vertical induction due to blade pitch offsets, highlighting significant discrepancies in predicted rotor loads between low-fidelity 2D models and higher-fidelity 2D approaches.

In addition, a validation study of FVM near-wake predictions was performed against experimental Particle Image Velocimetry (PIV) data at different blade pitch angles using a scaled-down X-Rotor model. The study qualitatively and quantitatively confirmed the capability of FVM to capture near-wake dynamics and blade forces, while also identifying limitations in cases with large blade pitch offsets. These limitations were traced to inaccuracies



racies in the input airfoil polar data at low Reynolds numbers, which significantly affected model accuracy.

The influence of rotor geometry on advective wake recovery under blade pitch offsets was also investigated by comparing the X-Rotor with an equivalent-thrust Darrieus H-Rotor using an Actuator Line Model (ALM) and CFD. Results revealed fundamental differences in the vortex systems generated by the two geometries across different pitch angles, and the corresponding effects on wake recovery rates were quantified. The study also demonstrated the sensitivity of ALM predictions to model inputs—including airfoil polars, regularisation kernels, and treatments of dynamic stall and flow curvature—thereby underscoring the challenges of validating wake-prediction models against low-Reynolds-number experiments.

Finally, the wake recovery of a VAWT wind farm comprising H-Rotors was examined, focusing on wake interactions, kinetic energy replenishment, and the influence of wind shear. It was shown that synchronously pitching the blades of all turbines increased the overall farm power density by 15–41% relative to the baseline case without pitch offsets. This improvement was attributed to enhanced kinetic energy replenishment through advective mechanisms driven by rotor tip vortices. The variation in power-density gains was linked to inter-turbine vortex interactions, which reduced replenishment efficiency in certain configurations.

Overall, this dissertation demonstrates that accurate prediction and control of VAWT performance require models that capture the inherently three-dimensional flowfield and wake dynamics. It establishes the FVM as a computationally efficient yet accurate tool for rotor-scale predictions, highlights the sensitivity of wake models to input conditions, and quantifies the role of rotor geometry and blade pitch offsets in shaping wake recovery. Most importantly, it provides the first proof-of-concept that synchronous blade pitching can substantially enhance power density in large offshore VAWT wind farms, thereby positioning VAWTs as a viable and competitive option for future high-density renewable energy systems.

SAMENVATTING

De toenemende vraag naar hernieuwbare energie heeft de zoektocht naar efficiënte en innovatieve oplossingen, met name in de offshore windenergiesector, verder aangescherpt. Hoewel horizontale as windturbines momenteel de markt domineren, zijn verticale as windturbines (VAWTs) naar voren gekomen als een veelbelovend alternatief – vooral voor offshore en stedelijke omgevingen, waar compactheid, lagere geluidsniveaus en een hogere windparkrendementen cruciaal zijn. Desondanks blijft grootschalige inzet van VAWTs beperkt door een onvolledig begrip van hun aerodynamische prestaties, zogdynamica en de stroomafwaardse effecten van deze wervels binnen windparken.

Naast de conventionele VAWT-ontwerpen worden nieuwe turbineconcepten ontwikkeld om de beperkingen van de traditionele Darrieus-rotor te overwinnen. Eén van deze concepten, de X-Rotor, is ontworpen om de genivelleerde energiekosten (LCoE) te verlagen en de concurrentiekracht van VAWTs op de offshore markt te vergroten. De geometrie van de X-Rotor introduceert echter van nature sterke driedimensionale stromingskenmerken, die niet adequaat kunnen worden berekend door de vaak gebruikte, numerieke goedkope, tweedimensionale modellen.

Dit proefschrift breidt het begrip van VAWT-aerodynamica op drie belangrijke gebieden: (a) het identificeert de verschillen in bladbelastingsvoorspellingen tussen numerieke modellen die ontstaan wanneer intrinsiek driedimensionale aerodynamische effecten worden verwaarloosd onder operationele omstandigheden; (b) het legt de relaties vast tussen rotor geometrie en zog-dynamica – zowel met als zonder zog-controlestrategieën – door het kwantificeren van het zogherstelproces en energierugwinning als gevolg van veranderingen in het wervelsysteem; en (c) het beoordeelt de effectiviteit van zog-controlestrategieën waarbij de bladhoek wordt gebruikt in grootschalige offshore VAWT-windparken onder gesimuleerde instroomcondities.

Ten eerste vergelijkt dit proefschrift systematisch de prestaties van bladen en rotor van de full-scale X-Rotor-geometrie over een reeks numerieke modellen, van tweedimensionale (2D) Blade Element Momentum (BEM) methoden tot driedimensionale CFD modellen waarbij het windturbineblad volledig wordt opgelost. Rotorprestatieparameters – waaronder vermogen, stuwkracht en normale en tangentiële bladkrachten – werden geëvalueerd voor verschillende tipsnelheidsverhoudingen en bladhoekinstellingen. De studie toonde aan dat vrije-zogwervelmodellen (FVM), die rekening houden met het volledige driedimensionale stromingsveld, een praktische balans bieden tussen rekenkracht en nauwkeurigheid voor het simuleren van VAWTs. Bovendien kwantificeerde de analyse veranderingen in verticale inductie als gevolg van bladhoekverstelling, waarbij aanzienlijke afwijkingen in voorspelde rotorbelastingen tussen minder-fideliteit 2D-modellen en meer geavanceerde benaderingen werden aangetoond.

Daarnaast werd een validatiestudie uitgevoerd vooruitgevoerd voor de voorspellingen van het zog dicht bij de rotor met FVM ten opzichte van ten opzichte van experimentele Particle Image Velocimetry (PIV) gegevens bij verschillende bladhoekinstellingen met een



geschaalde X-Rotor. De studie bevestigde zowel kwalitatief als kwantitatief dat FVM de zogdynamica dicht bij de rotor en bladkrachten nauwkeurig kan voorspellen, terwijl ook de beperkingen in gevallen met grote bladhoekverstelling werden geïdentificeerd. Deze beperkingen waren terug te voeren op onnauwkeurigheden in de input van de airfoil polar data bij lage Reynolds getallen, wat de modelnauwkeurigheid significant beïnvloedde.

De invloed van rotor-geometrie op zogherstel onder bladhoekverstelling werd verder onderzocht door de X-Rotor te vergelijken met een equivalent stuwkracht Darrieus H-Rotor met behulp van een Actuator Line Model (ALM) en CFD. Resultaten toonden fundamentele verschillen in de wervelsystemen die door beide geometrieën werden gegenereerd bij verschillende bladhoekinstellingen, en de bijbehorende effecten op het zogherstel werden gekwantificeerd. De studie toonde ook de gevoeligheid van ALM-voorspellingen voor modelinput aan – inclusief airfoil profielprestatie, regularisatiekernels, en behandelingen van dynamische stromingsloslating en stroomlijnkromming – waarmee de uitdagingen bij het valideren van zogvoorspellingsmodellen tegen lage Reynoldsgetalexperimenten werden benadrukt.

Ten slotte werd het zogherstel van een VAWT-windpark bestaande uit H-Rotors onderzocht, met focus op zoginteracties, kinetische energieherstel en de invloed van windscherping. Er werd aangetoond dat het synchroon instellen van de bladen van alle turbines de algehele windparkrendement met 15–41% verhoogt ten opzichte van het basisgeval zonder bladhoekverstelling. Deze verbetering werd toegeschreven aan verhoogd kinetisch energieherstel via advectione mechanismen veroorzaakt door rotortipwervels. De variatie in vermogensdichtheidstoename werd gelinkt aan interacties tussende wervels van de turbines, die de efficiëntie van het herstel in bepaalde configuraties verminderden.

Samenvattend toont dit proefschrift aan dat nauwkeurige voorspelling en controle van VAWT-prestaties modellen vereist die het inherent driedimensionale stromingsveld en de zogdynamica vastleggen. Het bevestigt FVM als een efficiënte maar nauwkeurige tool voor rotorprestatievoorspellingen, benadrukt de gevoeligheid van zogmodellen voor inputcondities, en kwantificeert de rol van rotorgeometrie en bladhoekverstelling bij het vormgeven van zogherstel. Het belangrijkste is dat het de eerste proof-of-concept heeft aangetoond dat synchrone bladinstelling het vermogen van grote offshore VAWT-windparken substantieel kan verhogen, waarmee VAWTs een haalbare en concurrerende optie vormen voor toekomstige hernieuwbare energiesystemen met een hoge energiedichtheid.

1

INTRODUCTION AND MOTIVATION

The present chapter introduces the dissertation by outlining the key challenges in offshore wind energy that serve as the motivation for this research. It also presents the primary research questions addressed in this work, followed by a concise overview of the content and objectives of each subsequent chapter.



1.1 BACKGROUND AND CONTEXT

The global energy landscape is undergoing a profound transformation, driven by the urgent need to reduce carbon emissions and transition towards cleaner, renewable sources of power [1]. Among the available options, offshore wind energy has emerged as one of the most promising solutions to meet growing energy demands sustainably. The offshore environment offers several natural advantages: steady wind patterns enhance energy yield, while the absence of terrain-induced turbulence improves turbine performance [2]. In addition, the vastness of the ocean allows for the installation of ever-larger turbines, capitalising on economies of scale to drive down the levelised cost of energy (LCoE) [3]. The minimal spatial constraints and reduced interference with coastal activities further strengthen the case for offshore deployment [4, 5].

The potential of offshore wind does not come without obstacles. Transmitting electricity generated at sea to the mainland demands extensive subsea cabling and sophisticated grid connections, which significantly elevate costs [6]. As the industry moves towards larger horizontal-axis wind turbines (HAWTs) and expansive offshore arrays, the associated logistical and financial burdens also rise. Addressing these challenges is essential to fully unlocking the promise of offshore wind energy as a central pillar of a sustainable energy future.

However, the most pertinent issue is that the power output from offshore wind farms falls short of its design expectation and provides lower return on investment than projected values [7, 8]. This shortfall is attributed to wind turbine wakes, as can be seen in Figure 1.1. As the wind turbine extracts kinetic energy from the wind, the turbine directly behind it experiences a lower wind speed, consequently producing less power than rated. These wakes are more significant offshore than onshore due to the lower turbulence which raises the time for this wake to recover. That translates to lower returns on investment, as the overall power output does not meet the expected levels. The indicated issue is augmented as the industry is focused on maximising individual turbine power, rather than optimising the collective output of the wind farm [9]. Investors and stakeholders may find the financial returns less attractive, potentially hindering further investment in offshore wind projects [10]. Practical measures to alleviate the wake and recover it include wake steering control mechanisms such as yaw [11–14] and tilt [15, 16], as well as other newer techniques such as the helix method [17, 18].

One promising alternative to these challenges is the use of vertical-axis wind turbines (VAWTs) (Figure 1.2). On top of existing advantages such as their design simplicity, wind direction independence, as well as having a lower center of gravity [19, 20], VAWTs also show sound promise in significantly alleviating the wake effects [21] and operating in highly turbulent conditions [22]. Traditionally, it has been documented that wakes produced by VAWTs recover much faster than that of HAWTs; the geometry and forcefield of VAWTs increases turbulent mixing, which spreads the low-energy wake rapidly [23–25]. This has, consequently, shown to potentially increase the total power output of the wind farm or maintain the standard output while occupying less offshore space. This multi-use approach to offshore space can lead to more sustainable and harmonious utilisation of marine resources. In addition to the inherent wake alleviating properties of VAWTs, recent studies on individual VAWTs have also shown wake steering capabilities [26–28] to further alleviate the wake and recover it faster.



Figure 1.1: Aerial view from the Southeast of wake clouds at Horns Rev on February 12, 2008 (© Vattenfall, Horns Rev 1 owned by Vattenfall. Photographer Christian Steiness)

VAWTs are incredibly versatile towards accommodating a variety of wake steering techniques. Due to their distinct operating principle, VAWTs have shown to steer the wake effectively using either blade pitching, strut pitching, blade tilt, externally mounted high-lift devices, or a combination of them. This inherent flexibility in design and control allows VAWTs to manipulate their wake, offering unique opportunities for performance optimisation and improved wake recovery within wind farms. These methods aim to redistribute the loads on the turbine, which in-turn induces lateral and vertical forces on the wake. These forces eject the wake either laterally or vertically and boosts the wake recovery process. While these methods have shown to improve wake recovery of an individual rotor, there is a lack of information about the effectiveness of these techniques in a wind farm. With increased lateral and vertical forces, the wake could replace the inflow of an adjacent wind turbine, which defeats the original intent of increasing the wind farm power output. Therefore, there is a need to explore VAWT performances on the wind farm scale.

At present, the offshore wind energy market favours existing HAWTs and their designs over VAWTs. This preference is driven by the extensive research and development that has gone into optimising HAWTs over the last three decades, making them the dominant and a very mature technology in the industry. As a result, VAWTs are still in their infancy in terms of practical implementation that requires further exploration and development. The complexity and fidelity of VAWTs need to be studied and refined to match the performance and reliability of HAWTs.



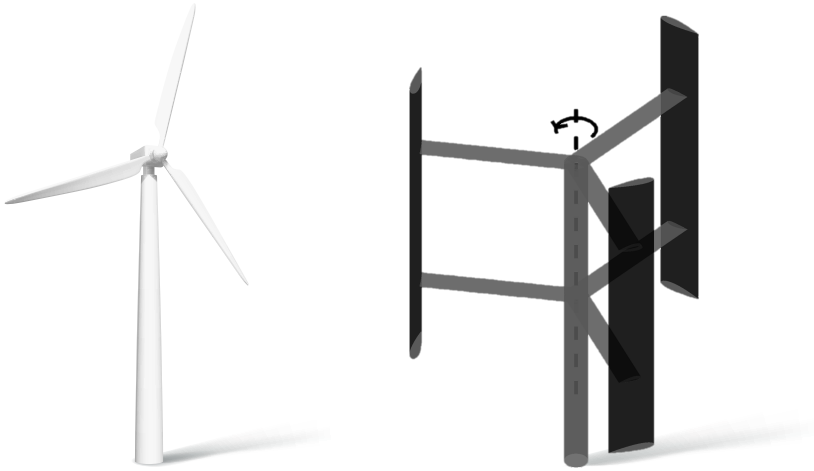


Figure 1.2: A horizontal-axis wind turbine (HAWT) on the left and an H-type vertical-axis wind turbine (VAWT) on the right

1.2 THESIS AIM AND THE RESEARCH QUESTIONS

As part of this exploration into VAWTs performance in the farms scale, the aim of this thesis is to understand the change in offshore wind energy production through the introduction of VAWTs with wake steering mechanisms. In this thesis, the first Research Question (RQ1) focuses on understanding the effect of vertical induction in the induction field of the rotor. After this, we decipher the influence on rotor geometry on the wake of the turbines (RQ2). These two aspects are important as the former informs us about the vertical wake deflection properties of individual VAWTs, while the latter describes how the wake recovery rates are affected by the shape of the rotor. This gives us insight on choosing a rotor geometry that will be analysed in the wind farm scale with wake control mechanisms (RQ3). They are elaborated below:

1. What level of numerical fidelity is required to model the loads and the near-wake of VAWTs with coned blades?
 - A What is the effect of the operating conditions on the loads across different numerical fidelities?
 - B How do we validate the near-wake across different operating conditions?
2. How does rotor geometry influence the wake recovery characteristics of a VAWT in the near- and far-wake?
 - A How can wake recovery be quantified for VAWTs with blade pitch control?
 - B What is the trend of wake deflection between rotors for fixed pitch offsets?
 - C How do the input parameters change the near- and far- wake characteristics?
3. How much does windfarm power density improve by using VAWT pitch control for wake recovery?

- A What correlation can be drawn for the momentum influx in the wake reenergization process for VAWT windfarms between blade pitch configurations?
- B How does wake recovery mechanisms vary with and without atmospheric boundary layer?

1.3 THESIS STRUCTURE

This thesis consists of 8 chapters. These are a collection of publications and non-published chapters to form a larger story line of VAWT wake controls analysis affecting individual VAWTs and those analyses being carried over to a VAWT wind farm.

The structure is shown below with a visual schematic connecting the research questions are shown in Figure 1.3.

- **Chapter 1: Introduction and motivation.** The current chapter provides the context and lays the background and the motivation of this thesis. It describes the role of VAWTs in improving the overall offshore wind energy power density through the wake steering mechanisms. This chapter also provides insight into the research aims, questions that drive the thesis as well as elaborates on the structure of the thesis.
- **Chapter 2: The state-of-the-art.** The chapter serves as a literature review into the different studies into VAWT geometries, VAWT rotor aerodynamics, wake interactions, as well as numerical methodologies aimed towards modelling the aforementioned VAWT rotor forces and flow physics.
- **Chapter 3: Numerical fidelity requirements to capture X-Rotor physics.** This chapter systematically compared several numerical models to capture the rotor level performance characteristics of the X-Rotor. Through this comparison, it aims to present the importance of accounting for the vertical-induction of the rotor, especially at different operating conditions.
- **Chapter 4: Near-wake characterisation and validation of a scaled X-Rotor.** The chapter discusses the validity of the near-wake of the scaled X-Rotor model as predicted by the free-wake vortex model CACTUS at different operating blade pitch offsets. The validation is conducted by comparing particle image velocimetry (PIV) results to the CACTUS simulations.
- **Chapter 5: The effect of rotor geometry on wake recovery.** The chapter compares the wake studies of two distinctly different VAWT rotor geometries of the X-Rotor and H-Rotor and sheds light on the physics behind the wake steering process for both rotors.
- **Chapter 6: Wake sensitivity to airfoil data, dynamic stall, and regularisation kernel.** The chapter discusses the sensitivity of *turbinesFoam*'s wake prediction to different airfoil data at low Reynolds numbers ($Re < 80K$), multiple dynamic stall models, and the regularisation kernel size. The results are compared to the full wake of the scaled X-Rotor captured by experimental PIV.



- **Chapter 7: Wake recovery physics in wind farms with wake control.** This chapter aims to qualitatively and quantitatively understand the implications of pitch-based wake steering in VAWTs when applied on VAWT wind-farms under wind shear.
- **Chapter 8: Conclusions and future recommendations.** This chapter presents an overview of the thesis' conclusions and new insights. It also provides an outlook for relevant future investigations.

Miscellaneous

This part covers additional information including a list of publications, curriculum vitae and the reference list.

- **List of publications:** This chapter gives an overview of the journal and conference articles published inside and outside the scope of this PhD dissertation.
- **Curriculum vitae:** This chapter provides a short summary of the personal and professional achievements.
- **References:** This chapter lists the literature referenced in this dissertation.

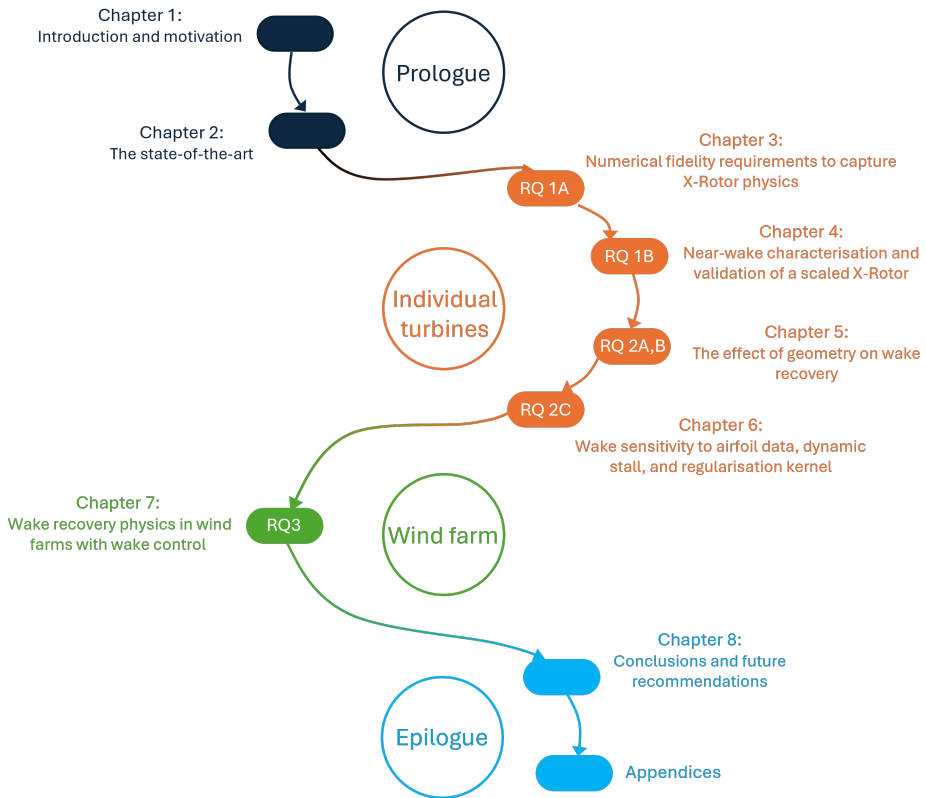


Figure 1.3: Thesis layout showing the connection between the research questions and the chapters.



2

THE STATE-OF-THE-ART

Chapter 1 sets the foundation for this dissertation by outlining the underlying motivation and the research questions that guide the study.

The current chapter presents a comprehensive review of the state-of-the-art in VAWT research, focusing on both rotor and wake aerodynamics of individual wind turbines and wind farms. Key developments in the historical evolution and modern design of VAWTs are outlined, followed by an overview of innovative concept geometries utilised in this dissertation. The chapter further examines current understanding of rotor and wake aerodynamics, highlighting the unique flow features and challenges associated with VAWTs. A detailed survey of numerical modelling approaches used in this dissertation is also provided, encompassing low-, medium-, and high-fidelity methods, along with discussions on the treatment of secondary aerodynamic effects. The chapter aims to identify critical gaps in existing knowledge and modelling practices, forming the basis for the research presented in subsequent chapters.



2.1 HISTORY OF VAWTs AND VAWT DESIGNS

The history of VAWTs is quite long and is rich in practical applications. VAWTs have been documented to have existed for more than a millennia, as the earliest usage points to 9th century Persia [29]. They used a panemone type VAWT which consisted a central vertical shaft connected to a series of wooden sails by a strut. The Persians used it primarily to pump water and for milling of grains.

Today, we broadly classify VAWTs as drag-driven, lift-driven, and hybrid VAWTs. Drag-driven VAWTs exists in different forms, such as the aforementioned panemone type as well as the more well-known Savonius design, see Figure 2.1. The Savonius was an improvement on the methods used by the Persians, as the turbine was essentially a cylinder cut in half along its axis and translated. This resulted in each half experiencing pressure on its front and suction on its back, giving a significant performance increase over the panemone VAWT. Other drag-driven turbines typically are variations of this basic design and are limited by performance due to their low efficiency. However, they have superior self-starting performance due to the pressure exerted on the front halves of the cylinder.

The lift-driven VAWTs rely on the blade generating lift in the rotational direction to generate energy. The earliest designs of a lift-driven VAWT goes back to the patent on the Darrieus VAWTs back in the early 1930s. The patent consisted of several designs, one of which is a Φ -shaped design, where the wing profile blades are connected to a central tower at the blade tips. Another one of the designs is the well known H-type Darrieus rotor, where the blades from the original patent are replaced with straight blades connected to the tower through horizontal struts. Both blades operated on the principle that when a relative flow exists on the suction and pressure side of the blades, lift is produced to generate torque and this continues. However, the reliance on existing relative flow as well as the high starting torque, makes them dubitable for self-starting. Additionally, variation of this relative inflow to the blades introduced high-variance in torque, which was not very favourable to the energy market at the time of introduction.

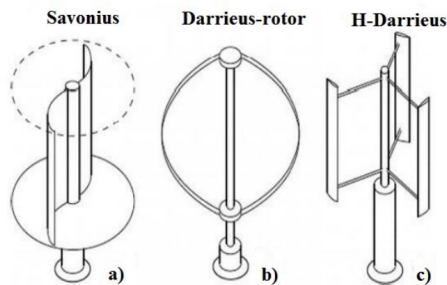


Figure 2.1: Different kinds of vertical axis wind turbines (VAWT): (a) Drag-driven (Savonius); (b) and (c) Lift-driven (Darrieus ϕ and H-type) adapted from Castellani et al. [30].

The hybrid VAWT design combined both drag- and lift-driven concepts into a single rotor to reduce the individual disadvantages of each design, but introduces additional drag where the overall power performance is far lower than the isolated Darrieus rotors, but only seeks to increase the self-starting performance [31].

In the late 1970s, the wind energy industry favoured the development of HAWTs over VAWTs due to their higher efficiency and simpler aeroelastic behaviour in steady conditions for large-scale rotors [32]. This preference led to a significant technological gap between HAWTs and VAWTs. Recently, however, there has been a resurgence of interest in VAWTs, particularly in the context of offshore wind energy, where reducing the cost of energy is a critical driver. As a result, numerous VAWT concepts have been developed to address this need. Möllerström et al. [33] documented H- and Φ -type Darrieus wind turbines, all rated above 100 kW, from the late 1970s to the present day.

In addition to these existing designs, several innovative projects have emerged, such as Wind Power Limited's Aero-generator X [34], ETI's Nova [35], Arkom's Tulyp Wind [36], Minesto's Tidal Kite Systems [37], and SeaTwirl's S3, S2.5, and S1 turbines [38]— most of which target the floating offshore market. Among these developments, a novel concept called the X-Rotor [39] has been proposed, offering a unique approach to harnessing wind energy with potential advantages in scalability, cost-effectiveness, and adaptability to offshore environments.

2.2 THE X-ROTOR TURBINE

The X-Rotor is a novel vertical-axis wind turbine concept that is designed to lower its LCoE for offshore applications. The turbine has two key novel features: an X-shaped primary rotor and the use of secondary tip rotors for power generation, see Figure 2.2. Rather than removing power from the main shaft of the primary rotor, the rotor speed is controlled by the thrust force on the secondary rotors, and all electrical power is extracted from the secondary rotors. The secondary rotors are attached at the lower blade tips and consequently see a significantly accelerated inflow speed due to the relative velocity at the primary rotor blade tips. In turn, this allows the secondary rotors to have a very small radius and a large rotational speed. This facilitates the use of cheap, lightweight, high-speed direct drive generators, as opposed to using gearboxes, which significantly reduce the capital costs associated with the turbine. Additionally, the low altitude and mass of the generators eliminate the need for jack-up vessels for maintenance, potentially significantly reducing the associated operations and maintenance costs [40]. The primary rotor is designed to increase the tip-speed ratio and swept area of the rotor compared to a traditional H-shaped VAWT for the same material used, while cancelling the overturning moments associated with V-shaped VAWT rotors [41, 42]. The upper blades of the X-Rotor are pitch controlled and are designed to shed aerodynamic power in above-rated conditions. The lower blades are not pitch controlled as any change in it would disrupt the operation of the secondary rotors. A recent study on the operations expenditure of the X-Rotor concept by Flannigan et al. [40] demonstrated large savings on the operational cost of energy compared to a HAWT. A similar feasibility study by Leithead et al. [39], showed up to 26% overall cost savings compared to HAWTs. The development of the X-Rotor concept is currently the subject of a European Union (EU) Horizon2020 project [43].



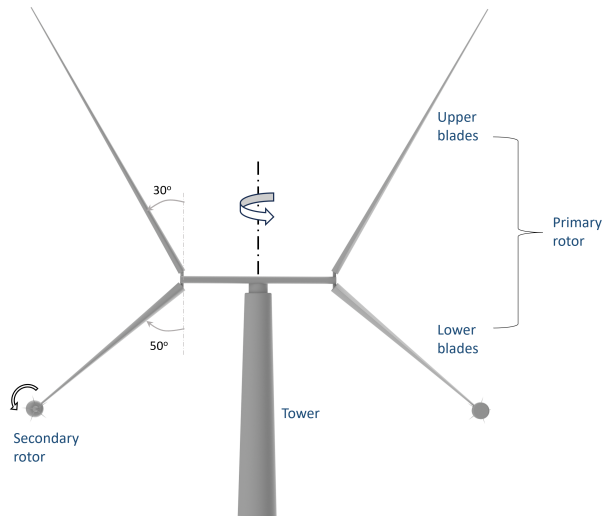


Figure 2.2: A render of the X-Rotor turbine.

This dissertation:

The H-type and the X-Rotor turbines play crucial roles in this dissertation. In Chapter 3 and Chapter 5, the X-Rotor is utilised to highlight the significant 3D aerodynamics introduced by the coned blades using various numerical tools, and a comparison between it and the H-Rotor's wake and recovery mechanism is conducted. Additionally, validation and sensitivity studies are conducted for numerical tools using the X-Rotor geometry in Chapter 4 and Chapter 6. In Chapter 7, the H-Rotor geometry is used to simulate a VAWT wind farm to understand the wake recovery mechanisms with atmospheric boundary layers.

2.3 VAWT AERODYNAMICS

Here, the basics of VAWT aerodynamics from two perspectives will be explained: (1) purely about the VAWT rotor forces, and (2) about the wake dynamics.

2.3.1 ROTOR AERODYNAMICS

The aerodynamics of HAWTs and other rotors are a result of the forces they generate. In the absence of a rotor, no force is applied on the wind to reduce its kinetic energy. When a wind turbine is placed in this flowfield, the blades exert an opposing force on the wind to extract energy, thereby altering the flow behind the rotor. VAWTs also follow the same principle. However, unlike the disc-like swept surface of HAWTs, VAWT blades trace a cylinder during their azimuthal rotation which changes the rotor load behaviour and, correspondingly, the flowfield of the rotor as well. A schematic of a VAWT as a 3D actuator

surface is given in Figure 2.3, with the freestream inflow U_∞ along the positive X-axis.

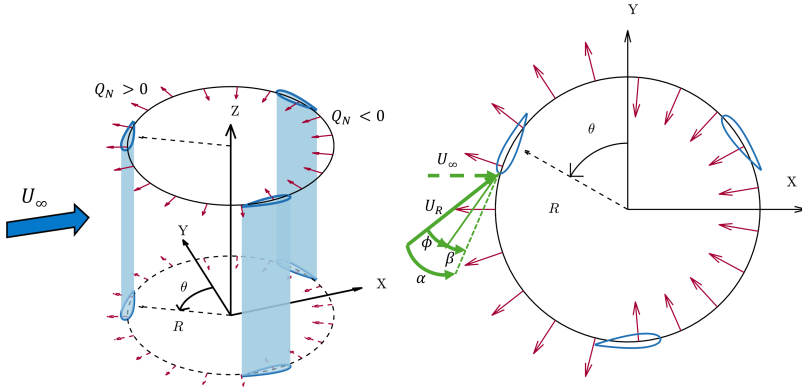


Figure 2.3: A schematic of the 3D actuator cylinder of an idealised VAWT with 3 blades (left) and the top-view of a 2D section from the cylinder with the blade angles (right). The red arrows depict an idealised normal load Q_N profile along the cylinder, where the loads pointing outwards are positive. θ depicts the azimuth, while R is the radius. X, Y, Z represents the coordinate system used in this thesis, with the rotor center placed at the origin. U_∞ is the freestream wind velocity, acting along the streamwise direction (X coordinate). For the blade element, U_R is the relative velocity (thick solid arrow), inflow angle ϕ , angle of attack α , and pitch angle β is shown in green. Dashed green line corresponds to the chord line of the element, while the solid green line is the tangent of rotation.

In an idealised VAWTs, the tangential loads Q_T are neglected, and the normal loads Q_N of the rotor are equally distributed and flip directions between the upwind ($X < 0$) and downwind ($X > 0$) halves of the cylinder. This occurs as the relative velocity U_R of the blades change continuously with azimuth θ , which consequently changes the angle of attack α . Therefore, at $\theta = 0^\circ$ and 180° the pressure and suction sides of the airfoil shifts, which results in the normal loads changing directions. However, in realistic VAWT loads, the loads would vary throughout the azimuth and the directional change in loads would occur at slightly different azimuths. The forcefield of a realistic VAWT can be best understood through a 2D Blade Element Momentum (BEM) formulation of a blade element along at the mid-span of the rotor, which is best described in De Tavernier et al. [44]. However a brief summary is provided here.

The relative velocity can be decomposed into velocities in the streamwise (X) and lateral (Y) directions, U and V respectively, as shown in Equation 2.1. Here, U is a function of the freestream velocity U_∞ , rotational velocity component of the blade section $\omega R \cos(\theta)$, and the velocity component induced due to the blade forces $U_{ind,X}$. Similarly, V is a function of the lateral components of these terms.

$$\begin{aligned} U &= U_\infty + \omega R \cos \theta + U_{ind,X}, \\ V &= \omega R \sin \theta + U_{ind,Y} \end{aligned} \quad (2.1)$$

By using these equations, the directional normal U_N and tangential U_T velocity components can be formulated, which is then used to obtain the angle of attack α (Equation 2.2).



$$\begin{aligned}
 U_N &= U \cos \theta - V \sin \theta, \\
 U_T &= U \sin \theta + V \cos \theta, \\
 \alpha &= \arctan(U_N/U_T) + \beta
 \end{aligned}
 \tag{2.2}$$

The current formulation of α ignores blade twist, as typical H-type VAWTs blades do not contain twist as the entire blade is designed to operate with the same inflow velocity. Additionally, as the rotor tends to produce lesser and lesser loads, the angle of attack approaches the geometric angle of attack which is given by Equation 2.3.

$$\alpha_{geom} = \arctan(\sin \theta / (\lambda + \cos \theta)) + \beta
 \tag{2.3}$$

For a given blade section airfoil profile with chord c and relative velocity U_R , the lift L and drag D can be easily evaluated through their respective coefficients C_L and C_D and α . Using the lift and drag, the normal F_N and tangential F_T forces of the blade section can be evaluated as shown in Equation 2.4, where ϕ is the inflow angle.

$$\begin{aligned}
 F_N &= L \cos \phi + D \sin \phi, \\
 F_T &= L \sin \phi - D \cos \phi
 \end{aligned}
 \tag{2.4}$$

The torque produced by a blade element is evaluated by the net force acting in the tangential direction of rotation multiplied by its radius R . The power P of the blade element can be obtained by integrating its torque with the rotational velocity ω . The thrust T of the rotor is also a function of F_T and F_N acting against the streamwise direction. Both these expressions can be visualised as seen in Equation 2.5, where B is the number of blades. Correspondingly, their coefficients C_P and C_T can be obtained when normalised by $0.5\rho U_\infty^3$ and $0.5\rho U_\infty^2$, respectively.

$$\begin{aligned}
 P &= (1/2\pi) \int_0^{2\pi} B(F_T(\theta) \cos(-\beta) + F_N(\theta) \cos(-\beta)) \omega R d\theta, \\
 T &= (1/2\pi) \int_0^{2\pi} B(F_N(\theta) \sin \theta + F_T(\theta) \cos \theta) d\theta
 \end{aligned}
 \tag{2.5}$$

Additionally, non-dimensional parameters such as rotor solidity (σ) and aspect ratio (AR) are used to represent the geometrical parameters of the rotor in 3D.

From these equations, we see that a 2D VAWT blade element's angle of attack varies with the azimuth, and consequently the blade forces. Typically, the forces in H-type VAWTs have been extensively studied only at $\beta = 0^\circ$ [21, 45–52]. These studies analysed the performance of the blades either through aerodynamic forces or aeroacoustic analyses at various tip-speed ratios λ , however they do not address the performance of the rotor when the blades are pitched. Over the past decade, there have been studies aimed at addressing this gap. Ferreira [53] initially documented that changing the pitch angle of the blades resulted in a redistribution of the loads between the upwind and the downwind halves of the rotor. Furthermore, Ferreira et al. [54] demonstrated further than with very

small pitch angles, the load can be shifted independent of the power generation of the rotor using potential flow. However, Rezaeiha et al. [55] showed that in viscous flows the power generation is not independent to load distribution. Later, LeBlanc and Ferreira [56] and LeBlanc and Ferreira [57] experimentally documented the load redistribution using strain gauge and particle image velocimetry respectively. Additionally, De Tavernier et al. [58] and Le Fouest and Mulleners [59] showed that applying varying pitch profiles could aid in optimising blade forces and power production for a VAWT.

2.3.2 WAKE AERODYNAMICS

The wake of a VAWT is strongly influenced by rotor loading and inflow conditions. This is evident from Equation 2.1, where the induced velocities $U_{ind,X}$ and $U_{ind,Y}$ arise from the rotor loading. The rotor load, governed by blade forces, generates a vortex system comprising spanwise-shed and trailing vortices. Shed vortices originate primarily from azimuthal variations in lift coefficient C_L and relative velocity U_R , while trailing vortices stem from the spanwise circulation distribution. These vortical structures – especially the tip vortices forming counter-rotating pairs – significantly influence the near-wake topology and are inherently three-dimensional [23–25, 53, 60–63]. Controlling or modifying these vortices offers a pathway to manipulate the wake and enhance its recovery [27]. A visualisation of the vortex system of a H-Darrieus turbine is presented in Figure 2.4.

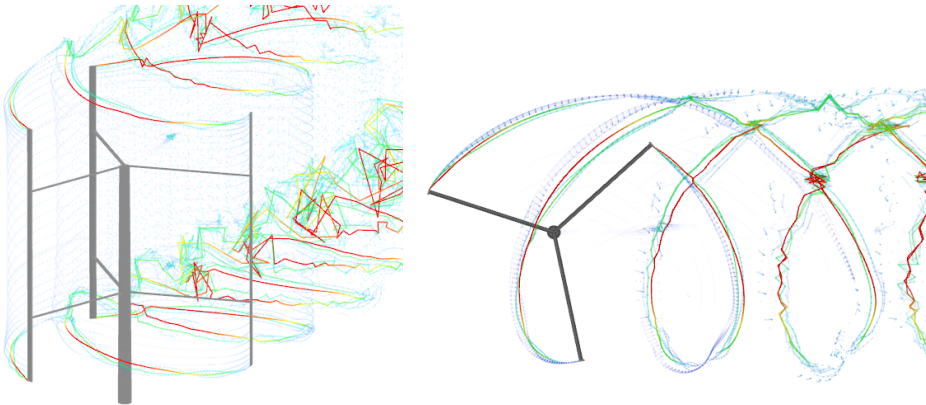


Figure 2.4: An isometric (left) and top-view (right) visualisation of the 3D vortex system of a H-Darrieus turbine. The regions of instability are regions where the blade interacts with the wake/vortices from previous blade passages. Vortex strength is indicated by colour, with blue representing the lowest values and red representing the highest.

Numerous experimental studies have investigated the wake of isolated VAWTs. For example, Tescione et al. [64] used stereoscopic particle image velocimetry (PIV) to examine tip vortex interactions, while Ryan et al. [65] used magnetic resonance velocimetry to characterise the three-dimensional flowfield, identifying dominant counter-rotating vortices. Araya et al. [66] observed wake similarities between VAWTs and circular cylinders beyond the near-wake. Rolin and Porté-Agel [67] linked the presence of counter-rotating vortex pairs to faster wake recovery in small-scale turbines within shear-layer inflow. More recently, Wei et al. [68] and Huang et al. [69] explored how blade geometry and loading



affect near-wake structures using 3D particle tracking velocimetry (PTV) and stereoscopic PIV, respectively.

Complementary numerical studies further support these findings. Tescione et al. [61] used a free-wake vortex model to demonstrate the influence of three-dimensional vortical structures in the near-wake. Large-eddy simulations (LES) by Shamsoddin and Porté-Agel [48] revealed the periodic and unsteady nature of VAWT wakes, with distinctive blade–vortex and blade–wake interactions. Subsequent work by Shamsoddin and Porté-Agel [70], Mendoza and Goude [71] showed that VAWTs operating in an atmospheric boundary layer benefit from enhanced vertical asymmetry in turbulence, accelerating wake recovery, often defined as 95% of freestream velocity. He et al. [72] highlighted the importance of capturing tip vortices, as 2D LES models significantly misrepresent wake structures compared to 3D LES. Other studies demonstrated that wake characteristics are sensitive to rotor solidity [73], loading distribution [74], and tip-speed ratio [75]. Comparative analyses of 3D models [76, 77] emphasised the importance of capturing three-dimensional blade loading to avoid overpredicting power, torque, and wake dynamics.

WAKE MIXING AND CONTROL

While most earlier studies focused on isolated turbines, in-situ applications involve turbine arrays, where wake control becomes essential for optimising farm-level performance. This is because the wakes of the first turbine in the array dictates the power available for the turbines downstream. Therefore, many methods exist to mitigate the wake produced by the turbines or restore freestream conditions downstream by compromising the performance of the first turbine. This concept will be referred to as ‘wake recovery’ for the remainder of this dissertation.

The idea of wake control can be best explained by using the Reynolds averaged momentum equations rearranged to represent the streamwise advection by all the other terms, as seen in Equation 2.6. This equation ignores the contribution of viscous diffusion and external forces, as they are not essential in this context.

$$\underbrace{\bar{U} \frac{\partial \bar{U}}{\partial X}}_{A_1} = \underbrace{-\bar{V} \frac{\partial \bar{U}}{\partial Y} - \bar{W} \frac{\partial \bar{U}}{\partial Z}}_{A_2} - \underbrace{\frac{1}{\rho} \frac{\partial \bar{P}}{\partial X}}_{A_3} - \underbrace{\frac{\partial \overline{U'U'}}{\partial X} - \frac{\partial \overline{U'V'}}{\partial Y} - \frac{\partial \overline{U'W'}}{\partial Z}}_{A_4}, \quad (2.6)$$

where the primes denote the fluctuations and the overbars denote the time-averaged quantities. X , Y , and Z are the spatial components while U , V , and W . To simplify the discussion, terms are grouped by labels A_n , where n runs from 1 to 4. A_1 is the advective transport of streamwise momentum, A_2 is the advective transport of lateral and vertical momentum, A_3 is the pressure gradient, A_4 is the momentum transport due to turbulence. For the purposes of this discussion, we only consider the streamwise turbulence terms.

If we simplify a turbine to essentially only produce streamwise thrust without any lateral or vertical forces, the primary contributor towards recovering the wake would be from the A_3 and A_4 terms, as a lower thrust yields a faster recovery than larger thrust. Additionally, larger turbulence transport promotes enhanced mixing which increases wake dissipation. The A_2 term would be a secondary contributor, as the lateral and vertical advection would purely be from the expansion of the streamtube, based on BEM theory. Therefore, it would make sense to identify methods to increase the contribution of A_2

to improve overall wake recovery. These methods are what we would refer to as 'wake control' in the rest of this dissertation. Increasing A_2 results in the transfer of momentum in the vertical and lateral directions, which would consequently deflect the wakes away from its previous path. The effect of displacing or deflecting the wake away from its baseline path would be referred to as 'wake deflection' in the rest of this dissertation. The simplest approach to achieve this would be by redistributing the turbine load to induce a lateral or vertical thrust in addition to its streamwise thrust.

In HAWTs, strategies such as yaw misalignment [11–14] and tilt control [15, 16] have been used to laterally or vertically deflect wakes. These work to deflect the wakes as by introducing a yaw misalignment, the turbine produces a lateral thrust in addition to the streamwise thrust, which increases the lateral advection of momentum. With turbine tilt, the turbine produces a vertical thrust component. More recently, dynamic induction strategies such as helix mixing have shown promise for enhancing turbulent mixing and accelerating wake recovery [17, 18] without utilising lateral or vertical advection.

In comparison, VAWTs naturally exhibit faster wake recovery than HAWTs [48, 78], partly due to inherent turbulence transport in the near-wake [64, 70, 79]. This indicates that the A_4 terms already contribute more than HAWTs towards wake recovery. However, this trend may not hold if the two turbines operate at the same power. In such cases, the lower power coefficient of the VAWT leads to a higher thrust, which consequently produces a lower energy wake [80]. However, unlike HAWTs, yaw misalignment is impossible while tilt control would only be possible with tilting the tower, which can create unwanted clearance issues for the blades. Therefore, a different method is required to manipulate the rotor loading for a VAWT. Fortunately, Ferreira [53] theorised that the rotor loading can be redistributed by altering the blade pitch angle, as can be inferred from Equation 2.2. As the wake of a VAWT is very three-dimensional the rotor loads directly affect the tip-vortices of the blade, which can be used to control the momentum advection in the wake. De Tavernier et al. [62] reinforced this theory, showing that by concentrating blade loads in either the upwind or downwind half of the rotor, the vortices change magnitude and direction significantly and consequently deflects the wake laterally or vertically. This concept is visually depicted in Figure 2.5 for a H-Rotor placed in a homogeneous inflow with three different types of loading conditions. With favouring either the upwind or the downwind halves of the rotor, the tip-vortices change strength, thereby increasing the contribution of A_2 terms by inducing stronger lateral and vertical components of velocity.

This was experimentally confirmed by LeBlanc and Ferreira [81, 82], who manipulated the azimuthal loading through fixed blade pitch. When the leading edge of the blade was pitched towards or away from the rotation axis, the upwind and downwind loading could be independently adjusted. Supporting simulations by Jadeja [26] showed that fixed blade pitch amplifies wake deflection via stronger tip vortices. Experimental validation of this effect on a two-bladed H-shaped VAWT confirmed significant lateral thrust variation with only minor reductions in streamwise thrust [27, 28]. Further, Huang [83] validated a Reynolds-Averaged Navier–Stokes (RANS) based actuator line method (ALM) using lab-scale experiments and extended the analysis to full-scale turbines. Their results demonstrated that blade pitching in both isolated VAWTs and a 1×3 inline array can achieve substantial performance gains for downstream turbines with minimal power loss for the upstream rotor.

Other than blade pitch, there are more methods in VAWTs to similarly deflect the



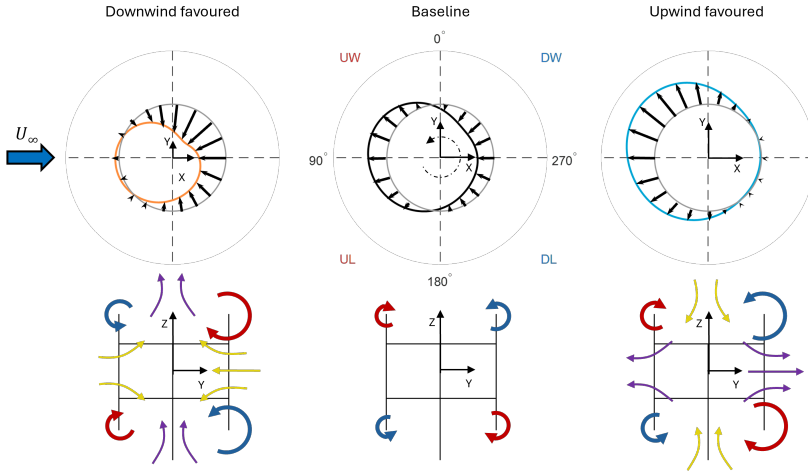


Figure 2.5: The first row depicts the a representation of the different rotor loading, namely the baseline case, upwind, and downwind favoured. The azimuth is shown in degrees and the inflow is from the left along the 90° line. for all cases. The actuator cylinder is represented by the grey circle. The quadrants of the azimuth are marked as upwind-windward (UW), upwind-leeward (UL), downwind-leeward (DL), and downwind-windward (DW). The second row shows the dominant streamwise tip-vortices in the flow downstream of the turbine represented by the curved arrows with blue for counter-clockwise direction. The yellow arrows indicate inflow while purple arrows indicate outflow.

wake. Guo and Lei [84] presented a unique approach of wake control by tilting the blades, where the tilt axis was perpendicular to the span of the blades. Their results documented a moderate increase in the available power in the wake of turbines with tilted blades compared to the blades without tilt. Decoupling the blades from the wake control and passing the role to the struts could be beneficial for the dynamic forces of the blade as demonstrated by Mendoza and Goude [85]. In their work, the wake control was purely done by pitching the struts, showing improved wake recovery through advection. Ribeiro et al. [86] studied the effect of combining both the pitched strut and pitched blades on the wake reporting further increase in wake recovery. More recently, the concept of fitting external high-lift devices on turbines also documented enhanced wake recovery by decoupling the blades from wake control [87–90]. However, as these concepts involve external equipment or additional controllers for struts, we study only wake control by controlling the blade pitch in this dissertation.

Previous studies of VAWT arrays, such as Dabiri [91], Kinzel et al. [92], Hezaveh and Bou-Zeid [93], Whittlesey et al. [94], Gharaati et al. [95], do discuss the benefits of VAWT wake recovery, however they only focus on the increased mixing by turbulence without the complementary advective process. Huang [83] focuses on a 1×3 inline array, with and without ground to show that the wake recovery process is increased by manipulating the tip-vortices, however documents that the effect is less pronounced with a ground, as the vortices are vertically asymmetric. Recently, Bensason et al. [96] experimentally demonstrates the advection process in a 3×3 H-type VAWT farm grid, however documenting the wake-wake interaction of neighbouring turbine arrays influencing the effectiveness of

the advection process.

All the aforementioned studies primarily focus on the H- Darrieus turbine. As a novel VAWT concept, the X-Rotor's wake and wake recovery studies are still in the early stages. However, recent experimental research on a scaled version of the primary rotor has provided insights into the rotor loading and the three-dimensional aerodynamics within its volume [97]. In addition, an experimental study of the X-Rotor with fixed pitch offsets of the upper blade showcases the wake-deflection capabilities [98], but could not capture the full frontal area of the X-Rotor to systematically understand the full-vortex system. Recently, the full wake of a 1:250 scaled model of the X-Rotor was captured through stereoscopic PIV by Bensason et al. [99] showcasing the complex vortex system of the X-Rotor and its wake recovery mechanism.

2.4 VAWT MODELLING

In the previous section we discussed the idea of both the rotor/blade loads as well as their impact on the wake. In this section, we would discuss the different numerical approaches that are utilised in this dissertation to replicate the load and wake behaviour of VAWTs.

Generally, numerical models are categorised based on how they represent either the rotor or the flowfield inside them. In this dissertation, VAWT numerical models are broadly classified into three categories based on the rotor representation: (1) low fidelity, (2) medium fidelity, and (3) high fidelity models. We consider high-fidelity as numerical tools that do not use empirical or semi-empirical relations to model the rotor. Therefore, these methods use the full 3D geometry of the blades at very high resolutions. Therefore, these approaches are extremely computationally intensive and expensive. Low fidelity models are those that do use empirical or semi-empirical relations, such as BEM, to represent the rotor forces in the setup. They generally have low computational demand. Medium fidelity models are in-between the low- and high- fidelity models and cover a very broad spectrum of models.

The following subsections tackle each numerical model briefly, organised by increasing levels of fidelity. This list is non-exhaustive as it only discuss the models used in this dissertation. Additionally, any modifications conducted to include the different rotor geometries is also addressed correspondingly. For a detailed overview of the mechanism of each model, De Tavernier et al. [44] provides a very accurate description of each model and their theory.

2.4.1 LOW FIDELITY MODELS

DOUBLE MULTIPLE STREAMTUBE MODEL

The Double Multiple Streamtube (DMS) model, developed by Paraschivoiu [100], is a 1D momentum-based model which is expanded to model 3D rotors through a double discretisation scheme in this thesis. Theoretically, 1D momentum approaches assume a streamtube that encompasses the forcefield of the rotor, with the rotor represented as a thin disc with uniform force distribution. In the DMS method, effectively considers a series of streamtubes spaces laterally across the 2D cross-section of the rotor with the upwind and downwind sections replaced by their corresponding force distribution. This model assumes that each lateral streamtube is independent of each other, and that the forcefield of the downwind half does not affect the forcefield of the upwind half. A schematic of the lateral



series of streamtubes with their corresponding upwind and downwind actuators are shown in Figure 2.6. Read and Sharpe [101] proposed an extension to the DMS model to account for interactions between streamtubes as well as the influence of the downwind half on the force field of the upwind half. However, this extension is not used in this dissertation due to time constraints.

The X-Rotor is modelled as a 3D rotor, where it is first decomposed into 2D slices along its height, then each slice is split into parallel streamtubes that cross the rotor circumference twice, as seen in Figure 2.6. Blade element momentum theory is first used to solve the flow at the upwind crossing point, then at the downwind crossing point assuming that atmospheric pressure has been recovered. Conservation of mass is assured by allowing streamlines to expand through the method proposed by Freris [102]. Morgan and Leithead [103] provides a detailed description of the implementation for the X-Rotor. The formulation of streamtube expansion means that there is no fixed azimuthal discretisation as the distance between streamlines is dictated by the loading on the rotor. Experimental validation studies for this model were conducted by Paraschivoiu [104], which shows that the model is effective at replicating the force field of the rotor for non-heavily loaded rotors. However, this model is based on multiple assumptions that can easily be broken by the regular operation of a VAWT due to the lateral induction.

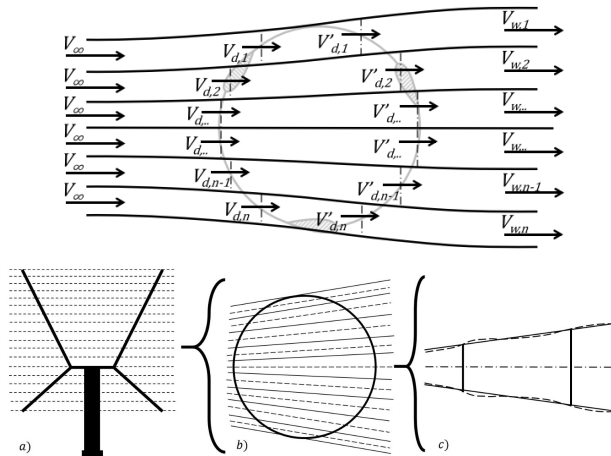


Figure 2.6: (Top) Schematic of the DMS streamtubes and the upwind and downwind actuators reproduced from De Tavernier et al. [44] for a 2D H-VAWT. (Bottom) The discretisation procedure of the X-Rotor in DMS reproduced from Morgan and Leithead [103]. Vertical discretisations are shown in (a). Each vertical plane discretised into streamtubes (solid) and its corresponding central streamline (dashed) is shown in (b). Streamtubes crossing the upwind and downwind actuators are shown in (c).

2D ACTUATOR CYLINDER MODEL

The 2D Actuator Cylinder (2DAC) model, developed by Madsen [105], is a 2D momentum model that adapts the actuator disk concept for the swept area of a VAWT. The model is based on the quasi-steady 2D Euler equations and a linearised solution [106, 107] is used in this model. This model solves for the induced velocities of the rotor ($U_{ind,X}$ and $U_{ind,Y}$

by using the force-field of the rotor in an iterative process coupled with the BEM approach. The model outputs the induced velocities as a solution of the Eulerian 2D momentum equations when represented in a Poisson type equation. Using Green's function to solve the Poisson type equations, the induced velocities are given by the linear solution as shown in Equation 2.7 and Equation 2.8. Q_x and Q_y are the streamwise and lateral rotor load components, ρ is the fluid density, x and y are the spatial locations at which the induction is evaluated, while η and ζ are the spatial coordinates of the actuator surface.

$$U_{ind,x} = \frac{1}{2\pi\rho U_\infty^2} \iint -\frac{Q_x(x-\eta) + Q_y(y-\zeta)}{r^2} d\eta d\zeta + \frac{1}{U_\infty^2 \rho} \int_{-\infty}^x Q_x d\eta, \tag{2.7}$$

$$U_{ind,y} = \frac{1}{2\pi\rho U_\infty^2} \iint -\frac{-Q_y(x-\eta) + Q_x(y-\zeta)}{r^2} d\eta d\zeta + \frac{1}{U_\infty^2 \rho} \int_{-\infty}^y Q_y d\eta$$

$$r = \sqrt{(x-\eta)^2 + (y-\zeta)^2} \tag{2.8}$$

For the X-Rotor, the 2DAC is used by discretising it into several 2D actuator cylinders along its height, as seen in Figure 2.7. Each slice is aerodynamically independent of the other, i.e., it does not account for induction in the axial/vertical orientation. This approach is similar to how the DMS model was expanded to 3D, however the 2DAC natively accounts for lateral inductions as well. While the assumptions used here are more reasonable compared to DMS, this model still does not take into account the influence of the finite blade lengths of the VAWT, which leads to vertical induction as well. There does exist a 3D actuator cylinder model, however an iterative version coupled to BEM is yet to come to fruition.

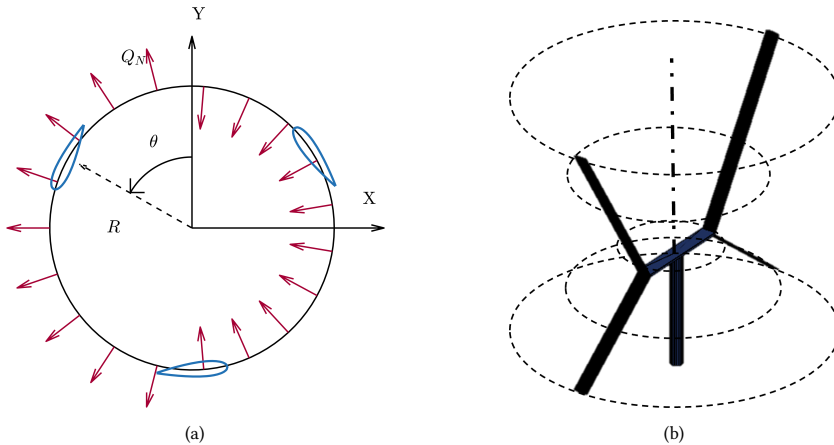


Figure 2.7: (a) The representation of the rotor normal load Q_N in the 2DAC approach. The tangential load Q_T would be along the arrow depicting θ . (b) Vertical discretisation procedure of the X-Rotor inside the 2DAC. These are constrained to the radius of the rotor at the specific height of the vertical 2D segment.



2.4.2 MEDIUM FIDELITY MODELS

In general, all medium fidelity models used in this thesis can be summarised as Actuator Line Models (ALM). ALM, first proposed by Sørensen and Shen [108], is a blade element formulation that represents wind turbine blades as discretised line elements with force profiles. While the rotor is represented as actuator lines, the models can be applied in either Eulerian or Lagrangian domains, as briefly explained below:

EULERIAN APPROACH

The forces produced are projected onto the fluid domain as source terms in the momentum equations through the means of a spherical Gaussian regularisation kernel, η , as described in Equation 2.9. This η is required to avoid the singularity from the vortex formed for each line element, which would otherwise induce instability in the finite volume cells.

$$\eta(r) = \frac{1}{\epsilon^3 \pi^{3/2}} \exp[-(r/\epsilon)^2], \quad (2.9)$$

where ϵ is the parameter that adjusts the width of this function and r is the distance between the cell and the line element. The significant advantage of this approach compared to the Lagrangian free-wake vortex methods is the inclusion of viscous forces as well as turbulence models in the flowfield. This results in a high degree of wake reproduction by the model, with variation correlating to the Eulerian mesh, and setup of the model, which is useful to understand the contribution of turbulence transport in the VAWT wake in addition to just advective transport terms.

Typically, many studies use this approach to model the wake while maintaining relatively cheap computational costs compared to high-fidelity approaches, as the body forces from the blades are injected into the fluid domain. Examples of common open-source libraries for ALM models in the Eulerian domain are SOWFA [109] and *turbinesFoam* [110]. Presently, the latter is the only open-source ALM tool available for VAWT modelling in the Eulerian domain. In this dissertation, we employ *turbinesFoam-v0.2.1* coupled with *OpenFOAM-v2106* and *-v2306* [111] to effectively project the turbines into the Eulerian fluid domain to primarily conduct wake analysis. A representative figure for streamwise velocity for a HAWT using the Eulerian approach is provided in Figure 2.8.

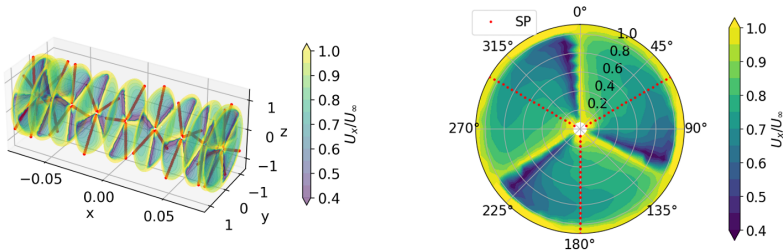


Figure 2.8: Normalised velocity at the rotor plane across the windward phase (left) and normalised velocity sampled by ALM on the rotor plane (right) of a HAWT. SP denotes the points where the velocity is sampled. Figure reproduced from Sanvito et al. [112].

LAGRANGIAN APPROACH

The blades, represented as discretized lifting lines, and the flowfield are coupled by a vortex lattice system formed by the surrounding bound, shed, and trailing circulations for each discretised blade section, as seen in Figure 2.9 along with the discretized version of the X-Rotor.

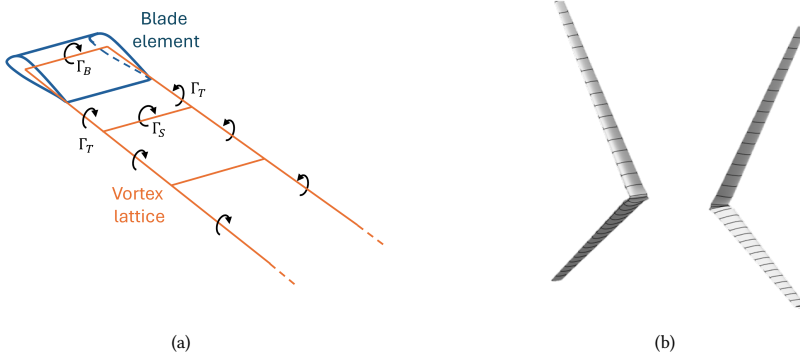


Figure 2.9: (a) The vortex lattice system of a single blade element along with the bound (Γ_B), shed (Γ_S), and the trailing (Γ_T) circulations. (b) The discretised blades of the X-Rotor VAWT.

The flow field is constructed using this vortex lattice, where the velocity is the arithmetic sum of the freestream velocity and the velocity induced by the vortices. This is determined using the Biot-Savart law [113], which expresses the velocity field as a function of the circulation of any line segment within the vortex lattice, as follows:

$$\vec{u}_a = \frac{\Gamma}{4\pi} \frac{\vec{r}_1 \times \vec{r}_2}{|\vec{r}_1 \times \vec{r}_2|^2} (\vec{r}_1 - \vec{r}_2) \cdot \left(\frac{\vec{r}_1}{|\vec{r}_1|} - \frac{\vec{r}_2}{|\vec{r}_2|} \right) \quad (2.10)$$

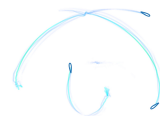
Here, \vec{u}_a represents the velocity vector at point a , while \vec{r}_1 and \vec{r}_2 are the displacement vectors from the ends of the vortex line segment to point a . The circulation of the vortex line segment is denoted by Γ .

This method is also known as a free-wake vortex model (FVM). The significant advantage of this model over the Eulerian approach is that a pre-defined spatial grid is not necessary, as the velocity information is stored in the aforementioned temporally evolving vortex lattice. However, to model complex flows with turbulence, the number of particles can increase significantly to represent small scale eddies, leading towards increased computational time.

In this dissertation, two popular FVM tools are used, namely:

The Code for Axial and Cross-flow TURbine Simulation (CACTUS) developed by Murray and Barone [114], is a three-dimensional vortex modelling tool for wind turbines. This is a tool that utilised the theory of free-wake vortex methods and applies it specifically to VAWTs.

QBlade is a turbine design and simulation tool to perform aerodynamic studies to facilitate the design of wind turbines developed by Marten et al. [115]. Later updates added



lifting-line simulation capabilities [116], that used a free-wake vortex model as well. In this software, the free-wake vortex method is capable of modelling both HAWTs and VAWTs.

2.4.3 HIGH FIDELITY MODELS

In these models, the blades are no longer simplified by semi-empirical relations to model the forces. Instead, the 3D structure of the blades are fully represented in the simulations and the blade forces are evaluated by modelling the flow around the blade itself. In general, these are extremely computationally expensive to model the dynamic VAWT flowfields. Once again, in this thesis, we employ two types of high-fidelity models.

BLADE-RESOLVED UNSTEADY REYNOLDS AVERAGED NAVIER-STOKES CFD MODEL

The Unsteady Reynolds Averaged Navier-Stokes (URANS) CFD model is an Eulerian approach to model the viscous flow around the airfoil/blade and the wake. In blade-resolved URANS simulations, the computational grid is defined around the blade to capture the full surface resolution of the wind turbine blade as well as the turbulent structures developed from the surface. This means that the geometry of the blades is accurately represented without any empirical relations, allowing for precise predictions of flow characteristics such as pressure distribution, velocity fields, and turbulence. The complete form of these equations represent unsteady, compressible, three dimensional viscous flows and may solve problems for which no analytical solution is available. The Navier-Stokes equations need to be combined with boundary conditions and may be used to determine the pressure and velocity field in the domain of interest, as a function of the forces exerted by the physical blades of the rotors.

In VAWTs, due to the highly periodic and unsteady nature of the blade passage in the flowfield, URANS can capture unsteady phenomena such as vortex shedding, blade wake interactions, and dynamic stall inherently. However, the turbulence cannot be inherently calculated and a closure model is required to evaluate the turbulent terms.

LATTICE-BOLTZMANN METHOD

The Lattice Boltzmann Method (LBM) is an Eulerian, mesoscopic approach to fluid dynamics that solves a discretized Boltzmann equation on a Cartesian grid. Fluid behaviour is captured through distribution functions that are associated with discrete velocities on the grid. These undergo local collisions and stream along lattice links, from which macroscopic quantities like density and velocity are recovered. A more detailed description of this method is presented in the work of Shan et al. [117]. The biggest advantage is the ability to naturally capture unsteady turbulence for complex geometries without requiring explicit turbulence closure modeling.

In this thesis, we employ LBM using the tool PowerFLOW 6-2021-R2 (PFLOW), developed by 3DS SIMULIA [118]. It solves the discrete, explicit, transient, compressible LBM equations by statistically tracking the streaming and collisions of fluid particles for a finite number of directions in the flowfield of the rotors. A Very Large Eddy Simulation (VLES) model is implemented to account for the effect of the sub-grid unresolved scales of turbulence. A two-equation $k-\epsilon$ re-normalization group is used to compute a turbulent relaxation time added to the viscous relaxation time. However, this model has a very high computational cost as the very fine turbulent structures need to be stored for each time-step.

2.4.4 SECONDARY EFFECTS

The blades of a VAWT experiences a varying angle of attack throughout its azimuthal cycle, due to the axis of rotation. This also imparts a curvilinear motion on the flow as the blades pass through it. These phenomenon introduces two additional effects, such as the following:

DYNAMIC STALL

Dynamic stall is an unsteady effect that occurs due to the airfoil operating in and out of stall results in a hysteresis [119–121]. Dynamic stall begins with the initiation of the leading edge flow separation which then leads to the leading edge vortex formation. Later, the flow will fully separate over the suction side of the airfoil as the vortex convects towards the trailing edge. As the airfoil starts to move back to pre-stall conditions, the flow starts to attach from the leading edge and finally attaches at the trailing edge. This dynamic effect results in a hysteresis curve, which is illustrated in Figure 2.10. This hysteresis effect is not captured in static airfoil polars, and obtaining dynamic polars for a wide range of flow conditions is impractical. Therefore, dynamic stall corrections are essential for methods that rely on static airfoil polars, especially for VAWTs at low Reynolds numbers. Typically, engineering models are used to correct dynamic stall effects which are typically empirical or based on wind tunnel measurements. Popular dynamic stall models are the Boeing-Vertol model [122], the Leishman-Beddoes (LB) model, which is adapted to wind turbines [123–125], the Øye model [126], the Gormont-Berg model [127], the ATEFlap model [128], and more recently the IAG model [129].

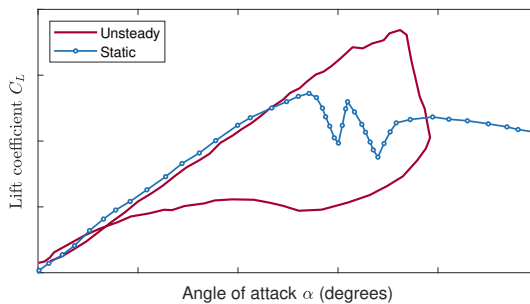
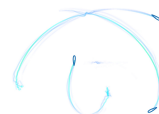


Figure 2.10: Illustration of the dynamic stall process showcased by the hysteresis of the lift coefficient. Adapted from Leishman [130]

FLOW CURVATURE

VAWT airfoils undergo circular motion over their azimuthal cycle, which can be decomposed into translation and pitching motion. This pitching component leads to a variation in the inflow along the chord that is typically not experienced by HAWTs, which introduces flow curvature effects that must be compensated for by an additional angle of attack or virtual camber [131–133]. This effect is magnified for a turbine with larger solidity, as the variation of relative velocity along its chord is larger than for a turbine with lower solidity. A representation of the flow curvature effects along with the virtual camber transformation are shown in Figure 2.11. Once again, engineering corrections exist for these effects as



suggested by Migliore et al. [131], where applying a virtual camber transformation is proposed. A different approach proposed by Goude [134] is to represent the angle of attack using a pitch rate and the chord mount position. Additionally, Mandal and Burton [135] theorised a correction factor from using thin-airfoil theory.

2

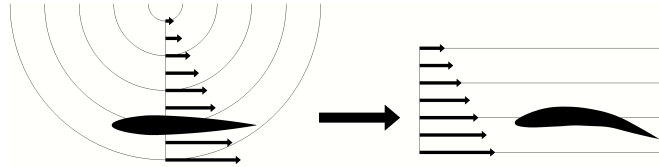


Figure 2.11: Illustration of the flow curvature effect (left) as well as the airfoil transformation technique (right). Reproduced from Van Der Horst et al. [136].

This dissertation:

All of the aforementioned numerical models are used at different chapters of this thesis. The DMS, 2DAC, URANS, and PFLOW models are used only in Chapter 3. The FVM models are used in Chapter 3 to compare against other models for the full-size X-Rotor, in Chapter 4 to validate the near-wake characteristics of the 1:100 scaled X-Rotor, and in Chapter 5 to tune the ALM model (*turbinesFoam*). The ALM model (*turbinesFoam*) is used in Chapter 6 to validate the 1:250 scaled X-Rotor, in Chapter 5 to identify the influence of VAWT geometry on the wake, and in Chapter 7 to model the VAWT wind farm. The dynamic stall corrections are only used in Chapter 4 and Chapter 6, while the flow curvature is only used in Chapter 7.

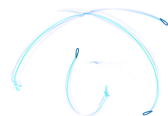
3

NUMERICAL FIDELITY REQUIREMENTS TO CAPTURE X-ROTOR PHYSICS

As discussed in Chapter 2, most performance metrics and aerodynamic loads of VAWTs are predicted using either two-dimensional or three-dimensional numerical models. However, since VAWTs inherently operate within a three-dimensional flow environment, the effectiveness of these models in accurately capturing rotor performance and loads—particularly under varying operational conditions such as different blade pitch offsets—remains uncertain.

Therefore, the objective of the present chapter is to conduct a systematic comparison of low-, medium-, and high-fidelity models across a range of operating conditions and blade pitch offsets, in order to assess their consistency and accuracy in predicting rotor loads and overall performance. The agreement between the models at different operating conditions are quantified for the rotor power, thrust, and blade forces, while the vertical induction is qualitatively compared at different blade pitch angles.

Parts of this chapter have been published in Giri Ajay, A., Morgan, L., Wu, Y., Bretos, D., Cascales, A., Pires, O., and Ferreira, C.: Aerodynamic model comparison for an X-shaped vertical-axis wind turbine, *Wind Energ. Sci.*, 9, 453–470, <https://doi.org/10.5194/wes-9-453-2024>, 2024.



3.1 INTRODUCTION

Accurate prediction of VAWT aerodynamic performance is essential for effective design and optimization, as it directly affects the power output and efficiency of the turbine [76, 100, 103, 104]. Different aerodynamic models for VAWTs have been researched and used, each with advantages and limitations, as seen in Chapter 2.

With the unique configuration of the X-Rotor, the influence of induction in the vertical direction is expected due to the coned blades of this geometry configuration. Therefore, to characterise the aerodynamics of the X-Rotor, it is necessary to understand the discrepancies between different aerodynamic models. In the works of Ferreira et al. [54] and De Tavernier et al. [62], the 3D aerodynamic effects of VAWTs with different loading conditions have been studied in detail but they do not cover that of VAWTs with coned blades, specifically for the X-Rotor.

Therefore, this chapter presents a comparative study of different aerodynamic models for the X-Rotor's primary rotor to understand their capacity to capture the 3D aerodynamics of the X-Rotor associated with fixed blade pitch offsets. Several numerical models ranging from low- to high-fidelity are used in this chapter to understand their agreement on predicting the rotor performance and loads. Furthermore, the influence of operating conditions, such as pitch offset, on the performance prediction across different fidelities are also presented.

3.2 METHODOLOGY

The current section briefs over the methodologies used in this chapter in Section 3.2.1 along with the setup to simulate the X-Rotor for all the models in Section 3.2.2.

3.2.1 AERODYNAMIC MODELS

Several aerodynamic models are used in this chapter to keep the comparison as insightful as possible. The models are elaborated in detail in Chapter 2, however a short summary of the models used along with their fidelity is presented in Table 3.1. The fidelity-level is based on the underlying physics of the model. Using a momentum-based approach is considered low-fidelity, a free vortex wake model is considered mid-fidelity and a blade resolved URANS approach is referred to as high-fidelity. The low- and mid-fidelity models used the airfoil polars that are discussed in Section 3.2.2.

Table 3.1: Models considered for benchmarking

Model	Method	Fidelity (colour in all plots)
DMS	Double multiple streamtube	Low (orange)
2DAC	2D Actuator Cylinder	Low (orange)
QBlade	QBlade free vortex wake	Medium (blue)
CACTUS	CACTUS free vortex wake	Medium (blue)
URANS	URANS with OpenFOAM	High (black)
PFLOW	Lattice Boltzmann VLES	High (black)

3.2.2 TEST SETUP

The full-size X-Rotor rotor geometry is used in this study. The rotor consists of a radius of 25 m and 75 m at the root and the tip of the blades respectively. The upper blades are attached at 30° from the vertical plane and therefore have a length of 100.0 m, and the lower blades are connected at 50° from the vertical plane and therefore have a length of 65.3 m. Both sets of blades have a linear taper in chord and relative thickness and utilise the symmetric NACA00XX aerofoil family. The blades are untwisted. The blade geometry at the root and tip are given in Table 3.2. For all simulation tools that are not blade resolved, polars are generated for the airfoil profile range of NACA0008 (root section) to NACA0025 (tip section) using XFOIL [137] at Reynolds number of $Re = 1.5 \times 10^7$ (based on the chord at the tip), and then extrapolated through the Viterna and Janetzke [138] method. In all models (except PFLOW) only the aerodynamically active portion of the rotor was modelled, meaning that the cross-beam connecting the rotor blades, and the tower are not modelled.

Table 3.2: The geometry for the X-Rotor blades, and intermediate values can be found through linear interpolation.

Blades	Section	Radius [m]	Cone Angle [$^\circ$]	Chord [m]	Thickness [%]
Upper	tip	75	30	5	08
	root	25	30	10	25
Lower	tip	75	50	7	08
	root	25	50	14	25

Due to the coned blades, the local tip-speed ratio pertaining to the local blade elements varies along the span and height. Therefore, the tip-speed ratios considered for analysis represent the value at the blade tips. Each of the low-fidelity and mid-fidelity models simulated the aerodynamic performance and loads of the turbine at a tip-speed ratio range of $\lambda = [2.5, 5]$ at 0.5 intervals with a fixed upper blade pitch range of $\beta = [-20^\circ, 20^\circ]$ with 5° intervals. Positive pitch corresponds to the upper blades pitching into the axis of rotation and negative pitch corresponds to the blades pitching away from the rotation axis. The pitching axis position varies from 25% chord at the root and 50% chord at the tips, as detailed in Appendix A. Figure 3.1 shows the difference between the airfoil orientation between positive and negative pitch offsets compared to no pitch offset.

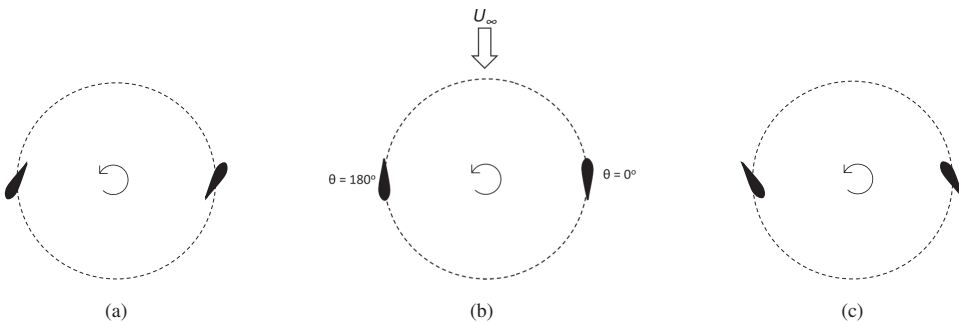


Figure 3.1: Top view of the upper blade tip with (a) negative, (b) zero, and (c) positive pitch offsets. θ indicates the azimuth and U_∞ is the freestream velocity



A homogeneous, constant, freestream velocity of $U_\infty = 12 \text{ ms}^{-1}$ is used for all low and mid-fidelity models. The 2DAC, CACTUS, and QBlade have 72 azimuthal discretisations per rotation, but this is not enforced in the DMS model, as the choice for uniform streamtubes is prioritized. The high-fidelity models used $\lambda = 5$ at $\beta = 0^\circ$ as their test cases with an inlet velocity of 12.5 ms^{-1} . Moreover, these models discretised the domain spatially and temporally. The momentum and vortex models are run iteratively until the difference in the power coefficient between consecutive iterations satisfies a convergence criterion of 10^{-3} . The vortex models use a second-order predictor explicit time advancement scheme and they completed 12 revolutions to meet the convergence criterion with an azimuthal resolution of 5° , as demonstrated from the convergence study in Appendix B. The convergence criterion value is chosen to give optimal accuracy for computational time, as a lower value becomes dependent on the interpolation scheme each model used to obtain the angle of attack from the polars. Therefore, the vortex model results presented here are from the last revolution of the rotor.

While the effects of flow curvature [131, 133, 139] and dynamic stall [119, 121] are shown to significantly affect aerodynamic performance, the low- and mid-fidelity models have been implemented without these effects. The choice to omit them is made in order to compare the underlying flow models as, at present, these codes do not employ identical correction factors for dynamic stall or flow curvature effects. Any one of these models could be updated with identical correction factors, however, a comparison of the most valid correction factors is beyond the scope of this article.

Both high-fidelity models inherently include flow curvature, dynamic stall, and viscous terms, as the rotor in these models is blade-resolved. Additionally, the PFLOW simulations include the secondary rotor in the lower blade, the tower, and the cross-beam that connects the two sets of blades together. As the secondary rotors experience high thrust, this is expected to decrease the tangential forces of the lower blade in the blade sections surrounding it across all azimuths, compared to the other simulation cases. As the cross-beam is not as aerodynamically significant compared to the blades of the rotor, the aerodynamic effects from this surface are neglected. The lower blade loads are also expected to be affected by the wake of the tower. However, this is expected to only have a significant impact around an azimuth of $\theta = 270^\circ$. The detailed setup information for the URANS and PFLOW models are listed in Appendix C and Appendix D

3.3 RESULTS AND DISCUSSIONS

This section goes over the results and discusses the observations and inferences made from the rotor power and thrust characteristics in Section 3.3.1. Later, the impact of the operating conditions on the forces are detailed in Section 3.3.2. Lastly, the influence of the operating conditions on the vertical induction are briefed in Section 3.3.3.

3.3.1 STUDY OF ROTOR POWER AND THRUST

The results for power and thrust of the X-Rotor are discussed in detail in Section 3.3.1 and Section 3.3.1. They are represented in terms of non-dimensional coefficients given by:

$$C_P = \frac{P}{\frac{1}{2}\rho A U_\infty^3}, \quad (3.1)$$

$$C_T = \frac{T}{\frac{1}{2}\rho AU_\infty^2}, \quad (3.2)$$

where P and T are the revolution-averaged power and thrust, A is the frontal area of the primary rotor ($12,870 \text{ m}^2$), U_∞ is the free-stream velocity, and ρ is the density of air, which is 1.225 kg/m^3 .

POWER

The variation of C_P with pitch angle β in the range of tip-speed ratios λ is presented in Figure 3.2. In these plots, it is observed that DMS severely deviates at $\beta = -10^\circ$ and for all negative pitch offsets from the other models. For positive pitch offsets, the model predicts different values, except at $\beta = 15^\circ$. There are two key features which lead to the breakdown of the DMS method in situations with pitch offsets. Firstly the DMS method does not consider the induction of the downwind portion of the rotor at the upwind actuator surface which becomes more critical as the loading is skewed to the downwind section at negative pitch offsets. Additionally, the streamtube expansion correction used in the DMS model over-predicts the contraction at the upwind actuator surface and the expansion at the downwind actuator surface. This leads to the region over which negative torque is produced to be contracted and the region over which the positive torque is produced to be extended leading to an over-prediction in power production in the case of negative pitch offsets. This shows that DMS is unreliable to evaluate the X-Rotor's aerodynamic performance, which is also observed by Ferreira et al. [54] for an H-type VAWT. Although it predicts similar values to the other models without pitch offsets, the model fails to capture the aerodynamic power profile of the X-Rotor.

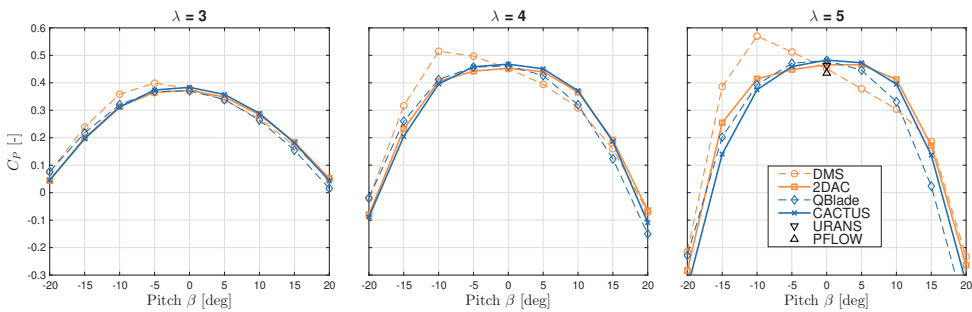


Figure 3.2: Variation in rotor power coefficient (C_P) with pitch angle at fixed tip speed ratios. Orange and blue correspond to the momentum and vortex models respectively. URANS and PowerFLOW results are also shown at $\lambda = 5$ for $\beta = 0^\circ$, corresponding with the black markers.

The mid-fidelity models agree well with each other in pitch ranges of $-10^\circ \leq \beta \leq 10^\circ$. The 2DAC model agrees with the CACTUS results for positive pitch offsets and agrees better with the QBlade results for negative pitch offsets. Compared to the URANS and PFLOW at $\lambda = 5$, the vortex models over-predict the power slightly (roughly 6%) in contrast to the momentum models agreeing well. While blockage effects can affect the C_P from the URANS simulations [140], the difference mainly arises from the use of polars in the vortex models versus performing a full blade-resolved study. This is demonstrated in an article conducted by Melani et al. [141] where they analysed the lift and drag coefficients



for a NACA0021 airfoil between XFOIL polars as well as the blade resolved 2D URANS results. The results showed significant differences at low Reynolds numbers, but at higher Reynolds numbers, the differences minimise but do not vanish. PFLOW predicts the least power, but this still is quite close to the other models despite modelling the secondary rotors and the tower. Rezaeiha et al. [142] demonstrated the power loss correlation with the dimensions of the tower, which explains the power deficit of the PFLOW observed here.

3

THRUST

The variation of C_T with pitch angle β and tip-speed ratio λ is shown in Figure 3.3. While the trends are preserved between models, the magnitudes differ significantly. At $\lambda = 3$ for $\beta \geq 0^\circ$, 2DAC and DMS match quite well with QBlade, until $\beta = 15^\circ$, while CACTUS predicts higher thrust. However at $\beta \leq 0^\circ$, QBlade moves away from the momentum models and agrees well with CACTUS. At $\lambda = 4$, all models predict different thrusts, with the momentum models systematically showing lower thrust with increasing λ compared to others. At $\beta \leq 0^\circ$, 2DAC and DMS agree well with each other except at large pitch offsets. This observation is enhanced at $\lambda = 5$, where the CACTUS and QBlade results estimate larger thrust values than the low-fidelity models. However, URANS and PFLOW agree quite well with the vortex models at $\beta = 0^\circ$. The DMS model under predicts the thrust values at high loading, indicating that the correction used for high blockage cases is inaccurate. Additionally, the dependence on pitch angle does not agree with the other models. This can again be attributed to the effects of on over prediction of streamtube expansion increasing the estimate of thrust as the loading is shifted to the downwind rotor half, and decreasing the estimate of thrust as the loading is redistributed to the upwind rotor half in a similar manner to the power as discussed in section Section 3.3.1. Furthermore, the DMS model is valid only for axial inductions between 0 and 0.5, which could be violated in the simulations here. 2DAC's low thrust prediction can be attributed to the limitation of the linear correction method, where it becomes less accurate at higher loading [54]. The difference between the URANS and the vortex models, at 2%, is primarily due to the use of polars in the vortex models vs blade resolved simulation of the URANS as discussed previously. All models deviate significantly at large pitch offsets, which in a way exaggerates the differences observed at small pitch offsets.

Overall, the vortex models seem to agree well with the high-fidelity models, suggesting the momentum models are not quite valid at these high tip-speed ratios.

3.3.2 STUDY OF BLADE FORCES

As the URANS and PFLOW predicted the results for one case, the normal and tangential loads are compared with the momentum and the vortex models. The momentum and vortex models are also analysed in detail for the set pitch offset cases.

BLADE FORCES - COMPARISON WITH HIGH-FIDELITY MODELS

The normal and tangential forces at $\lambda = 5$ and $\beta = 0^\circ$ for the upper and lower blades from all the models are shown in Figures 3.4 and 3.5, respectively. The upper blade normal forces of QBlade and the high-fidelity models match well in the upwind half, but the latter predict lower magnitudes in the downwind half. Additionally, in the lower blade, URANS

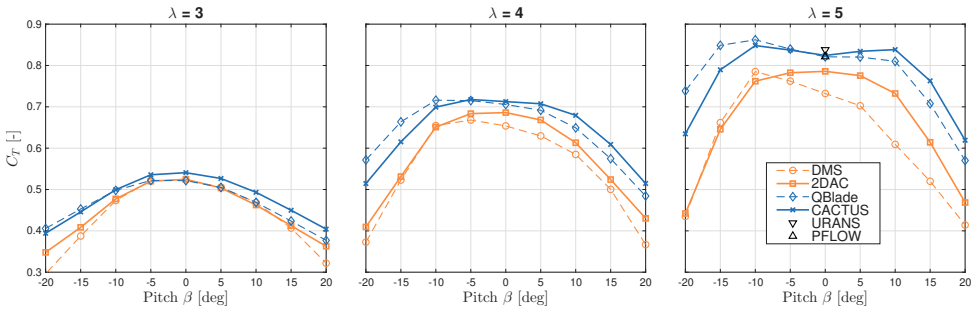


Figure 3.3: Variation in rotor thrust coefficient (C_T) with pitch angle at fixed tip speed ratio. Orange and blue correspond to the momentum and vortex models respectively. URANS and PowerFLOW results are shown at $\lambda = 5$ for $\beta = 0^\circ$, corresponding with the black markers.

systematically predicts higher forces than the other models while PFLOW indicates the fluctuation at $\theta = 270^\circ$ which is due to tower wake interaction. The upper blade tangential forces match quite well in the upwind half. But in the downwind half, URANS and PFLOW predict lower forces compared to the other models. This is also observed in the lower blades, except that PFLOW predicted lower forces in the upwind half as well. This is due to the forcefield created by the induction of the secondary rotor mounted on the lower blades. This induction of the secondary rotor has a small area of influence which does not affect the upper blades significantly. The difference between high-fidelity and other models in both normal and tangential forces is probably due to high flow separation occurring in the downwind half of the turbine. However, isolating its effect from the inherent flow curvature in the high-fidelity model is outside the scope of this paper.

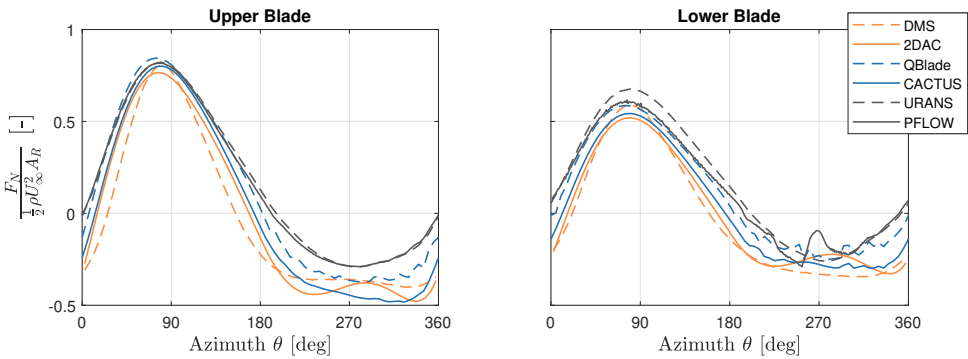
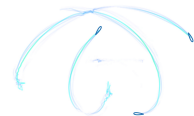


Figure 3.4: Non-dimensionalised normal forces at $\lambda = 5$ and $\beta = 0^\circ$ predicted by the momentum, vortex, and CFD models. Orange, blue, and grey represent momentum, vortex, and CFD models respectively. The frontal area of the rotor A_R is $12870m^2$.

BLADE FORCES - COMPARISON BETWEEN DIFFERENT PITCH-OFFSETS

By increasing λ , the loads on the blade increase, which is inferred from Figure 3.3. The results discussed henceforth are limited to $\lambda = 4$. Pitch offset cases of $\beta = -10^\circ, 0^\circ, 10^\circ$



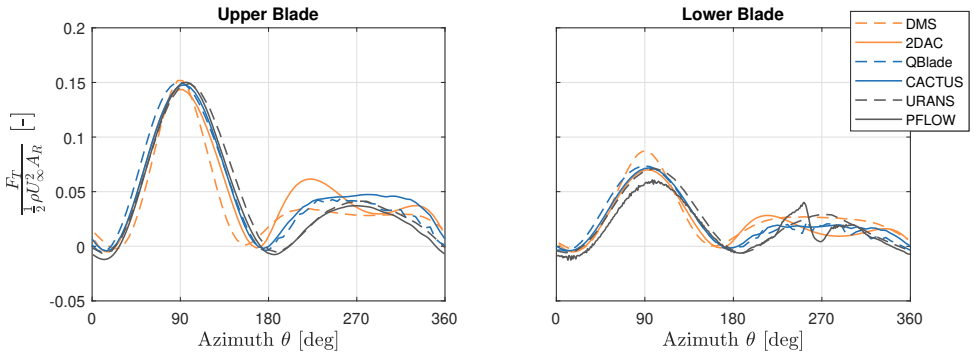


Figure 3.5: Non-dimensionalised tangential forces at $\lambda = 5$ and $\beta = 0^\circ$ predicted by the momentum, vortex, and CFD models. Orange, blue, and grey represent momentum, vortex, and CFD models respectively.

are chosen for further analysis. The forces of the turbine are calculated by integrating individual blade-element normal force contributions along the span of the blade. The normal forces for upper and lower blades are shown in Figure 3.6 and the tangential forces are shown in Figure 3.7.

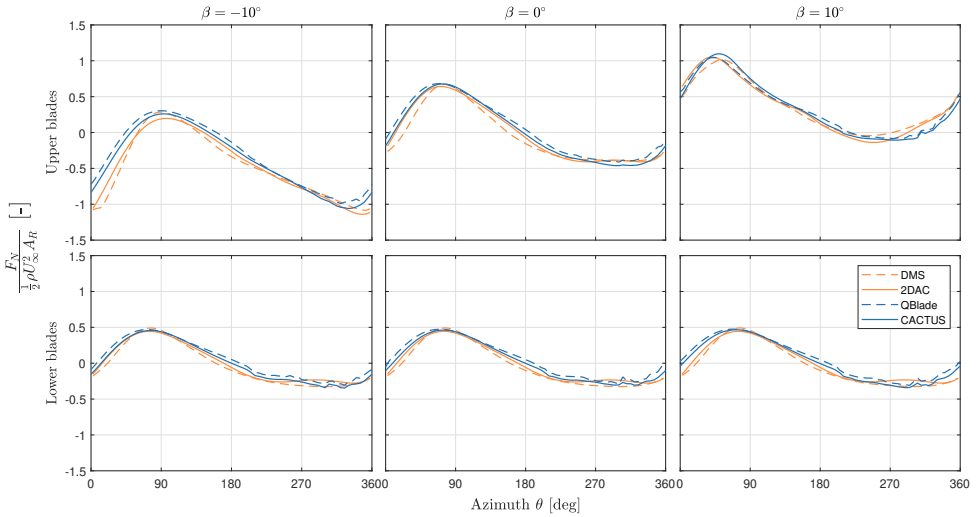


Figure 3.6: Non-dimensionalised normal forces from upper & lower blades for $\beta = [-10^\circ, 0^\circ, 10^\circ]$, $\lambda = 4$. Orange and blue are the momentum & vortex models respectively.

From the normal force data presented in Figure 3.6, at $\beta = 0^\circ$, the rotor is loaded more in the upwind half ($\theta = 0^\circ, 180^\circ$) than the downwind half ($\theta = 180^\circ, 360^\circ$). This is due to the VAWT experiencing asymmetric force distribution during operation, as demonstrated for an H-VAWT [106, 143]. Here, all models agree except for DMS which under-predicts the forces in the upwind half, although it agrees the peak force predicted by the other models. For negative pitch offsets, the force magnitude decreases at the upwind half of the rotor

and increases at the downwind half of the rotor, whereas the opposite occurs when the blades have a positive pitch offset. At $\beta = -10^\circ$, the models deviate in the first quarter of the azimuth for the upper blades. The momentum models predict larger force magnitudes than the vortex models. This is due to the large negative angle of attack observed because of the pitch offset, causing certain points along the span to approach stall conditions. This is also observed in the last quarter. At $\beta = 10^\circ$, the models agree well in general, but they deviate in the last azimuthal quarter for the upper blades. This difference arises from blades nearing stall conditions, as mentioned earlier, as well as some BVI being captured by the vortex models. Additionally, the rotor experiences a phase shift in the normal force as the pitch offset changes. The peak at $\beta = 0^\circ$ is observed before $\theta = 90^\circ$, while the peak for $\beta = -10^\circ$ is around $\theta = 90^\circ$, and the peak for $\beta = 10^\circ$ is observed around $\theta = 60^\circ$. This occurs as the blades experience stall earlier in the azimuth with positive pitch offsets and the opposite for negative pitch offsets compared to $\beta = 0^\circ$. This phase shift is not observed in the lower blade forces by the momentum models, as they are 2D models that do not take vertical induction into account.

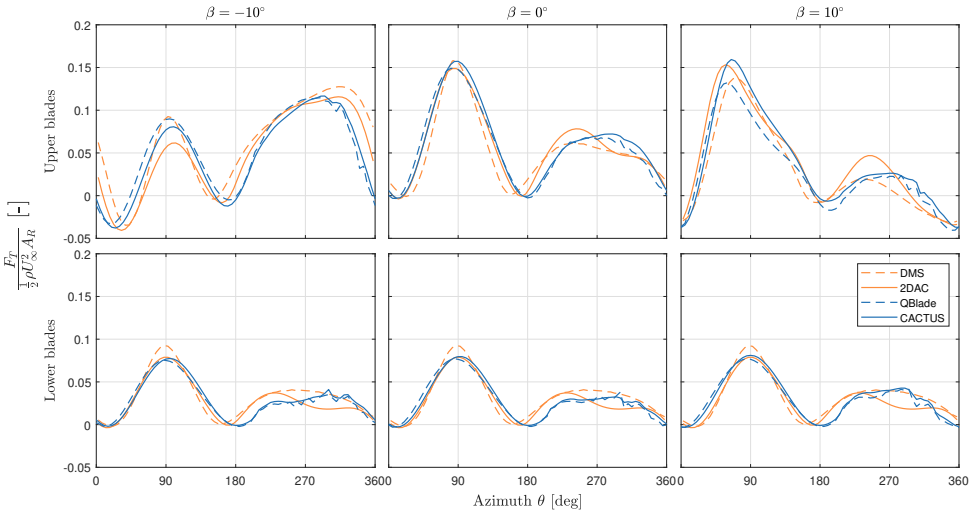
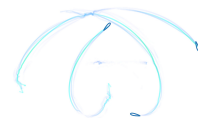


Figure 3.7: Non-dimensionalised tangential forces from upper and lower blades for $\beta = [-10^\circ, 0^\circ, 10^\circ], \lambda = 4$. Orange and blue are the momentum and vortex models respectively.

The tangential forces from Figure 3.7 also show the redistribution of forces to the upwind and downwind half with positive and negative pitch offsets respectively. For $\beta = 0^\circ$, the models behave similarly to the trends previously seen with the normal forces in the upwind half but vary severely in the downwind half where BVI exists. This effect is enhanced with pitch offsets. The DMS model consistently predicts a higher peak tangential force for the lower blade compared to the other models. The phase shift of the forces exists for the upper blades but not for the lower blades. Again, the vortex models show slight differences in the lower blades with pitch offset despite not pitching the lower blades. The momentum models predict identical forces for the lower blades throughout the range of pitch offsets as they are 2D models.



To enhance this difference seen in the lower blade, Figure 3.8 shows the normalized difference in the normal force of $\beta = 10^\circ$ and $\beta = -10^\circ$ with respect to $\beta = 0^\circ$ of the vortex models. The normal forces of the lower blades with pitch offsets vary from $\beta = 0^\circ$ by 6-7% from the vortex models. This shows a strong 3D aerodynamic effect of vertical induction for the X-Rotor in its operation, which is not accounted for by the 2D momentum models. This variation increases with tip-speed ratio or larger pitch offsets, as the loads increase. In the first azimuthal quarter, where the largest relative velocity is expected, the difference starts out at 5–6% but drops down to 0.5% by $\theta = 90^\circ$. This is due to the phase shift of the peak forces between the pitched and non-pitched case, which brings down the relative value. In the second azimuthal quarter, the difference is nearly zero due to the lower blade forces as the blades experience stall conditions. In the third quarter, the downwind passage of the blade flips the pressure and suction side, which inverts the magnitude of the force. In the last quarter, the differences are high due to the presence of BVI and the increase in force magnitude. This is shown by the $\beta = -10^\circ$ and $\beta = 10^\circ$ plots crossing each other around $\theta = 300^\circ$, where a sudden spike in the difference occurs and continues to diverge steadily beyond that. Additionally, CACTUS results show some jumps in the normal forces (notable ones at $\theta = 300^\circ, 330^\circ$, and 340°) that are due to BVI. However, QBlade shows large spikes in the entire downwind half of the rotor in contrast to the gentler spikes from CACTUS that are observed only in the last quarter. This can be attributed to the QBlade's turbulence vortex viscosity factor, which was introduced by Leishman [130] to account for increased vortex diffusion at highly turbulent flows. In QBlade, this affects the vortex core size at each time step, resulting in larger spikes compared to those of CACTUS.

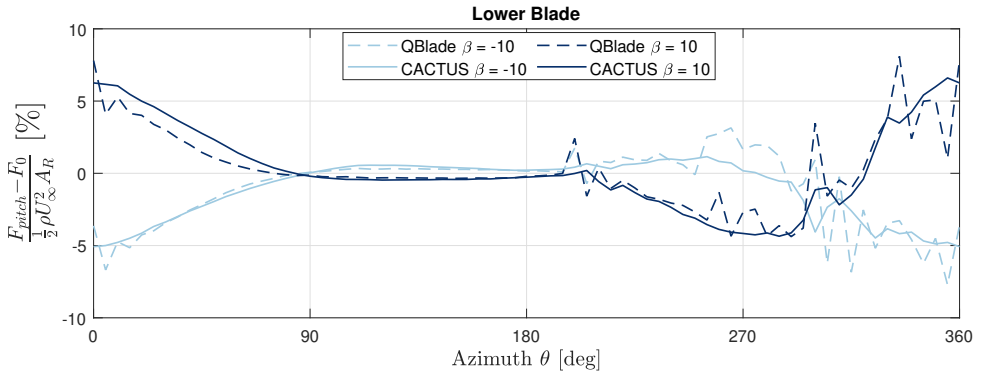


Figure 3.8: Percentage difference of non-dimensional normal forces at fixed pitch-offsets relative to zero pitch offset of vortex models. Light and dark blue indicate $\beta = -10^\circ$ and $\beta = 10^\circ$ respectively.

3.3.3 VERTICAL INDUCTION AND INFLOW

The X-Rotor consists of coned blades in its primary rotor geometry, therefore a component of the normal forces from the blade acts in the axial or vertical direction. As observed in Figure 3.8, the presence of vertical induction while pitching the upper blades significantly affects the forces in the fixed-pitch lower blades due to the change in force field towards the upwind and the downwind halves. CACTUS results for the vertical induction at mid-span of the X-Rotor blades along its azimuthal cycle are shown in Figure 3.9. QBlade results are

not considered as it does not store induction in all directions in its output. The vertical induction due to coned blades as well as the finite blade effects can be observed clearly at $\beta = 0^\circ$ for the upper blades, where the induction is mostly negative for the upwind half and mostly positive for the downwind half, which is due to the blade tip vortices as well as the coned blades of the X-Rotor. Furthermore, $\beta = -10^\circ$ is shown to be exhibiting positive induction overall in contrast to the negative induction shown in $\beta = 10^\circ$. The direction of vertical induction indicates that the tip-vortices also flip their direction, which causes a large change in the flowfield of the rotor. The lower blades clearly experience a difference in vertical induction as the pitch of the upper blade changes, which correlates well with the trends that are seen in Figure 3.8. Most differences can be observed in the first, third, and last azimuthal quarters, while the second quarter shows the least difference due to stalling of the blade. Furthermore, this shows the importance of vertical induction especially with blade pitch, where the force field changes the tip-vortex strength resulting in enhanced 3-dimensionality of results [27].

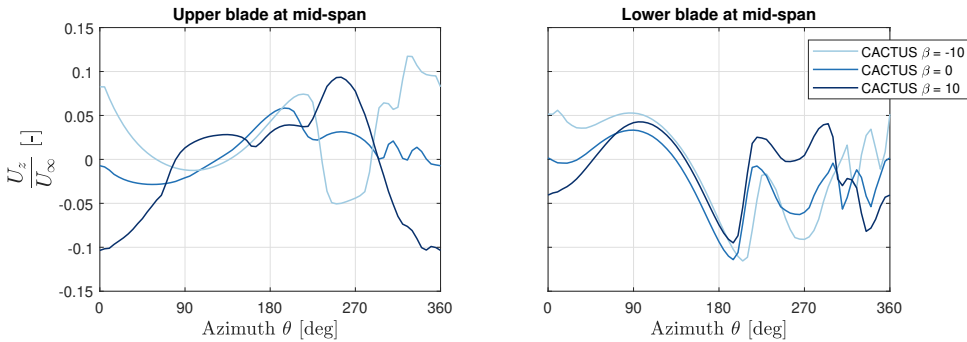
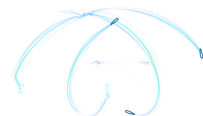


Figure 3.9: Vertical induction normalised by freestream (U_z/U_∞) at mid-span of upper and lower blades. Vertical induction results are from CACTUS for $\beta = [-10^\circ, 0^\circ, 10^\circ]$ indicated by light, medium, and dark blue profiles. Results are normalised by free-stream velocity.

As the tip-speed ratio is different along the span, the vertical induction also varies along the span. To obtain an overview of the spanwise variation of vertical induction at these pitch cases, Figure 3.10 shows contour plots of vertical induction as a function of span and azimuth. At $\beta = 0^\circ$, the upper blades seem to exhibit almost no vertical induction in the upwind half, while the lower blades produce small positive induction, with the tips showing the largest induction. In the downwind half, the upper blades show positive induction and the lower blades show negative induction. At $\beta = -10^\circ$, the upwind half is mostly dominated by positive induction from the root sections and the lower blades, with the tip-vortex of the lower blade giving negative induction at $\theta = 0^\circ$. This is because the upper blades are loaded more in the downwind half. At $\theta = 180^\circ$, the upper blades exhibit large positive induction, while the lower blades show mostly large negative induction. However, there exists a strong negative induction in the root region around $\theta = 300^\circ$ before transitioning to strong positive induction. Additionally, due to the downwind loading of the upper blades, the regions close to the tip until mid-span show very large positive induction. At $\beta = 10^\circ$, there is primarily strong negative induction in the first azimuthal quarter concentrated mostly in the upper blades due to large loading in the upwind half.



Whereas in the downwind half, there exists a dominant positive induction in the root region and the upper blades before transitioning to a strong negative induction in the last azimuthal quarter. Interestingly, it is observed that with pitch offsets, the root section is quite important despite a smaller local tip-speed ratio when compared to the tip. This is attributed to the root vortices that are formed as the upper and lower blade meet there. Change in pitch affects the vorticity system of the upper blade tips as well as the roots. Ultimately, the vertical induction varies quite significantly and it is seen that the induction on the lower blades is influenced heavily by that of the upper blades as well as the tip and root vortices.

3

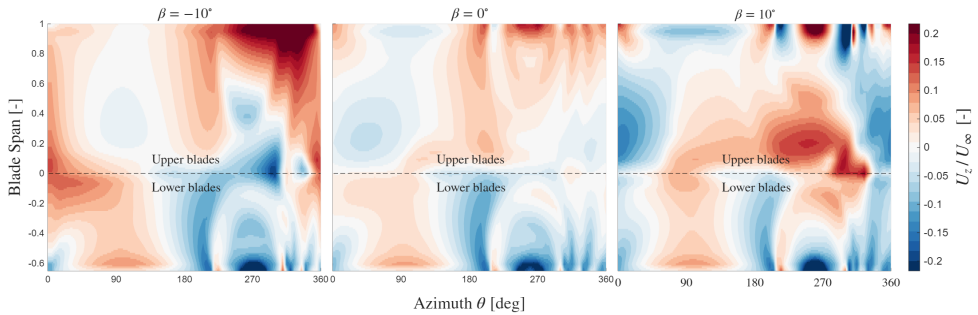


Figure 3.10: Vertical induction normalised by freestream (U_z/U_∞) as a function of azimuth and blade span. Results are from CACTUS for $\beta = [-10^\circ, 0^\circ, 10^\circ]$. The lower blade is represented with negative span values. Blade span is normalised with the maximum span, with 1 being the tip of the upper blades, 0 being the root, and -0.65 being the tip of the lower blades.

Overall, the force field of the rotor is subject to change with pitch offsets as the vorticity system changes [27]. Therefore, it can be said that VAWTs, not specifically limited to the X-Rotor, become highly 3D with pitch offsets as the vorticity system changes and the validity of 2D aerodynamic models dwindle with larger offsets.

3.4 CONCLUSIONS

A numerical comparison of different aerodynamic models was conducted to understand the aerodynamic characteristics and the performance of an X-shaped VAWT for a range of tip-speed ratios and pitch offsets. This study contributed the following: (1) a comparative study of different aerodynamic models for the X-Rotor's primary rotor and (2) the significance of 3D aerodynamics for the X-Rotor associated with fixed blade pitch offsets.

The models presented were: Double multiple streamtube (DMS), 2D Actuator cylinder (2DAC), QBlade lifting line (QBlade), CACTUS lifting line (CACTUS), PowerFLOW (PFLOW), Unsteady Reynolds Averaged Navier-Stokes CFD model (URANS).

This study showed that the DMS model performed almost on par with the other models in calculating rotor performance parameters when there was no pitch offset, but predicted significantly different results once blade pitch was introduced, as the validity of the streamtubes enclosing the downwind actuator began to fail. This worsened at high tip-speed ratios where the DMS models predicted power coefficients at Betz limit with pitch offsets.

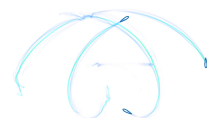
The 2DAC model offered consistent data at small pitch-offsets (between $\beta = [-5^\circ, 5^\circ]$). However, being inherently a 2D and a quasi-steady model, it did not capture the BVI and the effect of vertical induction of the X-Rotor. Moreover, it predicted the forces in the lower blade to be the same across all upper blade pitch offsets, which was not the case for the models that accounted for the vertical induction.

The thrust predicted by the momentum models was different from that of the vortex models. Moreover, these models were unable to capture the vertical induction effects and the BVI that occurred in the downwind cycle of the rotor. Therefore, the 2D momentum models were mostly inaccurate in predicting the thrust, power, or blade loads for the X-Rotor due to the influence of 3D aerodynamics.

The QBlade and the CACTUS open-source simulations offered great consistency with each other, including capturing the 3D aerodynamics effectively. The QBlade model showed huge turbulent viscosity spikes in its results occurring throughout the normal and tangential forces, which was a result of the vortex core and turbulent viscosity model used in the solver. This behaviour also translated to the blade-integrated forces where the QBlade slightly overpredicted the results compared to CACTUS. However, both their results remained consistent, suggesting their reliability over low-fidelity models for this specific rotor geometry.

URANS and PFLOW results were compared with the vortex and momentum models for power, thrust, and blade forces for one test case. Primarily, the URANS and PFLOW agreed very well with the thrust of the vortex models, although predicted slightly less power. This was because URANS had small domain sizes which caused enough blockage effects to affect the results, and the PFLOW modelled the tower as well as the secondary rotors which also caused slight power loss. Secondly, the downwind half of the turbine showed significantly lower force magnitudes, which was due to a combination of flow separation at the blades as well as the inherent flow curvature effects present in the CFD solvers.

The distribution of vertical induction over the span and azimuth was studied to understand the 3D aerodynamics of the X-Rotor, also with pitch offsets. The vertical induction was dominated primarily by the tip vortices (due to spanwise lift variation) in cases with no pitch offset. Interestingly, with pitch offsets the root vortex showed greater influence on the vertical induction for the X-Rotor despite operating at a much lower local tip-speed ratio. Due to the large vertical induction fluctuations through the azimuthal cycle of VAWTs at fixed pitch offsets, it concluded that the 2D models lose their validity in these conditions and for coned VAWTs.



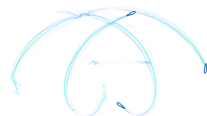
4

NEAR-WAKE CHARACTERISATION AND VALIDATION OF A SCALED X-ROTOR

In Chapter 3, various numerical models were compared, revealing that the geometry of the X-Rotor has a pronounced influence on blade loading across different operating conditions – an effect that could only be captured by medium- and high-fidelity models. However, the capability of medium-fidelity approaches, such as the free-wake vortex model, to accurately predict the near-wake characteristics of the X-Rotor remains uncertain.

This chapter addresses that gap by comparing the free-wake vortex model CACTUS against stereoscopic Particle Image Velocimetry (PIV) measurements for a scaled X-Rotor, with the aim of validating its near-wake predictions. Both qualitative and quantitative comparisons are carried out to assess the flowfield features with and without blade pitch offsets. Furthermore, the study provides insights into the three-dimensional aerodynamic effects introduced into the wake by the turbine’s coned blade geometry.

Parts of this chapter have been published in Giri Ajay, A., Bensason, D., and De Tavernier, D.: Validation of the near wake of a scaled X-Rotor vertical-axis wind turbine predicted by a free-wake vortex model, *Wind Energ. Sci.*, 10, 1829–1847, <https://doi.org/10.5194/wes-10-1829-2025>, 2025.



4.1 INTRODUCTION

Free-wake vortex models are a promising alternative, offering a relatively cost-efficient approach while capturing the 3D rotor loads of VAWTs, as demonstrated in Chapter 3. However, the models were only compared against higher-fidelity simulations in limited operational cases and could not be validated with experimental data due to the full-scale rotor size. Furthermore, it is unclear how effective the model is at capturing the near-wake characteristics of the turbine across different pitch offsets.

Free-wake vortex models have previously been experimentally validated in the near-wake for HAWTs [144–146]. Similar validations have been conducted for H-type VAWTs [61, 147, 148], demonstrating that free-wake vortex models are highly effective in accurately capturing the VAWT's near-wake. Bensason et al. [97] obtained phase-locked PIV data of the induction field of a scaled X-Rotor with no pitch offsets. The dataset consisted of planar slices at different locations inside the rotor volume to examine the influence of the coned blades on the vorticity field. Additionally, Bensason et al. [98] captured additional phase-locked data in the near-wake of the turbine with pitch offsets, focusing on their impact on the near-wake flow.

Therefore, this chapter aims to validate the near-wake aerodynamic characteristics of the scaled X-Rotor predicted by the CACTUS free-wake vortex model by comparing its results with wind tunnel measurements for both non-pitched and pitched cases. Furthermore, it examines the influence of the coned blades on blade loads and the flow field as a function of rotor height.

4.2 EXPERIMENTAL APPROACH

In this section, we provide a brief description of the rotor model used in the experiments and the experimental setup. Detailed information on setup and measurement techniques can be found in Bensason et al. [97] and Bensason et al. [98].

4.2.1 SCALED X-ROTOR MODEL

The test geometry is a purely geometrically scaled model of the full-size primary rotor, scaled by a factor of $\frac{1}{100}$. The top and bottom blades have a tip diameter of $D = 1.5$ m and cone angles of 30° and 50° , respectively, resulting in upper and lower spans of 1.00 m and 0.65 m, respectively. Aside from scaling, the primary difference between the full-scale turbine and the scaled model is that the latter consists of four straight NACA0021 airfoils with a constant chord of $c = 0.075$ m, attached to a stiff crossbeam of length 0.5 m with the same profile and chord. The rotor is supported by a tower with a diameter of 0.06 m. The model operates at a constant tip-speed ratio $\lambda = 4.0$ at $U_\infty = 4$ m/s, yielding a chord-based Reynolds number of $Re_c = 8.1 \times 10^4$ at the tip. The operating conditions are determined to obtain a thrust coefficient to be as close as possible to the optimal value of $C_T = 0.7$, without compromising the structural integrity of the rotor.

A visualisation of the tip-trajectory is provided in Figure 4.1. A constant inflow velocity of $U_\infty = 4$ m/s is assumed, neglecting the influence of induction. Blades (B) 1 and 2 represent the blades at azimuth $\theta = 0^\circ$ and 180° , corresponding to the rotor's perpendicular position to the flow where the frontal area is maximum, as labelled in Figure 4.1. The top (t) and bottom (b) blade pairs follow the same convention. The structures associated with each

blade (B1t, B2t, B1b, B2b) are distinguished by colour. As the blades progress over time, the resulting flow structures from each blade convect downstream, eventually overlapping and interacting with others. Visualisations of each phase are provided here as a reference for analysing the flow fields at the specified streamwise locations within the volumes.

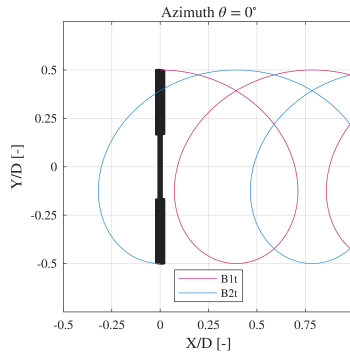


Figure 4.1: Top-view schematic of tip-trajectory of the top blades at azimuth $\theta = 0^\circ$. The tip-trajectory are mapped to each blade, in this instance labelled B1t and B2t, for the two blades in the top-half (t). Corresponding blades in the bottom half would be referred to as B1b and B2b respectively. No wake expansion or induction is assumed.

4.2.2 EXPERIMENTAL SET-UP

The experiments, detailed in Bensason et al. [97], are conducted in the Open Jet Facility (OJF) at TU Delft Aerospace Engineering, as illustrated in Figure 4.2. A controlled streamwise velocity of $U_\infty = 4$ m/s is maintained throughout the experiment. The resulting inflow has reported turbulence intensities of 0.5% within the testing region [149]. The measurement system captures phase-locked flow field measurements at various locations within the X-Rotor induction field. Normalised cross-stream locations $x/D = \{-0.435, -0.265, -0.065, 0, 0.065, 0.265, \text{ and } 0.435\}$ were measured at azimuths $\theta = \{0^\circ, 45^\circ, 90^\circ, 135^\circ\}$. At each cross-stream location, multiple planes are recorded along the y- and z-axes using a traversing system and then stitched together. Due to time constraints, not all phase and wake locations were measured, leading to variations in the number of planes recorded for each wake-phase pair. Additionally, because of the camera orientation relative to the measurement planes, frequent masking operations are applied to eliminate shadows. Given the placement of the particle image velocimetry (PIV) system, the measurements primarily focus on the windward half of the cycle ($Y/D > 0$).

4.2.3 UNCERTAINTY OF THE FLOWFIELD MEASUREMENTS

The diffraction-limited minimum image diameter is of practical significance for optical measurements such as PIV. Following Equation 4.1, the smallest particle image that can be obtained using the given imaging configuration is defined by d_{diff} [150].

In this case, the magnification factor is $M = 0.01$ (sCMOS camera catalogue, $6.5 \mu\text{m}$). The lens used has a focal length f of 106 mm, resulting in an object imaging distance (d_o) of 101 mm. The f-number $f_\#$ for this experiment is set to 8, and the sCMOS cameras have





Figure 4.2: Experimental setup in the OJF adapted from Bensason et al. [97]. The origin of the coordinate system is placed at the center of the crossbeam. The axis and direction of rotation are marked (anti-clockwise) with a curved arrow, and the tip radius R is marked. A visualization of the measurement plane is provided (green cone). A similar setup for the second experimental campaign is presented in Bensason et al. [98].

a wavelength of $\lambda = 523 \text{ nm}$ (catalogue). Consequently, d_{diff} is $10.1 \mu\text{m}$. Given a particle pixel diameter d_p of approximately $3 \mu\text{m}$, the ratio d_{diff}/d_p is 3.4.

$$d_{\text{diff}} = 2.44 \times f_{\#} \times (M + 1) \times \lambda \quad (4.1)$$

We can also examine the standard uncertainty in the mean flow field. Using the approach of Sciacchitano and Wieneke [151], the standard uncertainty is calculated with Equation 4.2. For each measurement, we average over $N = 120$ samples. The standard deviation of the velocity, σ_U , consists of all three velocity components and varies across the plane, both temporally and spatially. In general, regions with high vorticity, such as tip and shed vortices, exhibit a velocity standard deviation of $\sigma_U = 0.24 \text{ m/s}$, with the highest component occurring out of the plane, while the other two components are 0.19 m/s and 0.15 m/s . In wake regions where no vortical structures are present, the velocity standard deviation is lower, approximately $\sigma_U = 0.05 \text{ m/s}$, with all components being similar in magnitude. Using the highest value for calculation, the standard uncertainty of the mean velocity is $U_U = 0.02 \text{ m/s}$, which corresponds to 0.5% of the free-stream velocity.

$$U_U = \frac{\sigma_U}{\sqrt{N}} \quad (4.2)$$

A similar uncertainty analysis is conducted for the cases with blade pitch offset and is presented in detail in Bensason et al. [98].

4.3 NUMERICAL SETUP

In this section, the model and the input data used for the numerical setup is explained in Sections 4.3.1, 4.3.2, and 4.3.3. Lastly, the test matrix used for this chapter is detailed in Section 4.3.4.

4.3.1 FREE-WAKE VORTEX MODEL

In this study, we used the CACTUS free-wake vortex model to simulate the scaled X-Rotor, representing each of the upper and lower blades as lifting lines. The model is described in detail in Chapter 2, where the model uses a set of discretized line elements to model the blades of the rotors and the flowfield is modelled using a Lagrangian approach. The flowfield is essentially modelled as a vortex lattice with shed, bound, and trailing circulation lines produced from the blades. To model the circulation distribution, the NACA0021 blade airfoil profile is characterised using an airfoil polar dataset, which is further detailed in Section 4.3.2.

4.3.2 NACA0021 AIRFOIL DATASET AND ITS UNCERTAINTY

In our study, the experiments operate at a chord-based Reynolds number of $Re = 81 \times 10^3$. Melani et al. [141] collected experimental and numerical polars for the NACA0021 airfoil across different Reynolds number ranges: low ($40 - 80 \times 10^3$), medium ($80 - 700 \times 10^3$), and high ($\geq 700 \times 10^3$). In the low ranges, there is a significant deviation among the polar profiles, due to measurement uncertainties. In contrast, in the medium and high ranges, the polars exhibit much better agreement among each other. Therefore, we can understand that at these low Reynolds numbers, the polars are uncertain. Regardless, to present a very conclusive study, we generated the airfoil polars using XFOIL [137] at Reynolds number of $Re = 81 \times 10^3$ for the X-Rotor, with an Ncrit of 4, based on the experimental turbulence intensity. The static stall angle in this case is around $\alpha_{ss} = 9^\circ$. The post stall characteristics are obtained using a Viterna extrapolation technique [138].

To elaborate on the uncertainty of the polars, Figure 4.3 presents the lift coefficient C_l as a function of angle of attack α at the operational Reynolds number. In general, the polars predicted by XFOIL predict a steeper slope in the lift profile compared to the experiments. This is most clearly observed in the section before the static stall. This slope decreases with decreasing Ncrit value. However, it is very evident that there is a large discrepancy between the different polars - even among experiments. The two experiments profiles vary quite significantly due to uncertainty in measurement, corroborating the analysis of Melani et al. [141]. This highlights the challenges in achieving accurate airfoil data at these low Reynolds numbers and the importance of considering these uncertainties in aerodynamic analyses. In our study, we expect most discrepancies to be due to the uncertainty described here. We shall discuss these further in Section 4.4.

4.3.3 DYNAMIC STALL AND FLOW CURVATURE MODELS

Considering the operational Reynolds number of the scaled X-Rotor, we employ the Leishman-Beddoes (LB) dynamic stall model [124, 125], which is readily available in CACTUS. The LB model simulates the dynamic stall process by solving a set of first-order differential equations and utilising empirical data to represent delayed flow separation, vortex shedding, and hysteresis in lift and drag.

While flow curvature models provide a more accurate depiction of airfoil motion in VAWTs, we opt not to include it here for two critical reasons. (1) Implementing the flow-curvature model, such as Goude [134], to a rotor geometry with a large spanwise relative velocity distribution would make it exceedingly difficult to isolate the differences observed between CACTUS and experimental results to other factors. (2) Geometrical



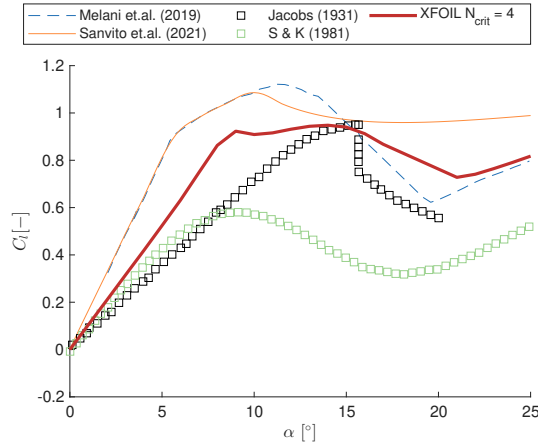


Figure 4.3: Comparison of lift coefficient C_l vs angle of attack α for NACA0021 airfoil datasets at $Re = 81 \times 10^3$. Markers correspond to the experimental datasets from Jacobs [152] (black) and Sheldahl and Klimas [153] (green). The blue dashed line and orange solid line correspond to the XFOIL polars generated by Melani et al. [141] and Sanvito et al. [154]. The red solid line corresponds to the XFOIL polars used in this study.

virtual airfoil transformations, such as Hirsch and Mandal [155], show large inaccuracies at high chord-to-radius ratios of $c/R > 0.2$, which is the regime that most of the X-Rotor blade operates in. Secondly, as CACTUS does not come inherently with a flow curvature correction model, implementing it oneself in the source code would be outside the scope of this study. Furthermore, attempting to pre-emptively correct the airfoil polars without calculating the relative velocities would result in unwarranted errors in CACTUS. We believe a flow curvature model is essential for this geometry, but would bring uncertainty to the results when the behaviour of the rotor with and without flow-curvature has not been tested for this geometry. This is indeed a limitation in our approach as the lack of flow curvature would introduce differences in the blade forces and affect the near-wake due to the change in vortex field. As highlighted by Goude [134], the flow curvature model would introduce a net positive angle of attack to the blade in the upwind half, which would redistribute the loads further upwind [69] and directly influence the wake.

4.3.4 CASE MATRIX AND SIMULATION PROCEDURE

To simulate the X-Rotor, the upper and lower blades are discretised into 18 blade sections each, which is the minimum required to achieve blade element independence of power, as seen in Giri Ajay et al. [156]. An additional blade section is included to smooth the transition between the upper and lower blades with fixed pitch offsets. The cross-beam and tower are not modelled, as their contributions are expected to be minimal and predictable, offering little additional insight into the aerodynamics of the X-Rotor. A constant vortex core model is employed, with the vortex core set to 100% of the chord-to-radius ratio. The simulations are run for 10 revolutions to ensure convergence, using a second-order predictor explicit time advancement scheme. A sensitivity analysis was conducted on vortex core size, dynamic stall, and the effects of lift and drag coefficients for the airfoil. To

maintain focus on the main findings, this analysis is presented separately in Appendix H. The conclusions drawn from the sensitivity study informed the final setup parameters summarised in Table 4.1. The solidity σ of the X-Rotor is determined using Equation 4.3.

$$\sigma = \frac{Nc(L_U \cos 30^\circ + L_L \cos 50^\circ)}{A}, \quad (4.3)$$

where N is the number of blades, L_U and L_L are the upper and lower blade spans, c is the chord, and A is the rotor frontal area. The angles correspond to the coned angles of the upper and lower blades.

Table 4.1: Description of the simulation setup for CACTUS.

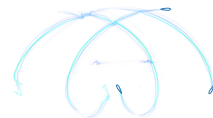
Parameters	Value
Rotor diameter (at the tips) D	1.5 m
Rotor chord c	0.075 m
Upper blade span L_U	1 m
Lower blade span L_L	0.65 m
Frontal Area A	1.287 m ²
Number of blades N	2
Airfoil profile	NACA0021
Tip-speed ratio λ	4
Inlet velocity U_∞	4 m/s
Air density ρ	1.207 kg/m ³
Solidity σ	0.15
Blade elements (per blade)	18
Azimuthal discretisation	72
Blade pitch β	-10°, 0°, 10°
Vortex core size (fraction of local chord)	1

4.4 RESULTS

In this section, we go through the results and discuss our observations and reasoning from the analysis of the case without pitch offsets. Firstly, we discuss the near-wake of the non-pitched case by analysing the velocity and vorticity field in Section 4.4.1. Later, similar analyses are conducted between the cases with pitch offsets in Section 4.4.2. Finally, we document the effects of the cone angle on the velocity field in Section 4.4.3.

4.4.1 VALIDATION STUDY - NON-PITCHED CASE

The streamwise velocity u/U_∞ and vorticity $\omega_x D/U_\infty$ contours at different azimuthal positions $\theta = [0^\circ, 45^\circ, 90^\circ, 135^\circ]$ are compared between CACTUS simulations and the experimental outputs in Figure 4.4 and Figure 4.5 respectively. The planes are located at $X/D = -0.27, 0.067, 0.27, 0.43$ and showcase the simulations in the upper tile and the experimental results in the lower tile for each phase. The plane $X/D = 0$ was not measured in the experiment as it produced considerable reflection inducing high uncertainty in the PIV processing.



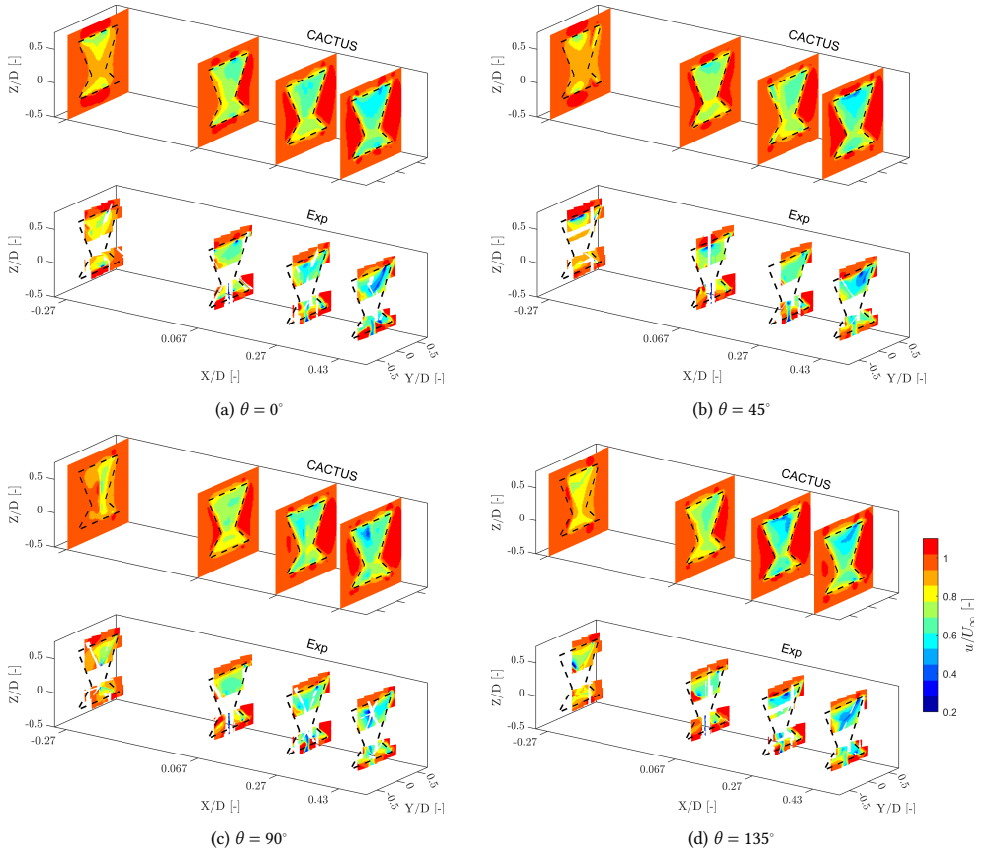


Figure 4.4: Normalised streamwise velocity (u/U_∞) contours of the X-Rotor at azimuths $\theta = [0^\circ, 45^\circ, 90^\circ, 135^\circ]$ respectively at downstream locations $X/D = [-0.27, 0.067, 0.27, 0.43]$ where D is the rotor diameter. The numerical and experimental results are shown in the upper and lower tile respectively. The black dash lines indicate the projected frontal area of the rotor on the corresponding plane. The x-axis is magnified to enhance visibility.

Overall, the velocity predictions within the rotor volume show good agreement with the experimental results, as observed in Figure 4.4, except for the wake of the tower, which is not modelled in CACTUS. The flowfield trends align well with experimental data, with velocity deficits accurately represented in the regions of blade passage across all azimuths. The induction in the upwind plane at $X/D = 0.27$ is also well predicted. Some minor discrepancies are expected, as CACTUS does not account for blade deflection and deformation caused by centrifugal forces and the high rotational speed of the rotor. This is particularly noticeable at the windward tips ($Y/D > 0$), where the experimental results show velocity deficits extending beyond the projected frontal area of the rotor—an effect not captured in CACTUS. At $X/D = 0.43$, CACTUS under-predicts the velocity deficit across all azimuths. This difference is likely due to the challenge of uncertainty with the polars, as previously discussed in Section 4.3.2. If the polars were closer to the true

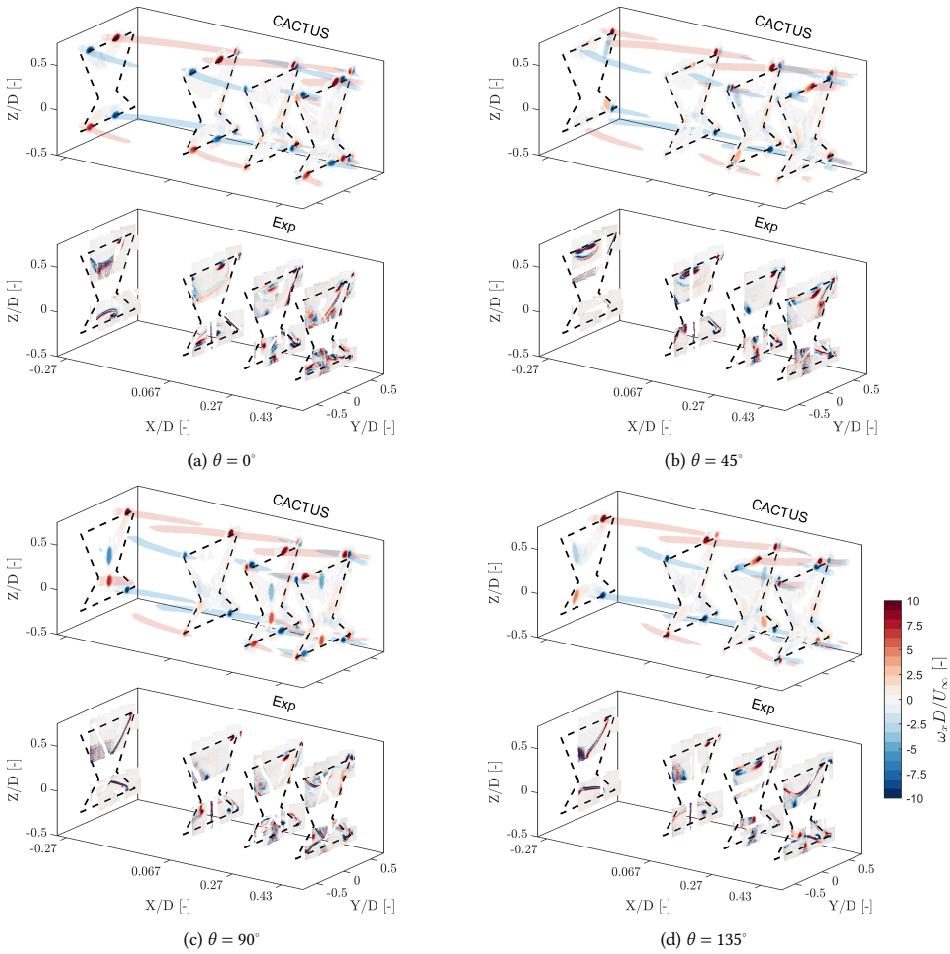
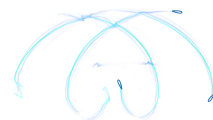


Figure 4.5: Normalised streamwise vorticity ($\omega_x D/U_\infty$) contours of the X-Rotor at azimuths $\theta = [0^\circ, 45^\circ, 90^\circ, 135^\circ]$ respectively at $X/D = -0.27, 0.067, 0.27, 0.43$ where D is the rotor diameter for CACTUS (top) and experiments (bottom). CACTUS isosurfaces are overlaid to show the evolution of the vortices with non-dimensionalised strength of 6 and above. The black dash lines indicate the projected frontal area of the rotor. Very low values of vorticity are hidden and x-axis is magnified to enhance visibility.

experimental airfoil behaviour, the difference could be minimised. This holds true for the rest of the results discussed in this study.

A similar trend is observed in the vortex structures in Figure 4.5, with the simulation results generally aligning well with the experiments. The elliptical vortical structures seen in the experiments correspond to the shed vortices from the blades, as detailed in Bensason et al. [97]. These vortices take on an elliptical shape due to the coned geometry of the X-Rotor blades. While the shed vortices are captured in the CACTUS model, they appear as faint smears e.g., in the upper half at $\theta = 0^\circ$ and $X/D = 0.067$, and are significantly



weaker in magnitude compared to the experimental results. This discrepancy is once again attributed to the airfoil polar uncertainty. The isosurfaces further illustrate the evolution of dominant vortices in the CACTUS simulations. Comparing with Figure 4.1, the vortices generated at $X/D = -0.27$ at $\theta = 0^\circ$ originate from the passage of B2t and B2b. At $X/D = 0.067$, these vortices intersect the windward tip, while the other dominant vortices are remnants from the previous cycle of B1t and B1b – evident from the isosurfaces – which reveal two sets of trailing vortices convecting downstream. This pattern extends to other planes and phases, highlighting vortex interactions between the blade passages of B1 and B2. At $X/D = 0.43$, the downwind passage of B1t and B1b generates three pairs of tip vortices in both the upper and lower halves of the rotor. This matches the experimental observations, although the absence of leeward planes in the measurements makes it challenging to confirm the presence of these vortex pairs definitively. Additionally, in the experiments, vortices tend to intersect the measurement plane at laterally farther locations than predicted by the simulations, e.g., tip vortices of B2t and B1t at $X/D = 0.067$ and $X/D = 0.43$. This discrepancy arises from blade deflection, which is not accounted for in CACTUS. As the blade tips deflect outward, the vortices are shed from a more laterally displaced position, affecting their subsequent convection paths.

Quantitative comparisons between the CACTUS model and the experimental results can be made by examining streamwise velocity profiles at various streamwise locations, both upstream and downstream of the rotor, across different azimuthal phases. Figure 4.6 presents these comparisons, showing streamwise velocity slices u/U_∞ as a function of X-Rotor height, evaluated at $Y/D = -0.125$ and $Y/D = 0.25$ for azimuthal positions $\theta = [0^\circ, 45^\circ, 90^\circ, 135^\circ]$.

As expected from the earlier contour comparisons, the CACTUS results align well with the experimental data. In the leeward slice ($Y/D = -0.125$), CACTUS consistently underpredicts the velocity in the lower half of the turbine, except in the most upwind plane. This discrepancy is attributed to the influence of the tower. In the experiments, the counter-clockwise rotation of the tower induces local flow acceleration on the leeward side, which is not accounted for in the CACTUS model. Since this region is close to the tower, its influence is more pronounced here than on the windward side. Additionally, CACTUS does not fully capture some of the velocity spikes observed in the experiments, particularly at $\theta = 45^\circ$ and $\theta = 135^\circ$. This discrepancy arises from two factors: blade deflection in the experiments and the velocity field resolution in CACTUS. The former affects vortex proximity to the measurement plane—blade deflection in the experiments can bring vortices closer than simulated, as seen at $\theta = 135^\circ$. The latter relates to the resolution of the volumetric velocity field obtained from CACTUS. Increasing the resolution to match the PIV planes would better capture these spikes but would also result in excessively large data files due to CACTUS's volumetric outputs. Another notable difference is the influence of the struts in the PIV data, which is evident at $\theta = 45^\circ$ and $X/D = 0.067$. In the windward slice ($Y/D = 0.25$), the differences between CACTUS and the experiments are lesser than the leeward side. The influence of the tower is minimised as there is no observable trend of overprediction or underprediction from CACTUS in the lower half of the rotor. The upwind plane has the best match while the differences increase as we move downwind. At $\theta = 135^\circ$, in the planes $X/D = 0.067$ and 0.27 have the most observable deviations. This is due to the blade wake interaction occurring at this azimuth which is under-represented in CACTUS

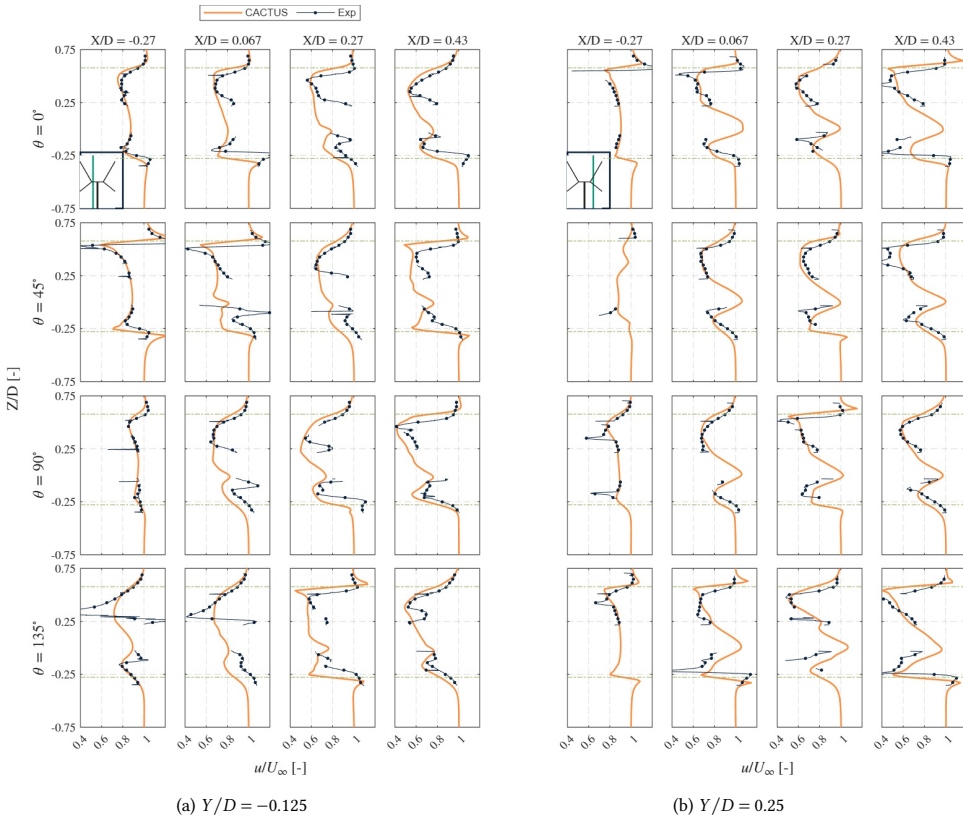


Figure 4.6: Comparison of the streamwise velocity u/U_∞ slices along the height of the X-Rotor at two lateral positions at discrete streamwise locations $X/D = [-0.27, 0.067, 0.27, 0.43]$ at phase locked azimuths $\theta = [0^\circ, 45^\circ, 90^\circ, 135^\circ]$. The inset figure in the first tile is presented to indicate the location of the slice with respect to the rotor - the green line is the Y/D slice along the height of the rotor.

compared to the experiment. Just as the leeward side, the peaks of velocity profiles occurs at different heights due to the deflection of blade not being modelled in CACTUS. Once again, the ability to resolve the spikes is largely dependent on the resolution of the velocity field obtained from CACTUS, notably seen at $X/D = 0.43$ for $\theta = 0^\circ$. Overall, the trends of the wake are captured and the velocity deficits are predicted well - which indicates that CACTUS can be a good tool to represent the velocities inside the volume of the X-Rotor.

4.4.2 VALIDATION STUDY - PITCHED CASE

Similar to the work by Bensason et al. [98], a positive pitch corresponds to orienting the leading edge towards the rotation axis, while a negative pitch directs it away. Additionally, in line with the original control strategy of the X-Rotor design [157], the lower blades are not pitched along with the upper blades. The experiments measured planes downwind of the rotor for all three pitch cases, $\beta = -10^\circ, 0^\circ$ (baseline), and 10° , at an azimuth of $\theta = 0^\circ$, but only for the upper blades.



To facilitate comparison, Figure 4.7 and Figure 4.8 present the normalised streamwise velocity u/U_∞ and vorticity $\omega_x D/U_\infty$ respectively, for the three pitch cases in both CACTUS simulations and experimental results.

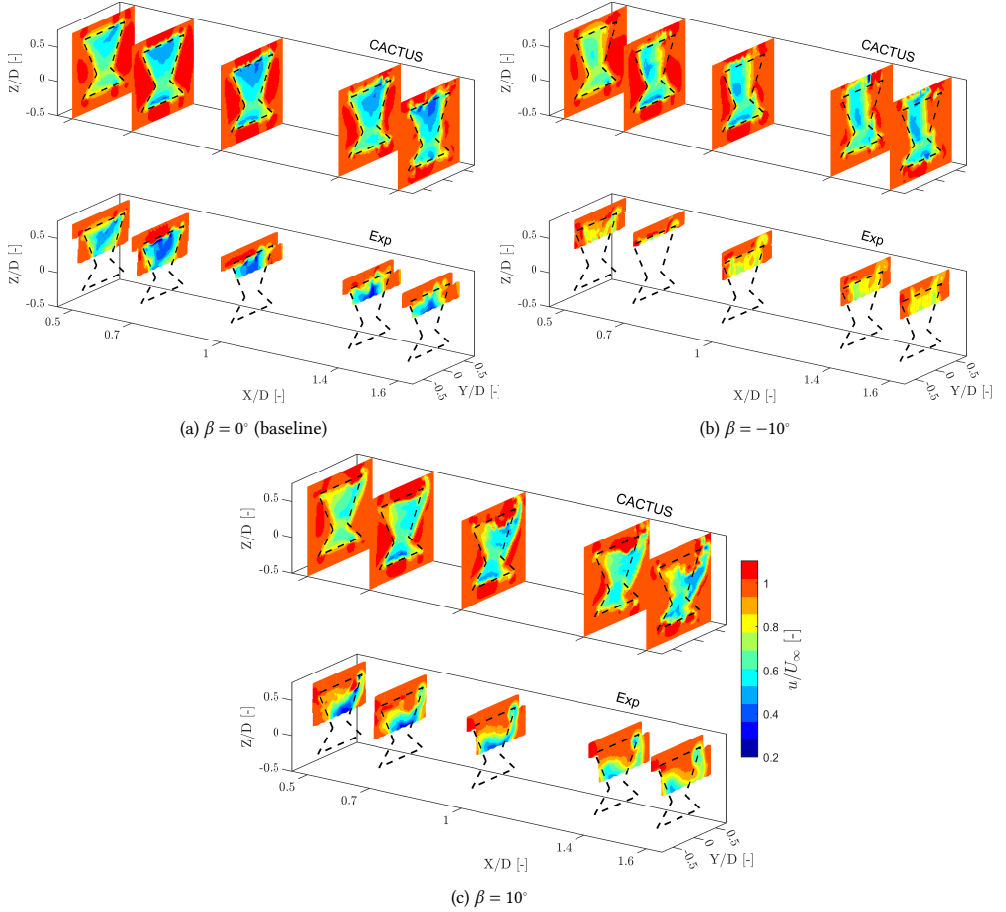


Figure 4.7: Normalised streamwise velocity (u/U_∞) contours of the X-Rotor with pitch offset $\beta = 0^\circ, -10^\circ, 10^\circ$ respectively at downstream locations $X/D = 0.5, 0.7, 1, 1.4,$ and 1.6 of the CACTUS (above) and experiments (below). The black dash lines indicate the projected frontal area of the rotor on the corresponding plane. The x-axis is magnified to enhance visibility.

The baseline pitch case effectively extends the analysis from Figure 4.4 and the discussion in Section 4.4.1. While the CACTUS model continues to capture the overall trends of the velocity profiles, it underpredicts the velocity deficit at $X/D = 1.4$ and beyond. The experimental results indicate that the wake centre is lower than predicted in CACTUS, though quantifying this displacement is challenging due to the limited number of measured heights in the experiments. The vortical structures observed in each plane are generally similar between CACTUS and the experiments, except for the shed vortex, which is visible at $X/D = 0.5$ in the experiments but not in CACTUS. Further downstream, the

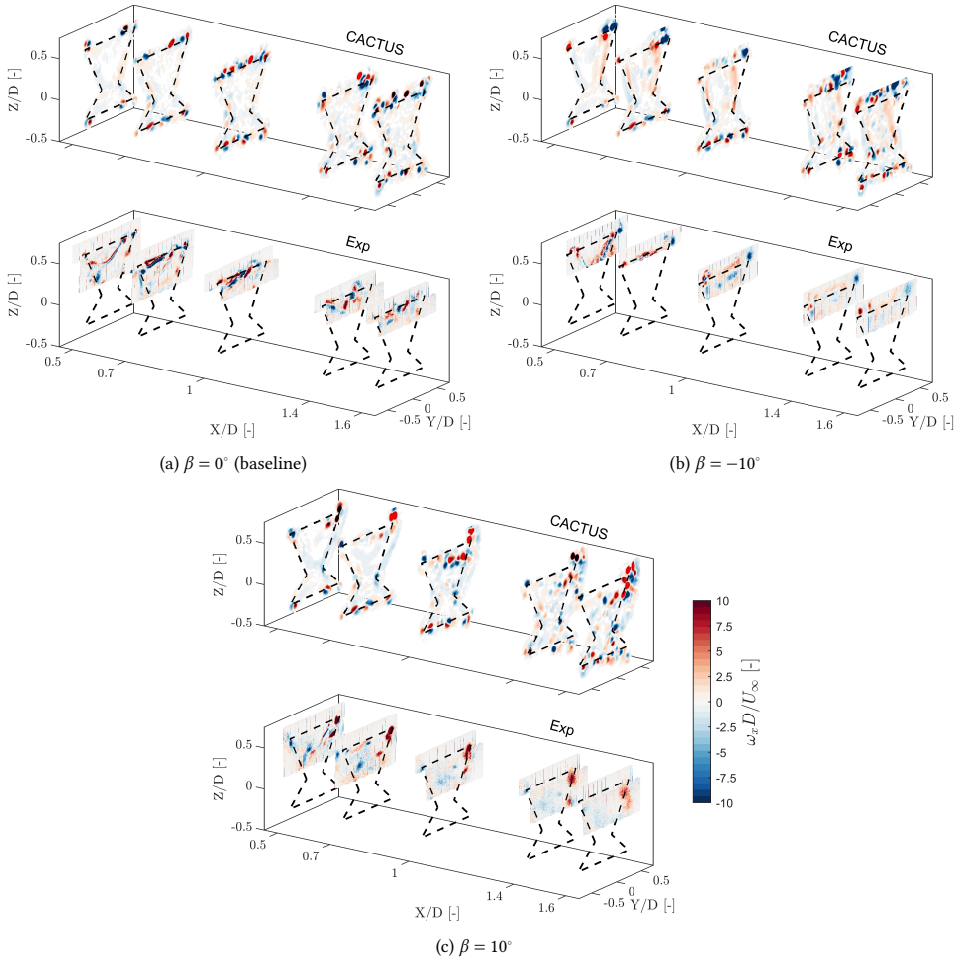
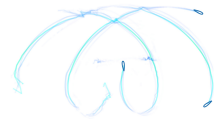


Figure 4.8: Normalised streamwise vorticity ($\omega_x D/U_\infty$) contours of the X-Rotor with pitch $\beta = -10^\circ, 0^\circ, 10^\circ$ respectively at $X/D = 0.5, 0.7, 1, 1.4,$ and 1.6 of the CACTUS (above) and experiments (below). The black dash lines indicate the projected frontal area of the rotor. The x-axis is magnified to enhance visibility.

vortical structures primarily consist of trailing vortices from the upper and lower blade tips. However, CACTUS appears to overpredict the vortex strengths, consistent with the discussion in Section 4.4.1. This discrepancy arises because, in the experimental results, the vortices exhibit dissipation, whereas in CACTUS, vortices generated in previous cycles remain dominant in the flow.

When pitched to $\beta = -10^\circ$, the lateral thrust of the rotor increases in magnitude, inducing a laterally inward flow into the wake [69, 158]. This results in wake inflow from the sides and vertical outflow, a pattern observed in both the experiments and CACTUS. However, differences arise in the velocity magnitudes and wake shape. CACTUS predicts stronger lateral flow on the windward side compared to the experiment, causing the wake



to contract more rapidly in this region. Additionally, CACTUS shows the wake starting to exit the top of the rotor area at $X/D = 0.7$, whereas this behaviour is not yet observed in the experiments. The discrepancy increases further downstream, attributed to the stronger tip-vortices predicted by CACTUS, which accelerate wake recovery compared to the experiments. Moreover, CACTUS predicts higher velocity deficits, suggesting a greater streamwise thrust than observed in the experiments. The large pitch angles in this configuration cause the turbine to operate at extreme angles of attack, well beyond stall, which significantly influences CACTUS predictions since it relies on polar data for load estimation. Bensason et al. [98] documented substantial unsteady flow separation and turbulence on the windward side at this pitch setting, explaining the stronger windward tip-vortex in CACTUS that leads to a more contracted wake. Additionally, the difference in circulation between the upper and lower blades results in a root vortex predicted by CACTUS. This vortex is visible in the windward root section and gradually moves upward downstream. Furthermore, CACTUS vortices do not dissipate as quickly as those in the experiments, further contributing to the observed differences.

4

In the $\beta = 10^\circ$ case, the opposite wake behaviour is observed: laterally exiting through the upper half of the rotor area while freestream air enters vertically from above. The experiments indicate significant wake deflection starting at $X/D = 0.5$, which is greater than the values predicted by CACTUS. Additionally, CACTUS underpredicts the velocity deficit within the rotor compared to the experiments until $X/D = 1$, beyond which most of the experimental wake exits the captured field of view. These discrepancies are primarily attributed to the vorticity distribution arising from the load distribution. In the experiments, a dominant windward tip-vortex facilitates freestream inflow from above. Meanwhile, the weaker vortices dissipate quickly, preventing them from significantly influencing the wake. In contrast, CACTUS, lacking viscous dissipation, produces numerous vortices near the windward tip, which intensify further downstream. This incorrect vortex representation leads to inaccurate velocity predictions, preventing CACTUS from capturing the downward movement of the wake. Interestingly, the wake in the lower half of the X-Rotor shifts laterally in the opposite direction to the upper half. This is due to the formation of a root vortex that induces lateral forcing on the lower half. Once again, differences in vortex dissipation contribute to this effect, while the experimental data show a dominant tip-vortex influencing vertical freestream influx, CACTUS instead predicts an accumulation of vortices near the upper half, altering the wake dynamics.

A quantitative analysis of the streamwise velocity profiles along the height of the X-Rotor is presented in Figure 4.9. To ensure consistency, we selected the same lateral locations as in the discussion from Section 4.4.1.

In the leeward slice, the velocity profile from the experiment in the baseline case is generally well represented by CACTUS, except at $X/D = 1.4$ and beyond, where discrepancies become more pronounced. This aligns with the earlier observation that CACTUS predicts the wake centre to be positioned higher than in the experimental results. For $\beta = -10^\circ$, a significant difference emerges between the predicted and measured values, with the experiments showing much higher velocities than CACTUS. This discrepancy increases further downstream, reaching up to 50% along the height. The primary cause of this difference is the previously discussed overprediction of tip-vortex strength in CACTUS. At $\beta = 10^\circ$, CACTUS predictions also deviate from experimental values. While the velocity

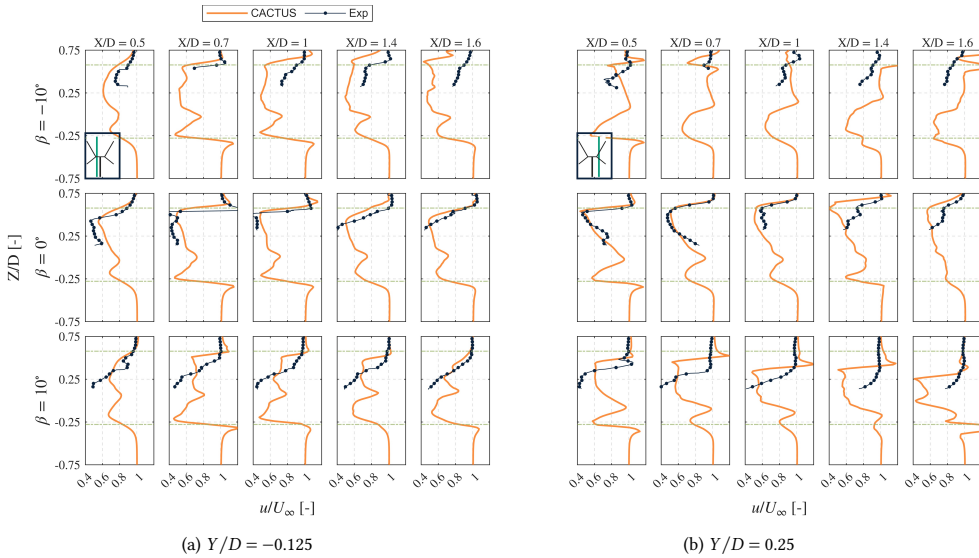


Figure 4.9: Comparison of the streamwise velocity u/U_∞ slices along the height of the X-Rotor at lateral position $Y/D = -0.125$ (left) and 0.25 (right) at discrete streamwise locations $X/D = [0.5, 0.7, 1, 1.4, 1.6]$ at pitch offsets $\beta = [-10^\circ, 0^\circ, 10^\circ]$. The inset figure in the first tile is presented to indicate the location of the slice with respect to the rotor - the green line is the Y/D slice along the height of the rotor.

profile aligns with the experiment over a small height range in certain planes, $X/D = 1$ and 1.6 , larger deviations occur near the root. This discrepancy is primarily due to the stronger leeward vortex predicted by CACTUS compared to the weaker vortex observed in the experiments. However, the differences in this pitch case at the leeward slice are generally smaller than those seen in the $\beta = -10^\circ$ case.

A similar pattern is observed in the windward slice—while the streamwise velocity profile is predicted relatively accurately in the baseline case, the pitched cases exhibit significant inconsistencies with the experimental profiles. These discrepancies are primarily attributed to differences in vortex strength predicted by CACTUS, which depend on the airfoil polars selected for the simulation. CACTUS struggles to accurately capture the increase in circulation induced by pitch offsets, as its predictions rely heavily on the input polars. Given that the static stall angle for these polars is $\alpha_{ss} = 9.1^\circ$, pitching the airfoils by $\beta = 10^\circ$ effectively shifts the C_l vs α profile such that the blade would mostly operate in deep-stall conditions throughout its azimuth. As the accuracy of XFOIL becomes questionable at deep-stall conditions (Section 4.3.2), the errors are compounded. Additionally, flow curvature effects could potentially mitigate these differences by improving the vortex representation in the pitched cases, but their influence on a coned blade remains unclear. Since the wake characteristics are directly linked to blade forces, a comparison of the predicted and experimental blade loads would provide further insight. However, blade load data is unavailable for this dataset.

Overall, CACTUS appears less effective in capturing the near-wake flowfield of the X-Rotor without pitch offsets. However, the general trends and behaviour of the wake



profiles predicted by CACTUS remain valuable for future research.

4.4.3 INFLUENCE OF CONE ANGLE ON THE VELOCITY FIELD

As the CACTUS model represents the flowfield of the case without pitch offsets well, we can consider its predictions on the flowfield to be valid.

In Chapter 3, we introduced the concept of vertical induction generated by the coned blades of the X-Rotor, both with and without pitch offsets. In this section, we extend that discussion by presenting the spanwise normal force distribution and spanwise angle of attack distribution as a function of azimuth in Figure 4.10. Additionally, we provide the blade-integrated forces to offer insight into the overall load contribution of the rotor. In both figures, we focus on the B1 alone, rather than the entire rotor, to facilitate a more detailed discussion of the downwind half of the rotation.

4

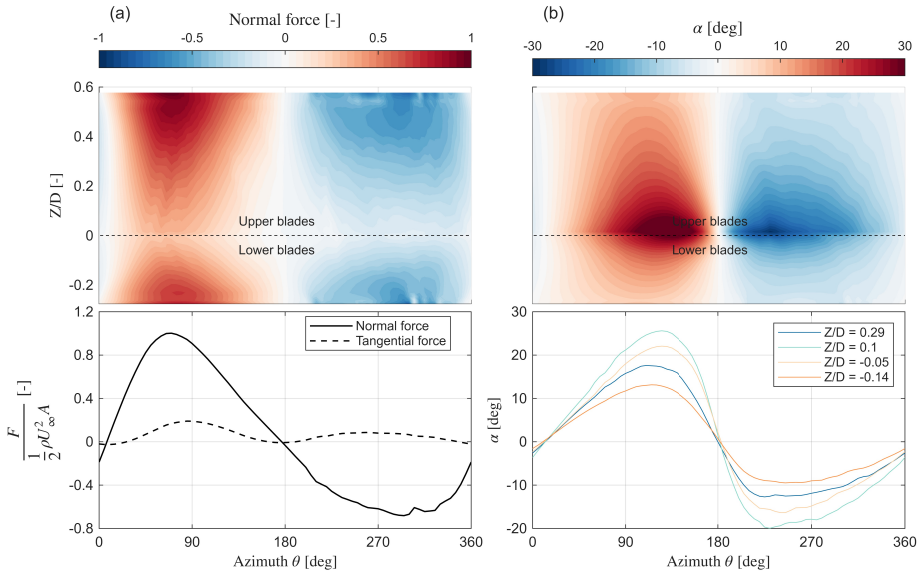


Figure 4.10: (a) Spanwise distribution of normal blade force as a function of height Z/D and azimuth θ in the top tile and blade integrated normal and tangential force as a function of azimuth in the bottom tile. Positive normal force is away from the axis of rotation and vice versa. Forces are integrated along both upper and lower halves of B1. (b) Angle of attack α variation along height and θ in the top tile, and bottom tile shows α at discrete locations along height.

In general, the forces in the upwind half are larger than in the downwind half, reaching their maximum near the most upwind and downwind positions. This behaviour is consistent with existing VAWT normal force profiles for non-pitched blades and aligns with our previous findings. The spanwise distribution reveals that forces are highest near the tip and lowest near the root section, which is expected as the local inflow velocity decreases closer to the root. However, some artefacts at the upper and lower tips indicate a local increase in load. Lifting-line methods consider induction only along a line at the centre of pressure, quarter-chord in this case, neglecting chordwise distribution effects. This often results in

an overestimation of loading near the tip [159]. As CACTUS does not currently incorporate a correction model for this issue, and implementing one is beyond the scope of this study, we neglect this local spike as it is not critical to our analysis. Consequently, the peak load along the span occurs around $Z/D = 0.5$ in the upper half and $Z/D = -0.23$ in the lower half, with a gradual reduction in magnitude towards the tips—an expected characteristic of a finite blade span representation in CACTUS. Interestingly, in the downwind half between $\theta = 270^\circ$ and 330° , the forces fluctuate near the tips while remaining relatively stable elsewhere. This is attributed to blade–vortex interactions, where the blades pass through tip vortices shed during the previous cycle. This interaction is also evident in the integrated forces, where a small spike is observed in the same azimuthal range. Using both another free-wake vortex model and a blade-resolved URANS approach, predicted a similar phenomenon, as seen from Chapter 3. Since the vortices exhibit minimal vertical convection, the rest of the downwind region remains largely unaffected by blade–vortex interactions, a consequence of the coned blade geometry.

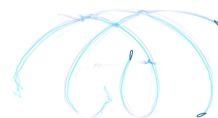
The angles of attack, α , decrease from the root toward the tips, reflecting the variation in local blade section rotational velocity along the height. Given that the static stall angle is $\alpha_{ss} = 9.1^\circ$, most of the blade operates in either post-stall or deep-stall conditions between $\theta = 90^\circ$ and 180° . The blade sections near the root ($Z/D = 0.1$ and $Z/D = -0.05$) experience deep-stall conditions, with peak α reaching 25° in the upwind half and 19° in the downwind half. This aligns with the observed low normal forces at these blade sections.

To understand the implications of the spanwise variation of normal forces on the flowfield, we present the non-dimensional time-averaged vertical component of velocity \bar{w}/U at different height sections as viewed from above in Figure 4.11.

At $Z/D = 0.29$, we primarily observe downwash within the rotor volume, driven by the vertical component of the normal forces from the upper blades. Interestingly, downstream of the rotor, downwash persists within the region bounded by the local diameter, whereas upwash dominates outside this region ($Z/D > |0.2|$). Moreover, this upwash is stronger on the windward side than on the leeward side, indicating the influence of the tip vortices. The windward tip vortex, over a full cycle, is stronger than the leeward tip vortex. This behaviour closely aligns with the observations of Bensason et al. [98], who reported a similar wake structure. Specifically, at $\beta = 0^\circ$ in their study, the windward tip vortex induced upwash on the windward side at this plane.

At $Z/D = 0.1$, the downwash is stronger than at the plane above and extends further into the wake. This is due to the cumulative contribution of downwash from the blade sections positioned above this plane. As a result, the downwash reaches further downstream while remaining laterally confined within the bounds of the local diameter. The influence of the upper tip vortices is reduced at this plane, as it is farther from the tips, which is evident from the lower intensity of the red regions.

In the lower half of the rotor at $Z/D = -0.05$, the region within the local diameter exhibits minimal upwash. This is because the downwash generated by the upper half counteracts the effect of the higher cone angle in the lower half, which results from the greater loads produced by the upper blades. Additionally, this plane captures the cumulative upwash generated by the entire lower half. However, the wake predominantly features a strong downwash—likely an effect of the lower tip vortex—but this influence does not extend significantly beyond $X/D = 1$. Around $Y/D = -0.25$, we observe a region of upwash



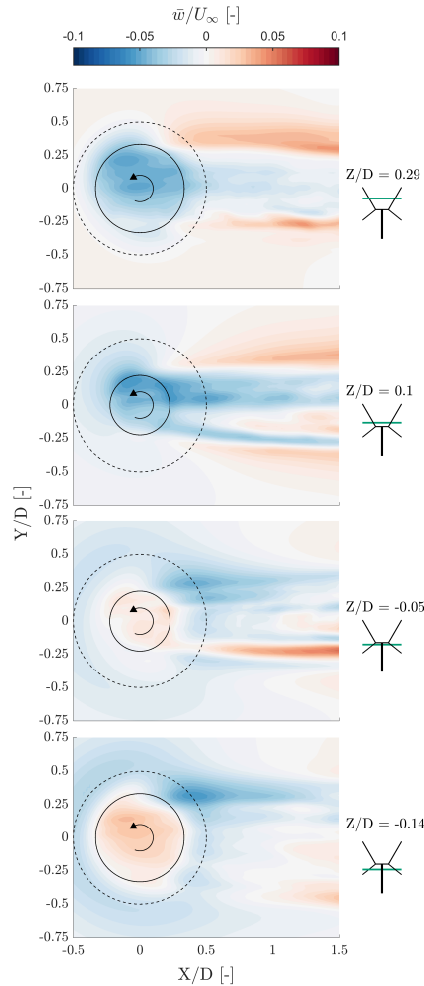


Figure 4.11: Time-averaged vertical component of the velocity field of the rotor at sections along the height of the rotor at $Z/D = 0.29, 0.1, -0.05,$ and -0.14 as viewed from the top. The inset figure shows the locations of the planes along the height of the X-Rotor graphically. The dashed black line indicates the tip-diameter of the X-Rotor and the solid black line indicates the local diameter corresponding to the height. Red indicates upwash (out of the plane) and blue indicates downwash (into the plane).

that extends from $X/D = 0.5$ to 1.5 . This is due to the cumulative effect of the shed vortices from both the upper and lower blades in the leeward region, as observed from the angle of attack plots. Near the root, these shed vortices induce a resultant upwash due to the difference in cone angles between the upper and lower blades.

Finally, at $Z/D = -0.14$, the region inside the local diameter is primarily characterised by upwash. However, as observed in the previous plane, the wake remains dominated by downwash. Once again, the windward side experiences stronger downwash than the leeward side, attributed to the windward tip vortex. Since the vortices shed by the lower

blades rotate in the opposite direction to those from the upper blades, this behaviour is expected. Additionally, the small region of upwash in the wake is likely caused by the leeward tip vortex.

Overall, the cone angle significantly influences the flowfield both inside and outside the rotor, and this effect is further amplified by the interaction of tip vortices when the blades are pitched.

4.5 CONCLUSIONS

We conducted a validation study of CACTUS, a free-wake vortex tool, against wind tunnel PIV measurements for a scaled X-Rotor VAWT, considering cases with and without blade pitch offsets. Additionally, we examined the influence of coned blades on the near-wake in the absence of pitch offsets, highlighting the significance of vertical induction for such VAWT geometries. The results from CACTUS were compared with phase-locked stereo PIV measurements taken at different azimuths.

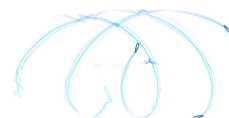
Our findings indicate that CACTUS effectively represents the flowfield within the X-Rotor volume and in the very near-wake for cases without blade pitch offsets. The model captures the trends and flow features well, though discrepancies in velocity magnitude arise due to the choice of model setup parameters. The discrepancies are primarily attributed towards the uncertainty in the airfoil data at the operational Reynolds number. Further inaccuracies stem from aeroelastic effects present in the experiments.

The spanwise distribution of blade forces shows a reduction in magnitude towards the root, as expected, due to the decrease in local inflow. Since the forces are more pronounced near the tips, it is evident that the coned blades significantly influence the flowfield by inducing vertical velocity.

Examining the effect of cone angle on the downstream flow, we found that a local downwash is generated within the rotor volume by the upper blades, while the lower blades produce an opposite effect. Additionally, the turbine wake exhibits substantial vertical flow ranging from 5–10% of the freestream even at the root sections, where blade forces are relatively small. This vertical velocity field is attributed to the rotor's tip vortices, which are expected to become more pronounced with pitch offsets as the blade loads are altered.

When comparing cases with blade pitch offsets, CACTUS exhibited significant discrepancies from the PIV results. While the general wake behaviour was captured, the rate of wake advection was misrepresented. These differences were primarily attributed to variations in tip-vortex size predicted by CACTUS, which stem from the chosen model setup parameters. Consequently, the discrepancies observed in the case without pitch offsets were amplified when pitch offsets were introduced, as the wake of a VAWT with blade pitch offsets is strongly influenced by tip vortices. Quantitative analyses revealed that in some instances, CACTUS predictions deviated by up to 50% from the experimental results. These differences also stem from the use of airfoil polars, which may not accurately represent the load profile at low Reynolds numbers, particularly at the large pitch offsets considered in this study. While careful tuning of the CACTUS setup for the specific case could help reduce these discrepancies, this potential reduction could not be quantified in the present study.

To conclude, CACTUS is an excellent tool for simulating the aerodynamics of the X-Rotor in the baseline case, accurately capturing the flowfield within the rotor volume



and the very near-wake. However, for cases with blade pitch offsets, a different modelling approach is needed to better predict the wake flow features, particularly in terms of vortex dissipation and evolution.

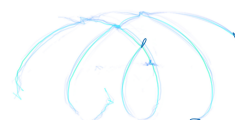
5

THE EFFECT OF ROTOR GEOMETRY ON WAKE RECOVERY

In Chapter 3, the vertical induction generated by the X-Rotor during its operational cycle was examined, along with the variations in its magnitude and direction under different blade pitch offsets. Furthermore, Chapter 4 explored the influence of pitch angle on the near-wake and induction field of the X-Rotor, revealing similarities to previous studies on wake control and wake recovery. However, unlike the well-documented mechanisms for the H-Rotor, the presence of strong root vortices in the X-Rotor's wake makes the underlying mechanism driving wake recovery less clear.

The present chapter aims to qualitatively and quantitatively investigate the wake recovery process and its governing mechanisms as influenced solely by rotor geometry. To this end, a full-scale X-Rotor VAWT and a scaled H-Rotor with equivalent thrust are analysed, both operating with fixed blade pitch. Quantitative metrics—including wake deflection, available power, mean kinetic energy fluxes, and momentum recovery—are evaluated for both rotors at different pitch offsets to characterise their wake behaviour and recovery potential

Parts of this chapter have been published in Adhyanth Giri Ajay, Carlos Simao Ferreira; A numerical investigation of wake recovery for an H- and X-shaped vertical-axis wind turbine with wake control strategies. *Physics of Fluids* 1 December 2024; 36 (12): 127161. <https://doi.org/10.1063/5.0244810>.



5.1 INTRODUCTION

While the aerodynamic characteristics of the X-Rotor have been previously examined through both experimental and numerical studies, as seen in Chapters 3 and 4, the wake recovery behaviour of this configuration remains less understood. The coned geometry of the blades introduces strong three-dimensional effects that fundamentally alter the formation and evolution of the shed vortices. These differences are expected to influence wake recovery when compared to the conventional H-Rotor, particularly under fixed blade pitch offsets that modify the circulation between the upper and lower halves of the rotor.

Previous investigations have shown that pitch offsets can induce wake deflection and modify power performance [27, 57, 62]. But a clear understanding of how these effects influence the downstream wake topology and recovery process is still lacking for different rotor geometries. In particular, the vortex system associated with the X-Rotor has not yet been characterised at far-wake locations or systematically compared against that of the H-Rotor.

Therefore, this chapter aim to identify the influence of rotor geometry on the wake recovery mechanism using pitch control. It systematically compares the the wake recovery physics of the X-Rotor in relation to the H-Rotor, focusing on the influence of fixed blade pitch offsets on the tip-vortices. The chapter also evaluates the recovery performance of both rotor types through qualitative and quantitative analyses. The chapter uses the ALM model in an Eulerian domain to simulate the wake and to perform the analyses.

5

5.2 METHODOLOGY

This section discusses the methodology used in this chapter. The setup for the ALM model (*turbinesFoam*) used is described in Section 5.2.1. The scaling information used for the H-Rotor geometry in Section 5.2.2, and the wake length scale used in the analysis is defined in Section 5.2.3. Finally, we highlight the X-Rotor geometry and the numerical setup used in this study in Section 5.2.4.

5.2.1 SIMULATION SETUP

The implementation we used here in this study is combining *turbinesFoam* library [110] with *OpenFOAM-v2106* [111]. In ALM models, the thrust T and the blade loading are preserved through the regularisation kernel parameter ϵ/Δ_{grid} , where Δ_{grid} is the local grid length [108]. As highlighted in Chapter 2, the regularisation kernel smears the forces from the rotor blades into the fluid domain to avoid large gradients in the fluid cells near the blades. The default values in *turbinesFoam* follows the suggestion of Troldborg [160] to choose $\epsilon/\Delta_{grid} = 2$. But later works of Martínez et al. [161] and Jha et al. [162] show that varying this parameter shows a significant change in blade loads and power estimations of the rotor. Therefore, we tuned ϵ/Δ_{grid} by performing a sensitivity study of the normal load profile as a function of ϵ/Δ_{grid} . The normal loads are compared with a free-wake vortex model - CACTUS [114] that is previously verified against blade-resolved URANS CFD models for the X-Rotor at different operating conditions Chapter 3 and validated against experimental particle image velocimetry (PIV) results in Chapter 4. A sensitivity study on the choice of ϵ/Δ_{grid} is presented in Appendix E, to not dilute the main findings of our study. Overall, we choose $\epsilon/\Delta_{grid} = 5$ for our implementation of the H-Rotor and

$\epsilon/\Delta_{grid} = 2$ for the X-Rotor for $\Delta_{grid} = D/40$. These values are constant along the span as the mesh resolution is also constant. The velocity sampling, used to evaluate the flow angle, is done at the center.

In this study, the flow is treated as incompressible, homogeneous, and Newtonian with a density of $\rho = 1.225 \text{ kg m}^{-3}$ and kinematic viscosity $\nu = 1.5 \text{ m}^2 \text{ s}^{-2}$. As mentioned earlier, we use the Unsteady Reynolds-Averaged Navier-Stokes (URANS) equations in the *pimpleFoam* solver in this study to capture the time-resolved wake. Furthermore, we implement the use of the $k-\epsilon$ turbulence closure model [163]. We chose this closure model than other popular approaches like the $k-\omega$ SST model [164] as we do not have a physical rotor that requires capturing the separation. Moreover, $k-\epsilon$ has been documented to show good prediction at higher tip-speed ratios of $\lambda \geq 3$ for VAWTs [47]. However, it is to be noted that $k-\epsilon$ without an additional injection in the flowfield has been shown to artificially increase the power production, which is a limitation of this approach [165, 166]. The inflow velocity U is kept at a constant 12 m s^{-1} with a low turbulence intensity TI of 0.22%.

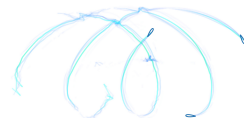
The simulation domain ranges from $-5D$ upwind to $15D$ downwind, where D is the rotor diameter corresponding to the simulation. This is in accordance with the suggestions from Rezaeiha et al. [50]. It extends laterally from $-4D$ to $4D$, and vertically from $-3.5D$ to $3.5D$. For this domain, a fine mesh region of resolution $D/40$ extends from $-1D$ to $7D$, enveloping up to $1D$ on either lateral and vertical directions from the rotor center. This region is encompassed in a coarser mesh region of $D/20$ resolution ranging from $-1.5D$ to $11D$ up to $1.5D$ either side laterally and vertically. The sides, top, and bottom edges of the domain are zero gradient, while the outlet is treated as an inlet-outlet boundary.

5.2.2 SCALING THE H-ROTOR

To compare the wake recovery capabilities between two different rotors, we choose key parameters that govern the geometry scaling and the thrust scaling of the rotor such as the frontal area A , aspect ratio AR , tip-speed ratio λ , and the thrust coefficient C_T . The H-Rotor is designed from scratch to match these parameters to that of the X-Rotor for this study. The geometry of the X-Rotor is provided in Leithead et al. [39] and Giri Ajay et al. [156]. Using these, the diameter D and height H can be obtained. However, to obtain the chord c we need to match T and λ , because T is a function of the chord and λ . The CACTUS model is once again employed here for the purpose of scaling the H-Rotor. This model is also previously tested for H-Rotor geometries [167], with caveats about using it primarily for high λ (≥ 4) and small angle of attacks α , ideally below static stall angle of airfoils. Therefore, for $\lambda = 4$, we identified the solidity of the H-Rotor using the expression $\sigma_H = Nc_H/D$ required to match the thrust of the X-Rotor, as seen in Figure 5.1, where N is the number of blades, c_H is the chord of the H-Rotor, and D is the diameter of the rotor.

5.2.3 CHARACTERISTIC LENGTH SCALE FOR THE WAKE SIMILARITY

Both the H-Rotor and the X-Rotor are scaled to have the same thrust T , frontal area A and aspect ratio AR . However, the diameters D of each rotor significantly different from each other because of their distinct shapes. Therefore, to maintain the similarity in the analysis of wake of these rotors, a characteristic length scale L is used to represent the distance downstream at which the wake of the two rotors attain similarity. We implement a modified concept of the 'momentum length scale' to normalise all the length scales in



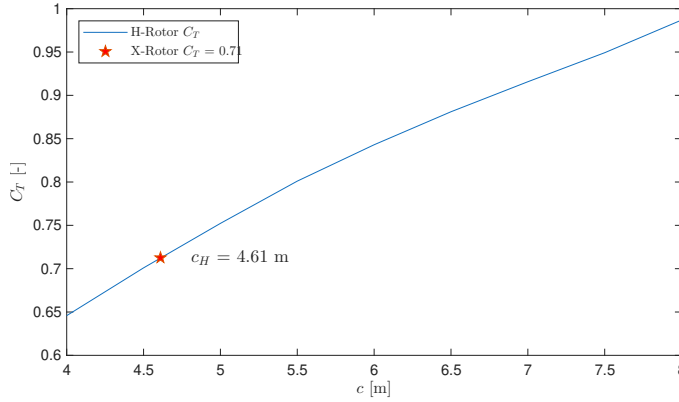


Figure 5.1: Thrust coefficient C_T as a function of chord c for the H-Rotor for tip-speed ratio $\lambda = 4$. The red star indicates the C_T of the X-Rotor also at $\lambda = 4$, from Giri Ajay et al. [156].

5

the streamwise direction, based on the implementation by Meunier and Spedding [168]. This implementation was later demonstrated by Shamsoddin and Porté-Agel [169] to work well for VAWTs. We modify this characteristic length scale from $L = \sqrt{(4/\pi)A}$ to $L = \sqrt{A}$, which we believe is an acceptable level of simplification considering our wake shapes with the pitch offsets would not converge to a disk-like shape, as documented by Huang et al. [27].

5.2.4 TEST GEOMETRY AND SETUP

After applying the scaling and identifying the solidity of the H-Rotor, both rotor dimensions as well as operational conditions with scaling information are provided in Table 5.1.

Table 5.1: Geometry and operating conditions of the two rotor configurations.

Rotor type	D [m]	AR [-]	σ [-]	A [m ²]	U [ms ⁻¹]	λ [-]
X-Rotor	150.00	0.857	0.17	12870	12	4
H-Rotor	122.55	0.857	0.05	12870	12	4

As the X-Rotor has coned blades with varying chord along the height, its solidity has to be evaluated for each blade section. The detailed geometry of the X-Rotor is available in Appendix A. Therefore, the σ for the X-Rotor is evaluated as $\sigma_X = N \sum c_i \Delta H_i / A$, where ΔH_i is the height between the discretized blade sections, and c_i is the mean local chord of the blade section. In addition to the coned blades, the X-Rotor's upper and lower blades are tapered with different airfoil sections from the root to the tip. The upper blade root is made up of a NACA0025 section with $c = 10$ m, while the lower blade root section is the same section but with $c = 14$ m. The detailed geometry of the X-Rotor is described by Giri Ajay et al. [156].

NACA0021 polars at chord Reynolds number $Re = 1.5 \times 10^7$ are generated using XFOIL and are used for the H-Rotor turbine. The X-Rotor has a constant Re value of 1.5×10^7 at each blade section along its span due to the constant product of relative speed and local

chord. The polars used here are from the verified data set presented in Giri Ajay et al. [156].

The secondary rotors are not included in the simulation of the primary rotor to enable a more direct comparison in the rotor scale. The tower is ignored in both rotor configurations to include only the lift-producing surfaces.

Three different pitch offsets (-10° , 0° , and 10°) of the blade are considered for each turbine. Positive pitch indicates leading edge pointing towards the rotation axis, while negative pitch is associated when the leading edge points away from it. Both the rotors have counter-clockwise rotation to be positive, and the azimuth $\theta = 0^\circ$ is considered to be where the leading edge is against freestream with the chord parallel to it.

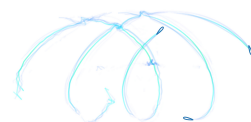
No dynamic stall models are used in this study as tuning the coefficients of the Leishman-Beddoes dynamic stall model would be different for both rotors. Neglecting dynamic stall can impact the regions close to the root with positive and negative pitch angles, which might reduce any differences observed between the rotors slightly. Additionally, flow curvature models are also ignored as it would be difficult to predict its impact on the coned blades of the X-Rotor. The simulations are computed over a flow simulations time of 300s, which corresponds to about 30 revolutions for the X-Rotor and 37 revolutions for the H-Rotor. The simulations, computed on Delft High Performance Computing Centre [170] with 48-core Intel XEON E5-6248R 24C 3.0GHz, took in total about 336 CPU hours for each case.

5.3 RESULTS AND DISCUSSION

This sections highlights the rotor level performance and loads assessment in Section 5.3.1, discusses the vorticity and velocity fields of the two rotors in Section 5.3.2, quantifies the wake displacement in Section 5.3.3, and evaluates and discusses the available power behind the two rotors in Section 5.3.4. To give further insight into the mechanism of the wake recovery, we present a discussion on the momentum recovery contributions =in Section 5.3.5 and into the mean kinetic energy flux in Section 5.3.6.

5.3.1 ROTOR PERFORMANCE AND LOADS ASSESSMENT

The distribution of normal load as a function of the pitch angle is given in Figure 5.2 for both H- (solid lines) and X- rotors (dashed lines). The loads are post processed based on the local information of inflow velocity, angles of attack, and the airfoil polars. We can observe that the loads are more evenly balanced between the upwind, labelled UW and UL, and the downwind halves, labelled DW and DL at $\beta = 0^\circ$, with slightly higher amplitudes in the downwind half. This is contrary to previously extensive documentation of VAWT blade loads [83, 98, 156], however, this odd behaviour is due to the lack of the flow curvature model. With the flow curvature model, the blade would experience a small increase in the inflow angle, which would result in a more upwind dominated load distribution at this pitch offset. Furthermore, we can see that the loads favour the windward direction, UW and DW. Therefore, we can expect the windward vortices to be more dominant in the system. We also notice that the X-Rotor loads are slightly higher than those of the H-rotor in the windward side. This means that the vorticity strengths of the X-Rotor would be higher.



At $\beta = -10^\circ$, we can see that the upwind loads are severely reduced and the highest loads are in the DW region. Based on the experimental documentation by Huang et al. [27] and Bensason et al. [98], the vortices originating from the DW region is the most dominant in the vorticity system. This is also indicative that most of the wake is produced by the downwind half, as it contributes most to the thrust of the rotor.

At $\beta = 10^\circ$, the loads redistribute to be dominant in the upwind region, with peak magnitude at UW. Contrary to the previous configuration, this means the vorticity system is dominated by the UW vortices. Therefore, the wake is mostly generated by the upwind half, and little variation in the wake can be expected as the flow passes through the downwind half as the loads are small. The implications of these loads on the vortex system and the wake is presented later in Section 5.3.2, along with a detailed discussion about the vortex systems themselves.

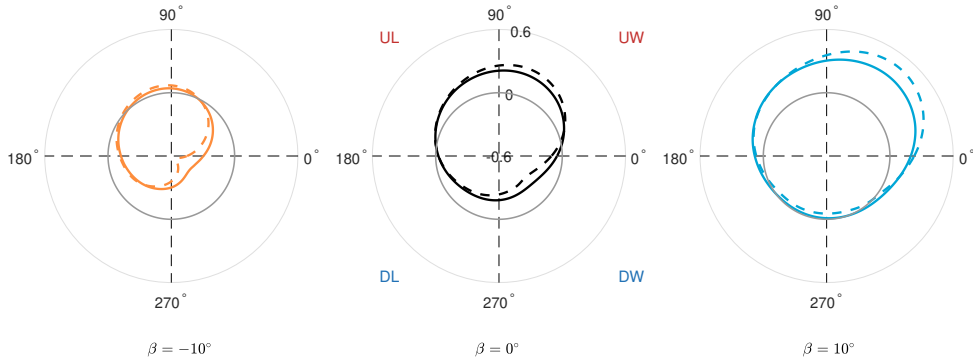


Figure 5.2: A polar plot of the normal loads of the H-Rotor (solid line) and X-Rotor (dashed line) at blade pitch offsets $\beta = [-10^\circ, 0^\circ, 10^\circ]$, from left to right respectively. The loads are normalised by the surface area of each corresponding rotor. The solid grey circle indicates null normal load, i.e., the loads are positive outside the circle and negative inside it. The center of the plot indicates a load of -0.6 while the circumference of the plot indicates a load of 0.6. The quadrants of the azimuth are marked as upwind-windward (UW), upwind-leeward (UL), downwind-leeward (DL), and downwind-windward (DW). The freestream is from the top along the 90° line.

With the redistribution of loads, the thrust in the streamwise and lateral direction also changes. The Table 5.2 presents the corresponding thrust in the streamwise C_{Tx} and lateral C_{Ty} direction, with the introduction of blade pitch angles. We did not consider the power performance of the two rotors in these cases, as we cannot draw meaningful conclusions due to the discrepancies between the tangential loads and the CACTUS model, as seen in Appendix E. Firstly, the streamwise thrust for both the rotors are quite similar, indicating that the scaling continues to be relevant, but the magnitudes are much lower than the design value of 0.71 as shown in Figure 5.1. This discrepancy is due to the way blade loads are projected in the fluid domain, which is further elaborated in Appendix E. We can see that for both the rotors, as the loads are redistributed to be DW dominant for $\beta = -10^\circ$, the streamwise thrust reduces from the baseline case but the lateral thrust magnitude increases significantly. Interestingly, the X-Rotor shows much higher lateral thrust values compared to the H-Rotor. This will be elaborated further while understanding the vortex system of the rotor. The converse is true when the loads are redistributed to be UW dominant at $\beta = 10^\circ$, and the lateral thrust is now in the opposite direction.

Table 5.2: The coefficient of streamwise C_{Tx} and lateral thrust C_{Ty} for both the H- and the X-Rotor at blade pitch angles $\beta = [-10^\circ, 0^\circ, 10^\circ]$.

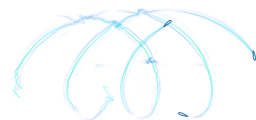
Pitch β	C_{Tx} [-]			C_{Ty} [-]		
	-10°	0°	10°	-10°	0°	10°
H-Rotor	0.56	0.65	0.55	-0.37	-0.03	0.28
X-Rotor	0.53	0.64	0.56	-0.52	-0.08	0.33

5.3.2 VORTEX SYSTEM AND CORRESPONDING VELOCITY FIELDS

To better understand the physics of the wake deformation, the vortex system produced by the two rotors will be addressed first. The time-averaged streamwise vorticity isometric contours ($\bar{\omega}_x D / U_\infty$) for the three pitch cases of both the rotors of $\beta = -10^\circ, 0^\circ, 10^\circ$ at several downstream locations ($X/L = 1, 3, 5, 7$, and 9) are presented in Figure 5.3. The windward side of the rotor is represented as $Y/D > 0$, and the leeward side is $Y/D < 0$. The rotor is centred at $X, Y, Z = 0$. For the H-Rotor, $Z = 0$ is equidistant between its two struts, while for the X-Rotor it is the root section of the X-Rotor where the upper and lower blades meet. The dominant vortices are marked as $R_{a,b}$, where R refers to the rotor type (H- or the X-Rotor), and subscript a depicts the lateral location of the vortex (windward/leeward) and b denotes its vertical location (top, root, bottom).

The $\beta = 0^\circ$ provides a baseline of the vortex system without any pitch offset. In the H-Rotor, we observe blade tip-vortices in both the windward and leeward sides, with the former much stronger than the latter, which is discussed in Section 5.3.1. The leeward vortices, $H_{l,t}$ and $H_{l,b}$, continue to remain insignificant to the vortex system as they lose energy due to turbulent dissipation beyond the near-wake region at $X/L = 1$. This is correlated to the variation of turbulence intensity TI in Appendix G. Meanwhile, the windward vortices stay relevant throughout the entire domain. In the X-Rotor, we observe higher vortex strengths. Otherwise, the X-Rotor vortex system exhibits similar behaviour except for the addition of the root vortices $X_{w,r}$ and $X_{w,b}$. This vortices, as previously documented by Giri Ajay and Simao Ferreira [158], arises from the difference in circulation between the upper and lower blades. Moreover, it moves vertically up and leeward as the wake propagates downwind due to the induced velocity field from $X_{w,t}$ and $X_{w,b}$. However, in this instance we see two in the windward side, and fainter pairs in the leeward side. They are the root vortices from the upper blade (red) and lower blade (blue) - as we see that the former is stronger in magnitude as the latter dissipates earlier. These root vortices will play an important role in the wake advection in the cases with pitch offset.

At $\beta = -10^\circ$, the downwind vortices dominate the vortex system even more, as previously discussed in Section 5.3.1. In both the rotors, the magnitude of all the vortices are significantly higher than the baseline $\beta = 0^\circ$ case, with the windward vortices remaining stronger than the leeward ones. For the H-Rotor, in the near-wake, both $H_{w,t}$ and $H_{w,b}$ cores can be observed to propagate leeward, due to their mutually symmetric induced velocity field. At further downstream locations, the leeward vortices influence this propagation by forcing them to move vertically away from the frontal area of the rotor. However, due to the difference in vortex strengths between the leeward and windward vortices, the leeward vortices tend to swirl around the stronger windward vortices, which is noticeable after $X/L = 7$. At far downstream locations, the dissipation of the vortex is more apparent and



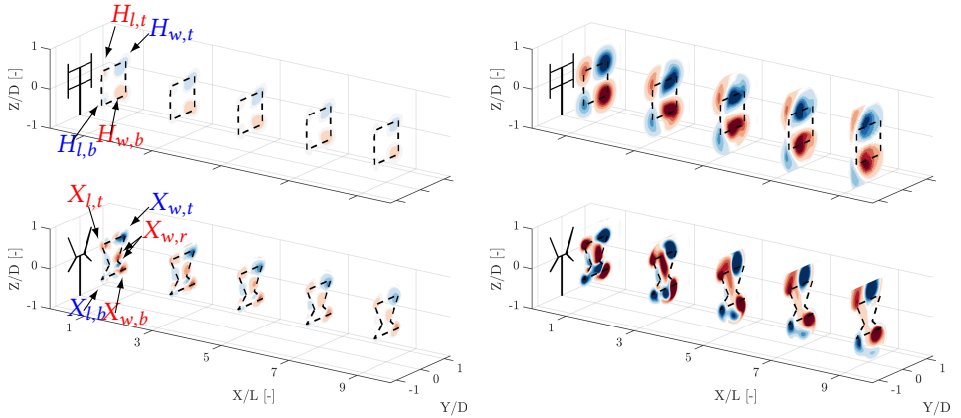
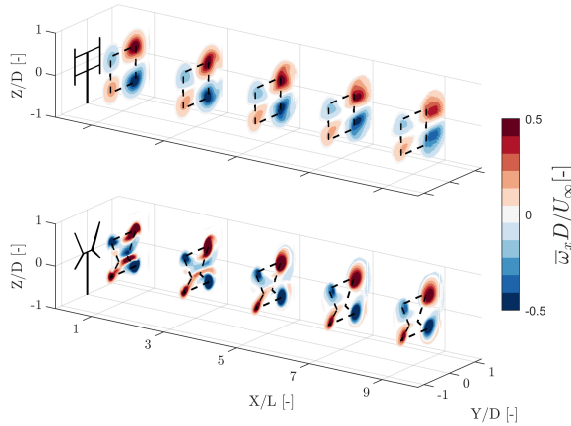
(a) $\beta = 0^\circ$ (baseline)(b) $\beta = -10^\circ$ (c) $\beta = 10^\circ$

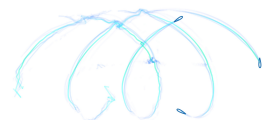
Figure 5.3: Normalised streamwise vorticity $\bar{\omega}_x D / U_\infty$ contours of the H-Rotor and X-Rotor with pitch offset $\beta = -10^\circ, 0^\circ, 10^\circ$ respectively at downstream locations $X/L = 1, 3, 5, 7,$ and 9 , where L is the characteristic streamwise length scale. The black dash lines indicate the projected frontal area of the rotor on the corresponding plane. The lateral Y and the vertical Z spatial coordinates are normalised the diameters D of each rotor respectively. The labelled vortices follow the rubric $R_{a,b}$, where R corresponds to the rotor type (H or X), subscript a indicates lateral location of the vortex (windward or leeward), while b depicts the vertical location of the vortex (top, bottom, or root). Counter-clockwise is considered positive viewed from downwind and vice-versa.

the vortices appear to be stagnated. In the X-Rotor, $X_{w,t}$ and $X_{w,b}$ are not symmetric, due to the presence of $X_{w,r}$, which causes them to propagate at different rates in the leeward direction. Meanwhile, $X_{w,r}$ is quite weak compared to the other vortices, as it can be seen dissipating earlier than the other vortices. This is in stark contrast with our previous findings in Giri Ajay and Simao Ferreira [158]. This is attributed to the upper and lower blade pitched equally in this study, which does not increase the circulation difference from the baseline case. Additionally, $X_{w,r}$ is propelled vertically by the other vortices as the flow moves downstream. However, we also notice both the $X_{w,r}$ increasing in magnitude with this pitch offset, further indicating these two windward root vortices originate from the upper (red) and lower (blue) blades. These vortices are much stronger than the baseline case, allowing rapid advection freestream from the windward side into the rotor area. This explains the lateral thrust, as seen in Table 5.2, being much higher than the H-Rotor. This affects the leeward movements of $X_{w,t}$ and $X_{w,b}$ and instead shows signs of moving vertically out of the frontal area of the rotor. As a result, at $X/L = 7$, $X_{w,t}$ is outside of the rotor frontal area in contrast to $X_{w,b}$. Additionally, the root vortex appears to coalesce with $X_{l,t}$ and together swirl around the windward tip-vortices beyond $X/L = 7$. Regardless, the $X_{w,t}$ and $X_{w,b}$ still remain significant in the system which should bring in freestream from the windward side into the frontal area of the rotor.

With the loads redistributed to the front in the $\beta = 10^\circ$ case, the vortices produced in the upwind half dominate the system. This is accurate to the discussion in Section 5.3.1. This is shown by the change in direction of the vortices from the $\beta = -10^\circ$ case. In the H-Rotor, $H_{w,t}$ and $H_{w,b}$ are mutually propelled towards the leeward side due to their induced velocities, while $H_{l,t}$ and $H_{l,b}$ appear to be stationary. This is due to the induced velocity from the windward vortices being considerably stronger than the leeward vortices, which negates the induced velocities from the leeward vortices for their lateral movement. At further downwind locations, $H_{w,t}$ and $H_{w,b}$, continue to mutually propel themselves leeward away from the frontal area of the rotor, approximately $1D$ leeward at $X/L = 7$, while simultaneously pulling the leeward vortices towards them. However, this is not quite significant as the vortices dissipate earlier due to the turbulence and have less impact on the flowfield. In the X-Rotor, the root vortices $X_{w,r}$ are observed again to be stronger and opposite to the baseline case, but at a much lower strength than all the other vortices in the system. Additionally, they are also much weaker than the $\beta = -10^\circ$ case, which makes the lateral thrust of this case align well with the H-Rotor. However, this affects the windward vortices from being mutually propelled as $X_{w,r}$ influence $X_{w,t}$ and $X_{w,b}$ that opposes their movement. $X_{w,r}$ get pulled by the windward tip-vortices in the near-wake and dissipate sharply after $X/L = 3$. Towards $X/L = 5$ and further downstream, the root vortices swirl around the windward tip-vortices, however does not appear affect the vortices significantly. The leeward vortices $X_{l,t}$ and $X_{l,b}$ also do not show signs of mutual propulsion, due to the negation of induced velocity, as observed in the H-Rotor as well.

The time-averaged streamwise velocity fields u/U_∞ corresponding to the vortex system are shown in Figure 5.4, where the dashed black lines trace the frontal area of the two rotor types. Values of u/U_∞ of unity and above have been removed from the plot for clarity of the wake shape.

The $\beta = 0^\circ$ serves as a benchmark to observe the wake shape without pitch modification. In the H-Rotor, the wake overall expands laterally and vertically outwards, driven by the



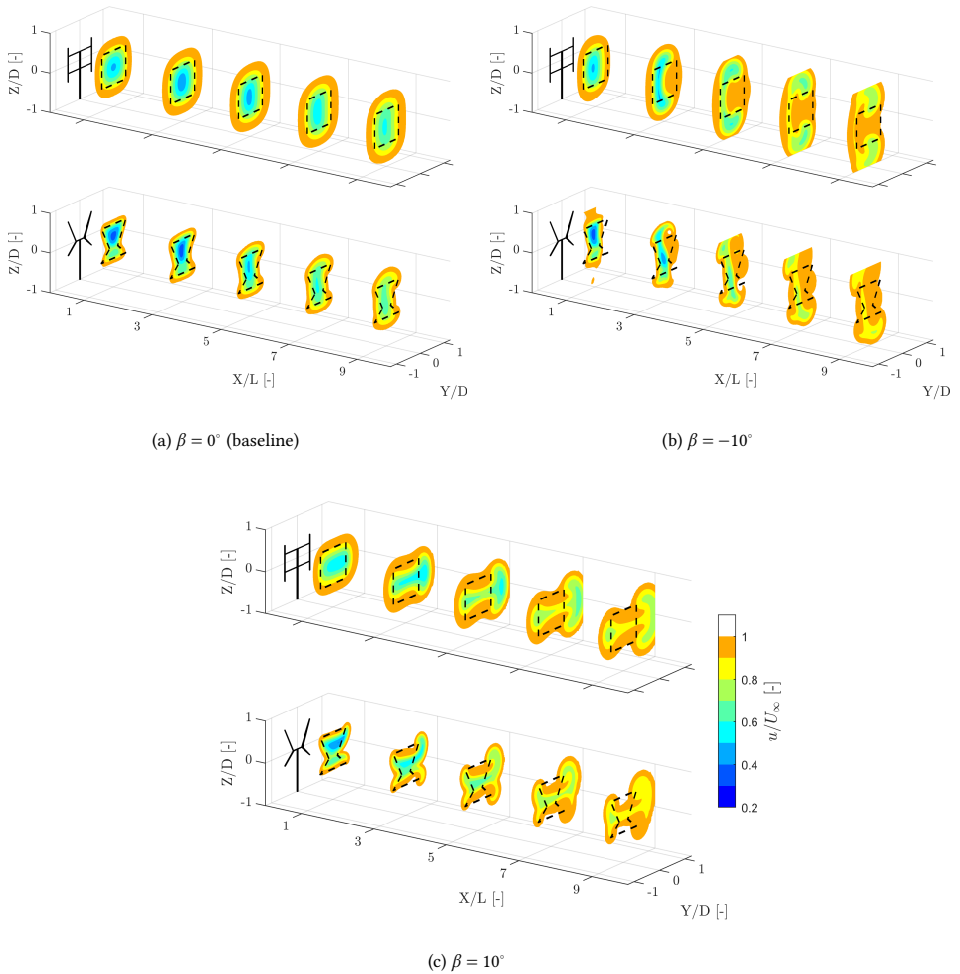


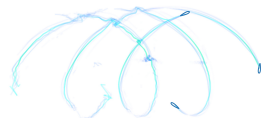
Figure 5.4: Normalised streamwise velocity (u/U_∞) contours of the H-Rotor and X-Rotor with pitch offset $\beta = -10^\circ, 0^\circ, 10^\circ$ respectively at downstream locations $X/L = 1, 3, 5, 7,$ and 9 , where L is the characteristic streamwise length scale. The black dash lines indicate the projected frontal area of the rotor on the corresponding plane. The lateral Y and the vertical Z spatial coordinates are normalised the diameters D of each rotor respectively. Values of freestream and above are hidden to enhance the visibility of the wake in this isometric perspective.

tip-vortices. Due to the streamtube expansion, the the velocity deficit in the wake increases until about $X/L = 3$, beyond which the deficit decreases due to the advection and turbulence. Due to the presence of the windward tip-vortices, the wake shape continues to be pushed vertically, until about $X/L = 5$ from which the vortices dissipate and the advection of the wake becomes less significant. Similar behaviour of the streamtube expansion as well as the vertical expansion is observed in the X-Rotor. However, there is a noticeably higher velocity deficit in the upper half of the rotor area while the lower half has a lower velocity deficit than the H-Rotor. In the X-Rotor, the upper blades produce much larger loads than

the lower half, which causes the thrust to be not symmetric between the top and bottom [156]. As the thrust is the same for both the rotors, the upper half produces larger velocity deficit to compensate for the lower half. Interestingly, the wake appears to recover faster than the H-Rotor, as at $X/L = 5$, the region with high velocity deficits in the X-Rotor are smaller than in the H-Rotor. This is attributed to higher turbulent contribution to the wake recovery, which is elucidated in Section 5.3.5 and in Appendix G.

At $\beta = -10^\circ$, there is an increased vertical expansion with large lateral contraction on the windward side for both rotors, which results in the wake being stretched vertically - much more than the baseline case. This is driven by the stronger tip-vortices that result in the leeward-vertical advection of the wake. In the H-Rotor, the two dominant windward vortices push the wake vertically out and bring freestream laterally into the frontal area of the rotor. It can be seen that at $X/L = 7$, almost all of the flow in the frontal area of the rotor is $90\% U_\infty$ and above, indicating good wake recovery compared to the baseline case. At $X/L = 7$ and beyond, due to the swirling of the leeward vortex with the windward vortex, the wake is observed to enter back into the frontal area of the rotor from the top and the bottom. For the X-Rotor, because of the asymmetric geometry as well as due to the root vortex $X_{w,r}$ moving vertically towards the $X_{l,t}$ and $X_{l,b}$, the wake in the top-half of the rotor ejects vertically out of the frontal area rapidly, while the bottom vortices mutually push the wake below. This is clearer at $X/L = 5$, where most of the wake is displaced above the rotor while only a small portion is displaced below the rotor. Moreover, due to the coned geometry of this rotor, the wake at $X/L = 7$ still remains inside the frontal area of the rotor in contrast with the H-Rotor where the wake is mostly outside. Similar to the H-Rotor, the wake of the X-Rotor at far downstream locations do shows signs of re-entering the frontal area of the rotor. However, the velocity deficits are much smaller due to the increased turbulence, as seen in Appendix G. This is reflected in the available power of the rotor, which is discussed in Section 5.3.4.

In comparison, at $\beta = 10^\circ$, the wake shape looks considerably different due to an increased lateral expansion on the accompanied by vertical contraction of the wake. This is observed at all downstream locations for both the rotors. In the H-Rotor, the two dominant windward tip-vortices work together eject a majority of the wake laterally by inducing a large lateral velocity component in the flow. This brings freestream to the frontal area of the rotor from the top and bottom due to the induced vertical velocity component. Similar to the $\beta = -10^\circ$ case, the wake recovery is much faster in this pitch offset compared to the baseline case. At $X/L = 7$, a large portion of the wake is outside of the frontal area, with the wake squeezed by the high momentum flow entering the rotor from the top and bottom. In the X-Rotor, as the $X_{w,t}$ is stronger than $X_{w,b}$, the most of the wake is laterally ejected by the former as see the wake also moving vertically up outside the rotor area. The leeward vortices also eject the wake out in the leeward direction, but is not as significant as the windward vortices. This pattern is also observed at planes further downstream. However, the velocity deficit inside the frontal area of the X-Rotor is significantly lower compared to the baseline case, which align with the results observed by Huang et al. [27] where the pitch offsets from the blades significantly aid the wake recovery process compared to the cases without any blade pitch offsets. Visually, it can be seen that the advection process subsides around $X/L = 7$, where the wake is recovered primarily due to the turbulence in the flow. In both these rotors, we can see the wake is not completely outside the rotor area,



in contrast to the far wake of $\beta = -10^\circ$. In this study, this difference is because the $\beta = -10^\circ$ amplifies the vortex strengths from the baseline case, while the $\beta = 10^\circ$ inverts the vortices - which is not as effective. The quantification of advection in these configurations can be clearly visualised in Section 5.3.5.

The next set of analyses entail quantification of the wake recovery, as well as providing insight into the mechanisms that drive the wake recovery process at each location in the streamwise direction.

5.3.3 WAKE DISPLACEMENT

To quantify the wake deflection due to advection, methods that characterise the wake shape is required based on the pitch angles for control strategies. The wake centre deflection is a common analysis method to characterise the wake center of HAWTs using either a Gaussian shape fitting algorithm [171, 172] or a "centre of mass" approach for HAWTs [13, 27, 173, 174] and VAWTs [27, 175]. Due to the pitched blades, the wake no longer fits the Gaussian shape. Therefore in this study we use the "center of mass" approach. This approach was initially used to characterise HAWT, where the wake shape is defined by a pair of counter-rotating vortices when the rotor is yawed or tilted. However, VAWTs such as the H- and the X-Rotor have multiple such pairs, top and bottom tip-vortices for the H- and additional root vortex pairs for X-Rotor, which leads to the wakes moving in both the windward and leeward directions. Therefore, the existing "centre of mass" method would not truly quantify the wake deflection, as there are several instances in VAWTs where these results can be misleading. For instance, in an idealised turbine where the vortices between the windward and leeward directions would be equal strength, with pitch offsets, the wake would move equally in both the windward and leeward directions - thus resulting in a null wake center displacement as the system becomes symmetric along the vertical-axis. While this is not true for a more realistic turbine, the results would nonetheless be a misrepresentation of the true wake advection capabilities of the turbine.

Therefore, for this study we modify the existing "center of mass" method to not provide the wake center deflection, but rather a wake displacement - a quantification of the shift in wake from middle of the rotor. In this method, the wake center shifts in the lateral $y_c(X)$ and vertical $z_c(X)$ directions are represented as:

$$y_c(X) = \frac{\iint |y| \Delta U(x, y, z) dy dz}{\iint \Delta U(x, y, z) dy dz}, \quad \text{and}$$

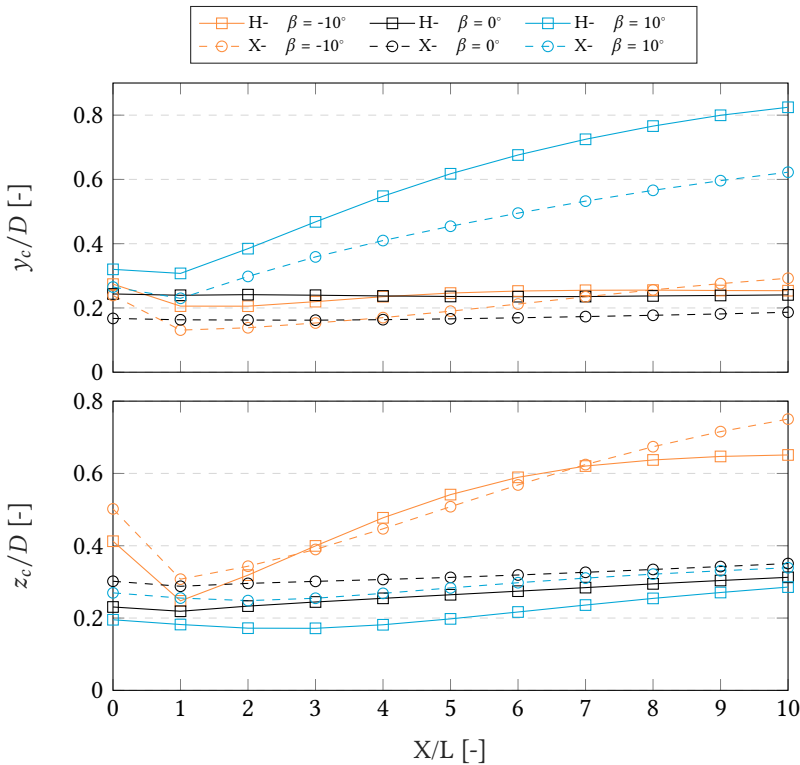
$$z_c(X) = \frac{\iint |z| \Delta U(x, y, z) dy dz}{\iint \Delta U(x, y, z) dy dz}, \quad (5.1)$$

where $|y|$ and $|z|$ would be the absolute of the spatial data, $\Delta U(x, y, z) = U_\infty - \bar{u}(x, y, z)$, \bar{u} is the time-averaged velocity and U_∞ is the free-stream velocity and the discrete surface integration is done over the entire cross-section slice of the domain at each discrete streamwise locations.

With the absolute values of spatial information, the integral of the leeward and windward wakes would no longer oppose each other. Instead the result would depict the average shift of the wake center in a given direction, which would be more meaningful and representative of the wake deflection in opposing directions with pitch offsets. This approach,

which is used in the analysis of this study, compromises the physical significance of the wake center in favour of better representing the wake deflection as a whole. To understand the physical wake center deflection, a brief analysis based on the traditional approach is discussed in Appendix F. The results and discussions from the traditional approach give insight into how the traditional quantification cannot be a good representation of wake deflection for VAWTs with blade pitch offsets.

The wake displacement in the lateral y_c and vertical z_c for the H- and the X-Rotor at pitch offsets $\beta = -10^\circ, 0^\circ, 10^\circ$ are presented in Figure 5.5 for downstream locations $X/L = [0, 10]$ for both rotors.

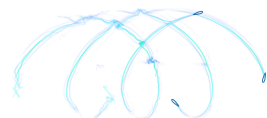


5

Figure 5.5: The wake displacement in the lateral (y_c/D) and vertical (z_c/D) directions. Solid lines with squares represent the H-Rotor, and dashed lines with circles represent the X-Rotor. Orange, black, and cyan indicate pitch offsets of $\beta = -10^\circ, 0^\circ, 10^\circ$ respectively.

In all cases, the wake displacement at $X/L = 0$ is not zero, unlike HAWTs. This is because the plane only captures the wake of the upwind half, with the wake displacements corresponding to the loads, as previously seen in Figure 5.2. The planes downstream of the rotor includes the wake of the downwind half, which shifts the wake more to the center. This results in a much larger wake displacement at $X/L = 0$, while subsequently reducing at $X/L = 1$.

At $\beta = 0^\circ$, both the rotors show lateral and vertical wake displacement. This is expected



as we are no longer analysing wake deflection, but rather a shift from the middle of the rotor. However, the y_c/D remains consistently in the same range. This quantifies the lateral contraction of the rotor, while showing gradual vertical expansion elucidated by the steady increase of z_c/D for both rotors.

At $\beta = -10^\circ$, the wake is ejected vertically out, without much lateral movement. This is observed by the large z_c/D throughout the domain, and low y_c/D . The y_c/D for both the rotors are, in the near-wake, higher than their corresponding values in the baseline case. This is because of the heightened lateral contraction due to the larger windward vortices in the near-wake, beyond which most of the wake is driven up and down by the upper and lower vortex pairs respectively. Moreover, beyond $X/L = 4$, the opposite occurs. As the wakes are ejected out of the rotor area, the windward vortex pulls them, this resulting in the slight windward movement of the wake regions with large velocity deficits. This effect artificially increases y_c/D in these downstream planes. Interestingly, the z_c/D of the H-Rotor becomes asymptotic after $X/L = 7$ in contrast to that of the X-Rotor. This is attributed to the swirling effect discussed in Figure 5.3, which reduces the vertical advection of the wake. The X-Rotor shows the largest z_c/D before $X/L = 3$ and beyond $X/L = 7$. The latter is due to the aforementioned swirling of the H-Rotor's windward vortices. The former is due to the uneven load distribution between the upper and lower halves of the X-Rotor. The upper half is loaded more heavily than the lower half, resulting in a region of larger wake deficit in the upper half.

Now, at $\beta = 10^\circ$, the opposite is expected as the wake undergoes a large lateral expansion and a large vertical contraction in both rotors. This is reflected in the large lateral wake displacement values for both rotors and the low vertical wake displacement. Between the H- and the X-Rotor, the y_c/D of the former is significantly larger than the latter. This is attributed to the two symmetric windward vortices of the H-Rotor that eject the wake laterally rapidly. For the H-Rotor, the wake displacement is asymptotic towards $y_c/D = 0.8$ after $X/L = 8$. This is because, as the wake is ejected laterally it forms a jellyfish shape beyond $X/L = 7$ due to the movement of the windward vortices. This causes the wake to be displaced vertically and begin to roll-up, which is characterised by z_c/D being increasing after the initial dip at $X/L = 3$. Meanwhile, the X-Rotor shows a nearly linear increase in y_c/D after $X/L = 2$, as the windward vortices are asymmetric and the roll-up of the wake is not achieved even at $X/L = 10$. But as the wake rolls up close near $X_{w,t}$, there is an increase of z_c/D from around 0.25 to 0.33 between $X/L = 3$ and 10.

From these results, it is difficult to understand which rotor or configuration is more favourable as seen with the $\beta = 0^\circ$ cases, even when the wake appears to have not advected, the wake displacement values are positive and significant. Therefore, understanding the capabilities of each configuration is still limited by this approach, but offers valuable quantitative insight into the wake steering capabilities of a VAWT with blade pitch offsets. We can address the limitation of this approach by pairing these results with other supportive quantification methods.

5.3.4 AVAILABLE POWER (AP)

To further characterise the wake through quantitative approaches, the AP estimation is a widely used method [15, 27, 176, 177] to understand the available power in the wind for a hypothetical identical wind turbine located downstream of the turbine producing the

wake. The normalised available power at a specific point in the domain (x_0, y_0, z_0) can be calculated by using

$$C_{AP}(x_0, y_0, z_0) = \frac{1}{A} \iint_S \frac{\bar{u}^3(x_0, y, z)}{U_\infty^3} dz dy \quad (5.2)$$

where C_{AP} represents the coefficient of available power (\bar{u}^3/U^3) and (x_0, y_0, z_0) is the location of the middle of the hypothetical downstream turbines (HDT), U_∞ is the freestream velocity, \bar{u} is the time-averaged velocity and A is the frontal area of the rotor. The integration surface S is the region encompassed by the frontal area of the turbine. For the H-Rotor it is a rectangle, while for the X-Rotor it is two trapezoids placed one above the other, as the HDT is assumed to be the same dimension as the turbine producing the wake. In this study, we obtain the AP for a HDT that is both inline and at an offset up to $1D$ laterally either side from the center of the turbine. This is similar to the moving window method that is employed by Huang et al. [27], and a schematic of the moving window for the integration is shown in Figure 5.6 where the HDT is offset by a distance y_0 from the rotor.

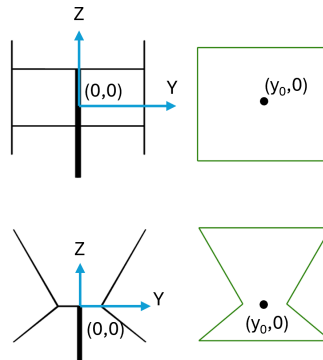


Figure 5.6: A schematic of the moving integration window for both the H-Rotor (top) and X-Rotor (bottom) to evaluate the AP. Both the rotors are positioned at origin $(0,0)$. The green contour represents the integration window corresponding to the each rotor's frontal area. y_0 is the distance by which the HDT is offset from the turbine producing the wake.

The coefficient of available power C_{AP} for an HDT at inline with the rotor is listed in Table 5.3 for both the turbines at all pitch offset conditions. As expected, there is an increase of inline AP for the both the rotors with fixed blade pitch offsets than without, due to the lateral and vertical advection of the wake. The $\beta = 10^\circ$ case shows the higher inline AP up to $X/L = 7$ for the X-Rotor, and for the H-Rotor the $\beta = -10^\circ$ shows the higher inline throughout the domain. For the X-Rotor, this primarily occurs with the increase in advection offered from the pitch case; as the wake curls up around windward tip-vortex, it is relatively easier for the wake in the upper half of the rotor to go out of the rotor area. As established earlier, the upper half of the X-Rotor produces more loads which results in higher local velocity deficits. Therefore, pushing this region out of the rotor area proves advantageous for the X-Rotor. For the H-Rotor, when the wake is ejected laterally it is stretched between the windward and leeward vortices - distributing some part of the wake

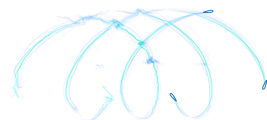


Table 5.3: The coefficient of available power C_{AP} for a HDT located inline to the rotor producing the wake at pitch offsets of $\beta = -10^\circ, 0^\circ, 10^\circ$ for both the rotors at downstream locations of $X/L = 1$ to 10. The blue values in the paranthesis indicates the gain in C_{AP} as a multiple of the $\beta = 0^\circ$ for the corresponding rotor.

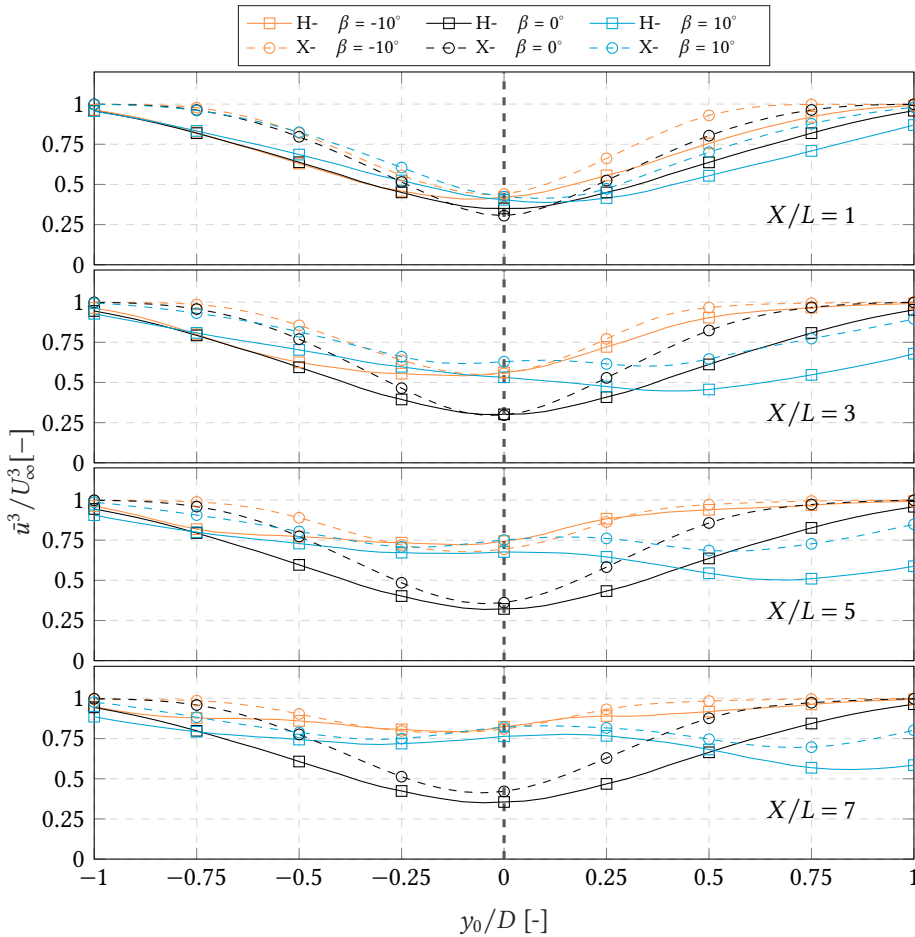
Pitch β	H-Rotor			X-Rotor		
	-10°	0°	10°	-10°	0°	10°
$X/L = 1$	0.42 (1.20x)	0.35	0.40 (1.15x)	0.44 (1.43x)	0.31	0.42 (1.38x)
$X/L = 3$	0.56 (1.87x)	0.30	0.53 (1.77x)	0.55 (1.85x)	0.30	0.63 (2.11x)
$X/L = 5$	0.74 (2.31x)	0.32	0.68 (2.10x)	0.69 (1.91x)	0.36	0.75 (2.07x)
$X/L = 7$	0.82 (2.32x)	0.36	0.76 (2.15x)	0.81 (1.91x)	0.42	0.82 (1.94x)
$X/L = 9$	0.83 (2.10x)	0.39	0.81 (2.06x)	0.88 (1.86x)	0.47	0.86 (1.82x)

inside the frontal area of the rotor, which is not observed in the $\beta = -10^\circ$ case. The inline AP becomes comparable to that of the positive pitch around $X/L = 9$ as the wake re-enters the frontal area of the turbine in this region observed in Figure 5.4. Between the two rotors the X-Rotor yields more inline AP with both pitch cases to the corresponding H-Rotor pitch cases.

Figure 5.7 provides insights on the wake advection affecting the AP of an HDT displaced laterally by y_o/D . The results show clear trends that the H-Rotor at $\beta = 10^\circ$ ejects the wake out the most, as the minimum AP is displaced from the center of the rotor rapidly, compared to the other configurations. Consequently, this also indicates that in a hypothetical windfarm any rotor placed with an offset would be at a disadvantage as it faces large power deficits that it would not have done with the other two pitch cases. The same applies to the X-Rotor as well, albeit to a lesser extent than the H-Rotor.

The $\beta = -10^\circ$ on the other hand, shows good promise in this regard. Not only does it yield higher AP directly inline, but it also consistently yields higher AP in the full range of y_o . The vortices ejecting the wake vertically does not hinder the lateral positioning of HDTs as the wake would not be able to physically interact with them. Moreover, the loss in AP in the leeward direction is minimised, allowing the possibility of placing turbines closer to each other in a wind farm setting. This is especially true for the X-Rotor, as the AP on the windward and leeward side show no large drops. We observe that other than at $X/L = 1$, the minimum AP point for the H-Rotor in this pitch offset still remains close to the inline position, and further downstream it behaves very similarly to that of the X-Rotor, while offering higher inline AP. At locations beyond $X/L = 5$, we can observe the continued wake recovery of the X-Rotor due to the higher turbulence compared to the H-Rotor.

Currently, this work neglects ground effect and does not consider the wake of any turbines adjacent to the one simulated here. The ground effect induces asymmetry in the vertical direction, which impacts the bottom tip-vortices interaction - as the vortices would now tend to move away from each other much faster closer to the ground than away from it. This could affect the wake recovery as the H-Rotor which relies on the symmetric nature of the vortices would no longer experience it, possibly curtailing the lateral advection rates. However, we are unable to further comment on this as it is beyond the scope of the present study. The wake deflected by adjacent turbines would also a valuable addition to shed light on the wake control methods in a farm setting. As these are outside the scope of this



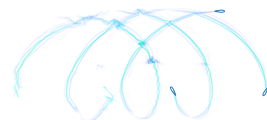
5

Figure 5.7: The coefficient of available power C_{AP} for an HDT with a lateral displacement y_0/D at downstream locations $X/D = 1, 3, 5,$ and 7 for all the pitch cases $\beta = -10^\circ, 0^\circ,$ and 10° . Windward is considered as positive y_0/D . The grey dashed line at $y_0/D = 0$ highlights the results of an HDT that is inline with the original rotor. Solid lines with the square markers represent the HDT for an H-Rotor, and the dashed lines with circle markers show results for an HDT for an X-Rotor. Black lines refers to $\beta = 0^\circ$, while orange and cyan represent the $\beta = -10^\circ$ and $\beta = 10^\circ$ cases respectively.

paper, future studies on this would be instrumental to understand the true capabilities of the wake recovery capabilities of these rotors.

5.3.5 STREAMWISE MOMENTUM RECOVERY RATES

To understand the wake recovery process, it is important to observe how the momentum is being transported. In this section, the Reynolds Averaged Navier-Stokes (RANS) equation is rearranged to balance the streamwise momentum transport by all the other terms. Moreover, following the approach of Bachant and Wosnik [60], Boudreau and Dumas [79],



and Huang et al. [27], the equation is divided by the streamwise velocity component \bar{u} . Therefore, the left hand side of the resulting equation (Equation 5.3) corresponds to the streamwise component of the streamwise velocity gradient. This is referred to as the streamwise wake recovery rate. The terms on the right hand side indicate the transport of momentum by the lateral and vertical components of the mean velocity fields. The next terms involve the contribution of the mean streamwise pressure gradient as well as the turbulent transport terms in the streamwise, lateral, and vertical directions. The viscous transport contribution has been neglected due to the sufficiently high chord based Reynolds number $Re = 1.5 \times 10^7$ as well as the lack of a shear layer in this study, as demonstrated by Bachant and Wosnik [60].

$$\frac{\partial \bar{u}}{\partial x} = \frac{1}{\bar{u}} \left[-\bar{v} \frac{\partial \bar{u}}{\partial y} - \bar{w} \frac{\partial \bar{u}}{\partial z} - \frac{1}{\rho} \frac{\partial \bar{p}}{\partial x} - \frac{\partial \bar{u}'u'}{\partial x} - \frac{\partial \bar{u}'v'}{\partial y} - \frac{\partial \bar{u}'w'}{\partial z} \right]. \quad (5.3)$$

As we use the URANS $k - \epsilon$ turbulence closure model, instead of using the Reynolds shear stress terms ($-\frac{\partial \bar{u}'u'_j}{\partial x_j}$) to calculate the turbulence transport contribution, we use the expression $\nu_T \nabla^2 \vec{U}$, where ν_T is the turbulent eddy viscosity and \vec{U} is the velocity vector field. This follows the approach employed by Bachant and Wosnik [178], where they compared the 2D and 3D RANS models against water-channel experiments of VAWTs. Furthermore, in these works, the terms are normalised by D/U_∞ , as they quantify the mean momentum recovery rate. In this study, as the wake deflects quite significantly with the blade pitch offsets, we instead integrate each transport term inside the area of the wake (99% U_∞). The wake area is considered as it offers insights into the contribution of each term even with severe wake deformation. Therefore, all the results are normalised instead by $1/(DU_\infty)$. Additionally, in this study we do not focus on the streamwise transport due to pressure. This is because our interest is to understand the contribution of the advective and turbulent transports due to the pitch offsets. Figure 5.8 shows the wake-integrated streamwise momentum recovery terms for the H- and the X-Rotor at $X/L = 1$ to 10 for all $\beta = [-10^\circ, 0^\circ, 10^\circ]$.

We can see that in general the advective transport terms are much larger than the turbulent terms in the near-wake for all cases. As we move downstream, the advective transport decreases rapidly and the turbulent transport increases to become comparable (around $X/L = 5$), before it gradually reduces again (after $X/L = 8$). This explains the velocity contours observed in Figure 5.4, where the velocity deficit for $\beta = 0^\circ$ decreases after $X/L = 3$, as the turbulence mixes in high momentum flow with the wake. Moreover, in all pitch cases, the turbulent transport contribution of the X-Rotor is higher than the H-Rotor. This is effectively due to the lower local velocity deficit present in the X-Rotor, which gives rise to high-energy turbulent eddies earlier when compared to H-Rotor. This is demonstrated in Appendix G.

The rest of the discussion will correlate the observations from Figure 5.4 to understand the momentum transport quantification while also shedding light on the wake characteristics. For the $\beta = 0^\circ$ case, both the rotors show higher contribution from the vertical transport terms until $X/L = 2$ as the vertical expansion of the wake replaces high momentum of the freestream with the low momentum of the wake (outside the rotor area). Beyond this, the freestream is transported more in the lateral direction which is reflected with

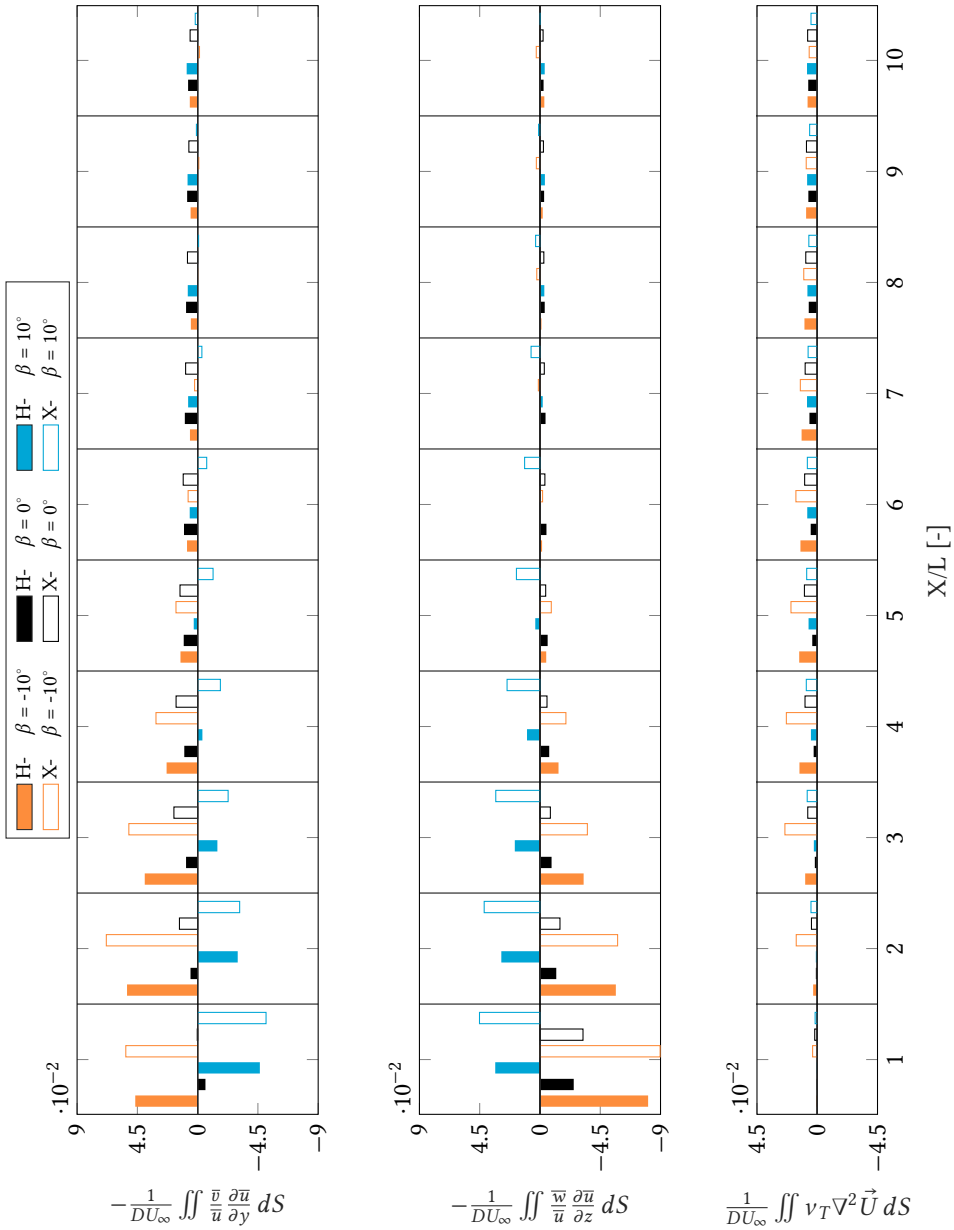
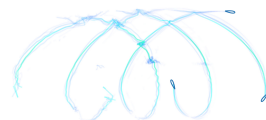


Figure 5.8: The streamwise momentum recovery/transport terms integrated in the wake region (S) for the H- and the X-Rotor at \$X/L = 1\$ to \$10\$ for all \$\beta = [-10^\circ, 0^\circ, 10^\circ]\$. All quantities are normalised by \$\frac{1}{DU_\infty}\$ after integration. The solid bars represents the H-Rotor momentum terms while the outlined bars represents the X-Rotor terms.

the higher lateral transport, before turbulence transport competes with it in the far wake region. Interestingly, the X-Rotor shows higher rates of momentum recovery in lateral



direction between $X/L = 2$ and 7 , while showing higher vertical momentum recovery rates between $X/L = 1$ and 3 . This explains the velocity profile of the X-Rotor, as the wake is mostly concentrated inside the frontal area of the rotor, with mostly freestream immediately outside the rotor area. This contrasts the wake of the H-Rotor as we observed a bigger spread of the wake from the rotor area.

At $\beta = -10^\circ$, the lateral and vertical contribution of momentum recovery is magnified for both the rotors when compared to the baseline case. In this case, the vertical transport overshadows the lateral transport terms at $X/L = 1$ as the wake is ejected vertically for both the rotors. However, the lateral terms become dominant from $X/L = 3$. This is explained by the rapid influx of high momentum flow into the frontal area of the rotors observed in the velocity contours between $X/L = 3$ and 5 , beyond which turbulent dissipation occurs. The X-Rotor shows higher momentum recovery rates than the H-Rotor in both directions, due to its higher vorticity strengths. Interestingly, at $X/L = 8$ and beyond, the vertical advection contribution in the H-Rotor increases slightly. This is due to the wake gradually re-entering the frontal area of the rotor. However, this value is insignificant compared to the lateral and the turbulent recovery rates, indicating that the momentum is increasing in these regions. Furthermore, the wake is mostly outside of the rotor area for the H- and the X-Rotor from $X/L = 5$, which indicates that any quantification of the recovery rates will be pertained to the wakes themselves and not correlated to the inline AP.

At $\beta = 10^\circ$, both the lateral and vertical momentum recovery rates of both rotors are still significantly larger than the baseline case, and remain dominant until the turbulence transport increases further downstream. The lateral transport is significantly negative as it replaces high momentum flow outside the rotor area with low momentum flow, while the vertical transport term does the opposite. For both the rotors, the lateral transport contributes slightly more than the vertical transport term until around $X/L = 3$, where the vertical transport contributes more towards momentum recovery. This explains the significant increase of freestream entering the rotor area from the top and bottom in both rotors. Notably, the both the advective transport in the X-Rotor remains relevant until $X/L = 7$, beyond which the turbulence becomes dominant. Another distinct observation for the H-Rotor is that the advective transport terms flip much earlier than for the X-Rotor. This is because the H-Rotor pushes the wake much farther laterally than the X-Rotor by $X/L = 5$ - which causes a pocket of high momentum to exist between the rotor frontal area and the low momentum wake that is displaced by a significant amount, also quantified in Figure 5.5. As we move downstream, the wake is further moved from the rotor area, which increases the size of this high momentum pocket, consequently increasing the contribution to momentum recovery. This occurs further downstream for the X-Rotor due to the lower wake lateral displacement of this configuration. The same phenomenon explains the flip in the vertical recovery rates as well.

5.3.6 MEAN KINETIC ENERGY FLUX

Understanding the flux of mean kinetic energy (KE) gives insight into the the power replenishment of wind farms. In this case, we primarily focus this study on the power replenishment of the mean kinetic energy for isolated H- and X-Rotors. This approach is also used before by Cortina et al. [179] to study an isolated wind turbine, and by Hezaveh and Bou-Zeid [93] to study the same in a wind farm. In this work, we follow the approach used

by the former than the latter. The mean KE of the flow is represented as $K = \frac{1}{2}(\bar{u}^2 + \bar{v}^2 + \bar{w}^2)$, where \bar{u} , \bar{v} , and \bar{w} are the time-averaged streamwise, lateral, and vertical components of the velocity field. Therefore, the flux of the mean kinetic energy Q_V through a closed control volume V behind these VAWTs can be obtained through Equation 5.4.

$$Q_V = \iiint_V \bar{u}_i \frac{\partial K}{\partial x_i} dV \quad (5.4)$$

The work by Cortina et al. [179] shows the use of divergence theorem to convert the volume integral to surface integrals for this term, which reduces Equation 5.4 to the surface integral of mean KE flux as shown in Equation 5.5.

$$Q_S = \iint_S (\bar{u}_i K) \hat{n}_i dS \quad (5.5)$$

The flux of mean kinetic energy also has other components from the energy equation, such as the turbulent KE production, viscous dissipation as well as the pressure flux terms. As our interest primarily lies in the lateral and vertical advective flux due to the blade pitch angles, this analysis will not constitute these terms as well as the advective flux in the streamwise direction. Figure 5.9 shows a representation of the control surfaces considered in this study, along which the fluxes are evaluated. In this study, we consider that fluxes entering the surface and going into the encompassed control volume is positive, and vice versa. Now, as the tangential components of velocity corresponding to each surface would not contribute to the flux, simplifications can be made to the flux terms as mentioned in detail in Cortina et al. [179].

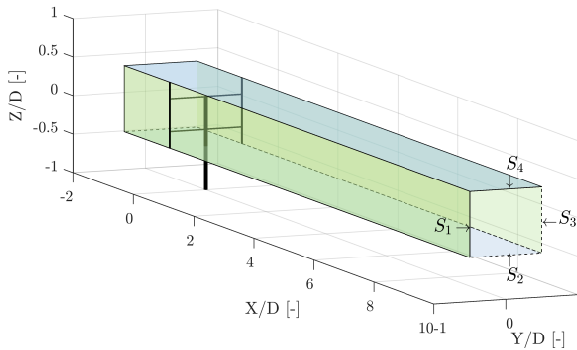
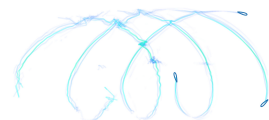


Figure 5.9: Schematic of the control surfaces (S_1 , S_2 , S_3 , S_4) along which the mean KE flux in the flow is evaluated. S_1 and S_3 , pass through the upper and lower tip of the rotors on the leeward and windward sides, respectively. Meanwhile, S_2 and S_4 pass through the lower blade tips and the upper blade tips, respectively. The fluxes entering the surfaces are considered positive.

The advective mean kinetic energy flux through the surfaces S_1 , S_2 , S_3 , and S_4 , integrated along the transverse length of the surface, is shown in Figure 5.10.

As expected, we observe that the fluxes through these surfaces are much larger for the pitched cases than the baseline case. For the baseline case, the mean KE flux is very low, if not null, save for the exception of S_3 , where the freestream is brought into the control



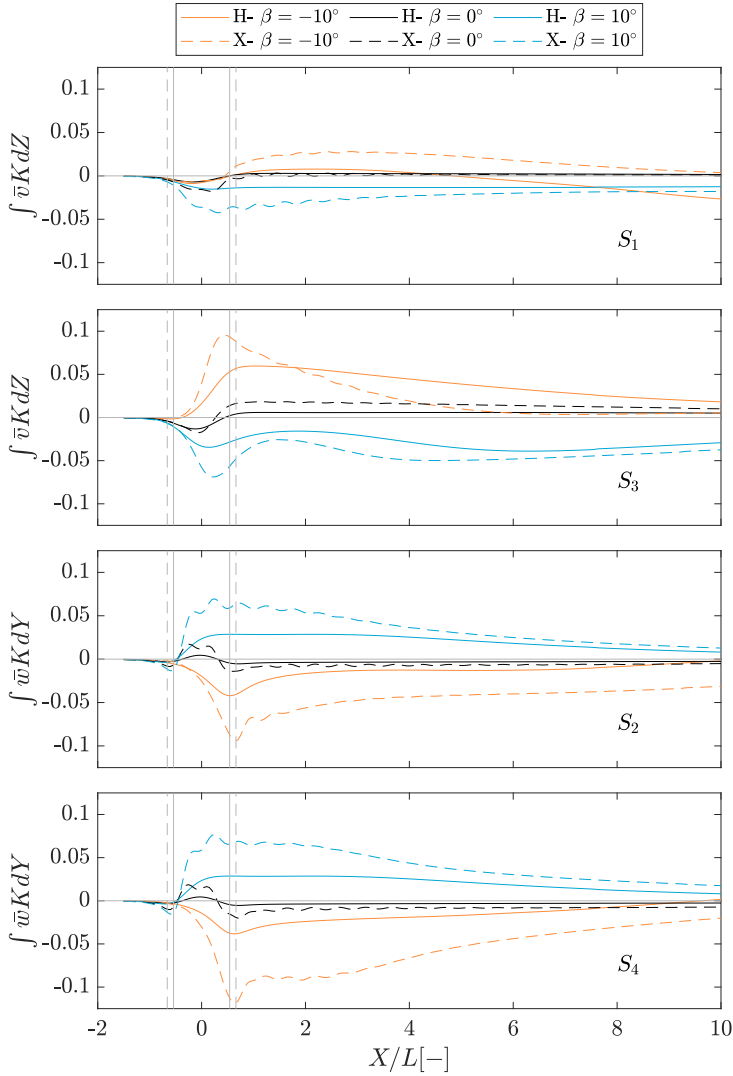


Figure 5.10: Line integrated advective flux of the mean KE, integrated along the transverse direction of the control surfaces S_1 , S_2 , S_3 , and S_4 , as a function of the streamwise location X/L , where L is the characteristic length scale. The flux terms are normalised by the term $1/U_\infty^3 L_i$, where U_∞ is freestream velocity and the L_i is the length of the control surface S_i over which the integral is computed. The grey vertical solid and dashed lines indicates the most upwind and downwind locations of the H- and X-Rotor, respectively. The solid grey horizontal line denotes zero flux of mean kinetic energy.

volume due to the vertical expansion of the wake. Additionally, in S_3 the X-Rotor reports marginally higher flux than the H-Rotor, due to the stronger vortices.

At $\beta = -10^\circ$, the kinetic energy flux is low at S_1 compared to the other surfaces. This is because the induced velocity by the leeward vortices are balanced by the windward

vortices at this location. This is also visibly noticeable in the velocity contours (Figure 5.4) where the wake loiters around the region of the S_1 surface. However, beyond $X/L = 5$, the H-Rotor shows negative flux, indicating the wake exiting S_1 . This continues to increase in magnitude as the windward vortices move towards the leeward side. At surface S_3 we see large positive flux for both rotors inside the rotor region. This occurs as a result of the freestream entering this surface for both rotors as the wake is pushed out vertically. However, this flux decreases sharply after for the X-Rotor, while this decrease is instead gradual for the H-Rotor. This is because, in the X-Rotor, the root vortex merges with the vortices in the upper tip, eventually propelling the upper vortices vertically out of rotor area. This happens at a much lower extent in the H-Rotor, which gradually continues to bring in high KE flow through this surface. In surfaces S_2 and S_4 , the H-Rotor sees the same quantity of flux exiting the surfaces, due to its symmetrical geometry. Meanwhile, as expected, the X-Rotor sees a larger flux through S_4 than S_2 due to the much stronger vortex pair at the top than the bottom of the rotor. The X-Rotor also sees much higher flux magnitudes due to the stronger tip-vortex pairs. However, while the flux magnitude through S_2 gradually reduces downstream, at S_4 it experiences a steeper reduction as the upper tip vortices propel each other further upward, while the bottom vortices do this at a much lower extent, thereby still inducing flux through S_2 .

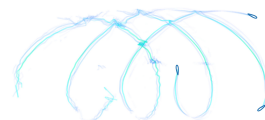
At $\beta = 10^\circ$, we see negative fluxes through S_1 and S_3 , while positive fluxes through S_2 and S_4 for both rotors. This is not surprising, considering the advection of velocity in this configuration. In all planes, there is a spike in the flux in the rotor region, while gradually tending towards zero, with the notable exception of S_3 . At S_3 , the spike is followed sharply by a decrease in magnitude at $X/L = 0.2$, which then increases after $X/L = 1.5$ to then decrease again after $X/L = 5$. This odd behaviour is because the wake center passing through S_3 , which causes a decrease in flux due to the lower mean KE, which then increases again after the windward wake center goes beyond S_3 after $X/L = 5$. This is also reflected in the quantification of wake displacement from Figure 5.5. This is more observable in this case than $\beta = -10^\circ$ as the flux is very unequally distributed between S_1 and S_4 . The X-Rotor exhibits this closer downstream than the H-Rotor due to the cohesion between the root and tip-vortices which pushes the wake quickly, and the root vortices dissipate. Again, due to the symmetric geometry of the H-Rotor, the fluxes entering through S_2 and S_4 would be equal, while the X-Rotor shows marginally higher value through S_4 than S_2 .

5.4 CONCLUSIONS

A numerical analysis of the wake recovery capability of VAWTs with fixed blade pitch as well as its mechanism between two distinct VAWT geometries, H- and X-, is analysed in this study. The study contributed the following: (1) provided insight into the parameters that drive the wake recovery mechanism between these rotor geometries, and (2) a systematic analysis to qualitatively and quantitatively characterise the wake recovery capability of the H- and the X-Rotor with fixed pitch offsets. The results are generated using the actuator line method (ALM) with *OpenFOAM* through the *turbinesFOAM* library.

The conclusions corresponding to mechanism of wake recovery between the two rotors are as follows:

- The vortex system of the two rotors are significantly different due to the distinct rotor



geometries, and it drastically affects the wake recovery mechanism associated with VAWT pitch offsets. The windward vortices become the dominant driver to advect the wake with blade pitch - for the H-Rotor the vortices work cohesively to push the wake out of the rotor and bring freestream vertically into the rotor area with the positive pitch case, while pushing the wake up vertically out with the negative pitch case. The X-Rotor, due to the asymmetric geometry, is seen to contribute more to the wake recovery through the upper half than the lower half, due to the higher vortex strengths associated with the upper blade loads than the lower blades. Additionally, the circulation difference at the root of the X-Rotor blades produces a root vortex that affects the overall vortex system in the near-wake in both pitch cases. In this study, the root vortex was less dominant compared to the tip-vortices, and aided the recovery of the wake in the upper half of the X-Rotor.

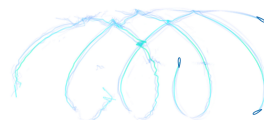
- The advection terms in both rotors play a crucial role in the wake recovery process of the rotors. In general, the advection dominates the near-wake, while turbulence takes over the recovery process from around $X/L = 5$. However, the magnitude of advection increases significantly with pitch offsets - increasing the recovery process tremendously. In the negative pitch cases, the contribution of turbulence also increases and stays relevant throughout the domain.
- For the X-Rotor, compared to the slower wake recovery while only allowing pitch control for the upper blades (Giri Ajay and Simao Ferreira [158]), the wake deflection is significantly improved in this study. This is due to the twin root vortices formed in the windward side, that work cohesively with the windward vortices to advect the wake. Moreover, the stronger lower blade tip-vortices now actively deflect the wake of the lower half.

The important conclusions that we gained about the quantification of the wake recovery are:

- Overall, pitching the blades to increase lateral and vertical advection proved to result in much higher inline available power (AP) than for rotors without blade pitch offsets. Pitching the blades showed an increase in inline AP of the H-Rotor by 2.3 times at $X/L = 5$ and by 2.08 times for the X-Rotor. The X-Rotor also showed the highest inline AP in the near-wake with the positive pitch configuration. However, after understanding the variation of AP at lateral offsets, it is evident that the H-Rotor at positive pitches decreases the AP laterally due to the lateral advection of the wake, which potentially can reduce the power of an adjacent turbine downstream. However, the negative pitch configuration does not have this significant drawback as the wake is vertically ejected from the rotor area - this increasing inline AP while not significantly compromising the AP in the lateral direction.
- Quantifying the vertical wake center deflection for H-Rotor can be misleading due to the vertical symmetry. Therefore, a slight modification of this approach is employed in this study shed light into the wake displacements with blade pitch offsets. The H-Rotor with the positive blade pitch showed the most lateral wake displacement, while both the rotors showed nearly the same wake displacements with the negative

pitch. Overall, understanding the displacement of the wake cannot be used as a stand-alone measure of wake recovery effectiveness, and required complementary analyses.

- The mean kinetic flux further emphasised the increase in mean kinetic energy behind the rotor through the lateral and vertical advection associated with the blade pitching. The X-Rotor showed the highest flux magnitudes in all configurations, as the vortices of the X-Rotor are much larger. Furthermore, as the rotor is asymmetric, the flux through the upper surface is much larger than the lower half for the negative pitch, while relatively equal with the positive pitch offsets.

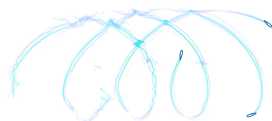


6

WAKE SENSITIVITY TO AIRFOIL DATA, DYNAMIC STALL, AND REGULARISATION KERNEL

Chapter 5 presented a comprehensive comparison of wake recovery mechanisms between H- and X-Rotor VAWT geometries using the Actuator Line Model (ALM). The model setup and its applicability were discussed in the context of large offshore rotors operating at high Reynolds numbers. However, as demonstrated in Chapter 4, at low Reynolds numbers the induction field and near-wake characteristics were found to be highly sensitive to numerical inputs, particularly the airfoil polars. This highlights the need to further investigate how both the near- and far-wake respond to variations in numerical modelling parameters under such conditions.

The present chapter addresses this need by analysing the sensitivity of the wake to key numerical inputs—namely, airfoil polars, dynamic stall modelling, flow curvature corrections, and regularisation kernel size—at low Reynolds numbers and across different blade pitch offsets. This analysis is conducted by comparing simulation results for a scaled X-Rotor VAWT against experimental Particle Image Velocimetry (PIV) measurements.



6.1 INTRODUCTION

The actuator line model is a very effective method to calculate the flowfield of VAWTs at different inflow and operational conditions. As detailed in Chapter 2, the model achieves this by combining blade-element methods to represent the turbine blades as discretized line elements. The flowfield is modelled using an Eulerian approach through the Navier-Stokes equations. The lift and drag profiles for each blade section of the VAWT blade are obtained by using lookup tables or airfoil polars based on the angle of attack of the blade section. At low Reynolds numbers, $Re < 80K$, uncertainties are introduced in the polars and lookup tables due to more prominent laminar separations [141]. Additionally, parameters such as the regularisation kernel ϵ also impact the wake as ϵ dictates how far the forces from the blades spread into the fluid domain from the line elements [162, 180, 181]. This leaves considerable variations in output of the wake.

Therefore, the aim of this chapter is to qualitatively and quantitatively understand the impact of the numerical parameters on the prediction of the wake, such as airfoil data, dynamic stall and flow curvature, and the regularisation kernel. The ALM model, using an Eulerian approach, is used to simulate the wake of the scaled X-Rotor geometry. The wake of different numerical input parameters are compared against experimental particle-image velocimetry (PIV) results [99] to assess their sensitivity.

6

6.2 METHODOLOGY

In this section, details of the test geometry followed by the experimental setup and conditions used to obtain the PIV results are provided in Section 6.2.1 and Section 6.2.2, respectively. Later, numerical setup and domain information is documented in Section 6.2.3.

6.2.1 SCALED X-ROTOR MODEL

The test geometry is a scaled version of the full-scale primary rotor, reduced by a factor of $\frac{1}{250}$, as designed and described in Bensason et al. [99]. The model is also effectively a scaled down version of the model presented in Chapter 4. The top and bottom blades have tip diameters of $D = 0.6\text{m}$ and cone angles of 30° and 50° , respectively, resulting in upper and lower blade spans of 0.375m and 0.238m . Similar to the setup described in Chapter 4, the scaled model comprises four straight NACA0021 airfoils with a constant chord length of $c = 0.03\text{m}$, each attached to a rigid crossbeam of length 0.2m having the same airfoil profile and chord. The blades are clean, i.e., without vortex generators, with a chord-mount position of $c/2$. The rotor is supported by a tower with a diameter of 0.015m . The model operates at a constant tip-speed ratio of $\lambda = 5.55$ under a free-stream velocity of $U_\infty = 0.375\text{m s}^{-1}$, resulting in a chord-based Reynolds number of $Re_c = 3 \times 10^4$ at the blade tip.

6.2.2 EXPERIMENTAL SETUP OF THE X-ROTOR

The experiments by Bensason et al. [99] were conducted in the Open-Jet Facility (OJF) at the Aerospace Engineering faculty of TU Delft. This wind tunnel has been extensively used for scaled VAWT studies [57, 64, 69], and features an octagonal outlet with a cross-sectional area of $2.85 \times 2.85\text{m}^2$, as shown in Figure 6.1. The facility is a closed-loop wind tunnel with a 3:1 contraction ratio, producing a free jet bounded by shear layers that have a

semi-angle of 4.7° . Within the test region, the reported turbulence intensity is 0.5% [149]. A region of uniform flow extends up to 6 m downstream of the outlet, fully encompassing the measurement zone for this experiment. The tunnel is equipped with a $2\text{ m} \times 3\text{ m}$ table with adjustable height to accommodate various model configurations.

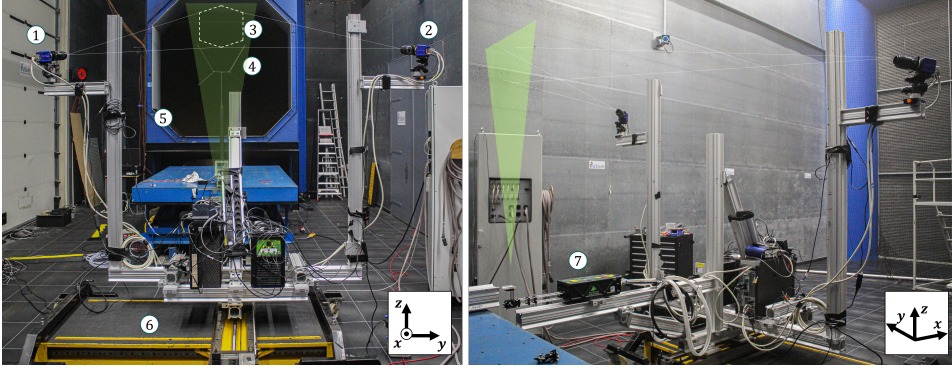


Figure 6.1: Experimental setup in the OJF from two different views. A visualization of the measurement plane (green triangle) is provided, along with a representation of the camera viewing direction. The main components are labeled and defined as follows: ① Camera 1, ② Camera 2, ③ field-of-view, ④ X-Rotor model, ⑤ OJF outlet, ⑥ Traversing system, ⑦ Laser.

Following the work of Sciacchitano and Wieneke [151] and Huang et al. [69], the expanded uncertainty $U_{\bar{U}_i}$ of the velocity for time-averaged measurements can be expressed as:

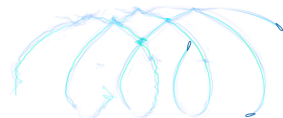
$$U_{\bar{U}_i} = k \frac{\sigma_{U_i}^*}{\sqrt{N}} \quad (6.1)$$

where $\sigma_{U_i}^*$ is the standard deviation of the velocity component U_i computed over $N = 300$ samples and i corresponds to either the streamwise (X), lateral (Y), and axial (Z) directions. This value is multiplied by the coverage factor $k = 1.96$ to convert the standard uncertainty to a 95% confidence interval. Across all pitch cases, the maximum uncertainty is observed at the most upwind measurement plane at $X/D = 1$, along the shear layer of the wake, consistent with the findings of Huang et al. [69]. The largest standard deviation occurs in the lateral velocity component for the positive pitch case, with $\sigma_{U_Y}^* = 0.59\text{ m s}^{-1}$, corresponding to an expanded uncertainty of $U_{\bar{U}_Y} = 0.07\text{ m s}^{-1}$.

The uncertainty of the streamwise vorticity component U_{ω_x} is calculated as ([151]):

$$U_{\omega_x} = \frac{U_{\bar{U}_{Y \text{ or } Z}}}{d} \sqrt{1 - 2\rho d} \quad (6.2)$$

where $U_{\bar{U}_{Y \text{ or } Z}}$ represents the standard uncertainty in maximum between the lateral or axial velocity component, d denotes the grid spacing of the interrogation window, and $2\rho d$ is the cross-correlation coefficient of the spatially correlated velocities. Given a final interrogation window size of 64 pixels and a scaling factor of 7.454 pixels/mm, the grid spacing is calculated as $d = 4.3\text{ mm}$. The cross-correlation coefficient is approximated as $2\rho d \approx 0.45$ [151]. Using the maximum expanded uncertainty of $U_{\bar{U}_Y} = 0.07\text{ m s}^{-1}$, the



uncertainty in the streamwise vorticity is estimated as $U_{\omega_X} = 11.9 \text{ s}^{-1}$. This uncertainty decreases by nearly an order of magnitude outside the wake's shear layer.

For further details about the experimental setup, see Bensason et al. [99] where the setup and results are discussed qualitatively and quantitatively.

6.2.3 NUMERICAL SETUP AND COMPUTATIONAL DOMAIN

Numerical simulations of this work are conducted using the ALM library *turbinesFoam* coupled with OpenFOAM v2306 [111], an open-source finite-volume-based CFD solver. In this study, the flow is treated as incompressible, homogeneous, and Newtonian with a density of $\rho = 1.225 \text{ kg m}^{-3}$ and kinematic viscosity $\nu = 1.5 \text{ m}^2 \text{ s}^{-2}$. The Unsteady Reynolds-Averaged Navier-Stokes (URANS) equations are used with the *pimpleFoam* [111] solver in this study to capture the time-resolved wake of the scaled X-Rotor. Furthermore, we implement the use of the $k - \epsilon$ turbulence closure model [163]. $k - \epsilon$ has been documented to show good prediction of performance of VAWTs at higher tip-speed ratios $\lambda \geq 3$ [182]. The inflow velocity U is kept at a constant 2.7 m s^{-1} with a low turbulence intensity TI of 0.5% to correspond with the inflow conditions used in the experiments [149]. The velocity sampling of the ALM library, where the flow angle is evaluated, is performed at the center.

The simulation domain ranges from $-5D$ upwind to $15D$ downwind. It extends laterally from $-4D$ to $4D$, and vertically from $-3.5D$ to $3.5D$. The domain size is in accordance with the suggestions from Rezaeiha et al. [50]. A visual representation of this along with the refinement zones are shown in Figure 6.2. For this domain, a coarser mesh region (Zone 1) of $D/20$ resolution ranging from $-1.5D$ to $11D$ up to $1.5D$ either side laterally and vertically. Inside it, a fine mesh region (Zone 2) of resolution $D/40$ extends from $-1D$ to $7D$, enveloping up to $1D$ on either lateral and vertical directions from the rotor center. This region is encompassed by the sides, top, and bottom edges of the domain are set to a zero gradient boundary condition, while the outlet is treated as an inlet-outlet boundary.

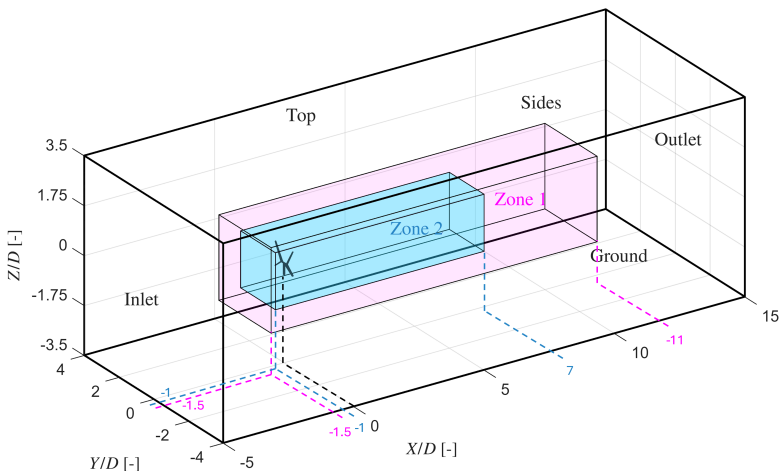


Figure 6.2: Illustration of the computational domain setup with refinement zones. The inflow comes from the bottom left to the top right. The magenta and cyan control volumes represent the refinement zones in the domain.

To serve as the input for the ALM at the operating Reynolds number, we generated the airfoil polars using XFOIL [137] for the X-Rotor, with an Ncrit of 4 (based on the experimental turbulence intensity). The post stall characteristics are obtained using a Viterna extrapolation technique [138]. Furthermore, due to the high-uncertainty of airfoil characteristics at this Reynolds number [141], we also used the airfoil characteristics measured by Sheldahl and Klimas [153] for the operational Reynolds number, henceforth referred to as S & K polars. A collection of available data at this Reynolds number is presented in Figure 6.3. It is interesting to note that some of these polars exceed the prediction based on the thin-airfoil theory. This is primarily due to the 21% thickness of the NACA0021 airfoil which produces higher lift at lower angles of attack at the cost of higher drag than the thin airfoil.

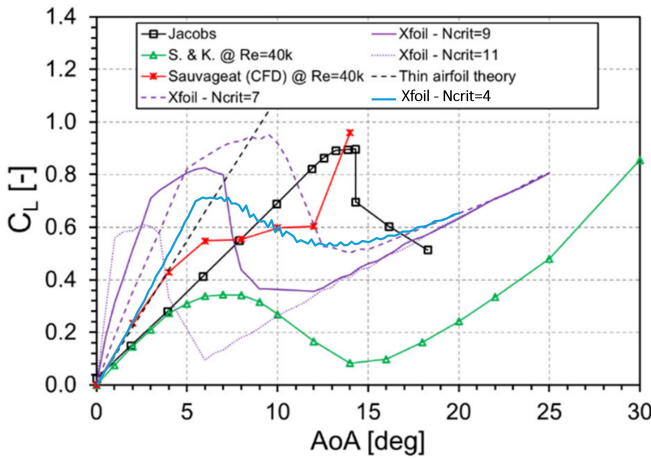


Figure 6.3: Lift coefficient comparison between existing datasets for NACA0021 airfoil at $Re = 40K$ modified from Melani et al. [141]. The solid blue line indicates the polar used in this chapter

To understand the sensitivity of the results to dynamic behaviour of the rotor, we employ the Leishman-Beddoes (LB) dynamic stall model [124, 125], which is readily available in *turbinesFoam*. Furthermore, to account for possible flow curvature effects for the current geometry where the chord-to-radius ratio $c/R > 0.1$, we also test the sensitivity towards using the Goude flow curvature model [134].

To simulate the X-Rotor, the upper and lower blades are discretised into 18 blade sections each. The cross-beam and tower are not modelled, as their influence on the wake are expected to be minimal and predictable, offering little additional insight. The solidity σ of the X-Rotor is determined using the derived expression: $\sigma = \frac{Nc(L_U \cos 30^\circ + L_L \cos 50^\circ)}{A}$, where N is the number of blades, L_U and L_L are the upper and lower blade spans, c is the chord, and A is the rotor frontal area. The angles correspond to the coned angles of the upper and lower blades. A summary of the essential simulation setup information is provided in Table 6.1, including the time control used for the simulation.

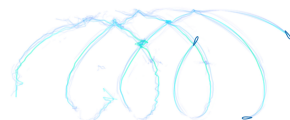


Table 6.1: Description of the simulation setup for *turbinesFoam*.

Parameters	Value
Rotor diameter (at the tips) D	0.6 m
Rotor chord c	0.03 m
Upper blade span L_U	0.375 m
Lower blade span L_L	0.238 m
Frontal Area A	0.206 m ²
Number of blades N	2
Airfoil profile	NACA0021
Tip-speed ratio λ	5.55
Inlet velocity U_∞	2.7 m s ⁻¹
Air density ρ	1.207 kg m ⁻³
Solidity σ	0.15
Blade elements (per blade)	18
Blade pitch β	-10°, 0°, 10°
Time step δt	0.00035 s
Number of revolutions	32
Fine grid length Δ	$D/40$
Normalised regularisation kernel ϵ/Δ	2
$CFL_{blade} \lambda U_\infty \delta t/\Delta$	0.350

6.3 RESULTS

The results section first explores the sensitivity of ALM results towards the input polars (Section 6.3.1) at low Reynolds numbers [141]. Later, the model's sensitivity is explored for the effects of dynamic stall and flow curvature (Section 6.3.2). The results are further explored towards the sensitivity of the regularisation kernel ϵ (Section 6.3.3), as this is important to effectively resolve the tip-vortices which dictates the flowfield.

6.3.1 SENSITIVITY TO AIRFOIL POLAR DATA

To understand how the airfoil polars affect the solution predicted by the ALM, the normalised streamwise velocity (u/U_∞) contours of the scaled X-Rotor are shown in Figure 6.4 between the experiments and ALM with XFoil polars as well as the S & K polars [153].

At a first glance, we can clearly see the discrepancies between these results. The XFoil polars cause the ALM to predict much lower velocities in the wake compared to the experiments. This is expected as the lift from the XFoil polars are significantly higher. The opposite is observed for the ALM with the experimental polars. Furthermore, the S & K polars are obtained at a Reynolds number that is in the same order of magnitude, but still underpredict the velocity deficit to the experiments. This indicates that at these Reynolds numbers there is a high level of uncertainty in the available data for NACA0021 airfoils. This was documented by Melani et al. [141], identifying that the XFoil and S & K polars are vastly different from each other. While there are other experimental lift curves available for the NACA0021, most of them have incomplete data or invalid assumptions to be tested here.

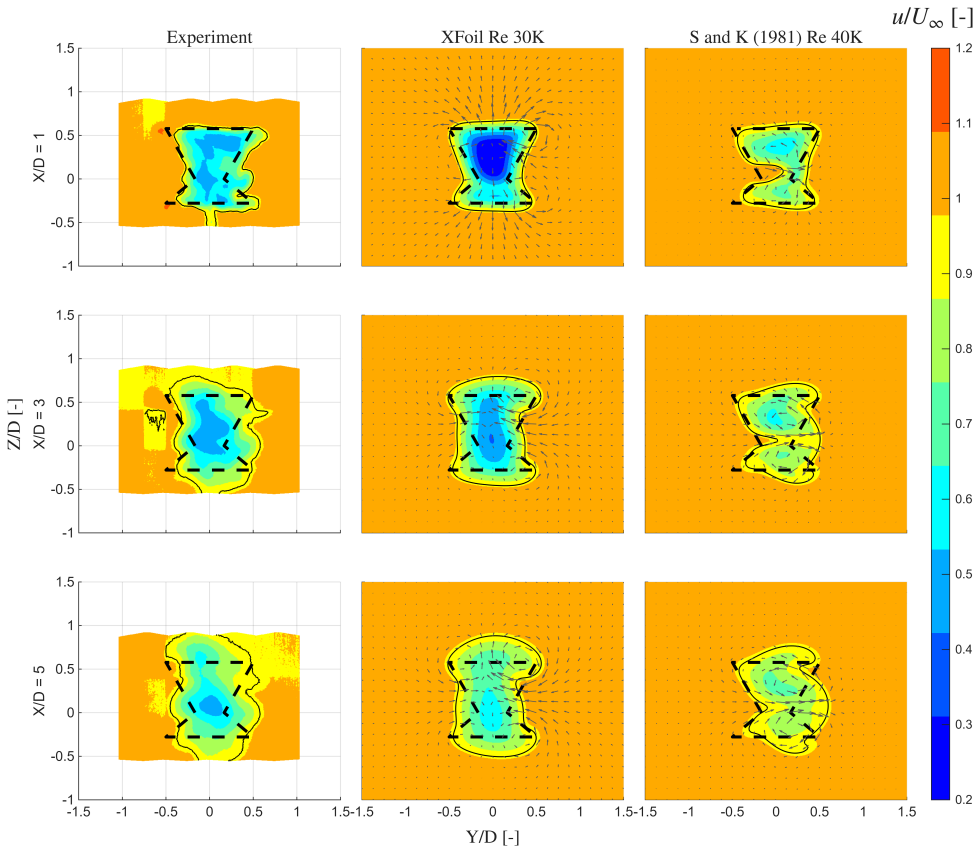
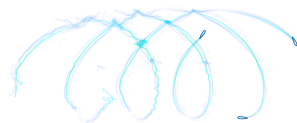


Figure 6.4: Normalised streamwise velocity (u/U_∞) contours of the scaled X-Rotor at downstream locations $X/D = 1, 3,$ and 5 . Results are shown for the experiments (1st column), ALM with airfoil polar inputs from XFOil (2nd column), and ALM with airfoil polars from experiments of Sheldahl and Klimas [153] (3rd column). The black dash lines indicate the projected frontal area of the rotor and the black contour line represents 95% of U_∞ .

However, while there is some similarity in the wake shape between the experiments and ALM with XFOil, the wake shape observed with the S & K polars is significantly different. This can be attributed to the root sections of the X-Rotor experiencing much larger local angle of attack α due to the cone angle compared to the XFOil. This is demonstrated through Figure 6.5, where the minimum and maximum angle of attack at the root section are -21.48° and 16° , respectively, for the XFOil polars and -29.26° and 19.44° , respectively, for the S & K polars. In contrast, the same values at mid-span of the lower blade are -8.98° and 8.98° , respectively, for the XFOil polars and -14.45° and 10.89° , respectively, for the S & K polars. This is because as the loads from the turbine reduce, the angle of attack tends to move towards the geometric angle of attack $\alpha_g = \tan^{-1}(\frac{\sin\theta}{\lambda + \cos\theta})$. This results in the observed higher α at the root section with the S & K polars, as the lift profiles are much lower in magnitude in comparison to the XFOil ones. This also results in the lower velocity deficit compared to both PIV experiments and XFOil inputs. Due to this high α , the root



blade sections exhibit a large lift values due to the post-stall behaviour captured by the S & K polars. This results in large flow advection near the root, which is quite unrealistic compared to the Xfoil profile as well as the experiments.

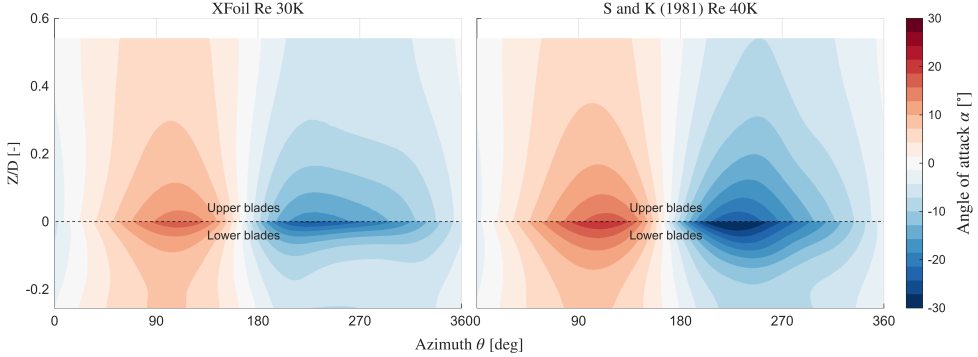


Figure 6.5: Angle of attack α variation along height and θ between the polar data from Xfoil and Sheldahl and Klimas [153].

6

Now, at further downstream locations ($X/D = 3$ and 5), we see that the wake topology moves further away from the experiments. This is effectively the compounding of prediction error in the near-wake. In addition, the ALM results show much faster recovery of the wake compared to the experiments. This can be attributed to the excessive dissipation and diffusion of CFD in general. This is also corroborated by the results of Ribeiro et al. [183] and Huang [83].

To quantify this difference in velocity profiles, the velocity slices at $Y/D = 0$ is shown in Figure 6.6. At $X/D = 1$, there is a peak difference of 65% under-prediction in velocity from the Xfoil inputs and a 54% over-prediction by S & K polars compared to the experiments. As we move further downstream, the over-prediction from S & K polars decreases as the wake recovers. Interestingly, the least difference between the Xfoil inputs and the experiments are observed between $X/D = 3$ and 4 . This is because in the experiments, the wake shows a velocity decrease due to the wake expansion typically observed in the near-wake of the rotors. Beyond $X/D = 2$, the wake starts to recover. However, as highlighted earlier, the excessive dissipation inherently present in ALM recovers the wake faster than ALM which results in ALM overpredicting the velocity between 15% to 20%.

Overall, we see a significant difference in the predicted velocity profiles based on the airfoil polars. Furthermore, due to the high uncertainty of these inputs, the ALM model is unable to accurately capture the flow features of the scaled X-Rotor at these low Reynolds numbers. We expect this difference to be further exaggerated with fixed blade pitch applied to the X-Rotor, which is discussed in Section 6.3.4.

6.3.2 SENSITIVITY TO DYNAMIC STALL AND FLOW CURVATURE EFFECTS

To gain insight into the sensitivity of this model with dynamic stall and flow curvature effects, Figure 6.7 shows the streamwise velocity u/U_∞ contours of the X-Rotor at the same downstream locations. The experiments are compared with ALM results with no dynamic

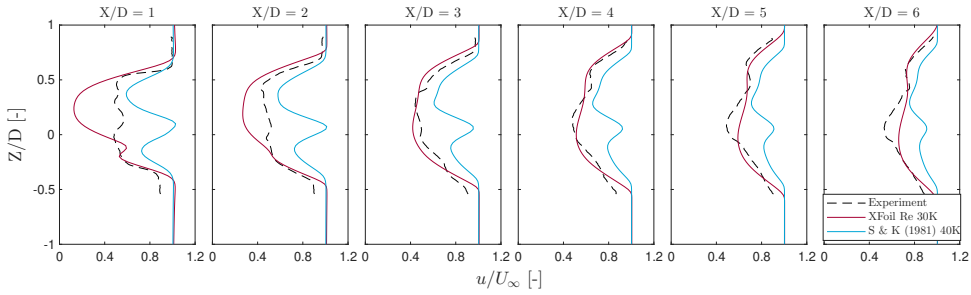


Figure 6.6: Normalised streamwise velocity (u/U_∞) slices of the scaled X-Rotor at $Y/D = 0$ at various downstream locations $X/D = 1$ to 6. Black dashed line, red solid line, and cyan solid line correspond to experiments, ALM with Xfoil input, and ALM with inputs from Sheldahl and Klimas [153], respectively.

stall or flow curvature, henceforth named 'ALM Baseline', ALM with the LB dynamic stall model, and ALM with the Goude flow curvature model.

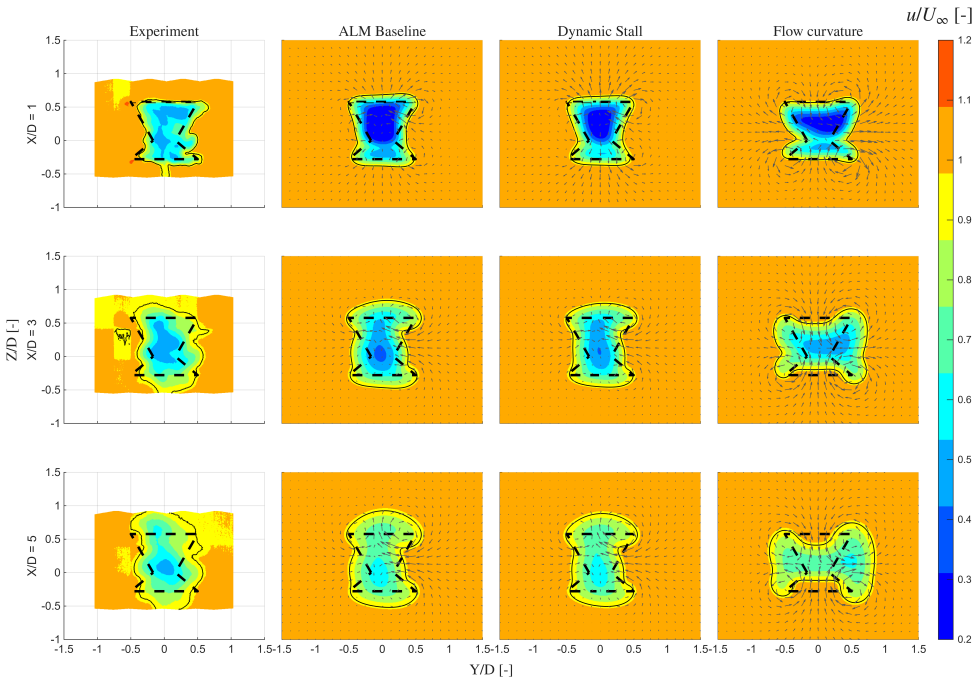
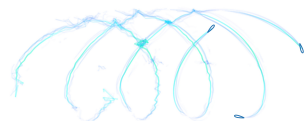


Figure 6.7: Normalised streamwise velocity (u/U_∞) contours of the scaled X-Rotor at downstream locations $X/D = 1, 3,$ and 5 . Results are shown for the experiments (1st column), ALM with no dynamic stall or flow curvature (2nd column), ALM with the LB dynamic stall model (3rd column), and ALM with the Goude flow curvature model (4th column). The black dash lines indicate the projected frontal area of the rotor and the black contour line represents 95% of U_∞ .

We can observe that the velocity profiles with and without dynamic stall model look very similar to each other. Some minor differences in the velocity magnitude is observed,



however the wake topology is not sensitive to the inclusion of dynamic stall. This is contrary to what can be expected of rotors operating at high angles of attack and the high rotational speed. This is likely because the difference between the averaged rotor loads between the two cases are not significant while still having different azimuthal load distribution, resulting in the time-averaged wake showing minor differences. Additionally, as the forces near the root of the X-Rotor is smaller compared to near the tips. Therefore, while dynamic stall would affect the root area due to the large angles of attack, its effect on the overall loads from the rotor would be overshadowed by the loads produced near the tips. Regardless, as seen previously, the velocity profiles are very dissimilar to the experimental results.

When the flow curvature model is included, the wake topology appears to be very different to the case without. The quivers reveal that with the flow curvature model, the tip-vortices flip in direction. This leads to the wake advecting laterally instead of the vertical advection observed without flow curvature. This occurs as the flow curvature model adds a net positive angle of attack to the blades. This causes the time-averaged vorticity fields to change as the upwind half of the rotor is more loaded than the downwind half. Therefore, in addition to significant difference in velocity magnitudes, the wake topology is also notably different from the experiments. This can be best observed at $X/D = 5$, where the experiments show the wake mostly ejecting from the top and bottom of the X-Rotor, while ALM with flow curvature shows the wake to eject laterally out. It is unclear why including the flow curvature model causes the flow to skew further away from the experiments for the X-Rotor where the majority of the blade operates at $c/R > 0.1$.

Overall, we can conclude that the results are not sensitive to the inclusion of dynamic stall model. However, the flow curvature models change the tip-vortices strengths of the rotor that alter the wake topology and skews the results away from experimental PIV flowfields.

6.3.3 SENSITIVITY TO REGULARISATION KERNEL ϵ

To understand the implication of the size of regularisation kernel ϵ , Figure 6.8 shows the streamwise velocity u/U_∞ contours of the scaled X-Rotor for a range of ϵ/Δ from 1 to 4.

It is clearly observed that regardless of the ϵ value, the wake topology does not seem to match that of the experiment as they all predict much lower velocities than the experiments. At $X/D = 1$, the lower values of ϵ closely predicts the wake shape of the experiments, compared to larger epsilon values. However at more downstream locations, the resemblance to the experiments reduces. This, as discussed earlier, is attributed to the airfoil input data rather than the ALM model itself. However, we can observe that with increasing ϵ , the wake diffusion increases significantly. This is expected, as increasing ϵ increases the spread of the force distributions from the blades. As a consequence, we can expect a reduction in the resolution of the shed and the tip-vortices of the blades, which results in the increased diffusion of the wake. Interestingly, between $\epsilon/\Delta = 1$ and 2, there exists only minor differences in the wake attributed to the higher diffusion. Notably, at $X/D = 3$, we can see that the wake shows minor differences in the velocity magnitudes.

Overall, it can be concluded that ALM is indeed sensitive towards the choice of the regularisation kernel ϵ . Furthermore, it is not straightforward to determine the local velocity and the angle of attack at the blade due to the reduction due to the diffusion of

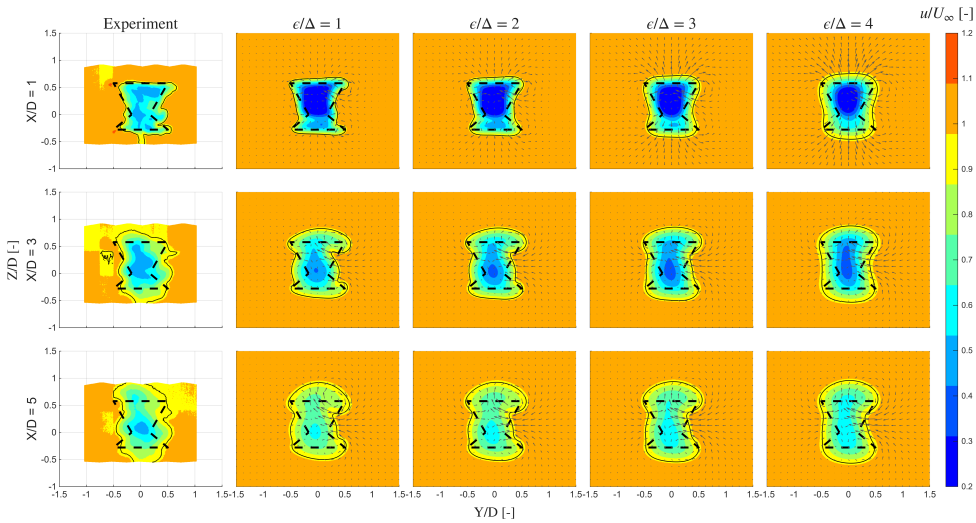


Figure 6.8: Normalised streamwise velocity (u/U_∞) contours of the scaled X-Rotor at downstream locations $X/D = 1, 3$, and 5 . Results are shown for the experiments (1st column), ALM with the ϵ/Δ varying between 1 to 4, where Δ is the local grid length. The black dash lines indicate the projected frontal area of the rotor and the black contour line represents 95% of U_∞ .

blade forces. One should pay significant attention towards this parameter while running ALM simulations as it can have a significant affect on the flowfield in the near-wake where advection is dominant. Existing guidelines on choosing a suitable value for this parameter are recommended to be followed for wind turbine simulations [162, 180, 181].

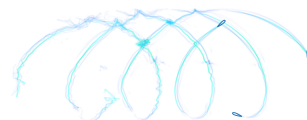
6.3.4 FIXED BLADE PITCH OFFSETS

As discussed earlier in Section 6.3.1, the uncertainty in the airfoil significantly affects the prediction of the flowfields by the ALM model. This would be further exaggerated when the blades undergo a pitch offset due to the increased angles of attack. Here, we further investigate the sensitivity of airfoil data with blade pitch offsets, by utilising the setup described in Section 6.3.1. In Figure 6.9, the streamwise velocity u/U_∞ contours of the scaled X-Rotor at downstream locations $X/D = 1$ for pitch offsets $\beta = -10^\circ, 0^\circ, 10^\circ$.

We can see that the prediction error from ALM gets transferred to the case with pitch offsets as the flowfields are different between the experiments and ALM. We consistently observe that the velocity deficit is overpredicted by the ALM model due to the inputs. This also results in quite dissimilar wake topologies as the vortex system that defines the wake are different, as can be seen from the quivers.

At $\beta = -10^\circ$, wake is ejecting the rotor vertically, however the freestream is predicted to enter from the windward and leeward side as opposed to only the leeward side from the experiments. This is a direct consequence of the airfoil inputs, as the experiments suggest that the windward tip-vortex is not dominant compared to the leeward vortex - resulting in the advection of freestream from the leeward half.

For $\beta = 10^\circ$, the freestream is seen to enter vertically in both experiments and ALM.



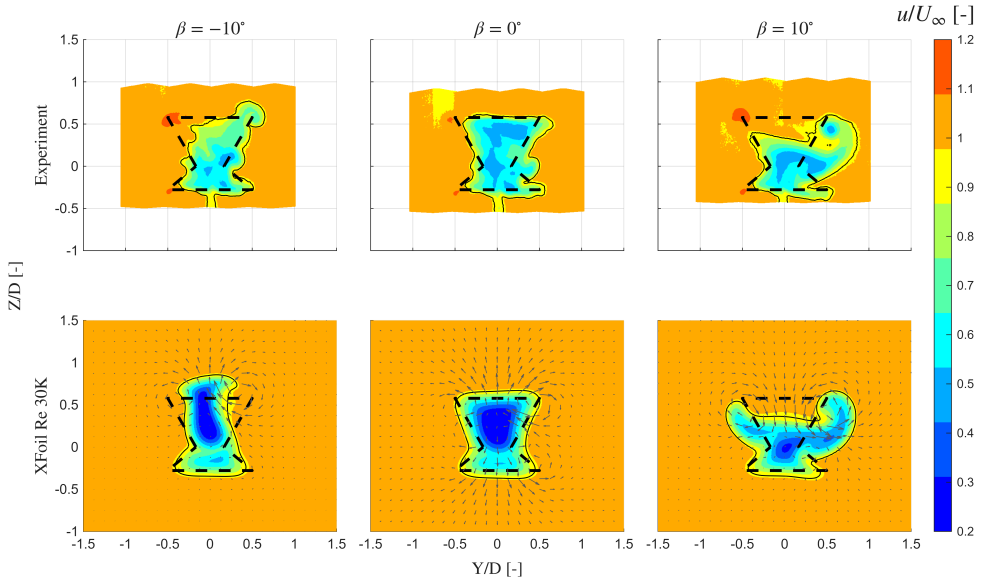


Figure 6.9: Normalised streamwise velocity (u/U_∞) contours of the scaled X-Rotor at downstream locations $X/D = 1$ for pitch offsets $\beta = -10^\circ, 0^\circ, 10^\circ$. The first row shows the results from the experiments, and the second row corresponds to the ALM results with Xfoil inputs. The black dash lines indicate the projected frontal area of the rotor and the black contour line represents 95% of U_∞ .

6

However, the wake is predicted to advect laterally out on both sides as opposed to just the windward side from the experiments. This is because the windward vortex is stronger in the experiments which advects the wake laterally out while the freestream enters from above. In ALM, the dominance of the windward vortex is not observed as the quivers show that both the windward and leeward vortex are almost equally effective at advecting the wake laterally.

6.4 CONCLUSIONS

In the present chapter, we showcase the sensitivity of the ALM model to airfoil inputs, dynamic stall and flow curvature effects, and the regularisation kernel ϵ at low Reynolds numbers by comparing it with time-averaged experimental PIV results. The analysis is conducted for a 1:250 scaled geometry of the X-Rotor at various pitch offsets.

With respect to input polars, we documented differences in the velocity profiles between the PIV results and ALM for both experimental measured and numerically generated polars. This is attributed to the high uncertainty of the inputs at the low Reynolds numbers of $Re \leq 80K$. These differences were further exaggerated with the introduction of blade pitch offsets, as both positive and negative pitch offsets were predicted differently from the PIV results. It was noted that at these low Reynolds number regimes, existing airfoil polars are significantly different from each other due to measurement difficulties at these Reynolds numbers. Therefore, as the inputs directly affect the predicted flowfield of the rotor, reducing the uncertainties of these inputs would improve the reliability of these

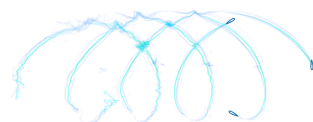
simulations.

The model, in the operating range of Reynolds number, did not show notable sensitivity towards the usage of dynamic stall corrections on the wake. However, the results may be different for rotor performance and loads. The inclusion of a flow curvature correction model introduced deviations to the wake topology compared to the experimental results.

The results also showed that the wake diffuses significantly more with the increase in regularisation kernel ϵ . This, however, affected the resolution of the wake negatively, as the wake was unable to resolve the full experimental wake shape at high ϵ values. At lower epsilon values, the wake shape is captured only in the near-wake while the far wake deviates significantly from the experimental results.

Based on the work here, we have a few recommendations for future validation studies utilising experimental data at low Reynolds numbers:

1. We recommend prioritising obtaining accurate and representative airfoil polars at the relevant low Reynolds numbers. As tools such as XFOIL are not designed to work at these Reynolds numbers, using high-quality CFD polars or experimental polars with detailed uncertainty quantification should help minimise discrepancy during validation studies.
2. Once obtaining accurate and representative polars, priority should then shift towards determining optimal regularisation kernel size. Guidelines from existing literature can be followed to get optimal setup conditions for ALM for each test case.



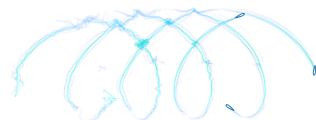
7

WAKE RECOVERY PHYSICS IN WIND FARMS WITH WAKE CONTROL

In the preceding chapters, the rotor, blade, and wake dynamics of an isolated turbine operating under ideal, homogeneous, and uniform inflow conditions were examined. These analyses provided critical insights into the intrinsic aerodynamic behaviour of the rotor and helped identify the mechanisms driving wake recovery through blade pitch control. However, the effectiveness of these pitch control strategies for enhancing wake recovery within VAWT wind farms has not yet been evaluated.

In the present chapter, the concept of blade pitch control is extended to the context of wake manipulation and energy replenishment in VAWT wind farms. The primary objective is to evaluate the efficacy of these wake recovery strategies and to quantify the overall farm performance with and without blade pitch offsets under wind shear conditions. Both qualitative and quantitative analyses are conducted to compare the effects of different pitch offsets on the farm wake, while quantitative assessments are provided to evaluate the corresponding rotor and farm-level performance.

Parts of this chapter are currently under review in Giri Ajay, A. and De Tavernier, D.: Enhancing wake recovery in vertical-axis wind farms through blade pitching, *Journal of Renewable and Sustainable Energy*, *under review*.



7.1 INTRODUCTION

The wake of vertical-axis wind turbines (VAWTs) has been extensively studied [24, 28, 48, 60, 63, 70, 98, 169], with findings highlighting the enhanced wake recovery enabled by turbulent mixing [21, 92]. More recent work has shown that introducing blade pitch offsets can further accelerate recovery, with improvements of an order of magnitude attributed to the additional advection generated by lateral and vertical blade forces in this configuration [27, 98, 183]. Chapter 5 of this thesis also demonstrated how wake recovery differs between H-Rotor and X-Rotor geometries. However, these effects have so far been examined only for isolated turbines under uniform inflow, limiting their applicability to more realistic conditions, such as wind shear and turbulence in the flowfield.

Gharaati et al. [95] conducted an LES study comparing VAWT wind farms composed of straight-bladed H-Rotors and helical rotors, demonstrating that the latter yielded higher mean farm power production. A follow-up study by Gharaati et al. [184] showed that the highly three-dimensional wakes generated by helical rotors enhanced turbulent transition, thereby improving overall wind-farm performance. However, these investigations did not account for advection effects introduced by blade pitch offsets. In this regard, Huang [83] performed a URANS study on three inline H-Rotor turbines under uniform inflow, reporting substantial increases of 35–45% in total power output when operating with fixed pitch offsets. Their results also revealed that ground effects strongly influenced wake topology and recovery, while raising concerns that advected wakes could negatively impact neighbouring turbine rows. This issue was first confirmed experimentally by Bensason et al. [96] in a 3×3 grid of scaled H-Rotor turbines, where pitched cases showed wake interactions with adjacent rows but still delivered significant increases in farm power compared to the unpitched baseline. Complementing these findings, Mendoza and Goude [71] investigated the wake recovery of VAWTs under sheared inflow conditions, highlighting how turbulence transition driven by terrain roughness alters wake topology and mixing, with direct implications for recovery.

Therefore, this chapter investigates the wake recovery process of VAWT wind farms with fixed blade pitch under sheared inflow conditions. The study employs an H-Rotor turbine modelled with the ALM in *turbinesFoam*. Both qualitative and quantitative analyses of the wake are presented, together with turbine-wise power and thrust results. In addition, overall farm-level performance metrics are evaluated for all simulated cases.

7.2 METHODOLOGY

In this section, the test cases and the layout of the wind farm used in this chapter will be presented with details on the geometry parameters in Section 7.2.1. Additionally, the numerical setup used to simulate all the test cases, along with the initial and boundary conditions are provided in Section 7.2.2.

7.2.1 TEST CASES AND WIND FARM LAYOUT

In this chapter, simulations are conducted on 3-bladed H-Rotor turbines arranged with an inline spacing of $5D$ and a lateral spacing of $3D$, where D denotes the rotor diameter. The spacing is selected to maintain consistency with the setup of Bensason et al. [96]. Only a single row of turbines is explicitly simulated, while adjacent rows, laterally offset by $3D$,

are represented using cyclic boundary conditions, as detailed in Section 7.2.2. A visual representation of the domain is illustrated in Figure 7.1.

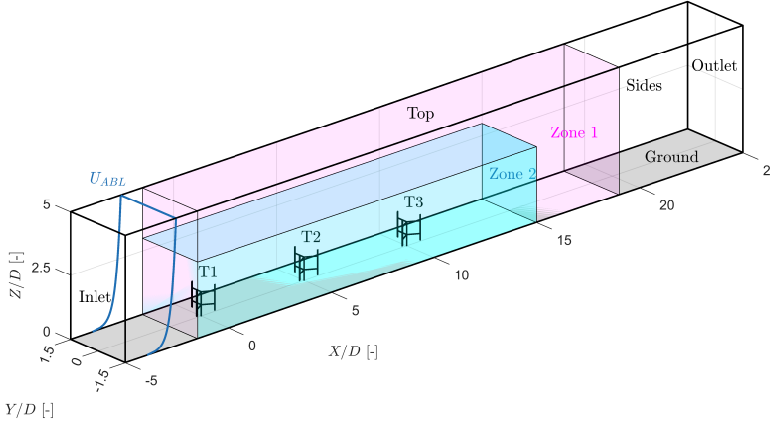


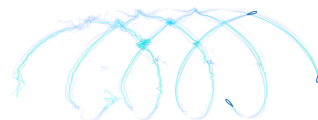
Figure 7.1: Illustration of the computational domain setup and the layout of the wind farm test case. The inflow comes from the bottom left to the top right. The wind farm consists of 3 H-Rotors (T1, T2 and T3) inline of each other with infinite sets of these represented by the cyclic boundary condition of the sides. The magenta and cyan control volumes represent the zones of refinement in the domain, elaborated in Section 7.2.2.

The H-Rotor turbine geometry follows the design of Huang [83]. The turbine has three straight blades with a rotor diameter of $D = 160$ m and an aspect ratio of $AR = 1$, operating at a rated power of 8 MW. Each blade has a chord length of $c = 4$ m and employs a NACA0021 airfoil profile. The airfoil polars are generated using XFOIL [137] at a Reynolds number of $Re = 15 \times 10^6$. The model employs the use of the Goude flow curvature model [134] and no dynamic stall model, as we observed that the wake is not sensitive to the dynamic stall in Chapter 6. The center of the rotor frontal area is positioned 110 m above the ground, providing sufficient clearance between the ground and the blade tips. The turbine is designed to operate at a tip-speed ratio of $\lambda = 4.5$, to follow the setup used by Huang [83]. Three turbines, T1, T2, and T3, are synchronously controlled, ensuring identical operating parameters across all machines. As T2 and T3 operate in the wake of T1, all turbines are set to operate at the same RPM instead of the same tip-speed ratio. Collective blade pitch of $\beta = -10^\circ$, 0° , and 10° are applied to assess wake deflection effects, consistent with the analyses in Chapter 5.

7.2.2 MODEL SETUP

The present study combines the *turbinesFoam* library [110] with *OpenFOAM-v2306* [111]. In actuator line models (ALM), the thrust T and blade loading are preserved through the parameter ϵ/Δ_{grid} , where Δ_{grid} is the local grid size [108]. Based on the tests described in Appendix E, a regularisation kernel size of $\epsilon/\Delta_{grid} = 2$ was selected for the H-Rotor turbine.

In this study, the inflow is modelled as incompressible and Newtonian, with a density of $\rho = 1.225 \text{ kg m}^{-3}$ and a kinematic viscosity of $\nu = 1.5 \text{ ms}^{-2}$. The wake is captured



using the Unsteady Reynolds-Averaged Navier–Stokes (URANS) equations implemented in the *pimpleFoam* solver, together with the k - ϵ turbulence closure model [163]. The computational domain extends from $-5D$ upstream to $25D$ downstream, where D is the rotor diameter. Laterally, the domain spans $-1.5D$ to $1.5D$, and vertically from $0D$ to $5D$. The domain lengths are consistent with the recommendations of Rezaeiha et al. [50]. Within this domain, a refined mesh region (Zone 2) with a resolution of $D/40$ covers $-1.5D$ to $15D$ in the streamwise direction, $-1.5D$ to $1.5D$ laterally, and $0D$ to $3D$ vertically. This region is embedded within a coarser mesh zone (Zone 1) with a resolution of $D/20$, extending from $-1.5D$ to $11D$ streamwise, $-1.5D$ to $1.5D$ laterally, and $0D$ to $5D$ vertically. Choosing a domain of this size is a compromise between computational time and accuracy, as our current setup results in a blockage ratio of $1/15$. This limitation can artificially inflate the power output of the turbines by roughly 15%, based on the work of Garrett and Cummins [185]. It is to be noted that this would apply for all the turbines, thereby maintaining the relative differences in power, which is explored in detail in Section 7.3.5.

The *atmosphericModels* library in OpenFOAM v2306 [186] is used to model the atmospheric boundary layer (ABL). The inlet mean streamwise velocity U is defined using a logarithmic profile, following Mendoza [187]. The roughness length is set to $z_0 = 10^{-4}$ m, typical of offshore conditions [188], and the reference velocity $U_\infty = 10 \text{ ms}^{-1}$ is specified at the rotor centre height Z_c . The inflow also includes a constant turbulence intensity of $TI = 8\%$, consistent with offshore measurements [189]. The boundary conditions for velocity U , pressure p , turbulence kinetic energy k , turbulence dissipation ϵ , and eddy viscosity ν_T are summarised in Table 7.1, with further details available in the OpenFOAM v2106 documentation [111]. Default constants are used unless otherwise stated, e.g., $\kappa = 0.41$ and $C_\mu = 0.09$. To account for the influence of other rows of turbines, *cyclic* boundary conditions are applied at the lateral sides. This allows the flow exiting the domain on one side to re-enter on the opposite side, replicating the effect of a co-rotating set of turbines spaced $3D$ from the simulated rotor centre. While a *zeroGradient* boundary condition was applied to the top boundary for the velocity, it is acknowledged that this does not strictly enforce the natural shear of an ABL inlet at that height.

Table 7.1: Boundary conditions used for the simulation cases immersed in ABL. *atmBoundaryLayer* and *WallFunction* are abbreviated as *ABL* and *WF*. For instance, *ABLInletVelocity* stands for *atmBoundaryLayerInletVelocity*.

	Inlet	Outlet	Ground	Top	Sides
U	<i>ABLInletVelocity</i>	<i>inletOutlet</i>	<i>noSlip</i>	<i>zeroGradient</i>	<i>cyclic</i>
p	<i>zeroGradient</i>	<i>uniformFixedValue</i>	<i>zeroGradient</i>	<i>zeroGradient</i>	<i>cyclic</i>
k	<i>uniformFixedValue</i>	<i>inletOutlet</i>	<i>kqRWF</i>	<i>zeroGradient</i>	<i>cyclic</i>
ϵ	<i>fixedValue</i>	<i>inletOutlet</i>	<i>epsilonWF</i>	<i>zeroGradient</i>	<i>cyclic</i>
ν_T	<i>calculated</i>	<i>calculated</i>	<i>atmNutmWF</i>	<i>zeroGradient</i>	<i>cyclic</i>

7.3 RESULTS

In this section, the results from the simulations are discussed in detail. First, qualitative results are discussed to understand the wake topology and the vorticity system of the windfarm in Section 7.3.1. Later, quantitative wake results are described and analysed to

understand the wake recovery between different pitch cases in Section 7.3.2, Section 7.3.3, and Section 7.3.4. Finally, turbine and farm wide performance are discussed for each pitch case, describing the effects of the pitch on turbine power and thrust, and power density in the farm in Section 7.3.5.

7.3.1 WAKE TOPOLOGY AND VORTICITY SYSTEM

To understand the flowfield, the time-averaged normalised streamwise velocity u/U_∞ and vorticity $\bar{\omega}_x D/U_\infty$ contours for the wind farm are presented in Figure 7.2 and Figure 7.3, respectively. The cross-stream slices are selected such that for each downstream rotor there are two planes located $2D$ and $4D$ downstream. The contour of the turbulence intensity TI is provided in Appendix I.

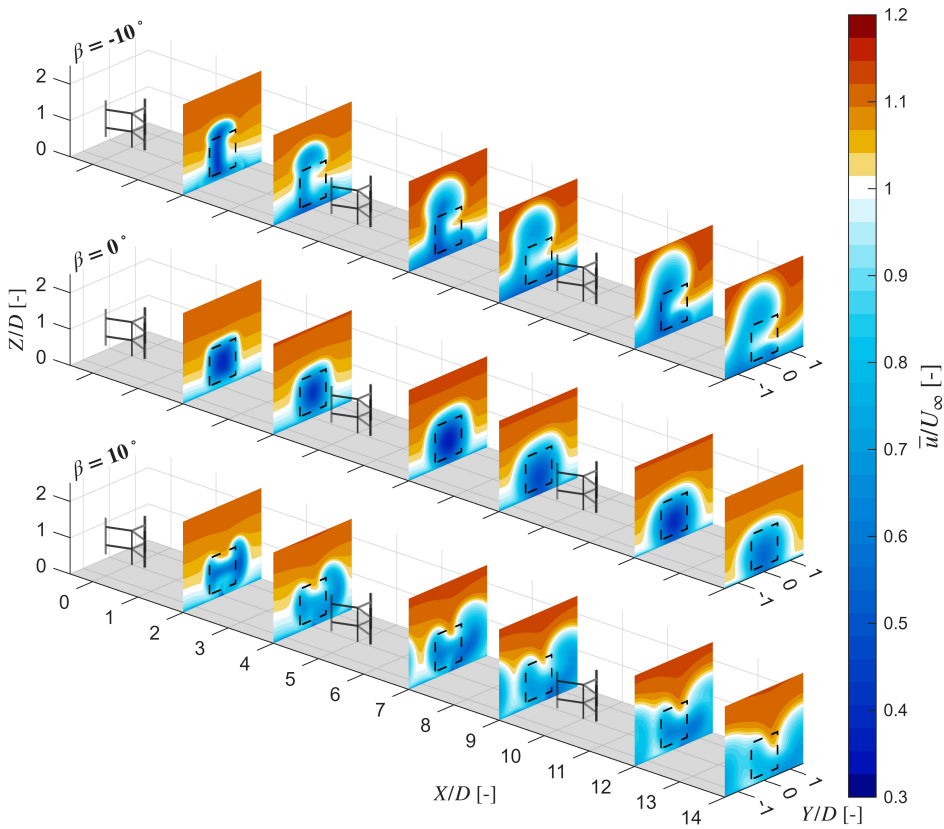
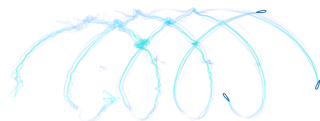


Figure 7.2: The normalised streamwise velocity \bar{u}/U_∞ contours for the windfarm at several downstream planes for blade pitch settings $\beta = -10^\circ, 0^\circ$ and 10° . The white in the colourmap indicates reference velocity U_∞ . The streamwise axis is magnified to improve visibility.

In the baseline case, the wake closely follows the projected frontal area of the rotor. The velocity is lowest at the rotor center, despite the sheared inflow, due to the stronger blade forces at mid-span relative to the tips, which is linked to the tip-vortices. As the wake



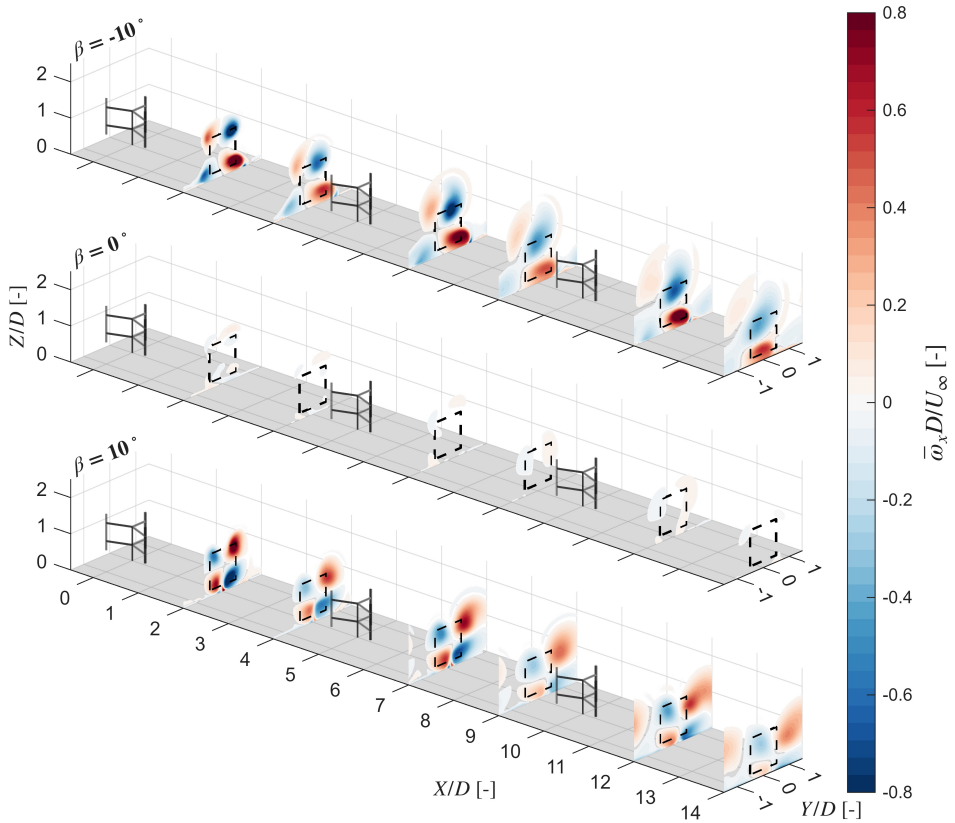


Figure 7.3: The normalised streamwise vorticity $\bar{\omega}_x D/U_\infty$ contours for the windfarm at several downstream planes for blade pitch settings $\beta = -10^\circ, 0^\circ$ and 10° . The black dashed line corresponds to the projected frontal area of the rotor on the plane. To improve visibility, streamwise axis is magnified and vorticity between -0.015 and 0.015 are removed from the plot. The vortices for $\beta = 0^\circ$ are one order lower in magnitude in comparison to the pitched cases.

expands downstream, diffusion becomes apparent, but there is no noticeable advection because the tip-vortices are weak. At $X/D = 4$, the velocity deficit is lower than at $X/D = 2$, indicating that turbulence dominates wake recovery at this location. Behind the second rotor at $X/D = 7$, a region of velocity deficit is observed again, although the wake shape is strongly influenced by the first turbine. The wake remains largely undisturbed by advection, and by $X/D = 9$, the velocity deficit decreases further, confirming that turbulence governs wake recovery in these regions. This trend continues with the third turbine, where the deficit at $X/D = 14$ is lower. Across all these planes, there is minimal influence from adjacent rotor wakes, as wake advection is weak in this configuration.

For $\beta = -10^\circ$, the strong windward tip-vortices cause significant advection of the wake. The wake is ejected vertically out of the rotor area, while high-energy flow is laterally brought into the rotor on the windward side. A smaller wake ejection is also observed from the leeward side. Overall, the velocity deficit in most planes is lower than in the

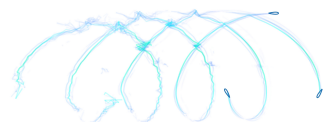
baseline case, as the streamwise thrust is partially redirected laterally due to the pitch offset. Unlike in Chapter 5, the ground and sheared inflow create an asymmetry between the upper and lower tip vortices, affecting the flow flux across the rotor area. At $X/D = 4$, the upper windward section experiences an influx of high-energy flow, whereas the lower windward section remains mostly low-energy. By $X/D = 7$, the wake retains much of the upstream shape, but the velocity deficit is reduced compared to $X/D = 2$, indicating turbulence-driven dissipation. The tip-vortices of the second turbine enhance advection, ejecting the wake further vertically and bringing high-energy flow down to rotor level. This also allows some flow from the adjacent turbine row to enter the plane near $Y/D = 1.5$, which becomes more pronounced at $X/D = 9$, although it does not significantly affect the inline wake. Simultaneously, the wake and tip-vortices diffuse and dissipate, slightly reducing high-energy flow in the rotor area. The windward tip-vortices appear to advect toward the leeward side, with the upper tip-vortex moving more than the lower, similar to the H-Rotor wake dynamics in Chapter 5. At $X/D = 12$ and 14, the leeward tip-vortices of the third turbine are weaker than the windward ones, slightly altering the wake shape on the leeward side. Consequently, the wake begins to exit the plane on the leeward side, potentially impacting the adjacent turbine row, while inflow from the right-adjacent row primarily affects the lower windward portion of the rotor, leaving most of the rotor area unaffected.

At $\beta = 10^\circ$, the vortex system is reversed compared to the -10° case, with windward vortices still dominating. As in Chapter 5, the wake is ejected laterally while high-energy flow is brought in vertically. However, due to vertical asymmetry, the lower half of the rotor contributes little to the high-energy inflow. The windward-upper section ejects more of the wake than the lower section, particularly evident from $X/D = 4$ downstream. Overall, the wake deficit in a majority of the planes is lower than in the baseline case, similar to $\beta = -10^\circ$. At $X/D = 4$, the windward-ejected wake reaches the edge of the plane as the tip-vortices shift windward. By $X/D = 7$, the wake downstream of the second rotor partially exits the plane at $Y/D = 1.5$, while inflow from the adjacent turbine row enters at $Y/D = -1.5$. At $X/D = 9$, the adjacent row interacts with the leeward wake, but turbulence-induced vortex dissipation limits its effect on the rotor area. Further downstream, at $X/D = 12$ and 14, the wake of the adjacent row merges with the third turbine's leeward wake due to interaction between leeward and advected tip-vortices, pushing the wake vertically upward. Consequently, the downward advection of high-energy flow becomes localized to the windward edge of the rotor, while vortex strengths weaken compared to $X/D = 2$ and 7 due to cumulative turbulence from all three turbines. Unlike the $\beta = -10^\circ$ case, the lower tip-vortices contribute minimally to wake dynamics.

Overall, the wake dynamics are influenced by the atmospheric boundary layer generated by the first turbine. The impact of adjacent turbines on the wake is only significant when the blade pitch configuration causes lateral deflection of the wake.

7.3.2 WAKE CENTER DEFLECTION

To quantify the effects observed in Section 7.3.1, we first look at the deflection of the wake center which is a popular method to analyse the wake. Similar to Chapter 5, we employ a "center of mass" approach to identify the wake center deflection. Unlike in Chapter 5, as the wakes inherently have asymmetry in both lateral and vertical directions due to the



wind shear, we use the existing formulation of this approach [13, 27, 173–175]. Therefore, the lateral and vertical wake center deflections, y_c and z_c respectively, can be evaluated using Equation 7.1.

$$y_c(X) = \frac{\iint y \Delta U(x, y, z) dy dz}{\iint \Delta U(x, y, z) dy dz}, \quad \text{and}$$

$$z_c(X) = \frac{\iint z \Delta U(x, y, z) dy dz}{\iint \Delta U(x, y, z) dy dz}, \quad (7.1)$$

where y and z is the spatial data, $\Delta U(x, y, z) = U_\infty - \bar{u}(x, y, z)$, \bar{u} is the time-averaged velocity and U_∞ is the reference velocity and the discrete surface integration is done over the entire cross-section slice of the domain at each discrete streamwise locations.

The wake deflection is presented in Figure 7.4 for both the lateral and vertical directions for all three pitch configurations.

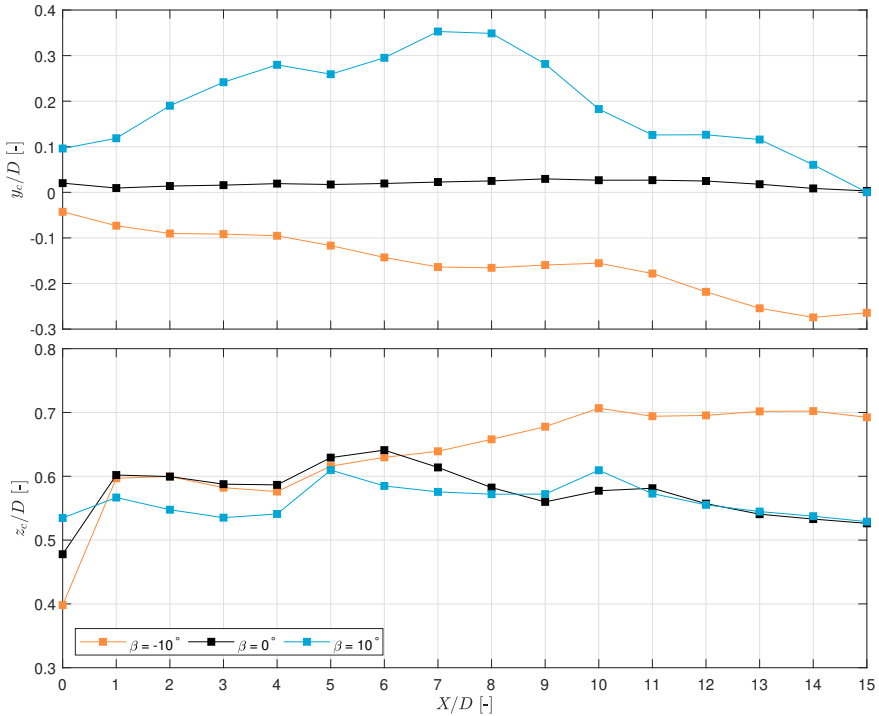


Figure 7.4: The wake center deflection in the lateral (y_c/D) and vertical (z_c/D) directions. Orange, black, and cyan indicate pitch offsets of $\beta = -10^\circ, 0^\circ, 10^\circ$ respectively.

The reference positions in the lateral and vertical directions are $y_c/D = 0$ and $z_c/D = 0.5$, corresponding to the rotor center. In the baseline case, the wake center exhibits minimal lateral movement, reaching only $y_c/D = 0.03$ at $X/D = 9$, owing to the weak streamwise tip-vortices generated at this pitch, as observed in Figure 7.2. At $X/D = 0$, the wake already shows a small deflection due to the forces from the upwind half of the rotor. Lateral stability

is largely compensated by vertical displacement: immediately downstream of the rotor, the wake center shifts slightly above the rotor center. This upward displacement is attributed to the spanwise distribution of blade loads, with lower energy near the ground resulting in weaker forces in the bottom half of the rotor. Beyond $X/D = 5$, the second rotor induces a further slight upward shift of the wake, again reflecting the rotor's load profile. As the wake dissipates downstream, the center gradually returns toward the rotor axis around $X/D = 9$, with a similar pattern observed further downstream due to the influence of the third rotor.

For $\beta = -10^\circ$, the wake center shifts laterally toward the leeward side. Around $X/D = 2-3$, the lateral deflection stabilizes at $y_c/D = -0.1$, but increases beyond $X/D = 5$ due to the tip-vortices of the second rotor, reaching $y_c/D = -0.17$ at $X/D = 8$. Further downstream, the third rotor causes additional leeward shift, with the maximum lateral deflection of $y_c/D = -0.28$ at $X/D = 14$, before slightly returning toward the windward side due to the wake from the adjacent turbine entering the plane. Vertically, the wake center begins below the rotor axis at $X/D = 0$, reflecting the spanwise distribution of blade forces from the upwind half. Between $X/D = 1$ and 4, it rises to $z_c/D = 0.6$, and is further shifted upward by the second rotor's tip-vortices to $z_c/D = 0.7$ at $X/D = 10$. Beyond this, the vertical position plateaus around $z_c/D = 0.7$, as the velocity deficit in the wake of the third rotor counteracts vertical advection despite its visual presence in Figure 7.2.

At $\beta = 10^\circ$, the wake center exhibits a pronounced lateral deflection toward the windward side, reaching a local peak of $y_c/D = 0.28$ at $X/D = 4$. The tip-vortices of the second rotor further advect the wake, shifting the center laterally to a maximum of $y_c/D = 0.36$ at $X/D = 7$. Downstream of this, the wake gradually moves back toward the rotor center, coinciding with it at $X/D = 15$, largely due to the influence of adjacent rotors. The wake from the neighboring turbine enters the plane on the leeward side, inducing a slight leeward shift. Vertically, the wake center shows minimal deflection, with minor movement concentrated near the rotor locations, otherwise remaining close to the rotor center.

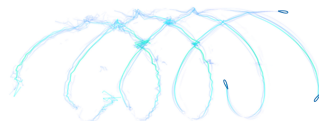
Overall, the $\beta = 10^\circ$ case exhibits the maximum lateral deflection of the wake, although its benefits for wake recovery are partially offset by the influence of adjacent turbines. In the $\beta = -10^\circ$ case, the wake center shows a consistent vertical deflection, reaching its peak only at far downstream locations. Despite these differences, both pitch-offset cases demonstrate a notable improvement over the baseline, making them significant for further analysis.

7.3.3 AVAILABLE POWER

To further quantify the effectiveness of these configurations in replenishing energy within the wake, the available power (AP) in the flowfield is considered using a hypothetical downstream turbine (HDT). Similar to the analysis in Chapter 5, the coefficient of AP at a specific point in the domain (x_0, y_0, z_0) can be calculated as shown by Equation 7.2.

$$C_{AP}(x_0, y_0, z_0) = \frac{1}{A} \iint_S \frac{\bar{u}^3(x_0, y, z)}{U_\infty^3} dy dz \quad (7.2)$$

Here, C_{AP} denotes the coefficient of available power, defined as \bar{u}^3/U_∞^3 , where U_∞ is the freestream velocity and \bar{u} is the time-averaged streamwise velocity component. The HDT's frontal area is represented by A , and the integration surface S corresponds to the region



enveloped within A . The inline available power in the wake of the turbines at discrete downstream locations is presented in Figure 7.5.

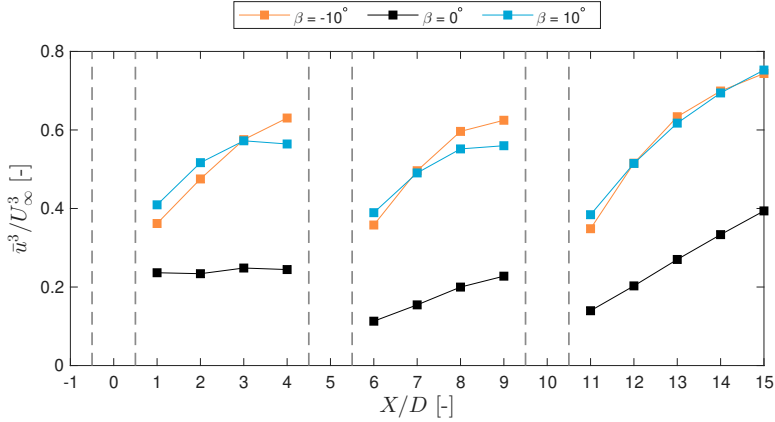


Figure 7.5: The inline available power C_{AP} of the H-Rotor wind farm. The grey dashed lines correspond to the boundaries of the swept volumes of the rotors and AP is not evaluated at these locations. Orange, black, and cyan indicate pitch offsets of $\beta = -10^\circ, 0^\circ, 10^\circ$ respectively.

For the baseline case, downstream of the first rotor, the coefficient of available power (C_{AP}) is 0.24 at $X/D = 1$, with a slight increase to 0.25 around $X/D = 3 - 4$. This rise is attributed to turbulent dissipation in the wake, as there is insignificant flow advection. Immediately downstream of the second turbine at $X/D = 6$, C_{AP} drops to 0.11 due to energy extraction by the rotor. The wake then recovers, reaching $C_{AP} = 0.23$ at $X/D = 9$, aided by increased turbulence intensity from the second rotor and residual turbulence in the wake. A similar trend is observed behind the third rotor, where C_{AP} rises from 0.14 to 0.4 between $X/D = 11$ and 15, reflecting further wake recovery driven primarily by enhanced turbulence, as advection remains minimal.

For $\beta = -10^\circ$, the C_{AP} is higher than the baseline at all downstream locations, due to the combined effects of strong advection and turbulent dissipation. The rate of increase in C_{AP} is also higher, rising from 0.36 at $X/D = 1$ to 0.63 at $X/D = 4$, corresponding to a 2.5 times increase in available power for the second rotor. Downstream of the second rotor, C_{AP} ranges from 0.36 to 0.62 between $X/D = 6$ and 9, reflecting a similar increase for the third turbine. Beyond the third rotor, the rate of C_{AP} increase is slightly higher than in the previous segments, rising from 0.35 to 0.74 between $X/D = 11$ and 15. This enhanced recovery is likely due to the combined effect of advection and turbulence, with turbulence contributing more significantly in this region.

For $\beta = 10^\circ$, the C_{AP} is consistently higher than the baseline at all locations. Comparing it to the $\beta = -10^\circ$ case provides further insight. At $X/D = 1$, C_{AP} is slightly higher at 0.41, due to the rotor thrust, as the velocity deficits in the wake are larger for $\beta = -10^\circ$. However, a crossover occurs by $X/D = 3$, and at $X/D = 4$, C_{AP} for the current case drops below the $\beta = -10^\circ$ value, reaching 0.56. This is likely caused by the induction of the second rotor. For $\beta = -10^\circ$, the rotor load is redistributed towards the downwind half, whereas the $\beta = 10^\circ$ configuration favours the upwind half. Consequently, the induction effect at $X/D = 4$ is

stronger in the current pitch case due to the higher influence of the upwind rotor loads. Downstream of the second rotor, a similar trend is observed: the current pitch case shows a higher C_{AP} of 0.39 in the near-wake, but beyond a crossover point further downstream, C_{AP} becomes lower than that of $\beta = -10^\circ$, with a value of 0.56 at $X/D = 9$. Similar patterns are seen downstream of the third rotor, where C_{AP} rises from 0.38 at $X/D = 11$ to 0.75 at $X/D = 15$. As in the $\beta = -10^\circ$ case, the rate of increase in available power is higher downstream of the third turbine due to the dominant contribution of turbulence to wake recovery. It is also noteworthy that C_{AP} values for the two pitched cases remain close downstream of the third turbine, indicating minimal influence of the advected wake from adjacent turbine rows at this stage. However, beyond $X/D = 15$, it is likely that the inline C_{AP} for the current pitch case may decrease slightly due to interaction with wakes from neighbouring turbines. This could not be verified within the present simulation domain, but it highlights a potential area for future investigation.

Overall, the pitched cases outperform the baseline in terms of higher available power (AP) both inline and downstream of the rotor. As expected, the inline AP values in this study are lower than those reported by Huang [83], primarily due to differences in the inflow as the present simulations employ a sheared velocity profile. Additionally, the higher turbulence near the ground contributes to enhanced wake recovery immediately downstream of the rotor.

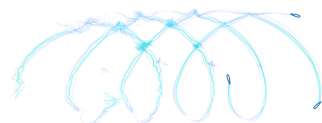
While the inline AP provides a useful measure of the rotor's wake recovery potential, its applicability is largely limited to inline wind-farm arrangements. To assess lateral effects, the AP of a HDT at different lateral offsets is shown in Figure 7.6. The discussion is limited to three downstream locations – $X/D = 3, 8,$ and 13 – so that each HDT is positioned $3D$ downstream of its upstream turbine.

At $X/D = 3$, the baseline case exhibits the lowest AP across most lateral offsets. The $\beta = 10^\circ$ case shows slightly lower AP than the baseline for $y_0/D \geq 0.45$ due to lateral advection of the wake towards the windward side. In contrast, the $\beta = -10^\circ$ configuration produces equal or significantly higher AP than the baseline across nearly the entire lateral range. However, because of leeward wake advection, AP on the leeward side is lower than in the $\beta = 10^\circ$ case, though still above the baseline.

At $X/D = 8$, downstream of the second turbine, a similar pattern is observed with a few notable differences. Near $y_0/D = -0.75$, the baseline case yields higher AP than the $\beta = -10^\circ$ case due to minimal advection in the baseline flow, whereas the leeward-shifted wake reduces AP for the pitched case. The minimum AP location for $\beta = -10^\circ$ has shifted leeward to $y_0/D = -0.42$, while for $\beta = 10^\circ$, windward wake advection positions the minimum AP at $y_0/D = 1$.

Finally, at $X/D = 13$, the baseline case remains lowest in AP across most lateral offsets. Exceptions occur at $y_0/D = -0.75$, where the baseline AP exceeds that of both pitched cases: for $\beta = -10^\circ$ due to leeward wake advection, and for $\beta = 10^\circ$ because of interference from the adjacent row of turbines. In the $\beta = -10^\circ$ configuration, the windward side continues to show the highest AP values, as wakes from adjacent rows do not advect sufficiently towards the rotor center.

Overall, this analysis indicates that the $\beta = -10^\circ$ configuration is the most effective for wind-farm layouts, both for turbines in-line and with lateral offsets. The $\beta = 10^\circ$ case can be advantageous for HDTs positioned at windward offsets; however, at far downstream



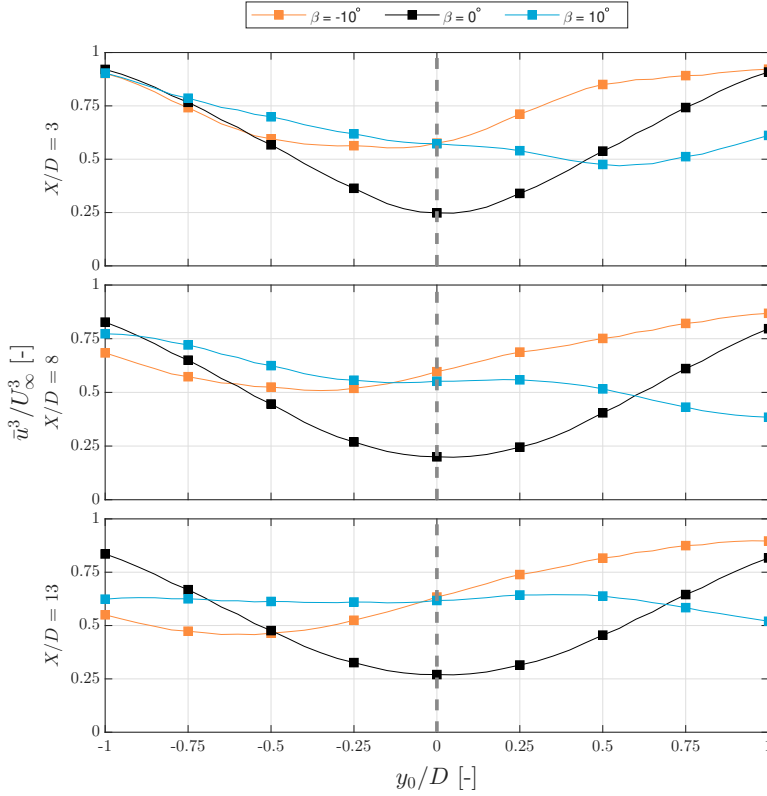


Figure 7.6: The available power C_{AP} for an HDT with a lateral displacement y_0/D at downstream locations $X/D = 3, 8,$ and 13 for all pitch cases. Windward is considered as positive y_0/D . The grey dashed line at $y_0/D = 0$ highlights the results of an HDT that is inline with the original rotor. Orange, black, and cyan indicate pitch offsets of $\beta = -10^\circ, 0^\circ, 10^\circ$ respectively.

locations, the wake advection may negatively impact the performance of these turbines.

7.3.4 MEAN KINETIC ENERGY FLUX

To better understand the replenishment of energy within the wind farm, we analyse the flux of mean kinetic energy (MKE), a method commonly employed by Hezaveh and Bou-Zeid [93], Cortina et al. [179] and Bensason et al. [96]. In Chapter 5, the focus was on overall MKE recovery driven by lateral and vertical advective forces. In the current chapter, we emphasise the streamwise MKE flux and the turbulent kinetic energy (TKE) flux, reflecting the dominance of the streamwise velocity component and the heightened turbulence present in the flowfield. Following Hezaveh and Bou-Zeid [93], the streamwise MKE transport in a wind farm can be expressed as shown in Equation 7.3.

$$\frac{\partial(\frac{1}{2}\bar{u}^3)}{\partial X} = -\frac{\partial(\frac{1}{2}\bar{v}\bar{u}^2)}{\partial Y} - \frac{\partial(\frac{1}{2}\bar{w}\bar{u}^2)}{\partial Z} - \bar{u}\frac{\partial(\overline{u'u'})}{\partial X} - \bar{u}\frac{\partial(\overline{u'v'})}{\partial Y} - \bar{u}\frac{\partial(\overline{u'w'})}{\partial Z} \quad (7.3)$$

In Equation 7.3, the terms with primes represent contributions from turbulent transport,

while the remaining terms correspond to advective contributions to the MKE flux. Following Cortina et al. [179], the flux through a closed control volume can be expressed as the volume integral of these MKE transport terms. Accordingly, and consistent with the approach in Chapter 5, the control volume used in this analysis is illustrated in Figure 7.7. The cross-stream (YZ) planes are omitted here, as the focus is on lateral and vertical fluxes arising from advection and turbulence. The control volume is discretised into four control surfaces, S_1 , S_2 , S_3 , and S_4 . Applying the divergence theorem, as demonstrated by Cortina et al. [179], the volume integrals are converted into surface integrals along the outer contour of the control volume. In this configuration, velocities normal to a surface do not contribute to the flux, allowing the surface flux Q_S to be expressed as in Equation 7.4.

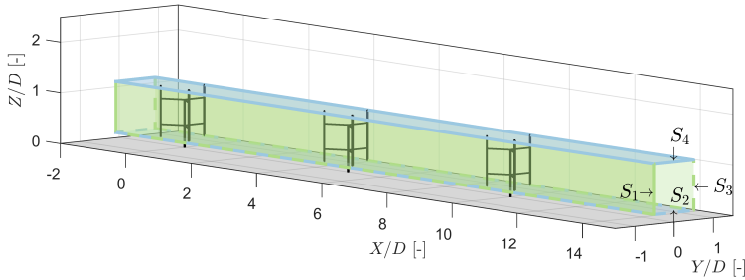


Figure 7.7: Schematic of the control surfaces (S_1 , S_2 , S_3 , S_4) along which the mean KE flux in the flow is evaluated. S_1 and S_3 pass through the lateral extremities of the rotors on the leeward and windward sides, respectively. Meanwhile, S_2 and S_4 pass through the lower blade tips and the upper blade tips, respectively. The fluxes entering the surfaces are considered positive.

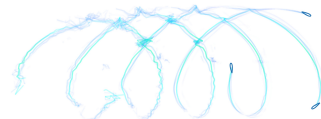
$$Q_S = \iint_S \bar{u} (0.5\bar{u}\bar{u}_i + \overline{u'u'_i}) \hat{n}_i dS \quad (7.4)$$

Here, \hat{n}_i denotes the unit vector normal to the surface S . All fluxes entering the control surfaces are considered positive. To facilitate visualization, the line-integrated advective and turbulent contributions to the MKE flux are presented as functions of the streamwise location in Figures 7.8 and 7.9, respectively.

For the baseline case, advective flux through the surfaces is negligible except at the rotor locations. This aligns with our earlier observation of wake expansion without significant lateral advection. Higher fluxes are seen at the rotors due to the induction effects, which expand the streamtube before settling downstream.

For the negative pitch case, fluxes are observed primarily through S_3 and S_4 . S_3 exhibits a steady influx of MKE from the high energy freestream, peaking at 0.126 just downstream of the second rotor. Through S_4 , there is a consistent outflux of MKE as the wake is ejected by the tip vortices, reaching peaks of 0.1. While smaller than the influx through S_3 , this configuration effectively ejects low-energy flow and draws in high-energy flow.

For the positive pitch case, fluxes are also concentrated through S_3 and S_4 . S_3 shows a consistent outflux of MKE, peaking at 0.07 near the third rotor, reflecting the low MKE



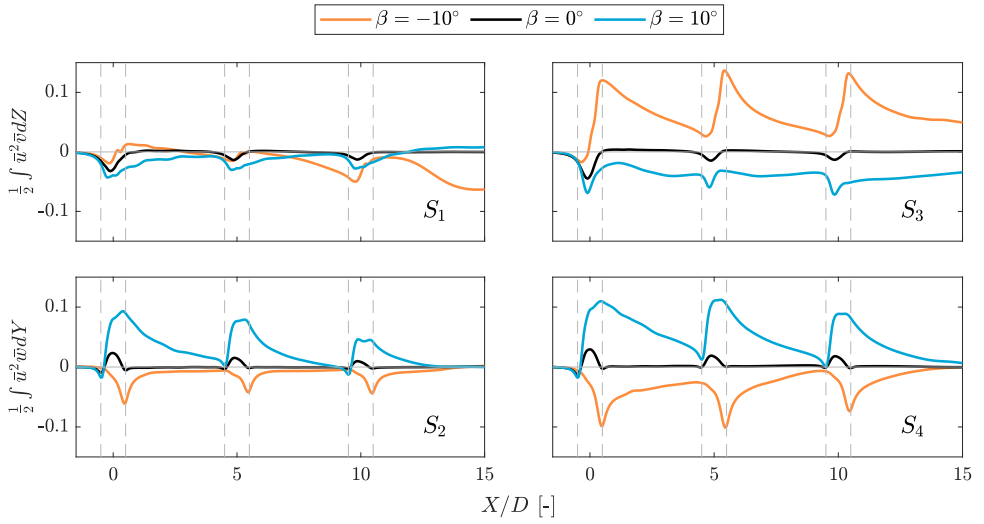


Figure 7.8: Line integrated advective flux of the MKE, integrated along the transverse direction of the control surfaces S_1 , S_2 , S_3 , and S_4 , as a function of the streamwise location X/D . The flux terms are normalised by the term $1/U_\infty^3 D$, where U_∞ is freestream velocity. The grey dashed lines indicates the most upwind and downwind locations of the rotors. The solid grey horizontal line denotes zero flux of mean kinetic energy.

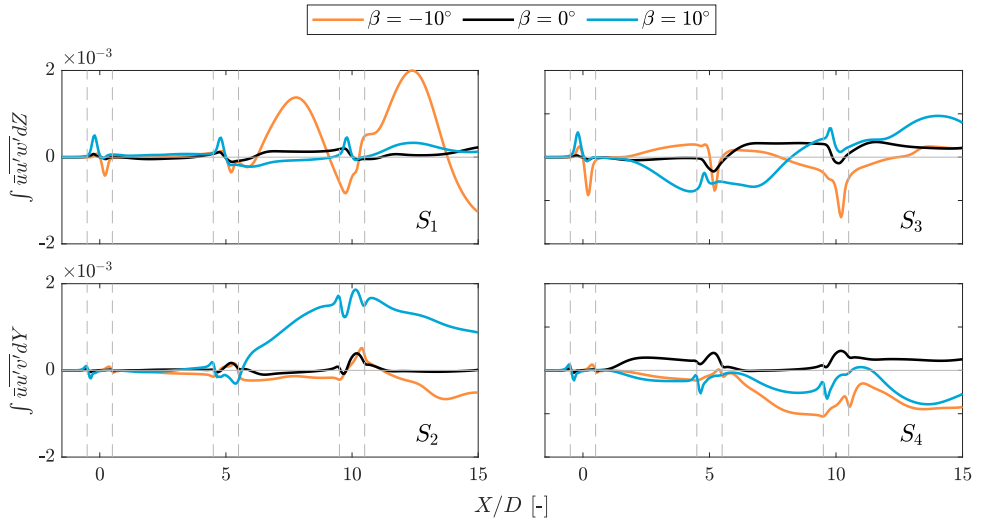


Figure 7.9: Line integrated flux of the turbulent MKE, integrated along the transverse direction of the control surfaces S_1 , S_2 , S_3 , and S_4 , as a function of the streamwise location X/D . The flux terms are normalised by the term $1/U_\infty^3 D$, where U_∞ is freestream velocity. The grey dashed lines indicates the most upwind and downwind locations of the rotors. The solid grey horizontal line denotes zero flux of mean kinetic energy.

in the wake. To compensate, S_4 provides a large influx of high-energy flow, peaking at 0.11. However, this influx is lower downstream of the third rotor, due to the advection of

leeward vortices from adjacent turbine rows.

Although S_2 is close to the ground, both pitch cases show non-negligible fluxes here, unlike the baseline case. Vertical asymmetry limits these fluxes compared to S_4 , with the positive pitch peaking at 0.09 near the first turbine before rapidly diminishing downstream. The negative pitch yields smaller peaks but maintains a more consistent flux across all three turbines. By $X/D = 14$, fluxes at S_2 tend toward zero in all pitch cases due to dissipation of the lower tip vortices.

Turbulent MKE fluxes are consistently two orders of magnitude smaller than advective fluxes. The baseline case shows little flux downstream of the first rotor, increasing steadily behind the second and third rotors. In the pitch cases, S_4 shows consistent MKE outflow, with higher magnitudes for the negative pitch. The most significant turbulent flux contributions appear through S_1 for the negative pitch and S_2 for the positive pitch, peaking downstream of the second rotor. For S_1 , influx increases rapidly due to enhanced mixing from the second rotor, reaching 0.001 at $X/D = 8$, followed by a decrease. A similar pattern occurs downstream of the third rotor. For S_2 , the positive pitch shows increased turbulence production downstream of the second rotor, driving MKE influx near the ground; however, this pattern does not persist past the third rotor, likely due to mixing from adjacent turbine wakes.

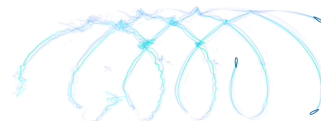
Overall, advection remains the dominant mechanism for replenishing MKE, with both pitch configurations demonstrating a net influx of high-energy flow into the rotor regions.

7.3.5 ROTOR AND FARM PERFORMANCE

In the previous sections, the wind-farm flow features resulting from the blade pitch offsets were analysed both qualitatively and quantitatively. In this section, the focus shifts to rotor- and farm-level performance metrics arising from these flow modifications. Specifically, the power and thrust coefficients of individual turbines C_P and C_T , respectively, as well as the overall farm power density PD_{farm} are presented in Figure 7.10. These parameters are all normalised using the reference velocity U_∞ . The farm power density is calculated by considering the power output of the observed row of turbines along with the two adjacent rows, relative to the total area covered by these turbines.

For the baseline case, the first turbine exhibits high performance with $C_P = 0.51$ and $C_T = 0.7$, closely matching the values reported by Huang [83], with minor differences attributable to the atmospheric boundary layer and the absence of a dynamic stall model in the current study. The second and third turbines, operating fully in the wake of the upstream rotor, show significantly reduced performance, with $C_P = 0.17$ and 0.16, and $C_T = 0.42$ for both turbines. This behaviour aligns with findings from Gharaati et al. [95] and Gharaati et al. [184] using LES simulations for various VAWT geometries. Despite this, the farm still achieves a power density of $PD_{farm} = 20.1 \text{ W m}^{-2}$, above average relative to existing offshore wind farms [190, 191]. It should be noted that this value corresponds to a farm area of $A_{farm} = 1.97 \text{ km}^2$, which is smaller than typical offshore farms, and would likely decrease slightly for larger layouts. Nonetheless, it provides a useful baseline for comparing pitch configurations.

At $\beta = -10^\circ$, the first turbine experiences a modest 9% reduction in power and a 7% increase in thrust relative to the baseline. However, this is more than offset by substantial gains in the downstream turbines, with power increases of 115% and 123% and thrust



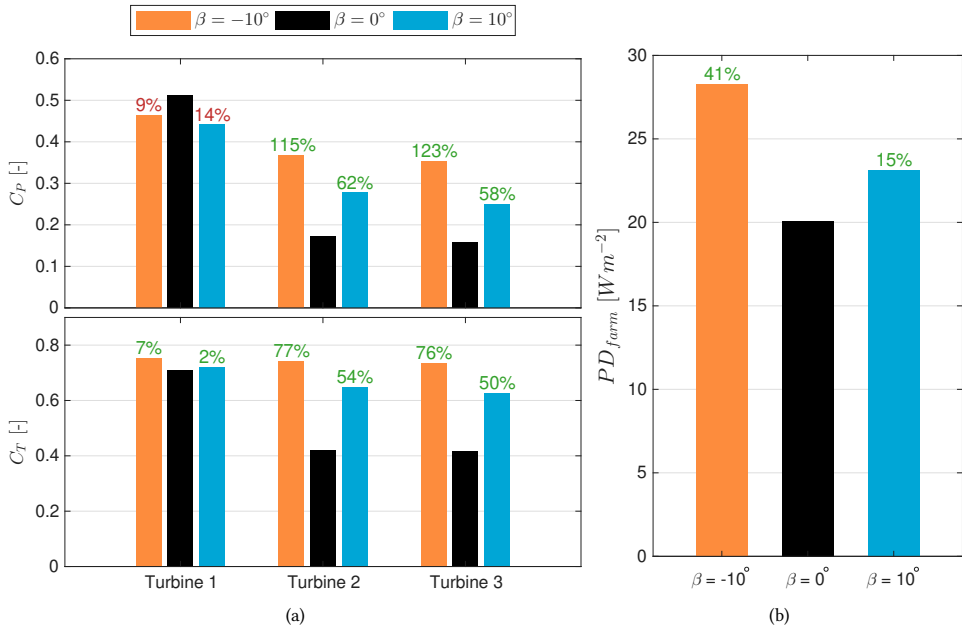


Figure 7.10: (a) The mean power C_p and thrust coefficients C_T for the three inline turbines at different pitch configurations. (b) The wind farm power density (PD_{farm}) for the three pitch configurations. Orange, black, and cyan colours represent the different pitch configurations. The values at the top of the bar represent the percentage gain (green) or loss (red) with respect to the baseline case.

increases of 77% and 76% for the second and third turbines, respectively. Consequently, the farm power density rises by 41% to $PD_{farm} = 28.25 W m^{-2}$, highlighting the effectiveness of this pitch configuration in enhancing overall wind-farm output.

The $\beta = 10^\circ$ configuration exhibits a larger power drop for the first turbine of 14%, with negligible changes in thrust. Gains for the second and third turbines are 62% and 58%, respectively, lower than the $\beta = -10^\circ$ case but still above the baseline. This results in a 15% increase in farm power density to $PD_{farm} = 23.11 W m^{-2}$. While still beneficial, the comparatively smaller gains suggest that a detailed optimisation considering structural, cost, and aerodynamic performance would be needed to determine the most practical configuration for VAWT wind farms.

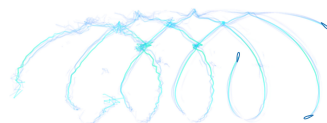
Overall, introducing blade pitch offsets improves wind-farm performance under sheared inflow conditions, significantly increasing farm-wide power output, albeit at the expense of the most upstream turbine's efficiency. It is to be noted that while these results are optimistic, the pitch angles used here are relatively extreme and unlikely to be implemented in practice for large-scale VAWTs due to increased unsteady loading between the upwind and downwind halves of the rotor.

7.4 CONCLUSIONS AND FUTURE EXPANSION

This chapter presents insights and analyses of wake recovery in VAWT wind farms operating with blade pitch control under wind shear. The test case represents a semi-infinite wind farm with lateral and streamwise spacings of $3D$ and $5D$, respectively, simulated using the ALM approach through *turbinesFoam* and *OpenFOAM*. In addition to wake recovery, turbine- and farm-level performance are evaluated for blade pitch offsets of $\beta = -10^\circ, 0^\circ$, and 10° . This study contributes directly to the concept of high power density offshore VAWT wind farms and serves as a proof-of-concept for the wake control strategy employed.

The results indicate that pitch-controlled blades provide a viable wake control mechanism. Pitching the blades inwards generates strong streamwise tip-vortices, enhancing the influx of high-energy flow from above the rotor while laterally ejecting the wake. Conversely, pitching the blades outwards flips the tip-vortices, leading to wake ejection above the rotor. The latter configuration is particularly effective, replenishing more energy in the farm and benefiting adjacent turbine rows. Mean kinetic energy (MKE) analyses confirm that this pitch configuration consistently introduces high-energy flow across all turbines. The presence of wind shear introduces asymmetry between the upper and lower tip-vortices, affecting wake topology, yet favorable gains from pitch control are still observed.

Turbine-level power analysis shows that these wake control strategies reduce the performance of the most upstream turbine, while substantially increasing the power and thrust of downstream turbines. This translates into a significant improvement in overall farm power density with increase of 15% for the pitched-in case and 41% for the pitched-out case compared to the baseline. These findings demonstrate both qualitatively and quantitatively the effectiveness of pitch control as a wake management strategy in VAWT wind farms.



8

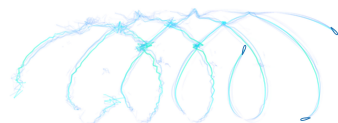
CONCLUSIONS AND FUTURE RECOMMENDATIONS

This dissertation advances the understanding of VAWT aerodynamics in three key areas: (a) it identifies the discrepancies in blade loading predictions among numerical models that emerge when the inherently three-dimensional aerodynamic effects are neglected under operational conditions; (b) it establishes the relationships between rotor geometry and wake dynamics—both with and without wake control strategies—by quantifying wake recovery and energy replenishment resulting from changes in the vortex system; and (c) it assesses the effectiveness of blade pitch-based wake control strategies in large-scale offshore VAWT wind farms subjected to simulated offshore inflow conditions.

The research presented in this thesis was driven by the following questions:

- 1. What level of numerical fidelity is required to model the loads and the near-wake of VAWTs with coned blades?*
- 2. How does rotor geometry influence the wake recovery characteristics of a VAWT in the near- and far-wake?*
- 3. How much does windfarm power density improve by using VAWT pitch control for wake recovery?*

In this chapter, the key findings of the thesis are presented in the context of these questions along with suggestions/recommendations for future work on VAWT modelling.



8.1 KEY FINDINGS

Research Question 1:

What level of numerical fidelity is required to model the loads and the near-wake of VAWTs with coned blades?

Due to the coned blades, the upper and lower blades of the X-Rotor exhibit a downwards and upwards induction, respectively, on the flow in the baseline case with no pitch offset. This results in the low-fidelity models unable to fully capture the loads of the X-Rotor, as they operate independent of the forces acting in the vertical direction. Medium-fidelity models capture the change in loads due to the vertical induction, and the change in loads in the lower blades when the upper blades are pitched.

When introducing pitch offsets, the rotor loads are redistributed to either favour the upwind or the downwind half. In low-fidelity approaches with pitch offsets, the trend of redistributing the load is captured, but it is inaccurate as it is unable to capture the change in vertical induction introduced by the root vortices. Medium-fidelity models reflect the change in vertical induction and also predict the change in load distribution across the upwind and downwind halves, while maintaining a low computational cost. Considering that the regular operational regime of the X-Rotor relies on stall regulation to limit power to its rated value, the forces predicted by 2D models may still provide accurate inputs for design and operational control strategies. However, this lies outside the scope of the present dissertation. Therefore, medium-fidelity models show promise as a viable solution to capture the rotor loads effectively in VAWTs during their operational cycle.

While comparing the near-wake of the scaled X-Rotor (1:100) between medium-fidelity vortex models and experiments, the vortex models effectively represent the flowfield within the X-Rotor volume and in the very near-wake for cases without blade pitch offsets. The model captures the trends and flow features well, although discrepancies in velocity magnitude arise due to the choice of model inputs. However, with blade pitch offsets, the vortex model shows inaccuracy due to uncertainty in the airfoil polars at high angles of attack at the low Reynolds number tested ($Re = 80,000$). Therefore, with pitch offsets, it remains unclear how accurately the vortex model performs, as it is limited by the availability of high-quality airfoil data covering the full range of angles of attack experienced during operation.

Research Question 2:

How does rotor geometry influence the wake recovery characteristics of a VAWT in the near- and far-wake?

The distinct geometries of the H-Rotor and X-Rotor give rise to fundamentally different vortex systems, which in turn influence how each rotor facilitates wake recovery when pitch offsets are applied. In both designs, windward-side vortices play a key role in redirecting the wake. For the H-Rotor, the upper and lower tip vortices operate in a coordinated manner: with positive pitch, they direct the wake laterally outward and draw freestream

vertically into the rotor region, while negative pitch causes the wake to deflect upward and bring freestream laterally inward. The X-Rotor, due to its inherent geometric asymmetry, exhibits stronger wake recovery in the upper half. This is primarily attributed to the greater vortex strength generated by the upper blades compared to the lower ones. Additionally, the difference in circulation near the blade roots generates a root vortex, which interacts with the overall near-wake structure in both pitch configurations. While not as influential as the tip vortices, this root vortex contributes to enhancing wake recovery in the upper part of the rotor wake. This difference results in significantly different wake-recovery levels, which is analysed further.

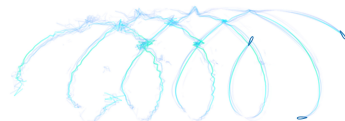
The effect of rotor geometry in both the near- and far-wake is analysed by quantifying the wake recovery. It is found that wake-centre deflection can be a misleading metric for VAWT wakes. This is because the vertical symmetry of the H-Rotor results in zero vertical wake-centre deflection, which makes the metric unsuitable when comparing against the X-Rotor, whose vertical asymmetry leads to measurable vertical deflection. Therefore, a modification to this approach is proposed in this thesis to address this inconsistency. However, even with this modification, the method does not provide insight into the underlying physics driving wake recovery. Analysing the streamwise available power offers this physical insight, as it allows us to distinguish the contributions of lateral and vertical advection as well as turbulent transport. In this thesis, it is shown that, under fixed pitch offsets, wake recovery in the near-wake is dominated by advection, whereas further downstream the turbulent transport terms become dominant. The kinetic energy flux complements the momentum recovery analysis by focusing on the transport of energy across a defined control surface rather than evaluating the entire wake volume. The available power metric also indicates the energy potentially extractable by downstream turbines. Furthermore, this thesis demonstrates the available power for small lateral offsets downstream, which provides insight into the effectiveness of turbine placement strategies – a relevant consideration given the use of staggered layouts in modern HAWT wind farms.

With respect to how the numerical inputs affect the wake, validating this model against the experimental wake results is challenging due to the large uncertainty in the airfoil inputs at these low Reynolds numbers. Moreover, the uncertainty in the inputs is amplified when blade pitch offsets are applied, making the comparison between the ALM and PIV results tedious. Additionally, the flow curvature and regularisation kernel settings also impact the flowfield, indicating that these settings quantitatively affect the wake recovery.

Research Question 3:

How much does windfarm power density improve by using VAWT pitch control for wake recovery?

Windfarm power density improved significantly using blade pitch offset by 15% for the case where the rotor blades are pitched inward and by 41% for the case where the blades are pitched outward. These are primarily due to the advection of the wake, where pitching outward ejects the wake above the rotor while replenishing the MKE in the windfarm through the windward side. The opposite occurs for the case with the blades



pitched in, which results in the wake of adjacent row of turbines interfering the vortex system of the observed turbine row. Therefore, we can conclude that momentum influx is substantially increased with the introduction of pitch offsets, with varying levels of improvement depending on the direction of said offset.

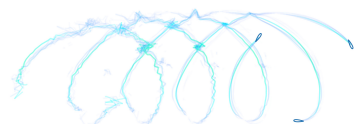
With the introduction of the wind shear, we observed increased vertical asymmetry in the wake of the turbine. This resulted in a change in the vortex topology from studies without wind shear, as the bottom tip-vortices of the blade are less effective at advecting the wake when compared to the upper tip-vortices. Furthermore, the presence of low-energy flow near the bottom of the turbine, due to the sheared inflow, inhibits the replenishment of kinetic energy in this region. As a consequence of the wind shear, the kinetic energy present above the turbine is higher than without the wind shear. This high-energy flow is utilised by the upper tip-vortices to replenish the wake faster than the baseline case from either above or windward into the wake.

8.2 FUTURE RECOMMENDATIONS

Like most research, there are still open issues and room to bridge the gap towards practical implementation of VAWTs and VAWT farms. The following are recommendations for future VAWT research that would follow up the work documented in this dissertation.

- Throughout this dissertation, the focus has been on VAWTs with fixed pitch blade offsets to perform preliminary studies to understand blade force profiles as well as the wake recovery characteristics of multiple turbine geometries. Moving forward, the focus should be shifted towards utilising active pitch profiles for VAWT blades, which can be optimised to achieve a net higher turbine power output while also aiding wake recovery. Furthermore, these profiles can be tuned to also have lower structural fatigue by reducing the unsteadiness on the turbine blade forces. Additionally, these profiles could also be part of a farm-wide control strategy to further improve the power density of the wind farm, without compromising the aforementioned metrics.
- The concept of using pitch control for wake recovery in VAWTs and VAWT farms have been discussed with steady inflow conditions. Implementing dynamic inflow conditions would be the logical next step to lead towards understanding the practical efficacy of pitch control.
- VAWT farm layouts in existing literature as well as this dissertation is very simplistic and idealistic. Therefore, exploring different VAWT farm layouts and the impact of using the pitch control on the wake recovery should be considered for future VAWT farm research. Furthermore, effort must be put into simulating VAWT windfarms with more downstream turbines to allow deeper investigation of inter-row wake interactions in larger wind farms and different farm layouts.
- In this dissertation, a simple wind shear model was used, which does not fully represent realistic atmospheric inflow conditions. Incorporating stratified inflow in future simulations would provide a more accurate estimate of the annual energy production (AEP) impact of pitch-based wake control strategies.

- As turbine geometries and technologies are driven by economical factors, development/utilisation of a cost model tailored for VAWT and VAWT farms would be very valuable to assess the financial implications of using pitch control strategies for wake control.
- Efforts must be made to develop a multi-mega Watt reference VAWT design that would aid in standardising future academic works. Additionally, it simplifies numerical validation, as there would be a good benchmark to refer to. Most importantly, it could heighten collaboration in VAWT research, which has been lacking due to research groups utilising unique geometries.
- Trade-offs must also be considered between operation and maintenance costs along with the aforementioned structural feasibility before implementing these wake control strategies in practice.



A

PARAMETRIC DEFINITION OF THE BLADE GEOMETRY

The upper and lower blade geometries of the full-scale X-Rotor VAWT is provided in Table A.1 and Table A.2, respectively.

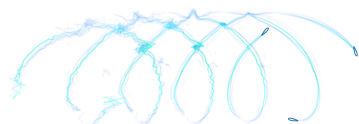
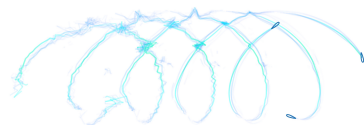


Table A.1: Parametric definition of the upper/top blade. Pitching axis of 0 implies the blade section pitches at the leading edge.

Section	Height (m)	Chord (m)	Radius (m)	Twist (°)	Pitching axis (fraction of chord)	Foil	Reynolds number
1	0.00	10.00	25.00	0.00	0.25	NACA 0025	1.5×10^7
2	5.09	9.71	27.94	0.00	0.26	NACA 0024	1.5×10^7
3	10.19	9.41	30.88	0.00	0.26	NACA 0023	1.5×10^7
4	15.28	9.12	33.82	0.00	0.27	NACA 0022	1.5×10^7
5	20.38	8.82	36.76	0.00	0.28	NACA 0021	1.5×10^7
6	25.47	8.53	39.71	0.00	0.29	NACA 0020	1.5×10^7
7	30.56	8.24	42.65	0.00	0.30	NACA 0019	1.5×10^7
8	35.66	7.94	45.59	0.00	0.31	NACA 0018	1.5×10^7
9	40.75	7.65	48.53	0.00	0.32	NACA 0017	1.5×10^7
10	45.85	7.35	51.47	0.00	0.33	NACA 0016	1.5×10^7
11	50.94	7.06	54.41	0.00	0.34	NACA 0015	1.5×10^7
12	56.04	6.76	57.35	0.00	0.36	NACA 0014	1.5×10^7
13	61.13	6.47	60.29	0.00	0.37	NACA 0013	1.5×10^7
14	66.22	6.18	63.24	0.00	0.39	NACA 0012	1.5×10^7
15	71.32	5.88	66.18	0.00	0.40	NACA 0011	1.5×10^7
16	76.41	5.59	69.12	0.00	0.42	NACA 0010	1.5×10^7
17	81.51	5.29	72.06	0.00	0.47	NACA 0009	1.5×10^7
18	86.60	5.00	75.00	0.00	0.50	NACA 0008	1.5×10^7

Table A.2: Parametric definition of the lower/bottom blade.

Section	Height (m)	Chord (m)	Radius (m)	Twist (°)	Pitching axis (fraction of chord)	Foil	Reynolds number
1	0.00	14.00	25.00	0.00	0.25	NACA 0025	1.5×10^7
2	2.48	13.59	27.94	0.00	0.26	NACA 0024	1.5×10^7
3	4.95	13.18	30.88	0.00	0.26	NACA 0023	1.5×10^7
4	7.43	12.76	33.82	0.00	0.27	NACA 0022	1.5×10^7
5	9.91	12.35	36.76	0.00	0.28	NACA 0021	1.5×10^7
6	12.38	11.94	39.71	0.00	0.29	NACA 0020	1.5×10^7
7	14.86	11.53	42.65	0.00	0.30	NACA 0019	1.5×10^7
8	17.34	11.12	45.59	0.00	0.31	NACA 0018	1.5×10^7
9	19.81	10.71	48.53	0.00	0.32	NACA 0017	1.5×10^7
10	22.29	10.29	51.47	0.00	0.33	NACA 0016	1.5×10^7
11	24.76	9.88	54.41	0.00	0.34	NACA 0015	1.5×10^7
12	27.24	9.47	57.35	0.00	0.36	NACA 0014	1.5×10^7
13	29.72	9.06	60.29	0.00	0.37	NACA 0013	1.5×10^7
14	32.19	8.65	63.24	0.00	0.39	NACA 0012	1.5×10^7
15	34.67	8.24	66.18	0.00	0.40	NACA 0011	1.5×10^7
16	37.15	7.82	69.12	0.00	0.42	NACA 0010	1.5×10^7
17	39.62	7.41	72.06	0.00	0.47	NACA 0009	1.5×10^7
18	42.10	7.00	75.00	0.00	0.50	NACA 0008	1.5×10^7



B

FREE-WAKE VORTEX AZIMUTHAL DISCRETISATION SENSITIVITY

A sensitivity study between 4 different azimuthal discretisations: 36, 60, 72, and 144 for FVM models are conducted for C_p convergence to obtain an azimuth change of 10° , 6° , 5° , and 2.5° per time-step respectively. The results can be viewed in Figure B.1. We found that between 72 and 144, there was only a 0.2% difference in C_p . As the trend shows, finer discretisations would yield less error. However, the 144 discretization case took nearly 3 times longer in computation time than the 72 discretisations case.

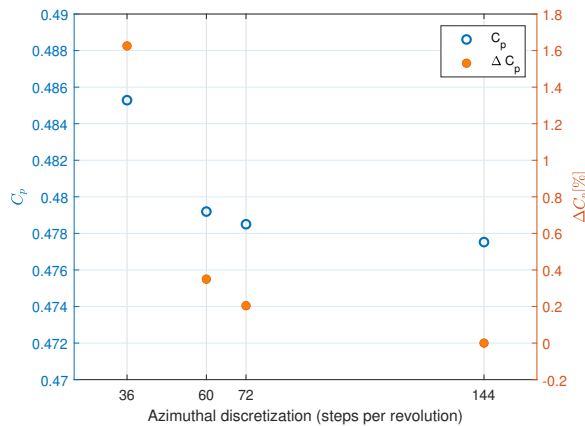
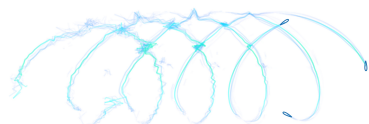


Figure B.1: Azimuthal discretization sensitivity study conducted for FVM for 4 different discretization levels. Y axis on the left shows mean C_p of last revolution from FVM models and the axis on the right shows the percentage error with respect to the power at 144 discretizations.



C

URANS CFD SETUP

Number of cells: 72 million

The mesh background is created using blockMesh. The mesh dimensions are provided in Table C.1.

Table C.1: Simulation domain description

	Minimum [m]	Maximum [m]	Number of cells	Element size [m]
X direction	-400	840	161	7.7
Y direction	-400	400	104	7.7
Z direction	-300	300	78	7.7

The mesh has been created using snappyHexMesh, where three refinement regions have been used:

- Annular disk in the upper blades. Axis (0 0 70) to (0 0 100), radius 90 with inner radius 60.
- Annular disk in the lower blades Axis (0 0 -55) to (0 0 -35), radius 90 with inner radius 60
- Cylinder Axis (0 0 -150) to (0 0 150) radius 200m

With regard to meshing levels, the rotor surface is meshed with a level 8 that leads to a minimum element size of: 0.96 m. The two annular disks are meshed with a level 5 which corresponds to a minimum element size of: 1.54 m. The cylinder is meshed with a level 3 with a minimum element size of: 2.56 m. To account for the boundary layer along the blades, the rotor is meshed with an expansion ratio of 1.2, with a minimum thickness of 1×10^{-8} (to capture the boundary layer, this thickness was necessary to maintain a Y^+ to be less than 1), and with 5 surface layers.

The rotation of the turbine is imposed in the domain using the arbitrary mesh interface (AMI) capability available in OpenFOAM. The boundary condition of the domain is listed in Table C.2.

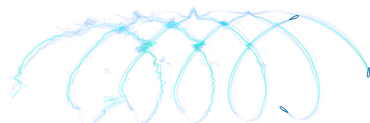


Table C.2: Boundary conditions

Boundary	Location [m]	Type [m]	Velocity condition	Pressure condition
XROTOR	N/A	Wall	movingWallVelocity	zeroGradient
Inlet	X = -400	Patch	freeStream	freeStreamPressure
Outlet	X = 840	Patch	freeStream	freeStreamPressure
Sides	Y = ± 840	N/A	freeStream	freeStreamPressure
Bottom	Z = -300	Wall	freeStream	freeStreamPressure
Top	Z = 300	Patch	freeStream	freeStreamPressure

C

The turbulence model used in the simulations is $k-\omega$ -SST. The baseline setup used the Euler discretization scheme for time and Gauss linear schemes for the gradients. Divergence schemes are Gauss linear Upwind for velocity, Gauss upwind for k , and ω . The Laplacian schemes used are Gauss linear limited corrected. Pressure-velocity coupling is achieved with the PIMPLE equations with 3 outer corrector routines. The under-relaxation factors for velocity and pressure are 0.9.

D

POWERFLOW SETUP

Table D.1: Grid and time-step sizes

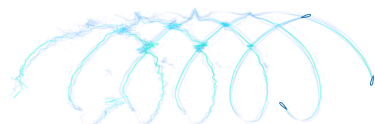
Resolution type	Δx (m)	Cell count	Time-step (s)
Coarse	9.525×10^{-3}	43.2 million	1.439×10^{-5}
Fine	4.76×10^{-3}	291.6 million	7.1942×10^{-6}

The finest cell size is 4.76×10^{-3} , which corresponds to 50 cells per average chord of the secondary rotor blade. The total number of cells and surface elements for this simulation is 291.6 million and 32.3 million respectively. The flow simulation time is 67.63 seconds which is equivalent to 9 primary rotor revolutions requiring 18995 CPU hours per revolution using Linux Xeon® Gold 6148 (500-core Skylake) 2.4GHz Platform.

The simulations conducted are of the primary rotor coupled with the secondary rotor and the tower. The dimensions and the operating condition of the secondary rotor is mentioned in Table D.2. Additionally, the thrust profile for one of the two secondary rotors for the last revolution from the PFLOW calculations is provided in Figure D.1.

Table D.2: Secondary rotor specifications

Number of blades	5
Rotor diameter (<i>m</i>)	9.4
Max C_p	0.27
Rotational velocity (<i>rad/s</i>)	43.275
Center effective wind speed (<i>m/s</i>)	61.2



D

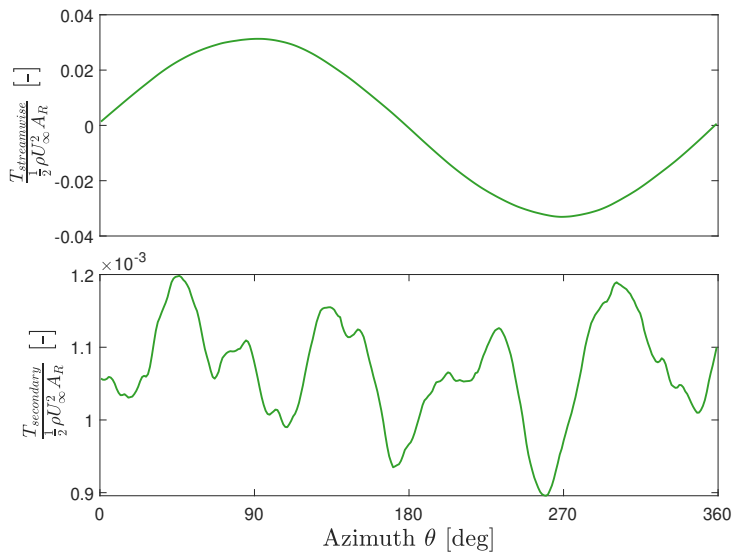


Figure D.1: Thrust of the secondary rotor over the azimuthal cycle of the primary rotor non-dimensionalised by the inflow velocity U_∞ and frontal area A_R of the primary rotor over the last azimuthal cycle of the PFLOW simulation. As the secondary rotor changes orientation at each azimuth, the thrust presented at the top is the drag force of the rotor against the freestream direction of the primary rotor and the bottom figure is the thrust acting along the rotation axis of the secondary rotor.

E

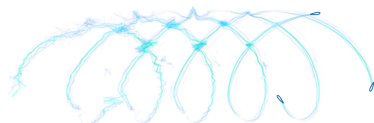
MODIFICATIONS TO TURBINESFoam

E.1 TUNING ϵ/Δ_{grid} FOR OPTIMUM BLADE LOAD REPRESENTATION

To tune the *turbinesFoam* model to give the best representation of the blade loads, we looked at varying the ϵ/Δ_{grid} along with mesh sizes Δ_{grid} . A similar sensitivity study is performed by Sanvito et al. [52] for ALM, while describing a novel velocity sampling method. Figure E.1 shows the variations of normal and tangential forces for the H-Rotor, integrated along the blade span, to ϵ/Δ_{grid} . The predicted forces from the free-wake vortex model CACTUS are also presented as a benchmark to attain with ALM. Comparing the normal forces, we understand that the ALM model variations all fall short of the CACTUS model in the upwind half, but a large spread is observed in the downwind half. With increasing ϵ/Δ_{grid} , the normal loads tend towards CACTUS plots in the upwind half, but overpredict the loads in the downwind half. The tangential force portrays a different story - all the ALM model variations predict larger loads than CACTUS. The difference is exacerbated in the downwind half, where reducing ϵ/Δ_{grid} causes the loads to approach CACTUS loads, while the upwind half does the opposite.

Using these two plots as a reference, $\epsilon/\Delta_{grid} = 2.5$ at a resolution of $D/20$ is the value chosen as it is the average of the two extremes. To capture the turbulence, the mesh resolution is doubled to $D/40$. However, to maintain the same load profiles, the ϵ/Δ_{grid} has to also be doubled, so that the physical value of ϵ remains the same. This is seen in the red lines, where $\epsilon/\Delta_{grid} = 5$ at $D/40$ matches very well with the $\epsilon/\Delta_{grid} = 2.5$ at $D/20$. Therefore, the chosen configuration was a rotor mesh resolution of $D/40$, with $\epsilon/\Delta_{grid} = 5$, which corroborates the results of Sanvito et al. [52].

The X-Rotor has different diameter D as well as chord c , which requires the sensitivity study to be repeated again. However, we set the mesh resolution to be the constraint, as we want to minimise variations between the two rotor simulations setups. Therefore, Figure E.2 shows the variations of normal and tangential forces for the X-Rotor, integrated along the blade span, to ϵ/Δ_{grid} . Here, we can observe that the increase in ϵ/Δ_{grid} leads



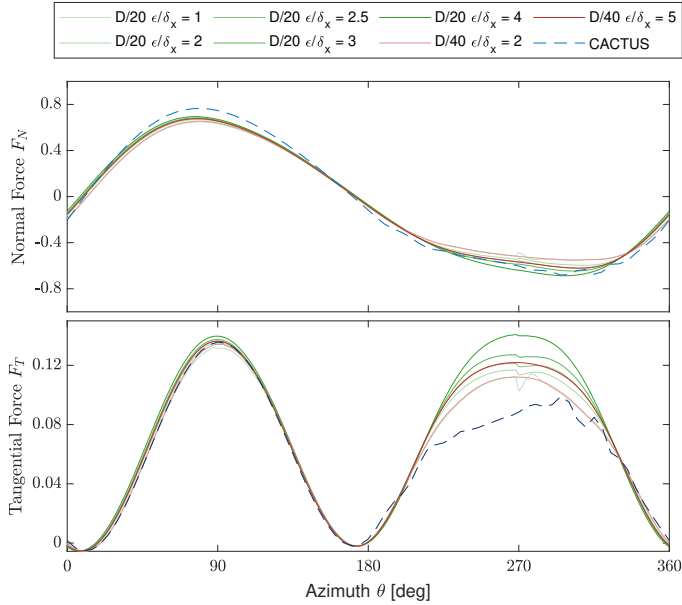


Figure E.1: Normal and tangential force variation of the H-Rotor with ϵ/Δ_{grid} and Δ_{grid} . Increasing opacity indicates increasing ϵ/Δ_{grid} , with the greens associated for grid resolution of D/20 and the red for D/40. The dashed line indicates blade loads from CACTUS. Loads are normalised by $1/(0.5\rho U^2 A)$

to increase in magnitudes of the loads. However, the loads in the upwind half are always underpredicted, while the loads in the downwind half are overpredicted - regardless of the ϵ/Δ_{grid} value. Furthermore, the tangential loads show similar pattern to the H-Rotor - increasing ϵ/Δ_{grid} brings the forces closer to CACTUS in the upwind half, but cause them to be overpredicted by a large amount in the downwind half. The difference in tangential forces is significant, and there is no obvious choice of ϵ/Δ_{grid} to be used in the study. We chose $\epsilon/\Delta_{grid} = 2$ at D/40 for the X-Rotor as this offers good balance in normal loads in the upwind and downwind halves, while not straying too far away from the tangential forces in the upwind half. The tangential forces would mostly affect the torque and the power performance, as the normal loads are not included. Regardless, as the wake of the turbines are characterised by the thrust, the normal load is of primary significance, and the results show variation from CACTUS, which we consider acceptable for this study.

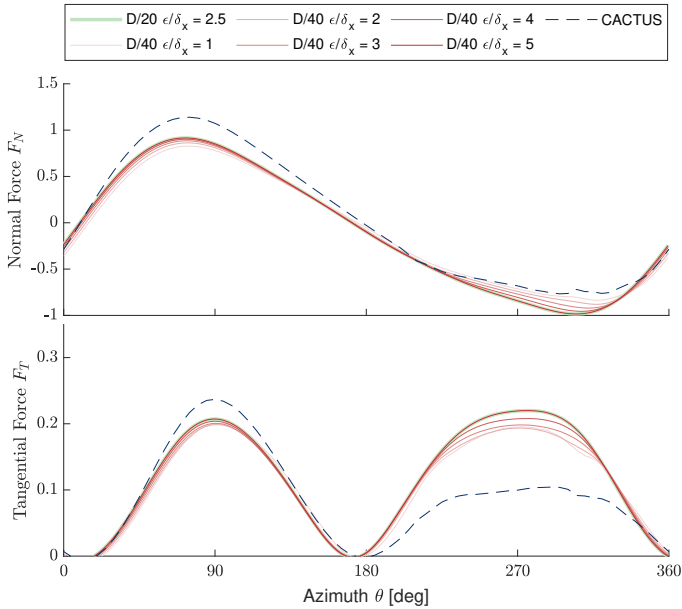
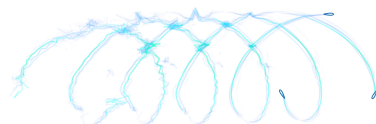


Figure E.2: Normal and tangential force variation of the X-Rotor with ϵ/Δ_{grid} and Δ_{grid} . Increasing opacity indicates increasing ϵ/Δ_{grid} , with the green associated for grid resolution of D/20 and the red for D/40. The dashed line indicates blade loads from CACTUS. Loads are normalised by $1/(0.5\rho U^2 A)$

E

E.2 INCLUSION OF CONE ANGLE

turbinesFoam, in its current published stage, does not accept inputs for the cone angle for rotor blades. Therefore, the model would not allow for the analysis of VAWTs with non-vertical span such as the DeepWind VAWT concept [192], or in this case the X-Rotor VAWT concept [39]. This leads to a false representation of the blade forces in the fluid domain, especially for the X-Rotor with two sets of coned blades. So the input parameters were modified to include a cone angle option. The modification is done after Line 132 in *turbinesFoam/src/fvOptions/crossFlowTurbineALSource/crossFlowTurbineALSource.C/createBlades()* and the modified source code is available on GitHub (Giri Ajay and Simao Ferreira [193]), which houses several branches with the different ϵ/Δ_{grid} values used to analyse the loads and the velocity fields of the rotor.



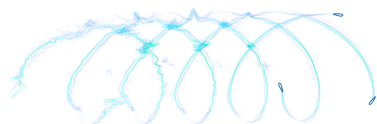
F

WAKE CENTER DEFLECTION

In this instance, we use the conventional approach of the "center of mass" to evaluate the wake center deflection. The wake center deflection is evaluated by:

$$y_c(X) = \frac{\iint y \Delta U(x, y, z) dy dz}{\iint \Delta U(x, y, z) dy dz}, \quad \text{and}$$
$$z_c(X) = \frac{\iint z \Delta U(x, y, z) dy dz}{\iint \Delta U(x, y, z) dy dz}, \quad (\text{F.1})$$

The Figure F.1 shows the wake center deflection for both the rotors at pitch cases $\beta = -10^\circ, 0^\circ, 10^\circ$. We can notice that the lateral deflection is quite evident and is captured well. This reflects that the $\beta = 10^\circ$ shows the highest lateral wake deflection due to the strong windward vortices advecting the wake out laterally. However, we see that the vertical wake center deflection is not captured at all for the H-Rotor. This is due to its symmetric geometry, where the wake is equally expanded/contracted in the vertical direction. The X-Rotor shows some difference, but that is mainly attributed to the difference in the upper and lower blade loads, which cause the values here to be higher. However, not much information can be drawn from this analyses as the vertical deflection of the H-Rotor is missing completely. This makes the results very misleading and leads to non-intuitive results.



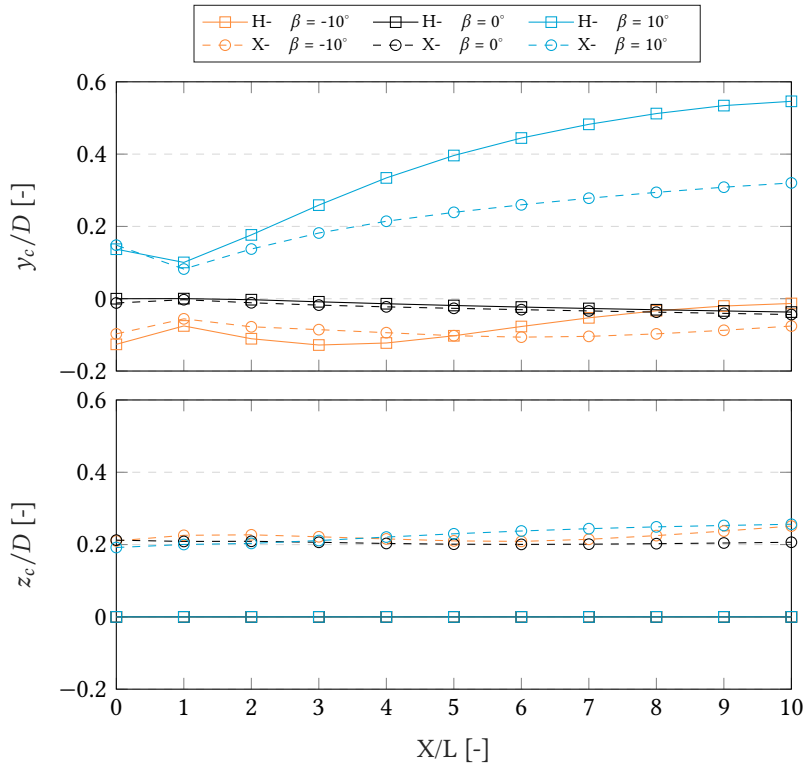
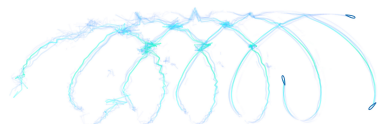


Figure F.1: The wake center displacement in the lateral (y_c/D) and axial (z_c/D) displacements. Solid lines with squares represent the H-Rotor, and dashed lines with circles represent the X-Rotor. Orange, black, and cyan indicate pitch offsets of $\beta = [-10^\circ, 0^\circ, 10^\circ]$ respectively.

G

TURBULENCE INTENSITY OF THE H- AND X-ROTOR

The turbulence intensity TI (in %) is showcased in Figure G.1 for the H- and the X-Rotor at $\beta = -10^\circ, 0^\circ, 10^\circ$.



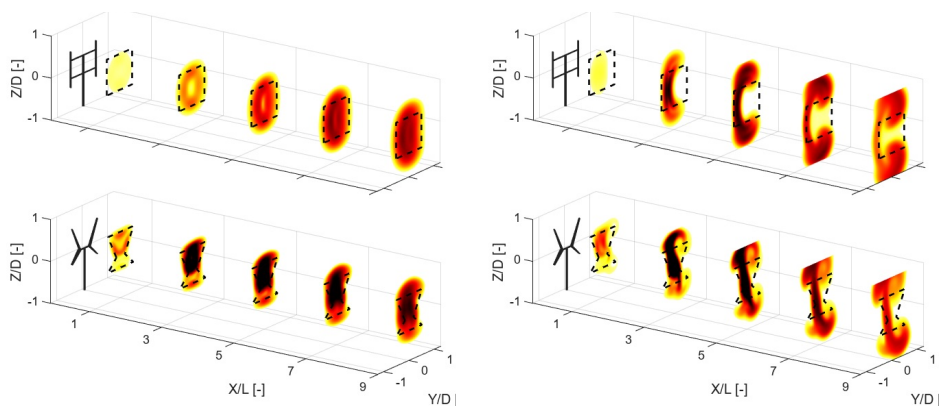
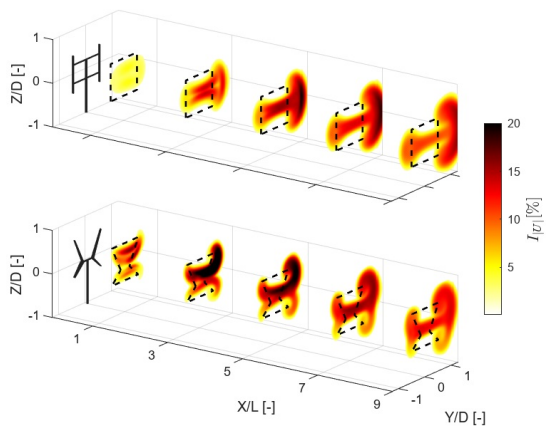
(a) $\beta = 0^\circ$ (baseline)(b) $\beta = -10^\circ$ (c) $\beta = 10^\circ$

Figure G.1: Turbulence intensity of the H- and the X-Rotor at $\beta = -10^\circ, 0^\circ, 10^\circ$ respectively at downstream locations $X/L = 1$ to 10 , where L is the characteristic streamwise length scale. The black dash lines indicate the projected frontal area of the rotor on the corresponding plane. The low turbulence intensities (less than 2%) were removed to enhance the visibility of the isometric plots.

H

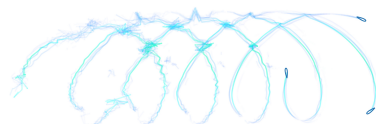
SENSITIVITY STUDY: INFLUENCE OF VORTEX CORE SIZE, DYNAMIC STALL, AND THE CHOICE OF REYNOLDS NUMBERS

With CACTUS, we initially started with the case without dynamic stall, with vortex core radius (the distance from the center of a vortex to the point where the maximum tangential velocity occurs) were set to 100% of the chord, and using the other settings presented in Table 4.1. We shall call this case the 'default' case. We wanted to address the sensitivity in the following points: (1) vortex core radius choice, (2) with and without dynamic stall model, and (3) lift C_L and drag C_D coefficients. While the first couple of points are more standard, we wanted to identify how sensitive are the results to the chosen airfoil polars - especially in the flowfield inside the rotor.

To address this, we first analyse the normalised streamwise velocity (u/U_∞) contours at azimuth $\theta = 0^\circ$ for these cases, available in Figure H.1. Here, only sensitivity to dynamic stall and increased C_L and drag C_D coefficients are discussed.

With the introduction of dynamic stall, some flow features that were not captured in the default case are now visible here, and they agree quite well with the flowfield from the PIV results - especially in the most upwind plane. This suggests that the dynamic stall model is essential to be accurate with the experiments. With an artificial increase in C_L and C_D of 15%, there appears to be some instability again, as the vortex core size for that case is small with respect to the vorticity strength it offers. However, we see significant velocity magnitude changes between the default case and this inside the rotor area, even at the most upwind plane. Overall, we understand that any changes to lift and drag still significantly affects the flowfield within the volume of the rotor, and that including dynamic stall more accurately represents the flowfield of the X-Rotor.

To identify the influence of the core vortex size, we present the integrated blade forces between the the default (now with dynamic stall), and the lowered bound and trailing



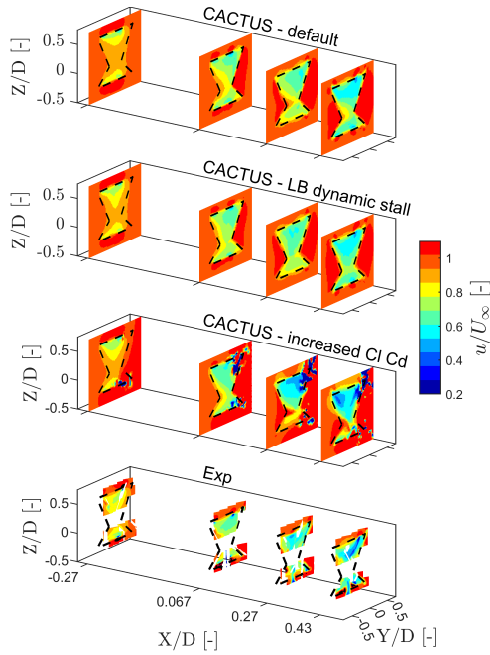


Figure H.1: Normalised streamwise velocity (u/U_∞) contours of the X-Rotor at azimuth $\theta = 0^\circ$ at downstream locations $X/D = -0.27, 0.067, 0.27, 0.43$ where D is the rotor diameter for different input conditions. The first tile is the default case, the second tile shows the use of dynamic stall, third tile shows a case with an artificial increase in C_L and C_D , and the last tile shows the experimental results. The black dash lines indicate the projected frontal area of the rotor on the corresponding plane. All spatial coordinates are normalised the diameters D . The x-axis is magnified to enhance visibility.

H

vortex core radius in Figure H.2.

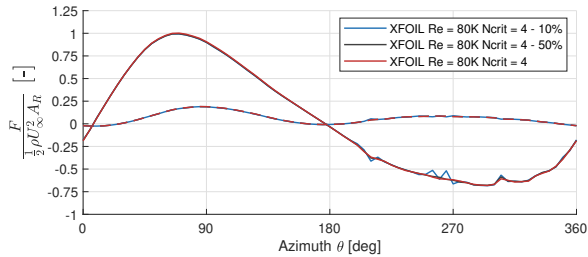


Figure H.2: Integrated blade forces F as a function of azimuth θ to show sensitivity to vortex core sizes. The solid lines represent the normal force and tangential force is represented by the dashed lines. Positive normal force is away from the axis of rotation and vice versa. Forces are integrated along both upper and lower halves of B1.

Between the default and 50%reduced vortex core size cases, we see very little difference in the force profiles. While moving down to 10% core radius, we see minor differences concentrated in the downwind half where blade vortex interaction is expected (around $\theta = 300^\circ$). This indicates that the forces, and by extension the wake, is not extremely

sensitive to the core vortex size.

To further elaborate this, we present the spanwise distribution of the forces for the same cases in Figure H.3.

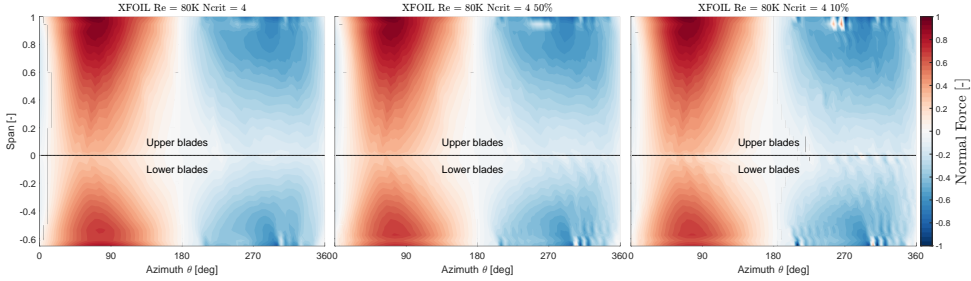


Figure H.3: Spanwise distribution of normal blade forces F_N as a function of azimuth θ . Positive normal force is away from the axis of rotation and vice versa.

We see that there is very minor differences between the first two tiles, as observed in the integrated forces. But, we notice that there are some artefacts in the third tile around $Z/D = 0.9$ and exists in the downwind windward regions. This reflects on we observed earlier, as the difference in the core radius is explicitly visible in the downwind half, where the simulation is approaching instability.

Comparing the velocity fields with 10% vortex core size and the default at $\theta = 0^\circ$ (Figure H.4) shows minor impact in the flowfield that we consider the solver to be relatively independent of the vortex core size.

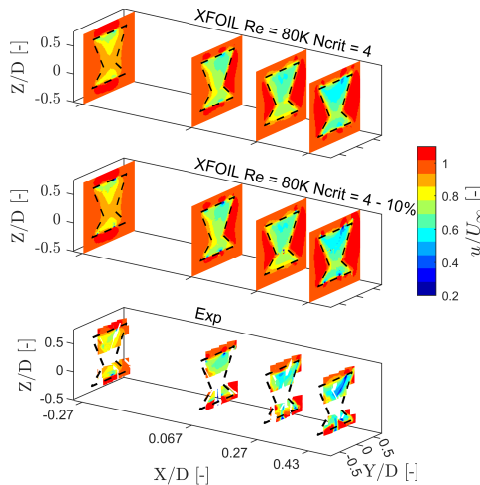
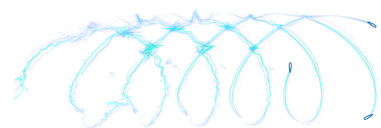


Figure H.4: Normalised streamwise velocity (u/U_∞) contours of the X-Rotor at azimuth $\theta = 0^\circ$ at downstream locations $X/D = -0.27, 0.067, 0.27, 0.43$ where D is the rotor diameter for different input conditions. The first tile is the default case, the second tile shows the case with 10% vortex core size, and the last tile shows the experimental results. The black dash lines indicate the projected frontal area of the rotor on the corresponding plane. All spatial coordinates are normalised the diameters D . The x-axis is magnified to enhance visibility.



Therefore, given these benefits of using dynamic stall in this analysis, we choose to operate with the Leishman-Beddoes dynamic stall implementation in CACTUS and proceed to use a higher than usual core-vortex radius due to the indifference of the blade forces to this parameter.

Regarding the convergence of the solution, we chose to opt for 10 revolutions, as it can be seen from Figure H.5 that beyond the 8th revolution, the errors fall below the order of appreciable difference to the results discussed in this study.

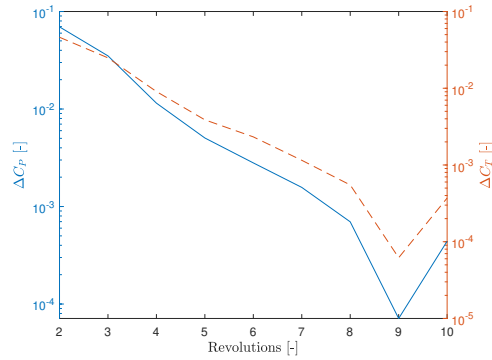
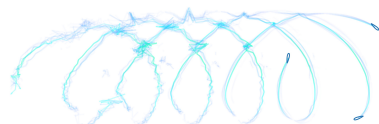


Figure H.5: Convergence plot of power and thrust. The Y-axes are in logarithmic scale

I

TURBULENCE INTENSITY OF THE H-ROTOR WIND FARM

The turbulence intensity TI (in %) is showcased in Figure I.1 for the H-Rotor wind farm at pitch angles $\beta = -10^\circ, 0^\circ, 10^\circ$.



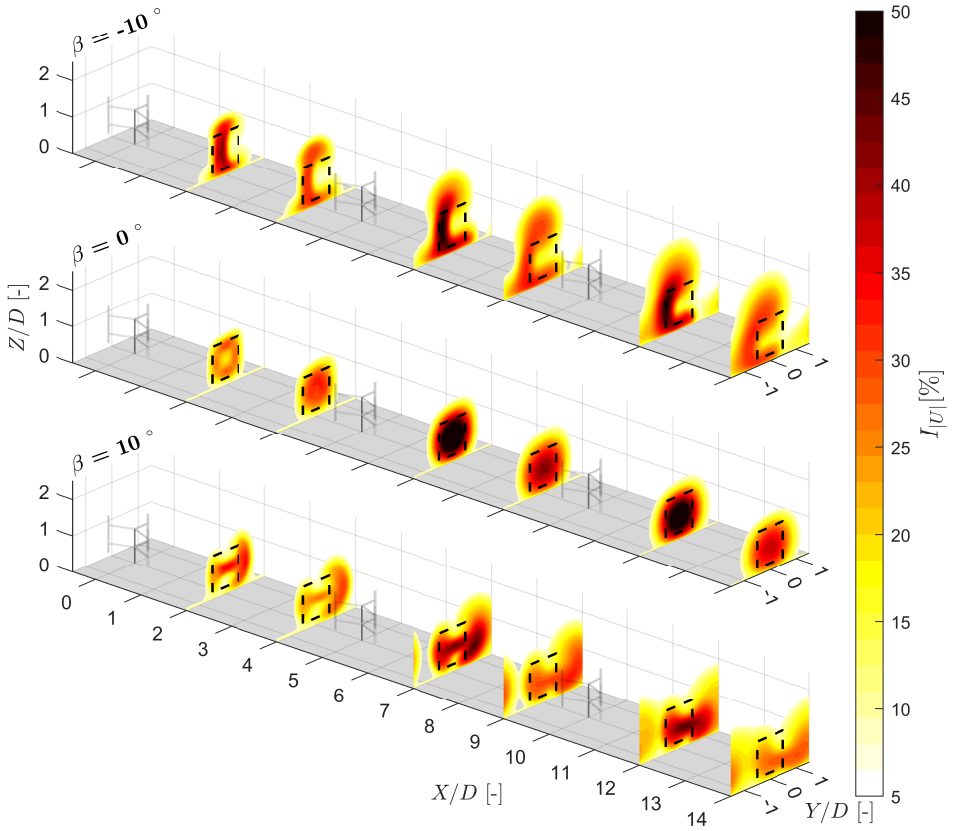
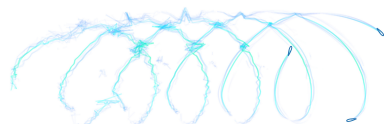


Figure I.1: Turbulence intensity of the windfarm with rotors at $\beta = -10^\circ, 0^\circ, 10^\circ$ respectively. The black dash lines indicate the projected frontal area of the rotor on the corresponding plane. The low turbulence intensities (less than 8%) were removed to enhance the visibility of the isometric plots.

BIBLIOGRAPHY

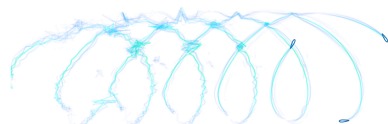
REFERENCES

- [1] Ahmed I. Osman, Lin Chen, Mingyu Yang, Goodluck Msigwa, Mohamed Farghali, Samer Fawzy, David W. Rooney, and Pow Seng Yap. Cost, environmental impact, and resilience of renewable energy under a changing climate: a review. *Environmental Chemistry Letters*, 21(2):741–764, apr 2023. ISSN 16103661. doi: 10.1007/s10311-022-01532-8.
- [2] Jianzhou Wang, Shanshan Qin, Shiqiang Jin, and Jie Wu. Estimation methods review and analysis of offshore extreme wind speeds and wind energy resources, feb 2015. ISSN 18790690.
- [3] P. K. Chaviaropoulos, H. J.M. Beurskens, and S. G. Voutsinas. Moving towards large(r) Rotors Is that a good idea? In *European Wind Energy Conference and Exhibition, EWEC 2013*, volume 2, pages 946–952, 2013. ISBN 9781632663146.
- [4] Mehmet Bilgili, Abdulkadir Yasar, and Erdogan Simsek. Offshore wind power development in Europe and its comparison with onshore counterpart, feb 2011. ISSN 13640321.
- [5] IREA Irena. Future of wind: Deployment, investment, technology, grid integration and socio-economic aspects. *Abu Dhabi*, 2019.
- [6] Rehana Perveen, Nand Kishor, and Soumya R. Mohanty. Off-shore wind farm development: Present status and challenges, jan 2014. ISSN 13640321.
- [7] Aaron Smith, Tyler Stehly, and Walter Musial. Offshore wind technologies market report. Technical report, National Renewable Energy Laboratory, 2015. URL www.nrel.gov/publications.
- [8] Philipp Beiter, Walt Musial, Patrick Duffy, Aubryn Cooperman, Matt Shields, Donna Heimiller, and Mike Optis. The Cost of Floating Offshore Wind Energy in California Between 2019 and 2032. Technical Report November, National Renewable Energy Laboratory, 2020. URL www.nrel.gov/publications. <https://www.nrel.gov/docs/fy21osti/77384.pdf>www.nrel.gov/publications.
- [9] Michael F. Howland, Jesús Bas Quesada, Juan José Pena Martínez, Felipe Palou Larrañaga, Neeraj Yadav, Jasvipul S. Chawla, Varun Sivaram, and John O. Dabiri. Collective wind farm operation based on a predictive model increases utility-scale energy production. *Nature Energy*, 7(9):818–827, aug 2022. ISSN 20587546. doi: 10.1038/s41560-022-01085-8.



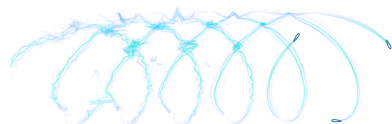
- [10] Nichila Groom and Nina Chestney. Global offshore wind industry poised to miss big targets as obstacles mount, 2025. URL <https://tinyurl.com/6fxx28r7>.
- [11] Majid Bastankhah and Fernando Porté-Agel. Experimental and theoretical study of wind turbine wakes in yawed conditions. *Journal of Fluid Mechanics*, 806:506–541, nov 2016. ISSN 14697645. doi: 10.1017/JFM.2016.595.
- [12] P. Fleming, M. Churchfield, A. Scholbrock, A. Clifton, S. Schreck, K. Johnson, A. Wright, P. Gebraad, J. Annoni, B. Naughton, J. Berg, T. Herges, J. White, T. Mikkelsen, M. Sjöholm, and N. Angelou. Detailed field test of yaw-based wake steering. In *Journal of Physics: Conference Series*, volume 753. Institute of Physics Publishing, oct 2016. doi: 10.1088/1742-6596/753/5/052003.
- [13] Michael F Howland, Juliaan Bossuyt, Luis A Martínez-Tossas, Johan Meyers, and Charles Meneveau. Wake structure in actuator disk models of wind turbines in yaw under uniform inflow conditions. *Journal of Renewable and Sustainable Energy*, 8(4): 43301, 2016. ISSN 19417012. doi: 10.1063/1.4955091.
- [14] Paul Fleming, Jennifer Annoni, Jigar J. Shah, Linpeng Wang, Shreyas Ananthan, Zhijun Zhang, Kyle Hutchings, Peng Wang, Weiguo Chen, and Lin Chen. Field test of wake steering at an offshore wind farm. *Wind Energy Science*, 2(1):229–239, 2017. ISSN 23667451. doi: 10.5194/WES-2-229-2017.
- [15] Juliaan Bossuyt, Ryan Scott, Naseem Ali, and Raúl Bayoán Cal. Quantification of wake shape modulation and deflection for tilt and yaw misaligned wind turbines. *Journal of Fluid Mechanics*, 917:1–28, 2021. ISSN 14697645. doi: 10.1017/jfm.2021.237.
- [16] Carlo Cossu. Evaluation of tilt control for wind-turbine arrays in the atmospheric boundary layer. *Wind Energy Science*, 6(3):663–675, 2021. ISSN 23667451. doi: 10.5194/wes-6-663-2021.
- [17] Joeri A. Frederik, Bart M. Doekemeijer, Sebastiaan P. Mulders, and Jan Willem van Wingerden. The helix approach: Using dynamic individual pitch control to enhance wake mixing in wind farms. *Wind Energy*, 23(8):1739–1751, aug 2020. ISSN 10991824. doi: 10.1002/we.2513.
- [18] Daniel Van Den Berg, Delphine De Tavernier, and Jan Willem Van Wingerden. Using the Helix Mixing Approach on Floating Offshore Wind Turbines. In *Journal of Physics: Conference Series*, volume 2265, page 042011. IOP Publishing, may 2022. doi: 10.1088/1742-6596/2265/4/042011.
- [19] T. F. Ishugah, Y. Li, R. Z. Wang, and J. K. Kiplagat. Advances in wind energy resource exploitation in urban environment: A review. *Renewable and Sustainable Energy Reviews*, 37:613–626, sep 2014. ISSN 13640321. doi: 10.1016/j.rser.2014.05.053.
- [20] Willy Tjiu, Tjukup Marnoto, Sohif Mat, Mohd Hafidz Ruslan, and Kamaruzzaman Sopian. Darrieus vertical axis wind turbine for power generation II: Challenges in HAWT and the opportunity of multi-megawatt Darrieus VAWT development. *Renewable Energy*, 75:560–571, mar 2015. ISSN 18790682. doi: 10.1016/j.renene.2014.10.039.

- [21] John O. Dabiri. Potential order-of-magnitude enhancement of wind farm power density via counter-rotating vertical-axis wind turbine arrays. *Journal of Renewable and Sustainable Energy*, 3(4), jul 2011. ISSN 19417012. doi: 10.1063/1.3608170.
- [22] Erik Möllerström, Fredric Ottermo, Anders Goude, Sandra Eriksson, Jonny Hylander, and Hans Bernhoff. Turbulence influence on wind energy extraction for a medium size vertical axis wind turbine. *Wind Energy*, 19(11):1963–1973, 2016. doi: <https://doi.org/10.1002/we.1962>. URL <https://onlinelibrary.wiley.com/doi/abs/10.1002/we.1962>.
- [23] Matthias Kinzel, Daniel B. Araya, and John O. Dabiri. Turbulence in vertical axis wind turbine canopies. *Physics of Fluids*, 27(11):115102, nov 2015. ISSN 1070-6631. doi: 10.1063/1.4935111.
- [24] V. Rolin and F. Porté-Agel. Wind-tunnel study of the wake behind a vertical axis wind turbine in a boundary layer flow using stereoscopic particle image velocimetry. In *Journal of Physics: Conference Series*, volume 625, page 012012, jun 2015. doi: 10.1088/1742-6596/625/1/012012.
- [25] P Chatelain, M Duponcheel, S Zeoli, S Buffin, D. G. Caprace, G Winckelmans, and L Bricteux. Investigation of the effect of inflow turbulence on vertical axis wind turbine wakes. In *Journal of Physics: Conference Series*, volume 854, page 012011, may 2017. doi: 10.1088/1742-6596/854/1/012011.
- [26] Ashutosh Jadeja. *Wake Deflection Technique for Vertical Axis Wind Turbines using Actuator Line Model in OpenFOAM*. Delft University of Technology, April 2018.
- [27] Ming Huang, Andrea Sciacchitano, and Carlos Ferreira. On the wake deflection of vertical axis wind turbines by pitched blades. *Wind Energy*, (October 2022):365–387, 2023. ISSN 10991824. doi: 10.1002/we.2803.
- [28] Ming Huang, Yugandhar Vijaykumar Patil, Andrea Sciacchitano, and Carlos Ferreira. Experimental study of the wake interaction between two vertical axis wind turbines. *Wind Energy*, 26:1188–1211, 11 2023. ISSN 1099-1824. doi: 10.1002/WE.2863.
- [29] A.Y. al Hassan and D.R. Hill. *Islamic Technology: An Illustrated History*. Cambridge University Press, 1992. ISBN 9780521422390.
- [30] Francesco Castellani, Davide Astolfi, Mauro Peppoloni, Francesco Natili, Daniele Buttà, and Alexander Hirschl. Experimental vibration analysis of a small scale vertical wind energy system for residential use. *Machines*, 7(2):35, may 2019. ISSN 20751702. doi: 10.3390/machines7020035.
- [31] Jingna Pan, Carlos Ferreira, and Alexander van Zuijlen. Performance analysis of an idealized darrieus–savonius combined vertical axis wind turbine. *Wind Energy*, 27(6):612–627, 2024. doi: <https://doi.org/10.1002/we.2904>.
- [32] B. S. Linscott, P Perkins, and J. T. Denner. Large, horizontal-axis wind turbines. Technical report, National Aeronautics and Space Administration, 1984. URL <https://ntrs.nasa.gov/citations/19840019259>.



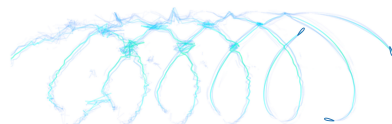
- [33] Erik Möllerström, Paul Gipe, Jos Beurskens, and Fredric Ottermo. A historical review of vertical axis wind turbines rated 100 kW and above, may 2019. ISSN 18790690.
- [34] Grimshaw Architects, Aerogenerator X project. URL <https://grimshaw.global/projects/industrial-design/aerogenerator-x/>.
- [35] D J Parsons, Julia Chatterton, F Brennan, and A Kolios. Carbon brainprint case study: novel offshore vertical axis wind turbines. Technical report, 2011. URL www.cranfield.ac.ukwww.carbonbrainprint.org.ukhttp://www.palisade.com/downloads/pdf/CBrainprint-CS02-NOVA.pdf.
- [36] Tulyp Wind – Arkom Windpower B.V. URL <https://www.tulypwind.nl/>.
- [37] Minesto - Kite Systems. URL <https://minesto.com/products/>.
- [38] SeaTwirl - S3, S2x, S1.5, S1. URL <https://seatwirl.com/products/>.
- [39] William Leithead, Arthur Camciuc, Abbas Kazemi Amiri, and James Carroll. The X-Rotor Offshore Wind Turbine Concept. *Journal of Physics: Conference Series*, 1356(1), 2019. ISSN 17426596. doi: 10.1088/1742-6596/1356/1/012031.
- [40] Callum Flannigan, James Carroll, and William Leithead. Operations expenditure modelling of the X-Rotor offshore wind turbine concept. In *Journal of Physics: Conference Series*, volume 2265, page 032054. IOP Publishing, may 2022. doi: 10.1088/1742-6596/2265/3/032054.
- [41] A. Kolios, A. Chahardehi, and F. Brennan. Experimental determination of the overturning moment and net lateral force generated by a novel vertical axis wind turbine: Experiment design under load uncertainty. *Experimental Techniques*, 37(1): 7–14, jan 2013. ISSN 07328818. doi: 10.1111/j.1747-1567.2011.00727.x.
- [42] Andrew Shires. Design optimisation of an offshore vertical axis wind turbine. *Proceedings of Institution of Civil Engineers: Energy*, 166(1):7–18, 2013. ISSN 17514231. doi: 10.1680/ener.12.00007.
- [43] XROTOR. X-ROTOR: X-shaped Radical Offshore wind Turbine for Overall cost of energy Reduction | XROTOR | Project | Fact sheet | H2020 | CORDIS | European Commission. URL <https://cordis.europa.eu/project/id/101007135>.
- [44] Delphine De Tavernier, Carlos Ferreira, and Anders Goude. Vertical-Axis Wind Turbine Aerodynamics. *Handbook of Wind Energy Aerodynamics: With 678 Figures and 33 Tables*, pages 1317–1361, 2022. doi: 10.1007/978-3-030-31307-4_64.
- [45] Mazharul Islam, David S.K. Ting, and Amir Fartaj. Aerodynamic models for Darrieus-type straight-bladed vertical axis wind turbines, may 2008. ISSN 13640321.
- [46] Robert Howell, Ning Qin, Jonathan Edwards, and Naveed Durrani. Wind tunnel and numerical study of a small vertical axis wind turbine. *Renewable Energy*, 35(2): 412–422, feb 2010. ISSN 09601481. doi: 10.1016/j.renene.2009.07.025.

- [47] Marco Raciti Castelli, Alessandro Englaro, and Ernesto Benini. The Darrieus wind turbine: Proposal for a new performance prediction model based on CFD. *Energy*, 36(8):4919–4934, aug 2011. ISSN 03605442. doi: 10.1016/j.energy.2011.05.036.
- [48] Sina Shamsoddin and Fernando Porté-Agel. Large eddy simulation of vertical axis wind turbine wakes. *Energies*, 7(2):890–912, 2014. ISSN 19961073. doi: 10.3390/EN7020890.
- [49] Stefania Zanforlin and Takafumi Nishino. Fluid dynamic mechanisms of enhanced power generation by closely spaced vertical axis wind turbines. *Renewable Energy*, 99:1213–1226, dec 2016. ISSN 18790682. doi: 10.1016/j.renene.2016.08.015.
- [50] Abdolrahim Rezaeiha, Ivo Kalkman, and Bert Blocken. CFD simulation of a vertical axis wind turbine operating at a moderate tip speed ratio: Guidelines for minimum domain size and azimuthal increment. *Renewable Energy*, 107:373–385, jul 2017. ISSN 18790682. doi: 10.1016/j.renene.2017.02.006.
- [51] Kartik Venkatraman, Andrea Bresciani, Julien Maillard, Stéphane Moreau, Julien Christophe, and Christophe Schram. Darrieus wind turbine noise propagation in urban environments. In *AIAA Aviation and Aeronautics Forum and Exposition, AIAA AVIATION Forum 2023*. American Institute of Aeronautics and Astronautics Inc, AIAA, 2023. ISBN 9781624107047. doi: 10.2514/6.2023-3646.
- [52] Andrea G. Sanvito, Agnese Firpo, Paolo Schito, Vincenzo Dossena, Alberto Zasso, and Giacomo Persico. A novel vortex-based velocity sampling method for the actuator-line modeling of floating offshore wind turbines in windmill state. *Renewable Energy*, 231(October 2023), 2024. ISSN 18790682. doi: 10.1016/j.renene.2024.120927.
- [53] Carlos Simão Ferreira. *The near wake of the VAWT 2D and 3D views of the VAWT aerodynamics*. PhD thesis, Delft University of Technology, 2009.
- [54] C. Simão Ferreira, H. Aagaard Madsen, M. Barone, B. Roscher, P. Deglaire, and I. Arduin. Comparison of aerodynamic models for Vertical Axis Wind Turbines. *Journal of Physics: Conference Series*, 524(1):012125, jun 2014. ISSN 1742-6596. doi: 10.1088/1742-6596/524/1/012125.
- [55] Abdolrahim Rezaeiha, Ivo Kalkman, and Bert Blocken. Effect of pitch angle on power performance and aerodynamics of a vertical axis wind turbine. *Applied Energy*, 197: 132–150, 2017. ISSN 03062619. doi: 10.1016/j.apenergy.2017.03.128.
- [56] Bruce LeBlanc and Carlos Ferreira. Estimation of blade loads for a variable pitch Vertical Axis Wind Turbine with strain gage measurements. *Wind Energy*, 25(6): 1030–1045, 2022. ISSN 10991824. doi: 10.1002/we.2713.
- [57] Bruce LeBlanc and Carlos Ferreira. Estimation of blade loads for a variable pitch vertical axis wind turbine from particle image velocimetry. *Wind Energy*, 25(2): 313–332, feb 2022. ISSN 10991824. doi: 10.1002/we.2674.



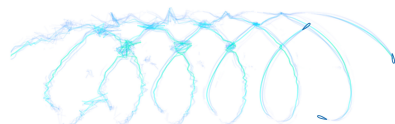
- [58] Delphine De Tavernier, Carlos Ferreira, and Gerard van Bussel. Airfoil optimisation for vertical-axis wind turbines with variable pitch. *Wind Energy*, 22(4):547–562, 2019. ISSN 10991824. doi: 10.1002/we.2306.
- [59] Sébastien Le Fouest and Karen Mulleners. Optimal blade pitch control for enhanced vertical-axis wind turbine performance. *Nature Communications*, 15(1):1–13, mar 2024. ISSN 20411723. doi: 10.1038/s41467-024-46988-0.
- [60] Peter Bachant and Martin Wosnik. Characterising the near-wake of a cross-flow turbine. *Journal of Turbulence*, 16(4):392–410, apr 2015. ISSN 14685248. doi: 10.1080/14685248.2014.1001852.
- [61] G. Tescione, C. J. Simão Ferreira, and G. J.W. van Bussel. Analysis of a free vortex wake model for the study of the rotor and near wake flow of a vertical axis wind turbine. *Renewable Energy*, 87:552–563, mar 2016. ISSN 18790682. doi: 10.1016/j.renene.2015.10.002.
- [62] D. De Tavernier, C. Ferreira, U. Paulsen, and H. Madsen. The 3D effects of a vertical-axis wind turbine: rotor and wake induction. *Journal of Physics: Conference Series*, 1618(5):052040, sep 2020. ISSN 1742-6596. doi: 10.1088/1742-6596/1618/5/052040.
- [63] B.P. LeBlanc. *Dynamics of the Pitch-able VAWT: A Study of the Dynamics of the Vertical Axis Wind Turbine with Individual Pitch Control*. Dissertation (tu delft), Delft University of Technology, 2024.
- [64] Giuseppe Tescione, Daniele Ragni, Chenguang He, Carlos Simao Ferreira, and Gerard G van Bussel. Piv-based analysis of 2d and 3d flow phenomena of vertical axis wind turbine aerodynamics. In *32nd ASME Wind Energy Symposium*, page 1080, 2014.
- [65] Kevin J Ryan, Filippo Coletti, Christopher J Elkins, John O Dabiri, and John K Eaton. Three-dimensional flow field around and downstream of a subscale model rotating vertical axis wind turbine. *Experiments in Fluids*, 57:1–15, 2016.
- [66] Daniel B Araya, Tim Colonius, and John O Dabiri. Transition to bluff-body dynamics in the wake of vertical-axis wind turbines. *Journal of Fluid Mechanics*, 813:346–381, 2017.
- [67] Vincent F-C. Rolin and Fernando Porté-Agel. Experimental investigation of vertical-axis wind-turbine wakes in boundary layer flow. *Renewable Energy*, 118:1–13, 2018. ISSN 0960-1481. doi: <https://doi.org/10.1016/j.renene.2017.10.105>.
- [68] Nathaniel J Wei, Ian D Brownstein, Jennifer L Cardona, Michael F Howland, and John O Dabiri. Near-wake structure of full-scale vertical-axis wind turbines. *Journal of Fluid Mechanics*, 914:A17, 2021.
- [69] Ming Huang, Andrea Sciacchitano, and Carlos Ferreira. On the wake deflection of vertical axis wind turbines by pitched blades. *Wind Energy*, 2023.

- [70] Sina Shamsoddin and Fernando Porté-Agel. A large-eddy simulation study of vertical axis wind turbine wakes in the atmospheric boundary layer. *Energies* 2016, Vol. 9, Page 366, 9:366, 5 2016. ISSN 1996-1073. doi: 10.3390/EN9050366.
- [71] Victor Mendoza and Anders Goude. Wake flow simulation of a vertical axis wind turbine under the influence of wind shear. In *Journal of Physics: Conference Series*, volume 854, page 012031. IOP Publishing, 5 2017. doi: 10.1088/1742-6596/854/1/012031.
- [72] Jiao He, Xin Jin, Shuangyi Xie, Le Cao, Yaming Wang, Y. Lin, and Ning Wang. Cfd modeling of varying complexity for aerodynamic analysis of h-vertical axis wind turbines. *Renewable Energy*, 145:2658–2670, 1 2020. ISSN 18790682. doi: 10.1016/j.renene.2019.07.132.
- [73] Yi Xin Peng, You Lin Xu, Songye Zhu, and Chao Li. High-solidity straight-bladed vertical axis wind turbine: Numerical simulation and validation. *Journal of Wind Engineering and Industrial Aerodynamics*, 193, 10 2019. ISSN 01676105. doi: 10.1016/j.jweia.2019.103960.
- [74] Antonio Posa and Elias Balaras. Large eddy simulation of an isolated vertical axis wind turbine. *Journal of Wind Engineering and Industrial Aerodynamics*, 172:139–151, 1 2018. ISSN 0167-6105. doi: 10.1016/J.JWEIA.2017.11.004.
- [75] Antonio Posa. Influence of tip speed ratio on wake features of a vertical axis wind turbine. *Journal of Wind Engineering and Industrial Aerodynamics*, 197, 2 2020. ISSN 01676105. doi: 10.1016/j.jweia.2019.104076.
- [76] D. De Tavernier, M. Sakib, T. Griffith, G. Pirrung, U. Paulsen, H. Madsen, W. Keijer, and C. Ferreira. Comparison of 3D aerodynamic models for vertical-axis wind turbines: H-rotor and Φ -rotor. *Journal of Physics: Conference Series*, 1618(5):052041, sep 2020. ISSN 1742-6596. doi: 10.1088/1742-6596/1618/5/052041.
- [77] P. L. Delafin, T. Nishino, A. Kolios, and L. Wang. Comparison of low-order aerodynamic models and rans cfd for full scale 3d vertical axis wind turbines. *Renewable Energy*, 109:564–575, 8 2017. ISSN 0960-1481. doi: 10.1016/J.RENENE.2017.03.065.
- [78] Victor Mendoza, Peter Bachant, Carlos Ferreira, and Anders Goude. Near-wake flow simulation of a vertical axis turbine using an actuator line model. *Wind Energy*, 22(2):171–188, feb 2019. ISSN 10991824. doi: 10.1002/we.2277.
- [79] Matthieu Boudreau and Guy Dumas. Comparison of the wake recovery of the axial-flow and cross-flow turbine concepts. *Journal of Wind Engineering and Industrial Aerodynamics*, 165:137–152, 6 2017. ISSN 01676105. doi: 10.1016/j.jweia.2017.03.010.
- [80] Victor Mendoza, Ashvinkumar Chaudhari, and Anders Goude. Performance and wake comparison of horizontal and vertical axis wind turbines under varying surface roughness conditions. *Wind Energy*, 22(4):458–472, 2019. doi: <https://doi.org/10.1002/we.2299>. URL <https://onlinelibrary.wiley.com/doi/abs/10.1002/we.2299>.



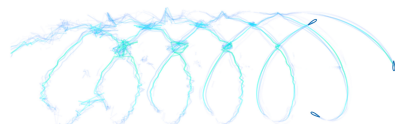
- [81] Bruce LeBlanc and Carlos Ferreira. Estimation of blade loads for a variable pitch vertical axis wind turbine with strain gage measurements. *Wind Energy*, 25:1030–1045, 2022. ISSN 10991824. doi: 10.1002/we.2713.
- [82] Bruce LeBlanc and Carlos Ferreira. Estimation of blade loads for a variable pitch vertical axis wind turbine from particle image velocimetry. *Wind Energy*, 25:313–332, 2 2022. ISSN 1095-4244. doi: 10.1002/we.2674.
- [83] Ming Huang. *Wake and wind farm aerodynamics of vertical axis wind turbines*. PhD thesis, Delft University of Technology, 2023.
- [84] Jia Guo and Liping Lei. Flow Characteristics of a Straight-Bladed Vertical Axis. *Energies*, page 23, 2020.
- [85] Victor Mendoza and Anders Goude. Improving farm efficiency of interacting vertical-axis wind turbines through wake deflection using pitched struts. *Wind Energy*, 22(4): 538–546, 2019.
- [86] André F.P. Ribeiro, Carlos S. Ferreira, and Damiano Casalino. Vertical axis wind turbine wake steering by pitched struts and blades. *Journal of Physics: Conference Series*, 2767:092004, 6 2024. ISSN 1742-6596. doi: 10.1088/1742-6596/2767/9/092004.
- [87] T J Broertjes, D Bensason, A Sciacchitano, and C Ferreira. Lift-induced wake re-energization for a vawt-based multi-rotor system. *Journal of Physics: Conference Series*, 2767:072012, 6 2024. ISSN 1742-6588. doi: 10.1088/1742-6596/2767/7/072012. URL <https://iopscience.iop.org/article/10.1088/1742-6596/2767/7/072012>.
- [88] Carlos Ferreira, David Bensason, Thomas J. Broertjes, Andrea Sciacchitano, Flavio A. C. Martins, and Adhyanth Giri Ajay. Enhancing wind farm efficiency through active control of the atmospheric boundary layer’s vertical entrainment of momentum. *Journal of Physics: Conference Series*, 2767(9):092107, jun 2024. doi: 10.1088/1742-6596/2767/9/092107. URL <https://doi.org/10.1088/1742-6596/2767/9/092107>.
- [89] Y. Li, W. Yu, A. Sciacchitano, and C. Ferreira. Numerical investigation of regenerative wind farms featuring enhanced vertical energy entrainment. *Wind Energy Science*, 10(4):631–659, 2025. doi: 10.5194/wes-10-631-2025. URL <https://wes.copernicus.org/articles/10/631/2025/>.
- [90] F. Avila Correia Martins, A. van Zuijlen, and C. Simão Ferreira. Proof of concept for multirotor systems with vortex-generating modes for regenerative wind energy: a study based on numerical simulations and experimental data. *Wind Energy Science*, 10(1):41–58, 2025. doi: 10.5194/wes-10-41-2025. URL <https://wes.copernicus.org/articles/10/41/2025/>.
- [91] J. Dabiri. Potential order-of-magnitude enhancement of wind farm power density via counter-rotating vertical-axis wind turbine arrays. *Journal of Renewable and Sustainable Energy*, 3(4):043104, 2011. doi: 10.1063/1.3608170.

- [92] Matthias Kinzel, Quinn Mulligan, and John O. Dabiri. Energy exchange in an array of vertical-axis wind turbines. *Journal of Turbulence*, 13(1):1–13, 2012. ISSN 14685248. doi: 10.1080/14685248.2012.712698.
- [93] Seyed Hossein Hezaveh and Elie Bou-Zeid. Mean kinetic energy replenishment mechanisms in vertical-axis wind turbine farms. *Physical Review Fluids*, 3(9):94606, 2018. ISSN 2469990X. doi: 10.1103/PhysRevFluids.3.094606.
- [94] R. Whittlesey, S. Liska, and J. Dabiri. Fish schooling as a basis for vertical axis wind turbine farm design. *Bioinspiration & Biomimetics*, 5(2):035005, 2010. doi: 10.1088/1748-3182/5/3/035005.
- [95] Masoumeh Gharaati, Nathaniel J. Wei, John O. Dabiri, Luis A. Martínez-Tossas, and Di Yang. Large-eddy simulations of turbulent flows in arrays of helical- and straight-bladed vertical-axis wind turbines. *Journal of Renewable and Sustainable Energy*, 15:63309, 11 2023. ISSN 19417012. doi: 10.1063/5.0172007/18259227/063309_1_5.0172007.AM.PDF.
- [96] David Bensason, Jayant Mulay, Andrea Sciacchitano, and Carlos Ferreira. Experimental demonstration of regenerative wind farming using a high-density layout of vertical-axis wind turbines. *Wind Energy Science*, 10(7):1499–1528, 2025. doi: 10.5194/wes-10-1499-2025.
- [97] David Bensason, Andrea Sciacchitano, and Carlos Ferreira. Near wake of the X-Rotor vertical-axis wind turbine. In *Journal of Physics: Conference Series*, volume 2505. Institute of Physics, 2023. doi: 10.1088/1742-6596/2505/1/012040.
- [98] David Bensason, Andrea Sciacchitano, Adhyanth Giri Ajay, and Carlos Simao Ferreira. A Study of the Near Wake Deformation of the X-Rotor Vertical-Axis Wind Turbine With Pitched Blades. *Wind Energy*, 2024. ISSN 10991824. doi: 10.1002/we.2944.
- [99] David Bensason, Andrea Sciacchitano, and Carlos Ferreira. On the wake re-energization of the x-rotor vertical-axis wind turbine via the vortex-generator strategy. *Wind Energy Science*, 2025. doi: 10.5194/wes-2025-3.
- [100] Ion Paraschivoiu. Double-multiple streamtube model for Darrieus in turbines. *NASA. Lewis Research Center Wind Turbine Dyn.*, 1981.
- [101] Seth Read and David Sharpe. An extended multiple streamtube theory for vertical axis wind turbines. 1980. URL <https://api.semanticscholar.org/CorpusID:109886850>.
- [102] L.L. Freris. *Wind Energy Conversion Systems*. Prentice Hall, 1990.
- [103] Laurence Morgan and William Leithead. Aerodynamic modelling of a novel vertical axis wind turbine concept. In *Journal of Physics: Conference Series*, volume 2257. Institute of Physics, may 2022. doi: 10.1088/1742-6596/2257/1/012001.



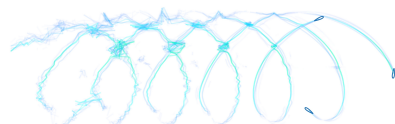
- [104] Ion Paraschivoiu. Aerodynamic Loads and Performance of the Darrieus Rotor. *Journal of Energy*, V 6(N 6):406–412, may 1982. ISSN 01460412. doi: 10.2514/3.62621.
- [105] H. A. Madsen. *The actuator cylinder: a flow model for vertical axis wind turbine*. PhD thesis, 1982.
- [106] H. Aa Madsen, U. S. Paulsen, and L. Vitae. Analysis of VAWT aerodynamics and design using the Actuator Cylinder flow model. *Journal of Physics: Conference Series*, 555(1):012065, dec 2014. ISSN 1742-6596. doi: 10.1088/1742-6596/555/1/012065.
- [107] Zhengshun Cheng, Helge Aagaard Madsen, Zhen Gao, and Torgeir Moan. Aerodynamic Modeling of Floating Vertical Axis Wind Turbines Using the Actuator Cylinder Flow Method. *Energy Procedia*, 94:531–543, sep 2016. ISSN 1876-6102. doi: 10.1016/J.EGYPRO.2016.09.232.
- [108] Jens Nørkær Sørensen and Wen Zhong Shen. Numerical modeling of wind turbine wakes. *Journal of Fluids Engineering, Transactions of the ASME*, 124(2):393–399, jun 2002. ISSN 00982202. doi: 10.1115/1.1471361.
- [109] Matt Churchfield and Sang Lee. Nwtc design codes-sowfa. Technical report, National Renewable Energy Laboratory, 2012.
- [110] Peter Bachant, Anders Goude, and Martin Wosnik. Actuator line modeling of vertical-axis turbines. *Wind Energy*, 2016. doi: <https://doi.org/10.48550/arXiv.1605.01449>.
- [111] H. G. Weller, G. Tabor, H. Jasak, and C. Fureby. A tensorial approach to computational continuum mechanics using object-oriented techniques. *Computers in Physics*, 12(6): 620–631, 1998. ISSN 0894-1866. doi: 10.1063/1.168744.
- [112] Andrea G Sanvito, Agnese Firpo, Paolo Schito, Vincenzo Dossena, Alberto Zasso, and Giacomo Persico. Insights into the dynamic induction in fowt surge motion using an actuator-line model. *Journal of Physics: Conference Series*, 2767:052064, 6 2024. ISSN 1742-6588. doi: 10.1088/1742-6596/2767/5/052064.
- [113] J. Katz and A. Plotkin. *Low-Speed Aerodynamics*. Cambridge University Press, 2009. ISBN 9780521665520. doi: 10.1007/978-1-4020-8664-9_3.
- [114] Jonathan Murray and Matthew Barone. The Development of CACTUS, a Wind and Marine Turbine Performance Simulation Code. *49th AIAA Aerospace Sciences Meeting including the New Horizons Forum and Aerospace Exposition 2011*, (January): 1–21, 2011. doi: 10.2514/6.2011-147.
- [115] D Marten, J Wendler, G Pechlivanoglou, C N Nayeri, and C O Paschereit. QBLADE: an open source tool for design and simulation of horizontal and vertical axis wind turbines. *International Journal of Emerging Technology and Advanced Engineering*, 3 (3):264–269, 2013.
- [116] David Marten. *QBlade: a modern tool for the aeroelastic simulation of wind turbines*. PhD thesis, Technische Universität Berlin, 2020.

- [117] Xiaowen Shan, Xue Feng Yuan, and Hudong Chen. Kinetic theory representation of hydrodynamics: A way beyond the navier-stokes equation. *Journal of Fluid Mechanics*, 550:413–441, 2006. ISSN 14697645. doi: 10.1017/S0022112005008153.
- [118] Dassault Systemes. Simulia powerflow user’s guide, 2021.
- [119] Christian Masson, Christophe Leclerc, and Ion Paraschivoiu. Appropriate dynamic-stall models for performance predictions of vawts with nlf blades. *International Journal of Rotating Machinery*, 4:129–139, 1998. doi: 10.1155/S1023621X98000116.
- [120] A. Buchner, J. Soria, D. Honnery, and A. Smits. Dynamic stall in vertical axis wind turbines: scaling and topological considerations. *Journal of Fluid Mechanics*, 841: 746–766, 2018. doi: 10.1017/jfm.2018.112.
- [121] Sébastien Le Fouest and Karen Mulleners. The dynamic stall dilemma for vertical-axis wind turbines. *Renewable Energy*, 198:505–520, oct 2022. ISSN 0960-1481. doi: 10.1016/J.RENENE.2022.07.071.
- [122] C T Tran and D Petot. Semi-empirical model for the dynamic stall of airfoils in view of the application to the calculation of responses of a helicopter in forward flight. *Vertica*, 5(48):35–53, 1980.
- [123] J Gordon Leishman. Challenges in modelling the unsteady aerodynamics of wind turbines. *Wind Energy*, 5(2-3):85–132, 2002. ISSN 1099-1824. doi: 10.1002/we.62.
- [124] W. Sheng, R. A. Mc D. Galbraith, and F. N. Coton. A new stall-onset criterion for low speed dynamic-stall. *Journal of Solar Energy Engineering, Transactions of the ASME*, 128(4):461–471, 2006. ISSN 01996231. doi: 10.1115/1.2346703.
- [125] W. Sheng, R. A. Mc D. Galbraith, and F. N. Coton. A modified dynamic stall model for low mach numbers. *Journal of Solar Energy Engineering, Transactions of the ASME*, 130(3):0310131–03101310, 2008. ISSN 01996231. doi: 10.1115/1.2931509.
- [126] Stig Øye. Dynamic stall simulated as time lag of separation. In *Proceedings of the 4th IEA Symposium on the Aerodynamics of Wind Turbines*, volume 27, page 28. Rome, Italy, 1991.
- [127] Ronald E Gormont. *A mathematical model of unsteady aerodynamics and radial flow for application to helicopter rotors*. Eustis Directorate, US Army Air Mobility Research and Development Laboratory, 1973.
- [128] M.H. Hansen, Mac Gaunaa, and Helge Aagaard Madsen. *A Beddoes-Leishman type dynamic stall model in state-space and indicial formulations*. Number 1354(EN) in Denmark. Forskningscenter Risoe. Risoe-R. Denmark. Forskningscenter Risoe. Risoe-R, 2004. ISBN 87-550-3090-4.
- [129] Galih Bangga, Thorsten Lutz, and Matthias Arnold. An improved second-order dynamic stall model for wind turbine airfoils. *Wind Energy Science*, 5(3):1037–1058, 2020. ISSN 23667451. doi: 10.5194/wes-5-1037-2020.



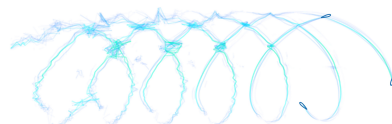
- [130] J Gordon. Leishman. *Principles of helicopter aerodynamics*. Cambridge University Press, Cambridge ; SE - xxxvii, 826 pages : illustrations ; 27 cm., 2nd ed. edition, 2006. ISBN 0521858607 9780521858601 1107013356 9781107013353.
- [131] P. G. Migliore, W. P. Wolfe, and J. B. Fanucci. Flow Curvature Effects on Darrieus Turbine Blade Aerodynamics. *Journal of energy*, 4(2):49–55, 1980. ISSN 01460412. doi: 10.2514/3.62459.
- [132] J. L. Cardona. Flow curvature and dynamic stall simulated with an aerodynamic free-vortex model for vawt. *Wind Engineering*, 8(3):135–143, January 1984.
- [133] John M. Rainbird, Alessandro Bianchini, Francesco Balduzzi, Joaquim Peiró, J. Michael R. Graham, Giovanni Ferrara, and Lorenzo Ferrari. On the influence of virtual camber effect on airfoil polars for use in simulations of darrieus wind turbines. *Energy Conversion and Management*, 106:373–384, 2015. ISSN 0196-8904. doi: 10.1016/j.enconman.2015.09.053.
- [134] Anders Goude. *Fluid Mechanics of Vertical Axis Turbines - Simulations and Model Development*. PhD thesis, Uppsala University, 2012.
- [135] AC Mandal and JD Burton. The effects of dynamic stall and flow curvature on the aerodynamics of darrieus turbines applying the cascade model. *Wind Engineering*, pages 267–282, 1994.
- [136] Sander Van Der Horst, Jelmer Van De Wiel, Carlos Simão Ferreira, and Néstor Ramos García. Flow curvature effects for VAWT: A review of virtual airfoil transformations and implementation in XFOIL. In *34th Wind Energy Symposium*, number January, pages 1–9, 2016. ISBN 9781624103957. doi: 10.2514/6.2016-1734.
- [137] Mark Drela. XFOIL: An Analysis and Design System for Low Reynolds Number Airfoils. In Thomas J. Mueller, editor, *Low Reynolds Number Aerodynamics*, Lecture Notes in Engineering, pages 1–12, Berlin, Heidelberg, 1989. Springer. ISBN 978-3-642-84010-4. doi: 10.1007/978-3-642-84010-4_1.
- [138] Larry Viterna and David Janetzke. Theoretical and experimental power from large horizontal-axis wind turbines. *NASA Technical Memorandum*, 10 1982. doi: 10.2172/6763041.
- [139] Francesco Balduzzi, Alessandro Bianchini, Riccardo Maleci, Giovanni Ferrara, and Lorenzo Ferrari. Blade design criteria to compensate the flow curvature effects in h-darrieus wind turbines. *Journal of Turbomachinery*, 137(1):1–10, 2014. ISSN 15288900. doi: 10.1115/1.4028245.
- [140] Abdolrahim Rezaeiha, Ivo Kalkman, and Bert Blocken. CFD simulation of a vertical axis wind turbine operating at a moderate tip speed ratio: Guidelines for minimum domain size and azimuthal increment. *Renewable Energy*, 107:373–385, jul 2017. ISSN 0960-1481. doi: 10.1016/J.RENENE.2017.02.006.

- [141] Pier Francesco Melani, Francesco Balduzzi, Giovanni Ferrara, and Alessandro Bianchini. An annotated database of low Reynolds aerodynamic coefficients for the NACA0021 airfoil. In *AIP Conference Proceedings*, volume 2191, page 20111, 2019. ISBN 9780735419384. doi: 10.1063/1.5138844.
- [142] Abdolrahim Rezaeiha, Ivo Kalkman, Hamid Montazeri, and Bert Blocken. Effect of the shaft on the aerodynamic performance of urban vertical axis wind turbines. *Energy Conversion and Management*, 149:616–630, oct 2017. ISSN 0196-8904. doi: 10.1016/J.ENCONMAN.2017.07.055.
- [143] Lucy Massie, Pablo Ouro, Thorsten Stoesser, and Qianyu Luo. An Actuator Surface Model to Simulate Vertical Axis Turbines. *Energies 2019, Vol. 12, Page 4741*, 12(24): 4741, dec 2019. ISSN 1996-1073. doi: 10.3390/EN12244741.
- [144] Tonio Sant, Gijs Van Kuik, Wouter Haans, and Gerard J.W. Van Bussel. An approach for the verification and validation of rotor aerodynamics codes based on free-wake vortex methods. In *31st European Rotorcraft Forum*, volume 2005, 2005.
- [145] Sandeep Gupta and J. Gordon Leishman. Validation of a free-vortex wake model for wind turbines in yawed flow. In *Collection of Technical Papers - 44th AIAA Aerospace Sciences Meeting*, volume 7, pages 4529–4543. American Institute of Aeronautics and Astronautics Inc., 2006. ISBN 1563478072. doi: 10.2514/6.2006-389.
- [146] Maarten J Van Den Broek, Delphine De Tavernier, Paul Hulsman, Daan Van Der Hoek, Benjamin Sanderse, and Jan Willem Van Wingerden. Free-vortex models for wind turbine wakes under yaw misalignment - a validation study on far-wake effects. *Wind Energy Science*, 8(12):1909–1925, 2023. ISSN 23667451. doi: 10.5194/wes-8-1909-2023.
- [147] Carlos Ferreira, Claudia Hofemann, Kristian Dixon, Gijs Van Kuik, and Gerard Van Bussel. 3D wake dynamics of the VAWT: Experimental and numerical investigation. In *48th AIAA Aerospace Sciences Meeting Including the New Horizons Forum and Aerospace Exposition*, 2010. ISBN 9781600867392. doi: 10.2514/6.2010-643.
- [148] Fanzhong Meng, Holger Schwarze, Fabian Vorpahl, and Michael Strobel. A free wake vortex lattice model for vertical axis wind turbines: Modeling, verification and validation. In *Journal of Physics: Conference Series*, volume 555, page 012072. IOP Publishing, dec 2014. doi: 10.1088/1742-6596/555/1/012072.
- [149] L.E.M. Lignarolo, D. Ragni, C. Krishnaswami, Q. Chen, CJ Simão Ferreira, and GJW Van Bussel. Experimental analysis of the wake of a horizontal-axis wind-turbine model. *Renewable Energy*, 70:31–46, 2014.
- [150] Ronald J Adrian and Jerry Westerweel. *Particle image velocimetry*. Number 30. Cambridge university press, 2011.
- [151] Andrea Sciacchitano and Bernhard Wieneke. Piv uncertainty propagation. *Measurement Science and Technology*, 27(8):084006, 2016.



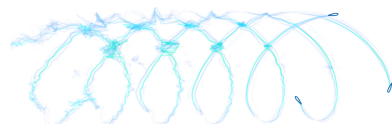
- [152] E N Jacobs. The aerodynamic characteristics of eight very thick airfoils from tests in the variable density wind tunnel (#391). Technical Report 3, National Advisory Committee for Aeronautics, 1931.
- [153] R. E. Sheldahl and P. C. Klimas. Aerodynamic characteristics of seven symmetrical airfoil sections through 180-degree angle of attack for use in aerodynamic analysis of vertical axis wind turbines. Technical report, Sandia National Laboratories, 1981.
- [154] Andrea Sanvito, Vincenzo Dossena, and Giacomo Persico. Formulation, validation, and application of a novel 3d bem tool for vertical axis wind turbines of general shape and size. *Applied Sciences*, 11:5874, 6 2021. ISSN 2076-3417. doi: 10.3390/app11135874.
- [155] C Hirsch and A Mandal. Flow curvature effect on vertical axis darrieus wind turbine having high chord-radius ratio. In *European Wind Energy Conference*, pages 405–410. European Wind Energy Conference, 1984.
- [156] A Giri Ajay, L Morgan, Y Wu, D Bretos, A Cascales, O Pires, and C Ferreira. Aerodynamic model comparison for an x-shaped vertical-axis wind turbine. *Wind Energy Science*, 9:453–470, 2024. doi: 10.5194/wes-9-453-2024.
- [157] William Leithead, Arthur Camciuc, Abbas Kazemi Amiri, and James Carroll. The x-rotor offshore wind turbine concept. In *Journal of Physics: Conference Series*, volume 1356, page 012031. IOP Publishing, 2019.
- [158] Adhyanth Giri Ajay and Carlos Simao Ferreira. Numerical study on wake recovery of vertical-axis wind turbines through fixed blade pitch offsets: H vs x rotors. In *Journal of Physics: Conference Series*, volume 2767, page 072010. IOP Publishing, 6 2024. ISBN 145.90.36.220. doi: 10.1088/1742-6596/2767/7/072010.
- [159] Jens N. Sørensen, Kaya O. Dag, and Néstor Ramos-García. A refined tip correction based on decambering. *Wind Energy*, 19(5):787–802, may 2016. ISSN 10991824. doi: 10.1002/we.1865.
- [160] Niels Troldborg. *Actuator Line Modeling of Wind Turbine Wakes*. PhD thesis, Denmark Technische University, 2009.
- [161] Luis A. Martínez, Stefano Leonardi, Matthew J. Churchfield, and Patrick J. Moriarty. A comparison of actuator disk and actuator line wind turbine models and best practices for their use. *50th AIAA Aerospace Sciences Meeting Including the New Horizons Forum and Aerospace Exposition*, 2012. doi: 10.2514/6.2012-900.
- [162] Pankaj K. Jha, Matthew J. Churchfield, Patrick J. Moriarty, and Sven Schmitz. Accuracy of state-of-the-art actuator-line modeling for wind turbine wakes. *51st AIAA Aerospace Sciences Meeting including the New Horizons Forum and Aerospace Exposition 2013*, (January):1–19, 2013. doi: 10.2514/6.2013-608.
- [163] W. P. Jones and B. E. Launder. The prediction of laminarization with a two-equation model of turbulence. *International Journal of Heat and Mass Transfer*, 15(2):301–314, 1972. ISSN 00179310. doi: 10.1016/0017-9310(72)90076-2.

- [164] F. R. Menter. Two-equation eddy-viscosity turbulence models for engineering applications. *AIAA Journal*, 32(8):1598–1605, 1994. ISSN 00011452. doi: 10.2514/3.12149.
- [165] Amina El Kasmi and Christian Masson. An extended k- model for turbulent flow through horizontal-axis wind turbines. *Journal of Wind Engineering and Industrial Aerodynamics*, 96(1):103–122, 2008. ISSN 0167-6105. doi: <https://doi.org/10.1016/j.jweia.2007.03.007>. URL <https://www.sciencedirect.com/science/article/pii/S0167610507000943>.
- [166] Navid Zehtabiyani-Rezaie and Mahdi Abkar. An extended k model for wake-flow simulation of wind farms. *Renewable Energy*, 222:119904, 2024. ISSN 0960-1481. doi: <https://doi.org/10.1016/j.renene.2023.119904>. URL <https://www.sciencedirect.com/science/article/pii/S0960148123018190>.
- [167] Martin Wosnik, Peter Bachant, Vincent S. Neary, and Andrew W. Murphy. Evaluation of Design & Analysis Code, CACTUS, for Predicting Cross-Flow Hydrokinetic Turbine Performance. *Sandia Report*, (SAND2016-9787), 2016.
- [168] Patrice Meunier and Geoffrey R. Spedding. A loss of memory in stratified momentum wakes. *Physics of Fluids*, 16:298–305, 2 2004. ISSN 1070-6631. doi: 10.1063/1.1630053.
- [169] Sina Shamsoddin and Fernando Porté-Agel. Effect of aspect ratio on vertical-axis wind turbine wakes. *Journal of Fluid Mechanics*, 889:R11–R112, 2020. ISSN 14697645. doi: 10.1017/jfm.2020.93.
- [170] Delft High Performance Computing Centre (DHPC). DelftBlue Supercomputer (Phase 1). <https://www.tudelft.nl/dhpc/ark:/44463/DelftBluePhase1>, 2022.
- [171] Ángel Jiménez, Antonio Crespo, and Emilio Migoya. Application of a LES technique to characterize the wake deflection of a wind turbine in yaw. *Wind Energy*, 13(6): 559–572, sep 2010. ISSN 10991824. doi: 10.1002/we.380.
- [172] Paul A. Fleming, Pieter M.O. Gebraad, Sang Lee, Jan Willem van Wingerden, Kathryn Johnson, Matt Churchfield, John Michalakes, Philippe Spalart, and Patrick Moriarty. Evaluating techniques for redirecting turbine wakes using SOWFA. *Renewable Energy*, 70:211–218, oct 2014. ISSN 09601481. doi: 10.1016/j.renene.2014.02.015.
- [173] Srinivas Guntur, Niels Troldborg, and Mac Gaunaa. Application of engineering models to predict wake deflection due to a tilted wind turbine. *European Wind Energy Conference and Exhibition 2012, EWEC 2012*, 2:1044–1049, 2012.
- [174] Lixiang Luo, Nilabh Srivastava, and Praveen Ramaprabhu. A study of intensified wake deflection by multiple yawed turbines based on large eddy simulations. In *33rd Wind Energy Symposium*. American Institute of Aeronautics and Astronautics Inc., 2015. ISBN 9781624103445. doi: 10.2514/6.2015-0220.



- [175] Nathaniel J. Wei, Ian D. Brownstein, Jennifer L. Cardona, Michael F. Howland, and John O. Dabiri. Near-wake structure of full-scale vertical-axis wind turbines. *Journal of Fluid Mechanics*, 914:A17, 2021. ISSN 14697645. doi: 10.1017/jfm.2020.578.
- [176] Lukas Vollmer, Gerald Steinfeld, Detlev Heinemann, and Martin Kühn. Estimating the wake deflection downstream of a wind turbine in different atmospheric stabilities: an LES study. *Wind Energy Science*, 1(2):129–141, jul 2016. ISSN 23667451. doi: 10.5194/wes-1-129-2016.
- [177] Haohua Zong and Fernando Porté-Agel. A point vortex transportation model for yawed wind turbine wakes. *Journal of Fluid Mechanics*, 890, 2020. ISSN 14697645. doi: 10.1017/jfm.2020.123.
- [178] Peter Bachant and Martin Wosnik. Modeling the near-wake of a vertical-axis cross-flow turbine with 2-d and 3-d rans. *Journal of Renewable and Sustainable Energy*, 8: 53311, 9 2016. ISSN 19417012. doi: 10.1063/1.4966161.
- [179] Gerard Cortina, Marc Calaf, and Raúl Bayoán Cal. Distribution of mean kinetic energy around an isolated wind turbine and a characteristic wind turbine of a very large wind farm. *Physical Review Fluids*, 1(7):1–18, 2016. ISSN 2469990X. doi: 10.1103/PhysRevFluids.1.074402.
- [180] Pankaj K. Jha, Matthew J. Churchfield, Patrick J. Moriarty, and Sven Schmitz. Guidelines for volume force distributions within actuator line modeling of wind turbines on large-eddy simulation-type grids. *Journal of Solar Energy Engineering, Transactions of the ASME*, 136, 8 2014. ISSN 01996231. doi: 10.1115/1.4026252.
- [181] L. A. Martínez-Tossas, M. J. Churchfield, and C. Meneveau. Optimal smoothing length scale for actuator line models of wind turbine blades based on gaussian body force distribution. *Wind Energy*, 20:1083–1096, 6 2017. ISSN 10991824. doi: 10.1002/we.2081. URL <https://onlinelibrary.wiley.com/doi/full/10.1002/we.2081><https://onlinelibrary.wiley.com/doi/abs/10.1002/we.2081><https://onlinelibrary.wiley.com/doi/10.1002/we.2081>.
- [182] S. McTavish, D. Feszty, and T. Sankar. Steady and rotating computational fluid dynamics simulations of a novel vertical axis wind turbine for small-scale power generation. *Renewable Energy*, 41:171–179, may 2012. ISSN 09601481. doi: 10.1016/j.renene.2011.10.018.
- [183] André F. P. Ribeiro, Carlos S. Ferreira, and Damiano Casalino. Vertical axis wind turbine wake steering by pitched struts and blades. *Journal of Physics: Conference Series*, 2767(9):092004, jun 2024. doi: 10.1088/1742-6596/2767/9/092004.
- [184] Masoumeh Gharaati, Shuolin Xiao, Luis A. Martínez-Tossas, Daniel B. Araya, and Di Yang. Large-eddy simulations of turbulent wake flows behind helical- and straight-bladed vertical axis wind turbines rotating at low tip speed ratios. *Physical Review Fluids*, 9:074603, 7 2024. ISSN 2469990X. doi: 10.1103/PHYSREVFLUIDS.9.074603/FIGURES/30/THUMBNAIL.

- [185] Chris Garrett and Patrick Cummins. The efficiency of a turbine in a tidal channel. *Journal of Fluid Mechanics*, 588:243–251, 2007. doi: 10.1017/S0022112007007781.
- [186] P. J. Richards and R. P. Hoxey. Appropriate boundary conditions for computational wind engineering models using the $\kappa - \epsilon$ turbulence model. *Journal of Wind Engineering and Industrial Aerodynamics*, 46-47(C):145–153, 1993. ISSN 01676105. doi: 10.1016/0167-6105(93)90124-7.
- [187] Victor Mendoza. *Aerodynamic Studies of Vertical Axis Wind Turbines using the Actuator Line Model*. Uppsala University, 2018. ISBN 9789151303383.
- [188] James F. Manwell, Jon G. McGowan, and Anthony L. Rogers. *Wind Energy Explained: Theory, Design and Application*. John Wiley & Sons, Chichester, West Sussex; Hoboken, NJ, 2nd edition, 2010. ISBN 978-1-119-99436-7.
- [189] Kurt S. Hansen, Rebecca J. Barthelmie, Leo E. Jensen, and Anders Sommer. The impact of turbulence intensity and atmospheric stability on power deficits due to wind turbine wakes at horns rev wind farm. *Wind Energy*, 15(1):183–196, 2012. doi: <https://doi.org/10.1002/we.512>.
- [190] B H Bulder, E T G Bot, and G Bedon. Optimal wind farm power density analysis for future offshore wind farms ECN cost model evaluation for large wind farms. Technical report, TNO Repository, 2018.
- [191] Peter Enevoldsen and Mark Z. Jacobson. Data investigation of installed and output power densities of onshore and offshore wind turbines worldwide. *Energy for Sustainable Development*, 60:40–51, feb 2021. ISSN 09730826. doi: 10.1016/j.esd.2020.11.004.
- [192] L Vita, U. S. Paulsen, T. F. Pedersen, H. A. Madsen, and F. Rasmussen. A novel floating offshore wind turbine concept. In *European Wind Energy Conference and Exhibition 2009, EWEC 2009*, volume 7, pages 4497–4502, 2009. ISBN 9781615677467.
- [193] Adhyanth Giri Ajay and Carlos Simao Ferreira. A modified version of *turbinesFoam* that accounts for coned blades. *GitHub*, July 2024. doi: 10.5281/zenodo.1234.

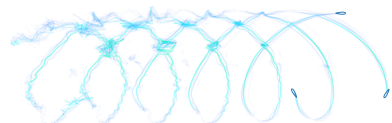


ACKNOWLEDGMENTS

Well, I've heard that a PhD is supposed to be one of the most rewarding yet challenging and stress inducing journeys of life. Luckily I had several awesome people from all over the world that made this journey waaaay easier than it was supposed to be.

I would like to give my deepest thanks to my PhD supervisory team. **Carlos**, firstly thank you for giving me the opportunity to do this PhD. You guided me so much during the formative years of my PhD, both academically and otherwise. From intense coding sessions to fun conferences, you always provided freedom to define how I want our meetings and interactions to be. I'm sure that the rocky start to my PhD could not have been rectified if not for your support and encouragement to explore my PhD in a different direction. I quite enjoyed our conversations about music and One Punch Man when we had some time to chill. It's a pity I couldn't continue working with you in the last year, and I hope you are recovering well! **Roeland**, it took a while after I started my PhD to actually meet you in person, but I'm extremely grateful for your support throughout my PhD. Your knowledge and wisdom about structures is immense, and I'm glad you could share a small percentage of it while working on the XROTOR project with me. I could not have done any of the structural and aeroelastic works without your support, and your constant encouragement and words of appreciation always gave me a mental boost. It is regretful that we could not publish the content that we accomplished together due to time constraints, but I deeply thank you for prioritising my thesis completion over other commitments. I also loved our conversations about classical music and other nerdy curiosities. **Delphine**, you stepped in when I most needed technical supervision despite your already busy schedule. I deeply thank you for that. I quite enjoyed our weekly meetings due to their refreshing change of pace and discussing extensive theories and ideas. Your role in defining the last portions of my thesis cannot be understated. Your sound technical advise to test out new hypotheses I brought up were extremely valuable. Thank you for being a part in this journey of mine.

I want to thank all the people I met at TU Delft (directly or indirectly), who made this PhD lively, memorable, and genuinely enjoyable. **Abhratej**, thanks for the wonderfully nerdy factoids and the niche book recommendations. **Abhyuday**, always a pleasure talking prog music, food, and travel with you; your FOOL t-shirt still makes me laugh. **Ali**, I never ran out of things to discuss with you; thanks for the dinners, games, and movie nights. **Anand**, I always appreciated your elaborate travel suggestions, especially for France. **André**, your humour and technical help were always welcome; I'm still waiting for Chill Man Music to return. **Andrea**, your short visit somehow turned into a great friendship; thanks for one of the most adventurous hikes of my life (and for the Pizzeria recipe). **Anwasha**, I enjoyed the funny stories you always have about Kiran or Flavio. **Augustin**, your humour and passion for cooking made every interaction fun; best of luck back in France. **Bruce**, thank you for your long-distance guidance on structural mechanics and using NASTRAN. **Carlos**, thanks for telling me your guacamole recipe. I'll definitely give it a shot. **Charis**, thanks for sharing both your numerical insights and



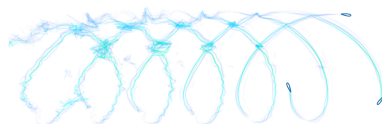
Greek recommendations. **Christina**, you gave me so much Naples food-related lore that I don't have space in my head anymore. **Clem**, your humour, competitiveness, and the infamous badminton smash incident will always stay with me. **Dachuan**, it was always a pleasure to laugh with you during the various dinners. **David**, starting and working on this PhD together made the process far more enjoyable (and occasionally far less productive). **Deepali**, I admire your dedication to fitness; thanks for the plant-care lessons and early presentation help. **Dong**, I need your training to become the next dumpling master. **Dylan**, your suits and larger-than-life personality always made conferences unforgettable. **Elian**, you and Flavio are amazing hosts and I always enjoyed the dinners. **Erik**, your creativity shaped many great gatherings, watch-parties, and deep video-game discussions. Hopefully there won't be anymore Covid-parties. **Evert**, your unique views on the world fascinate me. **Evita**, your and Erik's fun travels always brings a smile to my face. **Federico**, child-chess prodigy, I enjoyed the positive and cheerful energy you brought everywhere. **Felipe**, thanks for bringing good vibes and good times. **Fernanda**, it was fun to play badminton, whenever you managed to join. **Ferran**, it was really fun to work with you during the experiments and during the model development. Thanks for introducing Elden Ring to me! **Filippo**, I really enjoyed you as an office mate during your short visit. Thank you for taking me and David to the Escher museum. **Flavio**, thanks for hosting so many dinners and barbecues; your Instagram stories remain a constant source of either joy or agony. **George**, I enjoyed your curiosity and the way our conversations spiralled into deep dives. **Hafiz**, I enjoyed our conversations about Uncle Roger and his antics. **Haoyuan**, I'm sorry I can't type out your GIFs, but your humour and endless topics (from Pokémon to video games) were always fun. **Iaria**, our pranks on David helped me survive the first year; I still wonder whether my camera lens is on that mountain outside of Milan. **Ivan**, it was lovely to have you as an office mate during your brief visit here. **Jatinder**, I appreciated our corridor chats and your occasional badminton cameos. **Jelle**, your laid-back attitude and holiday-maximisation skills are inspirational; keep drumming! **Jiaxin**, thanks for the fun coffee-machine chats and for sharing your wonderful paintings and travel ideas. **Jingna**, you were a great office mate, prankster, and friend; before LLMs became mainstream, you saved my simulations many times. **Kiran**, thanks for the constant chats, the Tamil rants about David, the games, the races, and the badminton; may Malenia remain undefeated. **Laurie**, your visit to Delft sparked a key collaboration; thanks for the hikes and for sharing the best of Scotland and Cornwall. **Likhitha**, from our Masters to this PhD, you've always been a constant source of support. This acknowledgement section won't have enough space to list out all the things I need to thank you for, dumbo. **Livia**, our iPhone debates kept me entertained when work didn't. **Marie**, you and Ali have made all the impromptu dinners and movie nights very enjoyable! **Matteo**, thanks for all the laughs and for the pistachio liqueur. **Mehtab**, your conversations were always engaging, whether in Delft or Colorado; I await the launch of Inshallah Biriyani. **Mihir**, your dance videos gave me existential crisis, but you've been a solid friend otherwise. I hope your photography finally surpasses Reshma's. **Nikhitha**, I enjoyed our discussions on cultural differences and the perspectives you bring from your international experiences. **Nirav**, my simulations wouldn't have run properly without you troubleshooting them. **Olivier**, thanks for all the fun conversations about endurance racing. **Rention**, even with your rare office appearances, you always made things entertaining and gave me great rock/metal recommendations. **Ricardo**, Mr.

Finance, I miss your dad-jokes, but I do hope Fabiosh never finds me; next time rent a bicycle in the Netherlands, they don't run out of *stock*. **Rishi**, your contagious laughter brightened every day; from card games to anime deep dives, you always lifted the mood (even after I spoiled minor parts of *One Piece*). **Rushi**, I enjoyed our lunch-break chats and your calming vibe. **Saskia**, it was super nice to work with you on the optimisation algorithm. I really liked your self-reliance towards your thesis! **Seba**, your help with setting up the HPC made my entire PhD possible; thank you. **Sen**, I appreciated your relaxed conversations and our dinners at Hot King and Da Dong Bei. **Shantanu**, from music to badminton, you were a great rival and friend; thanks for pushing me to run again, and may your chess skills improve. **Shyam cheta**, nerding about photography and F1 with you and Simone was always fun, and practising Malayalam with you was comforting. **Simone**, despite your unhinged real life and social media presence, I enjoyed all the F1 memes, rants, and sim racing. **Sumit**, thanks for the casual chats and for the Japan hiking tips. **Udhaya**, I always enjoyed running into you and talking in Tamil. **Uri**, as a fellow *One Piece* manga reader, discussing theories made both the series and our PhDs more fun; our quest to ~~find the One Piece~~ finish the thesis on time was worth it. **Wei**, thank you for your support and collaboration during uncertain times. **Yan**, it was a pleasure to work with you on the XROTOR project and was always happy to hang out with you as well. **Yanan**, thanks for the early photography advice, and I stand by my belief that you don't have allergies to alcohol.

On to the other folks in the Netherlands. **Ranjan, Reddhi, and Arshdeep**, you eased my transition to the Netherlands significantly. From dinners, Diwali parties, and everything else, thanks for making my life here more fun! **Hemanth**, although we didn't meet often, it was nice to occasionally see a familiar face from Chennai. **Arivu**, you came to the Netherlands quite recently, but you definitely brought nostalgia from our SSN days. **Anish** and **Naveen**, you two being in Eindhoven made it difficult to meet often, but I always enjoyed meeting you both! Would be really nice to do something musical someday soon! **Diwakar**, thanks for the furniture and the camera! I hope to meet you sometime soon to see your wife and kid! **Sowmya**, it was nice to know a familiar face from SSN. Thanks for introducing me to things around Delft/The Hague.

Beyond the Netherlands, I am grateful for the friendships that have supported me across continents. **Aditya, Madhav, Sharan**, thanks for the occasional group video calls to lift my mood with our usual naaansense. I'm quite sure that I wouldn't have even started my PhD if not for you all. **Prajwal**, thanks for the game recommendations and it was fun to text about Baldur's Gate 3.

Equally important were the friends back home, whose presence never faded with distance. **Bharat**, you have always been a pillar of support and encouragement. Our Himalayan trip, your wedding, and our never ending video calls have been some amazing moments we shared during this time. Hopefully I'll see you here for the defence. **Kaavya**, your time in Europe was short, but it was memorable! I'll forever find your prison and travel stories memorable. **Ritwik**, our detailed talks about photography, travel planning, and everything else are always entertaining. I'm always jealous of your crazy travel plans, but I'm glad I could join you to the Himalayas a few years ago. **Durga**, the first year of my PhD would have been dull without your text messages and video calls! Thanks for all the fun conversations throughout the years! **Prem**, from countless gaming sessions,



WhatsApp debates, and everything else over the past 14 years, thanks for being an amazing friend that I can always talk to. **Baski**, Prem introduced us online, but I'm quite happy that we have become good friends for gaming.

Mummy, I'm sure you didn't understand most of what I did for the past 4-ish years, but I could not have done this without your eternal support. I am glad you were able to visit me during these years and have gained an appreciation for travelling around the world. To the rest of family, there are a lot of you so I have grouped you all here as this thesis is already long enough. Thanks for always being there for me, supporting me from many pockets around the world.

Bao, this PhD would have been infinitely less enjoyable without you. There were countless days when I ranted about my work, art, movies, TV shows, gaming triumphs and failures (Elden Ring and Baldur's Gate specifically), or the general state of the world, and you were always there to lend an ear. Those moments genuinely helped my mindset, both in and out of work. Whether it was concerts, travelling, cooking, gaming, or our never-ending inside jokes, I'm truly grateful that I could do all these with you. Who knows what other happy accidents we'll end up loving? Rallying, perhaps? xD Thank you for being the most caring, supporting, and fun person throughout this journey!

Adhyanth
Delft, November 2025


LIST OF PUBLICATIONS

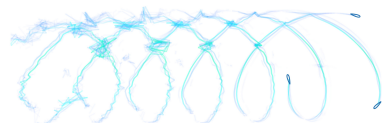
JOURNAL AND CONFERENCE PUBLICATIONS

9. S. van Nieuwstadt, **A. Giri Ajay**, W. Yu, *Multi-Objective Optimization of Vertical Axis Wind Turbine Pitch Control*, Journal of Physics: Conference Series, *accepted*.
8. **A. Giri Ajay**, D. De Tavernier, *Enhancing wake recovery in vertical-axis wind farms through blade pitching*, Journal of Renewable and Sustainable Energy, *under review*.
7. **A. Giri Ajay**, D. Bensason, D. De Tavernier, *Validation of the near-wake of a scaled X-Rotor vertical-axis wind turbine predicted by a free-wake vortex model*, Wind Energy Science, **10**, 1829–1847, 2025. DOI.
6. **A. Giri Ajay**, C. Ferreira, *A numerical investigation of wake recovery for an H- and X-shaped vertical-axis wind turbine with wake control strategies*, Physics of Fluids **36** (12): 127161, 2024. DOI.
5. D. Bensason, A. Sciacchitano, **A. Giri Ajay**, C. Ferreira, *A Study of the Near-Wake Deformation of the X-Rotor Vertical-Axis Wind Turbine With Pitched Blades*, Wind Energy **27** (11), 1388-1411 2024. DOI.
4. C. Ferreira, D. Bensason, T. J. Broertjes, A. Sciacchitano, F. Martins, **A. Giri Ajay**, *Enhancing Wind Farm Efficiency Through Active Control of the Atmospheric Boundary Layer's Vertical Entrainment of Momentum*, Journal of Physics: Conference Series **2767** (9), 092107, 2024. DOI.
3. **A. Giri Ajay**, C. Ferreira, *Numerical study on wake recovery of vertical-axis wind turbines through fixed blade pitch offsets: H vs X rotors*, Journal of Physics: Conference Series **2767** (7), 072010, 2024. DOI.
2. **A. Giri Ajay**, L. Morgan, Y. Wu, D. Bretos, A. Cascales, O. Pires, C. Ferreira, *Aerodynamic model comparison for an X-shaped vertical-axis wind turbine*, Wind Energy Science, **9**, 453–470, 2024. DOI.
1. **A. Giri Ajay**, KL Harikrishna, S Bharatharajan, MK Avinashilingam, *Design and development of light weight mechanical staircase climbing trolley with better stress distribution*, Journal of Chemical and Pharmaceutical Sciences, Special Issue 7, 192-194, 2017. DOI.

DATASETS

5. **A. Giri Ajay**, D. De Tavernier, *Supporting data for "Enhancing wake recovery in vertical-axis wind farms through blade pitching"*, 4TU.ResearchData, 2026. DOI.
4. **A. Giri Ajay**, D. Bensason, D. De Tavernier, *Supporting data for "Validation of the near-wake of a scaled X-Rotor vertical-axis wind turbine predicted by a free-wake vortex model"*, 4TU.ResearchData, 2025. DOI.

 Included in this thesis.



3. **A. Giri Ajay**, C. Ferreira, *Supporting data for research "A numerical investigation of wake recovery for an H- and X-shaped vertical-axis wind turbine with wake control strategies"*, 4TU.ResearchData, 2024. DOI.
2. D. Bensason, A. Sciacchitano, **A. Giri Ajay**, C. Simao Ferreira. *Supporting data belonging to publication: "A study of the near wake deformation of the X-Rotor vertical-axis wind turbine with pitched blades"*, 4TU.ResearchData. 2024. DOI.
1. **A. Giri Ajay**, L. Morgan, Y. Wu, D. Bretos, A. Cascales, O. Pires, C. Ferreira, *Aerodynamic model comparison for an X-shaped vertical-axis wind turbine (v0.2)*, Zenodo, 2023. DOI.

CURRICULUM VITÆ

Adhyanth GIRI AJAY

29-08-1996 Born in Coimbatore, India.

EDUCATION

2021 - 2025 PhD in Aerospace Engineering
Delft University of Technology, Delft, The Netherlands

2018 - 2020 Master of Science in Aeronautics and Astronautics
Purdue University, West Lafayette, USA

2014 - 2018 Bachelor of Engineering in Mechanical Engineering
SSN College of Engineering, Anna University, Chennai, India

2010 - 2014 Higher Secondary School
Chettinad Vidyashram, Chennai, India

EXPERIENCE

2021 - 2025 PhD Candidate
Delft University of Technology, Delft, The Netherlands

2020 - 2021 Research Associate
Indian Institute of Technology - Madras, Chennai, India

